Daniel Knez, MSc

Scanning transmission electron microscopy of metallic clusters and nanoalloys

DOCTORAL THESIS

to achieve the university degree of

Doktor der technischen Wissenschaften

submitted to

Graz University of Technology

Supervisor

Ao.Univ.-Prof. Dipl.-Ing. Dr.techn. Ferdinand Hofer

Institute of Electron Microscopy and Nanoanalysis

Graz, June 2017

AFFIDAVIT

I declare that I have authored this thesis independently, that I have not used other than the declared sources/resources, and that I have explicitly indicated all material which has been quoted either literally or by content from the sources used. The text document uploaded to TUGRAZonline is identical to the present doctoral thesis.

Date	Signature

Abstract

This thesis is devoted to scanning transmission electron microscopy of small metallic clusters and nanoalloys. Both experimental and computational methods were applied to study size, morphology and elemental distribution of these materials at atomic resolution.

The particles in question are grown with the superfluid helium droplet technique which distinguishes itself from other methods for nanoparticle synthesis by its high purity and flexibility. We explore a variety of sizes and morphologies, ranging from small clusters comprised of a few hundred atoms to elongated particles with core-shell morphology and complex kinked and branched structures with a lateral dimension of several hundred nanometres. Our focus lies on mono- and bimetallic clusters comprised of Ni, Au, Ag, AuAg, AuNi, or CrAu. From our experimental results, we are not only able to study thermodynamical and chemical characteristics of different material systems at the nanoscale; but also to draw conclusions about the physical properties of superfluid He droplets. As support we use classical amorphous carbon substrates as well as graphene and hexagonal boron nitride thin-films.

We apply a variety of analytical methods, such as electron energy loss spectrometry (EELS), energy dispersive X-ray spectrometry (EDXS), Z-contrast quantification, and principle component analysis. Furthermore, we developed strategies to reduce hydrocarbon contamination and studied beam induced sample changes.

Knock-on damage is found to be the predominant mechanism for the observed dynamics of pure metallic clusters. The principle mechanisms are elucidated via molecular dynamic simulations. For Ag and Ni we furthermore observe beam induced oxidation effects, accompanied by significant structural changes. The clusters are transformed to hollow and toroidal shapes driven by the nanoscale Kirkendall effect. We study the kinetics and give values for the mean oxidation rate via absolute EELS quantification and molecular dynamics simulations.

Kurzfassung

In dieser Arbeit widmen wir uns der Charakterisierung von kleinen metallischen Nanostrukturen mithilfe von aberrationskorrigierter, analytischer Rasterdurchstrahlungselektronenmikroskopie. Diese Strukturen werden dabei im Inneren von superfluiden Heliumtröpfchen synthetisiert. Diese Methode zeichnet sich durch die hohe Reinheit der abgeschiedenen Partikel und ihre hohe Flexibilität aus. Eine Reihe von Partikeln mit unterschiedlicher Größe und Morphologie, angefangen bei kleinsten Clustern, bestehend aus wenigen hundert Atomen, über core-shell Partikel mit elongierter oder linsenförmiger Morphologie, bis hin zu komplexen Nanostrukturen mit einer Vielzahl von Knicken und Verzweigungen. Die Strukturen, die in dieser Arbeit behandelt werden, bestehen aus Ni, Au, Ag, AuAg, AuNi oder CrAu. Als Substrat wurden neben klassischen, amorphen Kohlenstofffilmen auch Graphen und Dünnfilme aus hexagonalem Bornitrid verwendet. Die experimentellen Ergebnisse erlauben nicht nur Rückschlüsse auf die physikalischen Eigenschaften der Heliumtröpfchen; bedingt durch ihre hohe Reinheit war es uns auch möglich unterschiedliche Materialsysteme auf der Nanoskala zu studieren.
Die Untersuchungen erfolgten mit verschiedenen analytischen Methoden, wie Elektronenenergieverlustspektroskopie, energiedispersiver Röntgenspektroskopie, Z-Kontrast Quantifizierung und Hauptkomponentenanalyse. Darüber hinaus wurden Strategien zur Verminderung von Kohlenwasserstoffkontamination und elektronenstrahlungsinduzierter Probenveränderung entwickelt. Der Impulsübertrag der Elektronen auf den Atomkern wird dabei als der dominante Mechanismus bei reinen, metallischen Clustern identifiziert. Wir zeigen, dass diese Vorgänge durch Molekulardynamiksimulationen theoretisch behandelt werden können. Für Ni und Ag Strukturen wurden außerdem strahlinduzierte Oxidationsvorgänge beobachtet, welche von deutlichen Strukturänderungen begleitet werden. Angetrieben durch den Kirkendalleffekt werden die Cluster dabei zu hohlen und toroidalen Formen transformiert.

Acknowledgements

The present work would not have been possible without the direct or indirect help of many people. At this point I want to give my acknowledgements to them.

First of all I want to thank my supervisor **Prof. Ferdinand Hofer** for giving me the chance to work on this very interesting field of research at this renowned institute and for providing me the professional and financial framework. He always was the first point of contact for all kind of problems concerning my work and introduced me into the way of scientific work.

A particular debt of gratitude is also owed to my group leader **Prof. Gerald Kothleitner** and **Prof. Werner Grogger** for highly valuable discussions and for providing me professional support.

I also want to express my gratitude to the cluster group at the Institute for Experimental Physics, led by **Prof. Wolfgang Ernst** for the fruitful and highly interesting cooperation. There, I want to thank especially **Philipp Thaler**, **Alexander Volk**, **Martin Schnedlitz** and **Max Lasserus** for discussions and support.

Great thanks is owed to all of my **colleagues at the institute**, particularly my office colleagues **Georg Haberfehlner**, **Manfred Nachtnebel** and **Lukas Konrad**, and also to **Evelin Fisslthaler**, **Angelina Orthacker** and **Christian Gspan**. I had many inspiring discussions and a great time with them, in and outside of work. Especially, I want to thank **Thomas Ganner**, not only for his support with AFM experiments and his collegiality, but also for being a friend and moral support.

Acknowledgements have also to be given to the whole laboratory team, in particular **Martina Dienstleder** and **Manuel Paller** for supporting me with my work in the laboratory. Manuel also designed some 3D rendering artwork, that was used in this thesis and several publications.

Most importantly I want to thank **my family**, especially **my parents**, **my grandparents** and **my sister** for their backup and their tolerance during my whole academic study. Furthermore I want to thank all of **my friends** for their company and their mental support. Both family and friends helped me by relieving stress from me whenever I needed it.

My deepest thanks, however, is dedicated to my girlfriend **Johanna** not only for countless discussions, which greatly helped me with my work, but also for her understanding, her patience and her love.

Finally, I want to acknowledge financial support by the European Union within the 7th Framework Program (FP7/2007-2013) under Grant Agreement No. 312483 (ESTEEM2), the Austrian Research Promotion Agency (FFG) in the project SOLABAT (853627) and Quantitative Analyse innerer Grenzflächen (850220/859238) and by the Federal Ministry of Science, Research and Economy with the project “Infrastrukturförderung 2015”, because without money this thesis would also not have been possible.

Contents

1. Introduction

With the availability of aberration-correctors scanning transmission electron microscopy (STEM) has become one of the most versatile tools for the characterisation of nanostructured materials during the past decade. In combination with electron energy loss spectrometry (EELS) and energy dispersive X-ray spectrometry (EDXS) in principle chemical information can be extracted at atomic resolution [1–3]. Various techniques based on STEM have been developed, which proved to be especially useful for the characterisation of small metallic nanostructures [4–7].

Interest in such structures increased in recent years by virtue of their outstanding physical properties [8]. This is particularly true for nanoparticles, comprised of less than a few thousand atoms [9]. For such particles the term "cluster" has been introduced. Clusters distinguish themselves from molecules by their varying size and composition. The high percentage of low-coordinated surface atoms in clusters gives rise to promising applications, but also imposes difficulties in terms of their stability and reactivity in environmental conditions. By combining different species, clusters can be modified to prevent unwanted reactions and oxidation effects or to tailor, for instance, their optical and magnetic properties [10–13].

The clusters and nanostructures that were investigated within this work have been synthesised with the He droplet technique at the Institute for Experimental Physics of the Graz University of Technology. In literature, first experiments with He droplet doping were conducted to study superfluidity on a microscopic scale and to perform molecule spectroscopy [14–18]. More recently, it has been shown that He droplets also provide a gentle, low temperature 0.37 K environment for cluster growth. The cluster sizes and morphologies can be controlled by adjusting the He droplet size and the pickup conditions [19]. Previous work has shown that this method is capable of depositing Ag clusters in a range of size between 60 and 6000 atoms [20], or wire shaped Si particles with multiple Ag cores [21]. In principle such structures can be deposited on arbitrary substrates with high purity and a variety of morphologies, which is not achievable with other techniques. The growth conditions in the He droplets strongly influence the morphology of the obtained clusters. The existence of quantum vortices results in elongated and wire shaped cluster morphologies [22–24]. Vice versa information about the physical properties of the droplets can be obtained by structural analysis of the deposited clusters. For instance, the question if segmented patterns of pure Ag wires are caused by intrinsic mechanisms inside the He droplets or occur during deposition, caused some controversy in literature [21, 25]. This issue has been clarified within our work [22].

In all studies, that have been conducted in advance about cluster deposition with He droplets, classical transmission electron microscopy (TEM) was used as primary characterisation tool [20, 21, 26–28]. Previous high resolution TEM investigations at our institute revealed the influence of substrate interaction on the morphology of small Ag clusters [29]. When clusters start to contain more than one element, information about elemental distribution is highly valuable. Therefore, one of the main goals of this thesis is to obtain new insights by taking advantage of state-of-the-art STEM. However, previous experiments revealed several problems, which hindered the use of HRSTEM with sufficient contrast, resolution and signal-to-noise ratio (SNR), to allow the element sensitive analysis and quantification of clusters. One issue concerned hydrocarbon contamination, which is a common phenomenon in electron microscopy. If a signal generated by only a few atoms needs to be detected, even small amounts of hydrocarbon contaminants make it difficult to gain useful results. Another limiting factor is beam induced damage. STEM has to be classified as destructive method in many cases, due to the high current densities occurring in a highly focused electron beam. This is especially true for small metallic clusters with a high percentage of low-coordinated, and therefore, weakly bound atoms.

Based on these preliminary experiences we aimed to improve sample preparation, characterisation and data analysis techniques, towards quantitative elemental analysis at atomic resolution, even on smallest structures.

The methods used are described in-depth in chapter 2 of this work. We start with a brief introduction of basic physical principles of STEM imaging and EELS and EDXS signal generation. We describe the procedures that are needed to perform “atom counting” by means of quantitative high-angle annular dark field (HAADF) imaging. Basic quantification techniques using EELS and EDXS are briefly introduced. On the post-acquisition side we present techniques to increase the signal-to-noise ratio with sophisticated data evaluation, based on principal component analysis (PCA), for both: image and spectral data sets.

Chapter 3 is devoted to the theoretical and computational part of this thesis. We study electron beam induced damage effects at energies and doses typically used in STEM analysis. Our goal was to develop methods to reduce, or possibly even to take advantage, of beam induced effects in metallic clusters. To this end we developed a new molecular simulation code, which enables us to gain deeper understanding about beam induced dynamics, dependent on material, structure and experimental conditions.

The experimental results are presented in chapter 4. In the first section we present work on the use of 2D materials as cluster supports in the TEM, which has been shown previously for graphene [30, 31]. With such substrates the background signal caused by the substrate can be minimised, allowing even single atom spectroscopy [32, 33]. However, it has also been shown that many metals mediate the etching of graphene under electron irradiation [34], which has not been observed for hexagonal boron nitride (h-BN) [35]. We applied previously gained experience in the preparation of atomically thin, free-standing graphene to produce ultra-thin boron nitride films as cluster supports for TEM based characterisation methods. As a proof of concept we deposited clusters on bilayer h-BN and demonstrated its capability for EELS analysis.

The next section within the results chapter is devoted to the electron induced oxidation of metallic nanostructures. The oxidation is accompanied by significant morphology changes and hollowing effects, due to the nanoscale Kirkendall effect (NKE). The Kirkendall effect generally denotes the void formation due to differences in diffusivity at solid interfaces. Usually this effect is thermally activated [36, 37], but the activation energy can also be provided by high-energy electrons. We report and discuss the creation of single crystalline NiO ring structures consisting of less than 3000 nickel atoms and the oxidation of Ag nanowires at cryo-conditions. We demonstrate the possibility to trigger a chemical reaction in a highly localised manner with a focused electron beam and explore the underlying mechanisms.

Bimetallic clusters, with core-shell morphologies, are the focus of the next section. Three different material systems, AuAg, NiAu and CrAu, were investigated. We explored the thermodynamic properties and stability of each system at room temperature. For NiAu particles we conducted *in situ* heating experiments. One important question was if a non-noble metal like Ni or Cr can be protected from oxidation by a Au shell.

Finally, we present a method to obtain quantitative, three-dimensional structural information from a single metallic cluster, comprised of only about 600 atoms, based on HAADF contrast information. It has previously been shown that the HAADF signal can be used for atom counting [38]. Our approach is based on previous work by Jones et al. [4], combined with a Metropolis Monte Carlo energy minimisation technique.

2. Methods

Analytical high-resolution (scanning) transmission electron microscopy (STEM) was the main tool used for the characterisation of nanostructures within this thesis. The most important experimental methods applied here are briefly explained in the following chapter. Other important methodical aspects within this work included sample preparation and data processing. Both will also be covered by this chapter.

2.1. Transmission Electron Microscopy

Electron microscopy, being the most important tool for the characterisation of nanostructured materials, has undergone a rapid development in recent years. Especially, developments in the field of computer technology and the advent of correctors for the aberrations of electron lenses have pushed the field forward. These developments nowadays allow imaging and chemical analysis at the single atomic scale.

Transmission electron microscopy (TEM) relies on the effect that thin samples with a thickness of usually below 100 nm, can be penetrated by high energy electrons. These electrons are also referred to as primary electrons. Due to different types of interactions these electrons undergo with sample atoms, they carry a lot of information about the sample after transmission. This is true also for electrons (secondary electrons, Auger electrons) and photons (X-ray, Cathodoluminescence) that are generated during such interactions. Some of the information they carry can then be extracted by different detection and analysis techniques. Figure 2.1 gives a illustration of generated signals. Those which were used in this thesis are described briefly in the following.

In principle we distinguish between two modes in TEM.

In conventional TEM (CTEM) the sample is illuminated by a parallel beam and image formation is done mainly by the objective lens followed by projection lenses, which are located after the specimen. Thus the resolution of the instrument is mainly limited by objective lens aberrations. Images are usually recorded with a CCD array, either located after the projection lenses or after an energy filter attached to the end of the microscope column. This energy filter is called GIF (Gatan imaging filter) in the following. The GIF allows to select electrons which lost a certain amount of energy in the specimen and thereby energy filtered images (EFTEM) can be acquired. The CTEM mode is similar to the configuration in a light microscope operated in transmission.

In scanning mode (STEM), an electron beam is focused to a tiny probe, which is scanned over the sample. Images are recorded pixel by pixel. In modern aberration-corrected microscopes the electron probe can be as small as 50 pm, which is approximately the size of a hydrogen atom. One big advantage of this mode over CTEM is the possibility to control the lateral position of the beam very precisely. Analytical information can therefore be obtained highly localised. The instrumental resolution is limited by aberrations of the probe forming lenses (condenser lens system). Another important advantage is the availability of a vast amount of signals at the same time. Electrons scattered to different angles can be collected with detectors, located at different positions collecting electrons scattered to different angles. Dependent on the angular range of the detector we can distinguish between high-angle annular dark field (HAADF), annular dark field (ADF) and bright field detectors. The angular range can be varied with the camera length and can give complementary information. At the same time characteristic X-rays, generated by ionization events, can be detected by energy dispersive X-ray spectroscopy (EDXS) and the energy loss of primary electrons due to inelastic scattering can be analysed with an electron energy loss spectrometer (EELS).

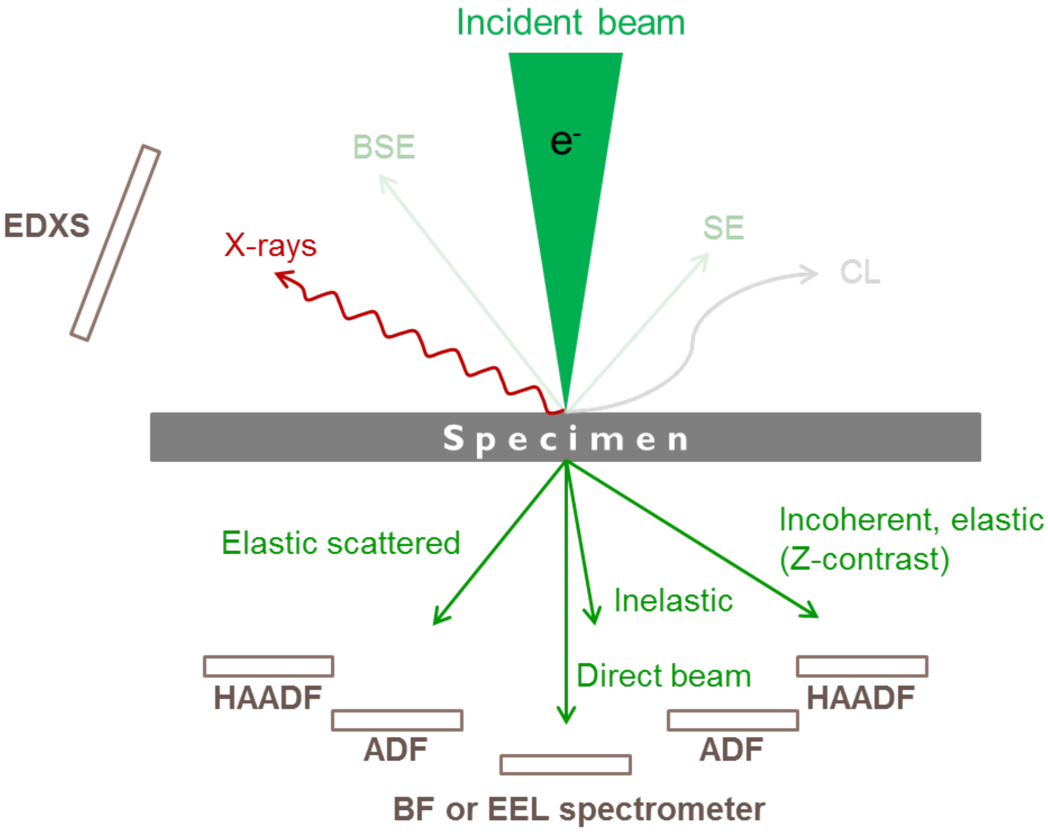

Figure 2.1.: Signals which occur during electron interactions; those which are not used in our TEM instruments are drawn in lighter colors (CL stands for cathodoluminescence)

The availability of all these signals at the same time allows to collect a high amount of information in a short time. This is especially useful for samples which are sensitive to electron radiation or in *in situ* experiments.

2.2. The ASTEM Microscope

For most of the result presented within this thesis the ASTEM microscope has been used. ASTEM stands for “Austrian Scanning Transmission Electron Microscope” and was build by FEI Company, Eindhoven/Netherlands. A picture of the microscope is given in Figure 2.2.
It provides following features:

- It has a high brightness electron gun (X-FEG), providing a current of 0.6 nA in a 0.1 nm probe.
- An electron monochromator, based on a Wien filter, which allows EELS with an energy resolution with less than 0.2 eV.
- The microscope can be operated in a wide electron energy range between 60 and 300 keV (60, 80, 200, 300 keV), provided by a high stability high tension source.
- It is equipped with a probe corrector for the correction of spherical- and higher order aberrations.
- It is equipped with a windowless, 4 quadrant EDXS spectrometer (ChemiSTEM) with a high collection angle of 0.7 sr.
- For EELS a Quantum energy filter, build by Gatan Inc. USA, is attached, which allows high speed acquisition of both the low-loss and high-loss EELS range simultaneously (DualEELS).

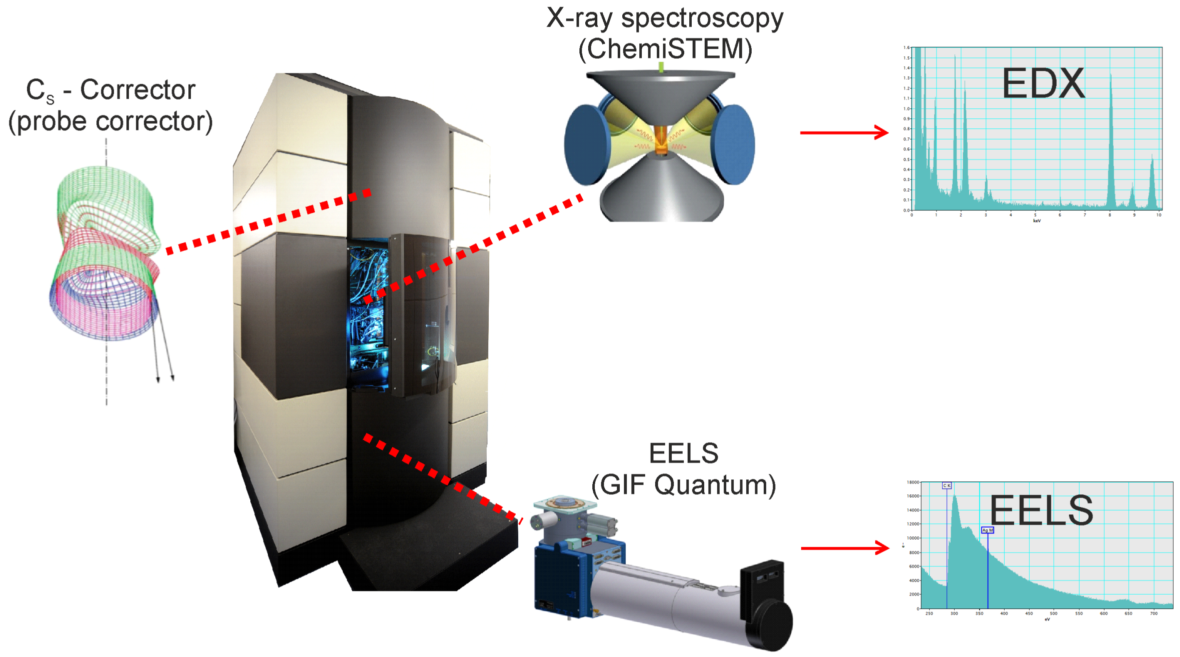

Figure 2.2.: Main components of the ASTEM microscope, that was used within this work.

With this configuration the ASTEM is a highly flexible instrument and allows the use of a variety of characterisation techniques. The most important of these, that were used in the present thesis are described concisely in the following sections.

2.3. Electron Energy Loss Spectrometry

An important tool for analytics in TEM is electron energy loss spectrometry (EELS), which will be described briefly in this section.

2.3.1. Basics

With EELS the energy loss of primary electrons with energy E_0, which undergo different types of inelastic scattering events inside the sample, can be analysed. Electron matter interactions are very complex and manifold [1, 3, 39]. Besides elastic scattering by Coulomb interaction with atomic nuclei, electrons can scatter

- from the nucleus or a bound electron while emitting a photon (Bremsstrahlung).
- by raising an atomic electron to an excited state or by nonatomic, collective processes such as plasmon- or phonon excitations (excitation).
- by knocking out a bound electron which leaves the atom ionized (ionization).

The latter leads to characteristic edges in an EEL spectrum, which can be used not only for elemental characterisation and quantification of the sample. Furthermore the empty density of states above the Fermi level cause oscillations superimposed over the edge. This fine structure thus contains information about the electronic configuration of the atoms (electron energy loss near edge fine structure, ELNES).

2.3.2. Quantitative EELS

The intensity of the edge signal in EELS can also be used for elemental quantification [40, 41]. The methodology will be explained in the following.

The first step in almost every EELS analysis is the subtraction of the background from the ionization edge. This is mostly done by fitting a power-law function to the pre-edge spectrum. This fit is extrapolated to the edge region and subtracted from the edge. In thick samples often a preceding deconvolution with the low-loss spectrum is performed, in order to remove the influence of plural scattering [1]. The edge intensity I_{edge} is given by Eq. (2.1).

$$I_{edge} = P_{\mathrm{edge}} \cdot I_{\mathrm{T}} \quad \text{with} \quad P_{\mathrm{edge}} = N \cdot \sigma_{\mathrm{edge}} \cdot e^{-\frac{t}{\lambda_{\mathrm{edge}}}} \tag{2.1}$$

where P_{edge} denotes the probability of ionization, I_T the total transmitted intensity, σ_{edge} the cross section for a single ionization event, N the number density of atoms, t the specimen thickness and λ_{edge} the mean free path for ionisation scattering. We assume that electrons contributing to the edge intensity have only undergone one single ionization scattering event. This assumption is reasonable for a thin sample due to the relatively large mean free path λ_{edge} compared to the sample thickness. The exponential term is therefore close to unity and we can write:

$$I_{\mathrm{edge}} \approx N \cdot \sigma_{\mathrm{edge}} \cdot I_{\mathrm{T}} \tag{2.2}$$

Eq. (2.2) can now be used to calculate the number of atoms N contributing to the edge per unit area. Unfortunately, we have to account for several influences to obtain accurate quantification results, which requires some modifications of Eq. (2.2).

1. the intensities are not measured over the full solid angle (0-4π sr), but only within the collection angle β. Luckily, inelastically scattered electrons are predominantly forward scattered.
2. only a certain range ΔE of energy loss is acquired
3. the edge intensity falls to the background level relatively fast
4. the background fit becomes increasingly inaccurate with distance from the edge onset

Therefore, σ_{edge}, I_{T} and I_{edge} are functions of the width of the considered energy range ΔE and the collection angle β used in experiment. Figure 2.3 gives an illustration on the definition of this angle. I_T can only be used if there is only single scattering and is hence replaced by the intensity of the zero-loss peak I_0, σ_{edge} has to be replaced by the partial scattering cross section $\sigma_{\mathrm{edge}}(\beta,\Delta E)$ and I_{edge} by the edge intensity within a certain energy range $I_{\mathrm{edge}}(\beta,\Delta E)$. Eq. (2.2) then becomes:

$$N = \frac{I_{\mathrm{edge}}(\beta,\Delta E)}{\sigma_{\mathrm{edge}}(\beta,\Delta E) I_{\mathrm{T}}} \tag{2.3}$$

Eq. (2.3) can be used for absolute quantification. If we want to quantify two elements A and B relative to one another the zero-loss intensity cancels out and we obtain:

$$\frac{N_A}{N_B} = \frac{\sigma_{edge,B}(\beta,\Delta E)}{\sigma_{\mathrm{edge,A}}(\beta,\Delta E)} \cdot \frac{I_{\mathrm{edge,A}}(\beta,\Delta E)}{I_{\mathrm{edge,B}}(\beta,\Delta E)} \tag{2.4}$$

Knowing $\sigma_{\mathrm{edge}}(\beta,\Delta E)$ is the major challenge in EELS elemental quantification. We can use either experimental spectra from known standards or cross sections from theoretical calculations. The first approach is problematic due to the large number of influences. Ideally a reference spectrum should be acquired under the same experimental conditions ($\beta,\Delta E,E_0$), with the same bonding characteristics (fine structure) and the same sample thickness. Therefore, reliable reference spectra are not available in most cases and we only use theoretical models in this work. Theoretical calculations mostly either rely on the hydrogenic approximation or the Hartree-Slater model. These are also the two approaches implemented in Digital Micrograph by Gatan, which was used for quantification thoroughly within this work. The hydrogenic cross section model is the most simplest model. It assumes an isolated hydrogen atom with the charge of the nucleus being that of the desired species. The Schrödinger equation for the electron wave function can then be solved analytically. Screening effects can also be accounted via reducing the charge of the nucleus appropriately. Since outer shell electrons are completely neglected, the hydrogenic model is more suited for the quantification of K edges. Hence, it also ignores any fine-structure. The advantage of the hydrogenic model is its simplicity and its relatively modest computational demand.

The Hartree-Slater model also starts with the assumption of an isolated atom. By using a Hartree-Slater wave function for the initial and the final state, the characteristic shapes of the edges can be predicted[3, 42]. However, white lines in L and M edges, that are caused by transitions to unoccupied bound states, can not be modelled. These can either be excluded from the quantification by appropriate choice of the energy window or need to be calculated separately.

Practically, all these calculations are implemented in a parametrised form, which also accounts for the experimental conditions used for acquisition. These parametrised models are then fitted to the experimental spectrum. Additionally, in STEM the effect of the convergent beam has to be considered, especially if the convergence angle α is similar to or larger than the collection angle β. This is done via an effective reduction factor for the scattering cross section [1].

2.4. Energy Dispersive X-ray spectrometry

Energy Dispersive X-ray spectrometry (EDXS) is the other important elemental analysis tool in TEM and will be briefly explained in the following section.

2.4.1. Basics

After an ionisation event, electrons in the atomic shell of a specimen atom are in an excited state. The hole in a inner shell needs to be refilled by an electron of one of the higher shells. During the relaxation of the atom to its ground state, the excess energy is emitted either by an Auger electron or an X-ray photon. The energy of the latter depends on the energy of the corresponding electronic shells and is characteristic for each element. In principle this is also true for Auger electrons. However, they are regularly not used in TEM experiments, because they are readily absorbed in the specimen and the remaining signal, that can be expected from the specimen surface, is rather weak. The generation of Auger electrons and X-ray photons are two competing processes. For low Z elements Auger electron emission is dominating. The probability an ionised atom emits a X-ray photon is given by the fluorescence yield. The natural width of the emitted X-ray lines is typically 1-5 eV, determined by the life time Δt of the excited state via Heisenberg's uncertainty principle ($\Delta E \Delta t \geq \hbar/2$). However, the resulting sharp Lorentzian shape is degraded during detection to a Gaussian shaped peak with a FWHM (full width at half maximum) of approximately 60-200 eV over the typical energy range of 0-20 keV. The energy dependent resolution is a detector property and can be described by the so called Fano factor [43]. The energy resolution of a detector is often given at the Mn K_α line at 5.9 keV. Effects like incomplete charge collection (ICC), escape peaks, sum peaks, stray radiation and energy dependent absorption effects in the specimen and the holder will further distort the acquired spectrum [1]. In crystalline specimens additionally coherent bremsstrahlung peaks can occur in the spectrum. The orientation of a crystalline specimen also has a significant influence on the measured X-ray intensity due to channelling (Borrmann effect) [1, 44]. One should hence avoid strong diffraction conditions. We should bear in mind that the performance of the detector with its electronics and the geometric setup can have huge influence on EDXS results. The main advantages of EDXS are, that a spectrum can be acquired over a large energy region (up to 40 keV) with a high signal-to-background ratio, even for thicker samples. Thus elements in an unknown sample can quickly be identified. The high energy range makes it also very suitable for heavier elements.

However, absorption of low energy X-rays in the specimen, the specimen holder and in the detector limits the suitability of EDXS for light element analysis [45]. At the low energy region also an increased background signal impedes peak extraction. This background signal is caused by bremsstrahlung, generated via electrostatic interactions of the primary electrons with sample nuclei. According to Kramers' law the intensity of the bremsstrahlung increases with decreasing energy [46]. In the lowest energy range absorption in the specimen and the detector again leads to a decrease until it approaches zero at zero energy. All these effects have to be considered for adequate quantitative elemental EDXS analysis.

2.4.2. Quantitative EDXS Analysis

Similar to elemental quantification in EELS, first the background must be subtracted. There are mainly two approaches to achieve this in an automatic manner, model fitting and filtering. In the modelling approach an accurate model for the background is being fitted to the background between the characteristic peaks, according to the Kramers' background model. This function is then subtracted from the intensities of the characteristic peaks.

Top-hat filtering, in contrast, removes the background via convolution of the discrete spectrum with an appropriate chosen filter function [47]. This corresponds to the second derivative of this data set. Thereby, a constant offset and a steady slope in the data set is removed. The bremsstrahlung background shows a slow variation compared to the characteristic peaks, and is hence filtered out by this procedure. Note that top-hat filtering is pure mathematics and not related to any physical laws. Badly chosen filter parameters will lead to erroneous results. However, especially in the low energy region below 1 keV, top-hat filtering is often useful because a Kramers' background fit becomes difficult, due to the large amount of overlapping peaks.

If there are only a few peaks in a few spectra to evaluate it seems reasonable to determine the peak intensity individually, after the background has been subtracted. Prior to that it must be ensured that no strong absorption edges, neither from the detector nor from sample species, are within the peak energy range. These edges can cause a significant jump of the background signal. This can be done via the NIST tables for X-ray mass attenuation coefficients (MAC) [48, 49], for instance. Some EDXS software packages, such as Bruker Esprit 1.9, consider these absorption edges during background modelling. After background removal Gaussian curves ($f(x) = a \cdot \exp\left(\frac{(x-x_0)^2}{2b^2}\right)$, with the fitting constants a,b and x_0 the peak position) can be fitted to the characteristic peaks. The intensity then corresponds to the area of the Gaussian function:

$$\int_{-\infty}^{\infty} a \cdot e^{\frac{(x-x_0)^2}{2b^2}} \cdot dx = a \cdot b \cdot \sqrt{2\pi} \tag{2.5}$$

The FWHM of such a function can be calculated with:

$$\text{FWHM} = 2\sqrt{2\ln(2)}b \tag{2.6}$$

The detected X-ray intensity of a single peak from element A can be calculated using Eq. (2.7).

$$I_A = C_A \rho t D_e N_0 \frac{\sigma_A \omega_A a_A}{M_A} \frac{\Omega}{4\pi} \varepsilon_A \tag{2.7}$$

where N_0 is Avogadro's number, σ_A the total ionisation cross section for an atom of element A, ω_A the fluorescence yield, a_A the relative transition probability (the probability a certain line within a family occurs) M_A the atomic weight, Ω the detector solid angle and ε_A the detection efficiency at the specific peak energy. D_e denotes the total electron dose in number of electrons $D_e = \frac{I_P \tau_l}{e}$, with I_P being the probe current, e the elementary charge ($e = 1.602 \times 10^{-19}$ C and τ_l the total live time. The latter is the time in which the detector counted X-ray photons. It is determined by the real time τ_r minus the dead time τ_d.
Different existing quantification methods, such as the Cliff-Lorimer or the ζ-factor method basically rely on different subsumptions of the factors in Eq. (2.7). Although, there was also a lot of work done with ζ-factors, we only use the k-factor method for the results that are presented within this thesis.

2.4.2.1. The k-factor Method

The k-factor has been introduced by Cliff and Lorimer and is therefore also referred to as Cliff-Lorimer method [50]. They showed that if two X-ray intensities for two elements are gathered simultaneously under the same conditions, Equ. (2.7) can be written as ratio for each element A and B:

$$\frac{C_A}{C_B} = k_{AB} \frac{I_A}{I_B} \tag{2.8}$$

C_A and C_B are the concentrations of the corresponding elements in wt% ($C_A + C_B = 100\%$). k_{AB} is a sensitivity factor and often called k-factor or Cliff-Lorimer factor. This is only true if the thin-film criterion is fulfilled, which means that absorption and fluorescence in the specimen can be ignored. k_{AB} is then only a function of Z, the atomic number. k-factors can be determined experimentally from specimen with known composition or from first principle calculations. The experimental determination is practically often difficult because a thin specimen with known composition throughout the sample that has to be stable under the electron beam needs to be found. Therefore, we often rely on theoretical k-factors. Often these calculated k-factors for each element are given relative to Si K. It has to be noted that calculated k-factors are not very accurate, since uncertainties in the ionisation cross section and varying detector parameters are hard to include. Typically the relative error is about ±10% for K and ±20% for L and M intensities [1].

2.5. Z-contrast Quantification

With the advent of aberration correctors in STEM, imaging of single atoms or columns of atoms in a crystalline specimen became feasible. The incoherent character of high angle scattering of incident electrons with the Coulomb field of the atomic nuclei renders the contrast in HAADF images highly Z-dependent. It is, therefore, referred to as Z-contrast. Assuming unscreened Rutherford scattering the HAADF intensity I is proportional to Z^2. The intensity of atoms in a column or of different species A and B can then simply be summed up ($I_{sum} \propto Z_A^2 + Z_B^2$) [2]. In practice the Z dependency deviates from Z^2 and varies as a function of the detection angle. In general, a Z^n dependency with n being between $4/3$ and 2 can be expected [51, 52]. Moreover, n also varies as a function of Z due to screening effects and, especially for thicker samples, also inelastic scattering contributions can be expected. The contrast is also highly dependent on the angular range of the detected electrons, given by the inner and outer detection angle of the HAADF detector (θ_i and θ_o, see Figure 2.3a).

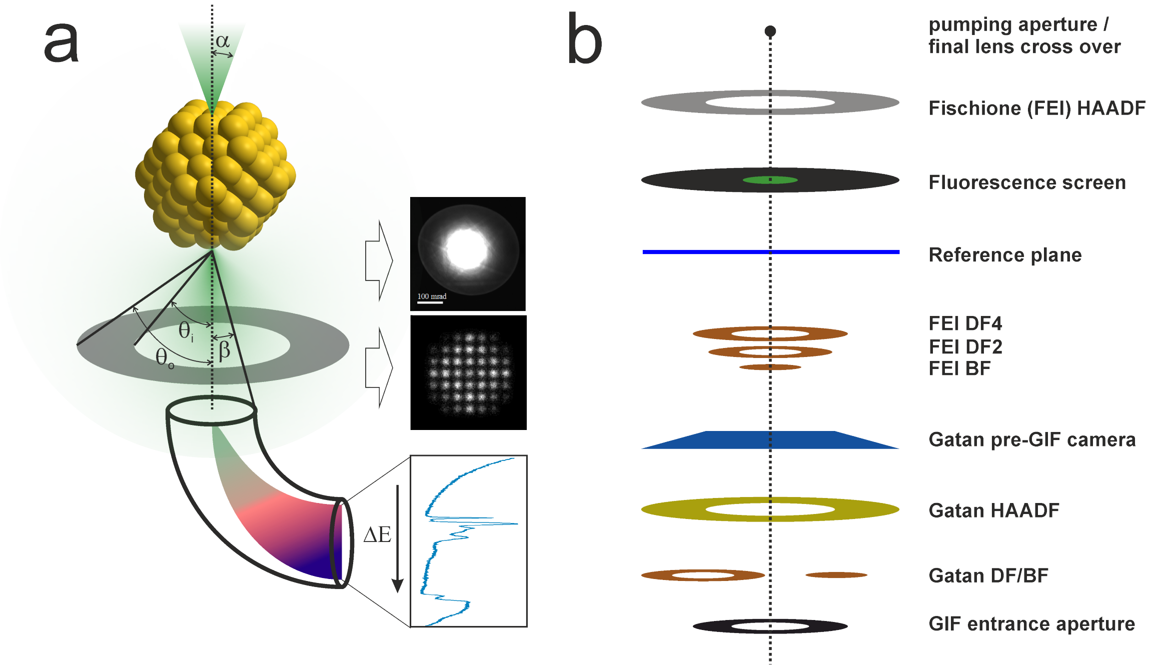

Figure 2.3.: (a) Definition of the most important angles for STEM HAADF imaging and EEL spectroscopy. The convergent beam with a semi-angle α is scanned over the sample. Within the specimen electrons are scattered elastically and inelastically to different angles. Elastically scattered electrons within an angular range $[\theta_\mathrm{i},\theta_\mathrm{o}]$ are used for HAADF imaging. The electron optics between specimen and HAADF detector generates a flux pattern. The detection angle β for inelastic scattered electrons is defined by the entrance aperture of the GIF. (b) Position of the different detectors in our FEI Titan microscope (redrawn from an illustration created by Prof. Werner Grogger).

2.5.1. Channelling and Limiting Effects

With increasing sample thickness channelling plays a significant role. Electrons that are negatively charged are attracted to the positively charged atomic nuclei and have to travel through the potential field of the crystal. This results in a focusing effect towards the atoms. The electrons are thereby channelled along the atomic columns. Hence, the intensity at each atom site increases with thickness. Another consequence of this effect is that the atoms in a column do not contribute equally to the image intensity. The strongest contribution comes from the atoms close to the first channelling peak. The probe is then spread over a wider angle, and further scattering during propagation through the sample causes a featureless background signal in the image. There are several other effects which can effect the linearity of the obtained HAADF intensity with sample thickness, such as convergence angle, detection angle, sample mistilt, defocus, lens aberrations or probe size. Despite all these influences it has been shown in several studies that for a sufficiently thin specimen (less than 10 unit cells, dependent on Z and electron energy), all these effects can be neglected, or at least taken into account, if the intensity integrated over the whole column is used (probe-position integrated cross section) instead of the maximum peak intensity. [4, 38, 53, 54].

Bearing these limiting effects in mind, atoms in thin films or nano clusters can be directly counted by using an HAADF image [38]. To this end, the imaging system has to be characterised precisely. Especially the inner detection angle of the detector and the detectors non-uniform sensitivity have to be well known. If the outer detection angle is high enough, which is usually the case for HAADF imaging conditions, it is far less important due to the rapid decrease of the differential elastic scattering cross section with scattering angle θ (see 3.1b).

Jones et al. developed a MATLAB tool, called “Absolute Integrator” to automate the steps needed for HAADF quantification [4]. It is based on a column wise intensity integration of a HAADF image of an oriented and crystalline specimen. The image is segmented into Voronoi cells based on the column centers. Under consideration of the intensity contribution of a homogeneous underlying substrate, a sensitivity map of the HAADF detector and optionally the electron flux map at the detection plane, scattering cross sections are calculated for each atomic column in units of Mbarn.

As mentioned above, intensity integration over each cell avoids some influences from:

- Changes of convergence angle
- Defocus
- Aberrations
- Incoherences of the electron source
- Small sample mis-tilts (<3 mrad)
- Small amounts of noise

compared to peak intensities used for quantification.Note that results are still influenced by

other parameters, such as primary energy, detector angles, magnification, image sampling and distortions (drift, instabilities and scanning distortions) [55]. For larger probe-tails or thicker

samples, approaches based on Gaussian fits may be advantageous over Voronoi cells [56]. An interesting list of influences of several instrumental imperfections on HAADF quantification has been presented recently by Krause et al. [57].
The main drawback of this quantification technique, as presented in the cited papers and applied in this work, is that the sample needs to be oriented perpendicular to the electron beam, which is practically difficult with small clusters. Practically, one has to select particles which are oriented by chance. The method is also not applicable for polycrystalline cluster morphologies due to the lack of translational symmetry, which is common for small clusters (see section 3.4.1).
However, with the knowledge of the scattering cross-section of a single atom, we still can determine the amount of atoms contributing to a cluster, even if its structure cannot directly be resolved for some reason (e.g. lack in crystallinity or resolution, beam damage,...). HAADF quantification is also not very effective for composite particles comprised of materials with a large difference in atomic number, due to the $\approx Z^2$-dependency of the HAADF contrast. This is true for example for the NiO nanoclusters analysed in section 4.2.1 of the present work (see section 4.2.1.10 for more details).

2.5.2. Procedure for the Determination of the Detector Angles

In order to perform quantitative HAADF measurements, the imaging system of the STEM instrument must be characterised. In the following we present a procedure that has been used on our ASTEM.

2.5.2.1. Acquisition of a Detector Sensitivity Map

In the following we describe a possible way to record a sensitivity map of the desired HAADF detector, similar to a description by Jones [56]. Therefore the microscope is set to diffraction-off conditions at an intermediate convergent angle (e.g. 20 mrad) without a sample inserted. The beam current is chosen as low as possible so not to harm the detector or to distort the obtained sensitive map, but high enough to be measured accurately. A current of about one tenth of the beam current used for the actual experiment seems to be a reasonable choice (e.g. 10 pA). The detector gain is chosen so that over saturation is avoided. If the scanning mode is then activated, the beam is scanned in the diffraction plane and hence over the detector. We deactivated the Descan function in the microscope user interface in order to increase the angular scanning range. After choosing an appropriate magnification, focus and pixel time, a sensitivity map of the detector can be acquired. Such sensitivity maps are shown in Figure 2.4 for several detectors attached to our microscope. Note that all the detectors show significant sensitive variations. In the map for the FEI DF4 detector four quadrants are clearly visible. Each quadrant can in principle addressed separately. Hence, this detector can be used for differential phase contrast imaging.

This procedure needs to be performed for every Z-contrast quantification measurement. Detector settings such as gain and brightness need to be kept the same for the whole experiment

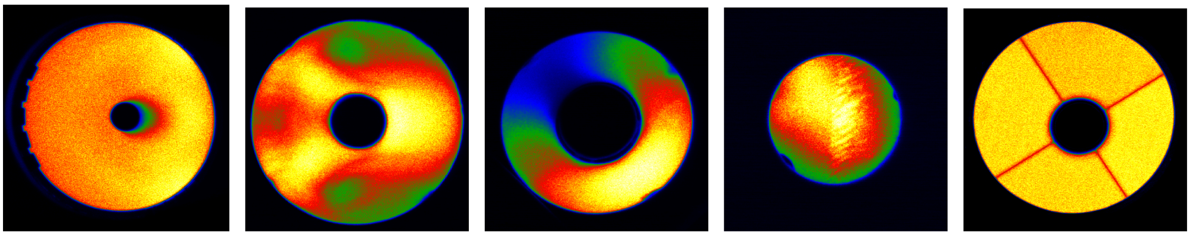

FEI HAADF Gatan HAADF Gatan ADF Gatan BF FEI DF4

Figure 2.4.: Detector sensitivity maps of several detectors attached to our FEI Titan microscope

to avoid influences of non-linearities. We also use the same dwell-time for both the sensitivity maps and the experiment. The currents that were used for both the detector mapping and the experiment are measured either by simply using the screen current values or more precisely by using the drift tube of the GIF.

Due to its well suited angular range we used the Fischione HAADF detector (also called FEI HAADF in the microscope user interface) for all HAADF quantification experiments within this thesis.

2.5.2.2. Measuring the Detection Angles

The most important geometric quantity, that must be known for HAADF-quantification as well as for quantitative image simulations, is the minimum detection angle of the HAADF detector disk. The maximum detection angle is far less important, due to the power-law like behaviour of the elastic scattering cross section. For instance, 1 mrad variation in the inner angle causes a change of 4% in the detected intensity, while the same variation in the outer angle changes the intensity by only 0.06%, assuming a annular detection range of 60-200 mrad and the NIST cross-section curve for Au and an energy of 300 keV [58].

To measure the detector angles we switch to STEM-mode (diffraction on) and centre the CBED disc on an appropriate camera, located after the detector. The shadow of the inner detector ring needs to be visible on the camera, at least partly.

The active detector area is not the same as the detector shadow visible on the camera. So we need to locate the region were the detector starts to detect electrons. To this end, while scanning, the diffraction shift is used to move the CBED disc until a signal is detected. For this we use the live-histogram function of Digital Micrograph. We constantly keep scanning with a 256x256 pixel scanning window, using a dwell time of 2.4 ms. A corresponding histogram, that is actualised automatically after each scan, changes significantly if the detector starts to count electrons. At this position a CCD image of the CBED disc is acquired. Repeating this procedure in each direction reveals the inner dimensions of the active detector area, which corresponds to the inner diameter of the active detector area, as it can be seen in the sensitivity map. Figure 2.5 exemplary shows such a series of shadow images (Fischione HAADF, 91 mm nominal camera length, Pre-GIF CCD camera). To minimize the movement of the CBED disc, the highest magnification should be chosen and the Descan option should be activated in the UI.

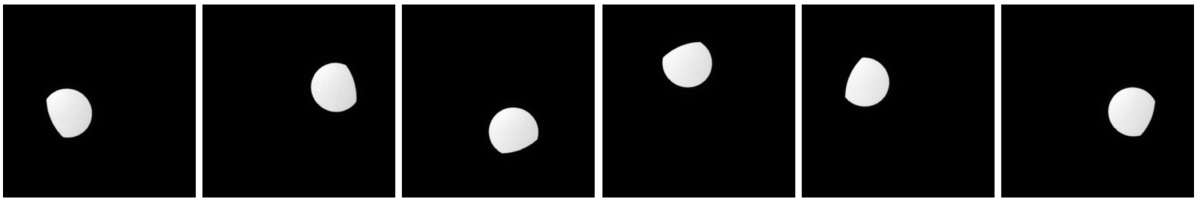

Figure 2.5.: Series of several CBED disc positions, each touching the border of the active detector area.

These images are combined in a colour map as shown in Figure 2.6b. Circles are then fitted to the CBED discs to extrapolate the position of its outer edge. Note that it may be necessary to calibrate the camera beforehand using a gold standard for example. In our case that was done by means of the cross-grating and the inner Au(111) diffraction ring, located at 8.36 mrad (300 kV), which corresponds to $2\theta_B$, where θ_B is the Bragg angle calculated with Braggs law, Eq. (2.9).

$$\begin{aligned} \theta_B &= \arcsin\left(\frac{n\lambda}{2d_{hkl}}\right) \\ \text{with} \quad d_{hkl} &= \frac{a}{\sqrt{h^2+k^2+l^2}} \\ \text{and} \quad \lambda &= \frac{h}{\sqrt{m_e E\left(1+\frac{E}{2m_e c^2}\right)}} \end{aligned} \tag{2.9}$$

Where λ denotes the relativistic electron wave length (1.97 pm @ E = 300 keV), E the electron kinetic energy, m_e the electron rest mass and c the vacuum speed of light. d_{hkl} is the distance between lattice planes in a cubic lattice. For the (111) plane we get $d_{111} = a/\sqrt{3}$ with the lattice constant a = 408 pm for Au [59]. The calibration should be done in STEM mode, because the objective lens settings might be slightly different in TEM diffraction mode [1].

Before we start to acquire the shadow images, we also need to ensure that the CBED discs are large enough to allow precise extrapolation beyond the visible part of the detector. The center of the discs should still be visible when the disc touches the active detector area. If this is not the case, the convergent angle needs to be changed accordingly. Furthermore, the circular shape of the CBED discs needs to be checked and adjusted using diffraction stigmators.

We developed a Matlab tool, in order to facilitate the evaluation procedure. With this tool all circle fitting to both the CBED discs and the detector shadow were performed. The user is guided through the steps by a graphical interface. The only thing that needs to be known is the exact angular diameter of the CBED disc. The corresponding colour map and the detector sensitivity map (optionally) need to be on hand in TIF file format. Following steps are then performed within the Matlab script:

1. Define the borders of each CBED disc with index i in the image by manually choosing some of its bordering pixels with mouse clicks
2. The coordinates of these pixels are used for a circle fit applying a method proposed by Taubin [60].

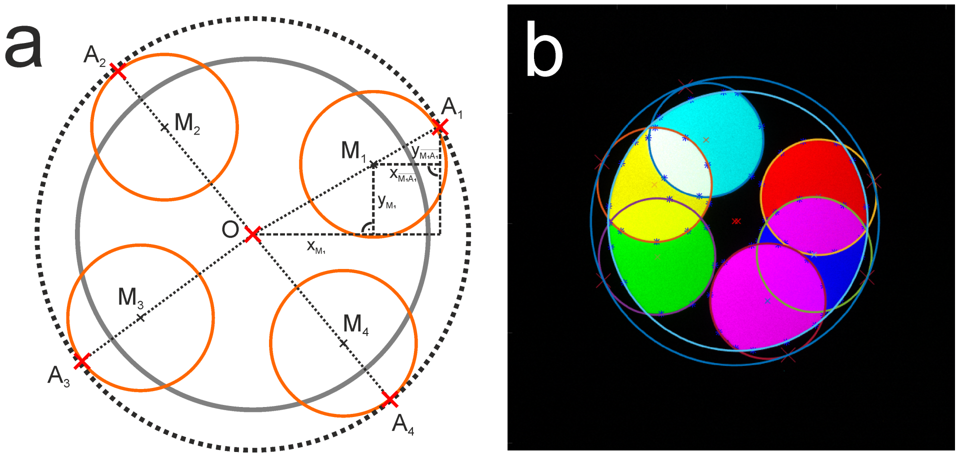

Figure 2.6.: (a) Geometric considerations for the determination of the active inner detection angle of an (HA)ADF detector. The orange circles represents the CBED discs touching the active detector area (dashed circle) at point marked by red crosses. The grey circle represents the shadow the detector casts on the CCD. (b) Example result of the automated detector angle evaluation using our Matlab tool based on the considerations in (a). (Fischione detector on Pre-GIF CCD at 91 mm camera length and 19.6 mrad convergence angle

3. Define the border of the shadow of the detector hole. Again a circle is fitted to the pixel coordinates, that were determined manually
4. The coordinates of the points A_i, where the detector touches the active area are then calculated using the centre coordinates of both the CBED discs (x_{M_i}, y_{M_i}) and the detector hole $O(0,0)$. By means of the laws for congruent triangles we can then calculate $x_{\overline{M_iA_i}}$ and $y_{\overline{M_iA_i}}$ (Eq. (2.10)).

$$x_{\overline{M_iA_i}} = \frac{\overline{M_iA_i} \cdot x_{M_i}}{\overline{OM_i}} \quad \text{and} \quad y_{\overline{M_iA_i}} = \frac{\overline{M_iA_i} \cdot y_{M_i}}{\overline{OM_i}} \quad \text{with} \quad \overline{OM_i} = \sqrt{x_{M_i}^2 + y_{M_i}^2} \tag{2.10}$$

5. A circle is fitted to all points A_i. Its radius $\overline{M_iA_i}$ corresponds to the inner detection angle of the active detector area θ_i, after including the angular calibration factor.
6. Finally, the user will be asked if he wants to estimate the ratio of the outer to the inner detection angle $R_\mathrm{o}/R_\mathrm{i}$ from a detector sensitivity map (optionally).

It should be noted that in step 4 we assume that the circles that are defining the detector hole and the active detector area are concentric in point O. In general this is not the case, as it can also be seen in Figure 2.6b. However, this assumption seems to be reasonable, since small deviations obviously do not have a strong influence on the position of A_i. Furthermore, in step 5 we assume that the active area can be defined by a circle. Due to large variations in the detector sensitivity this is also just an approximation (see Figure 2.4). Thus, the response of the detector to the CBED disc is not the same in each direction. From the $R_\mathrm{o}/R_\mathrm{i}$-ratio the outer angle θ_o can be calculated, wherever the angle is not limited by the geometry of the microscope column. However, this value can only be a rough estimation, because lens aberrations come into play at

Table 2.1.: Manufacturer values for the dimensions of the Fischione HAADF, Gatan HAADF and Gatan ADF detectors, attached at our FEI Titan microscope

detector	R_i **[mm]**	R_o **[mm]**	$R_\mathrm{o}/R_\mathrm{i}$
Fischione (FEI) HAADF	4.25	26	6.12
Gatan HAADF	8.4	30	3.57
Gatan ADF	5.4	12.1	2.24

larger angles during acquisition of the sensitivity map. In the following we therefore rely on manufacturer values for $R_\mathrm{o}/R_\mathrm{i}$ (see Table 2.1).

Over 50 shadow images as shown in Figure 2.5 have been acquired and evaluated for all camera lengths between 29.5 and 145 mm, according to the procedure given above. In Figure 2.8 results for the inner and outer detector angles for the three most frequently used dark field detectors on our system are plotted.

Note that no outer angles are given for the Fischione HAADF detector, since they are purely limited by the geometry of the post specimen lens system (projection lenses) for all of the given camera lengths (between 29.5 to 145 mm). The maximum scattering angle reaching the detector θ_{max} can be imaged simply by imaging the intensity distribution of the electron beam in diffraction mode, while it is positioned on a thick sample area. Intensity distributions captured via this way are referred to as flux pattern in literature [4, 54]. Usually, these patterns should be radial symmetric, if no image corrector is installed on the microscope. Examples, for such flux-patterns are shown in Figure 2.7, for the three camera lengths, for which the flux-pattern can be imaged by the Pre-GIF CCD camera. For larger camera lengths up to 115 mm the flu-screen camera must be used instead, which has a lower resolution and much lower imaging quality.

Obviously, the flux-pattern can not be aligned to a circular shape for the two lowest camera lengths by using diffraction stigmators. This we have to bear in mind if we want to use these camera lengths for quantitative imaging or image simulations. The manufacturer (FEI) gives an angle of 200 mrad for the maximum detector angle θ_max, limited by the flux pattern, for all camera lengths between 29.5 to 145 mm. However, our measurements show that this value is not constant, but increases constantly from 177 mrad at 46 mm camera length to 242 at 115 mm. All measured values for θ_max are listed in 2.2 and plotted in Figure 2.7.

The detection angle θ can be calculated with $\theta = \arctan\left(\frac{R}{L}\right)$, where R is the (outer or inner) radius of the detector and L the (real) camera length. Accordingly a $\arctan x$ function has been used for a fit to the data. It should also be noted that the results for the Gatan HAADF detector suffer from large variations, because only a small part of its inner hole can be imaged by the GIF-camera. So the circle fit is based only on this small part of the shadow, which has a negative influence on the consistency of the results. Therefore, we recommended to use the fitted values instead of the measured ones for this detector. For all other detectors, however, the measured values should be used.

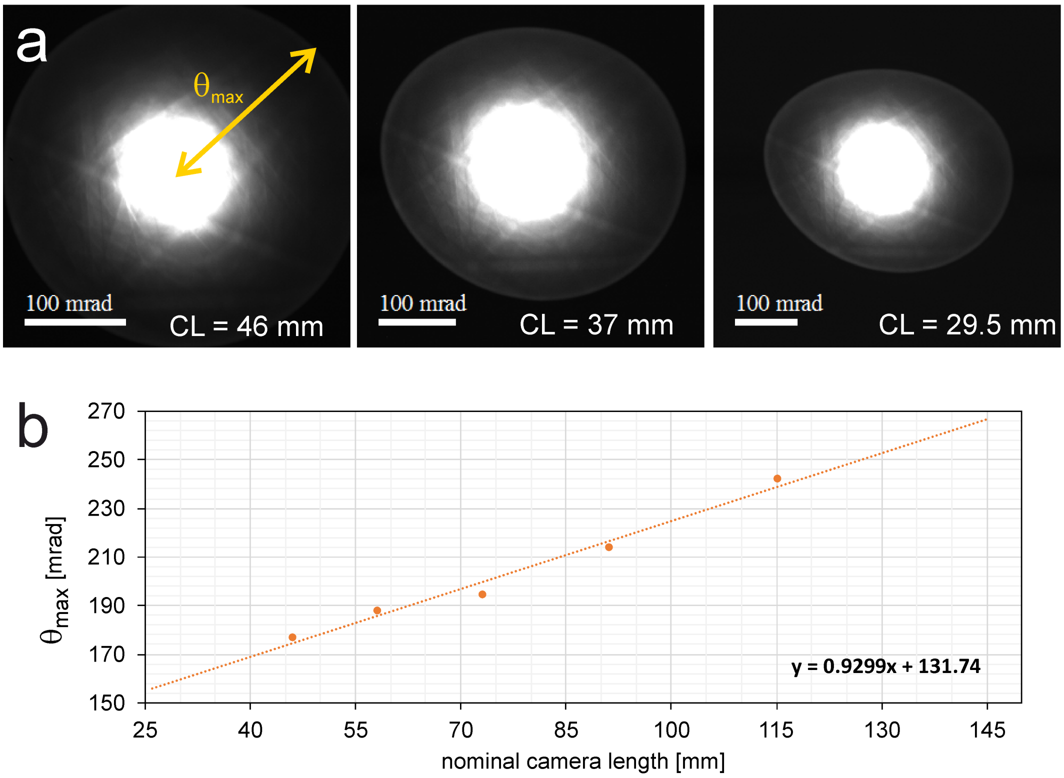

Figure 2.7.: (a) Flux-pattern on our FEI Titan microscope at 3 different camera lengths, imaged by the pre-GIF CCD. (b) maximum detectable angle θ_{max} as function of the nominal camera length, lower two camera lengths were excluded due to their non-circular shape, for the highest camera length the flux pattern was to large to be imaged by any of the installed camera systems. A linear fit has been applied to ease extrapolation.

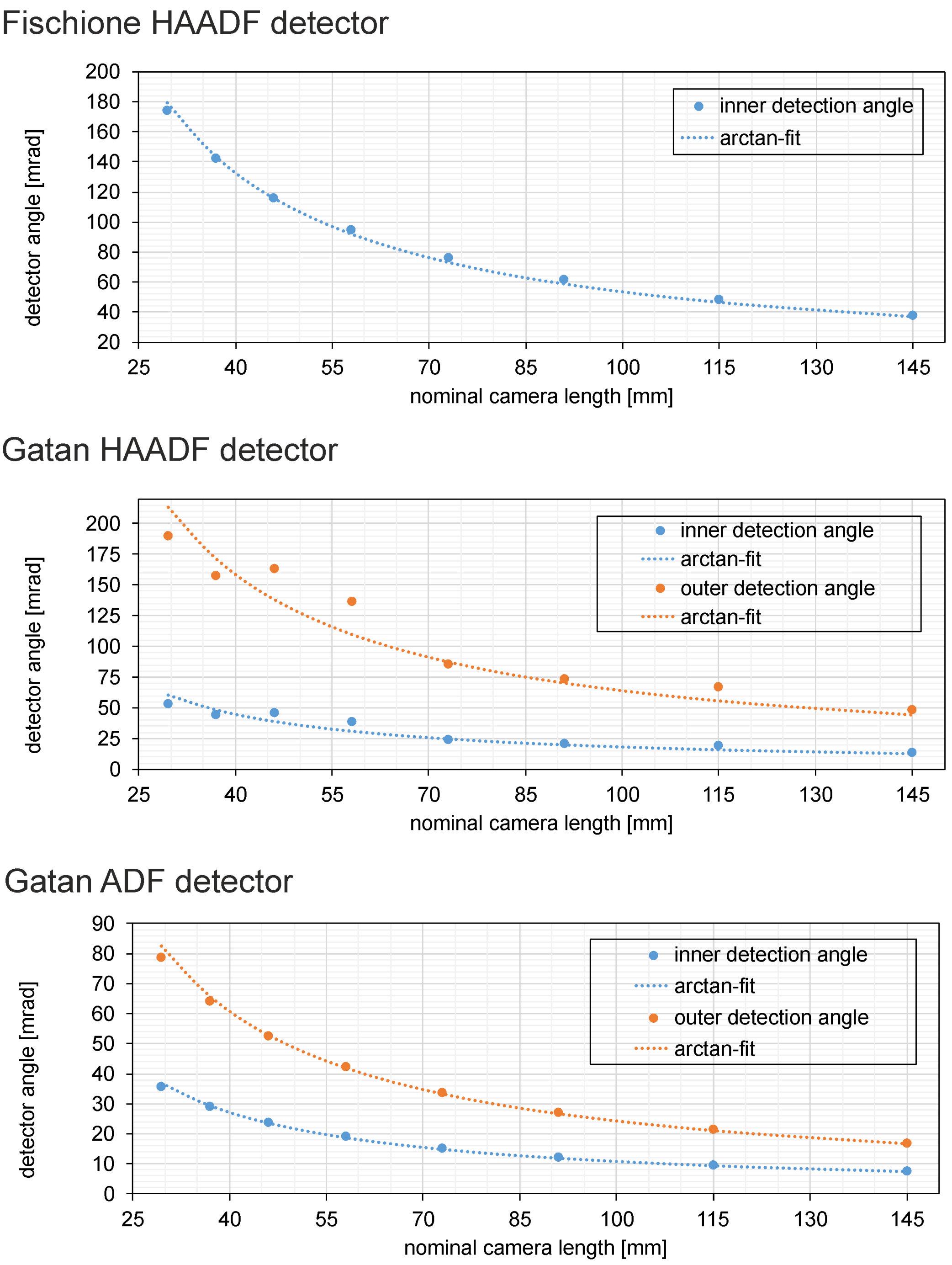

Figure 2.8.: Inner and outer detection angles for the three most important dark field detectors on our system for all nominal camera lengths between 29.5 and 145 mm.

In the following tables (2.2, 2.3, 2.4) all values are listed, that were used for the graphs in Figure 2.8.

Table 2.2.: Measured inner detection angles θ_i for the Fischione HAADF detector, together with the values obtained from an arctan-fit. The outer angle is limited by the maximum detection angle θ_max, given by the flux-pattern.

CL [mm]	θ_i [mrad]	fit to θ_i [mrad]	θ_max [mrad]
29.5	174.4	179.4	-
37	143.0	143.6	-
46	116.7	115.8	177
58	94.9	92.0	188
73	76.5	73.2	194
91	62.2	58.7	214
115	48.8	46.5	242
145	38.4	36.9	-

Table 2.3.: Measured inner (θ_i) and outer (θ_o) detection angles for the Gatan HAADF detector, together with the values obtained from an arctan-fit, respectively

CL [mm]	θ_i [mrad]	fit to θ_i [mrad]	θ_o [mrad]	fit to θ_o [mrad]
29.5	53.2	60.1	190.0	213.6
37	44.1	47.9	157.5	171.2
46	45.8	38.6	163.6	138.2
58	38.3	30.6	136.8	109.9
73	24	24.3	85.7	87.4
91	20.6	19.5	73.4	70.2
115	18.8	15.4	67.1	55.6
145	13.5	12.2	48.2	44.1

Table 2.4.: Inner and outer detection angles for the Gatan ADF detector

CL [mm]	θ_i [mrad]	fit to θ_i [mrad]	θ_o [mrad]	fit to θ_o [mrad]
29.5	36.0	36.9	80.7	82.6
37	29.3	29.4	65.7	65.9
46	24.1	23.7	54.0	53.0
58	19.3	18.8	43.2	42.1
73	15.5	14.9	34.7	33.4
91	12.5	12.0	28.0	26.8
115	9.8	9.5	22.0	21.2
145	7.7	7.5	17.3	16.8

2.6. Imaging and Spectroscopy on the Noise Floor

The high current densities occurring in modern, aberration corrected microscopes make high demands on sample stability and the skills of the operator. Obtaining high quality data is a matter of time which is limited by beam damage effects. Often this results in both images and spectra suffering from low signal-to-noise-ratios. Beam damage effects are explained in more detail in section 3.1 of this work. Beside sample damage also beam generated contamination can hinder high quality data acquisition (see section 2.7 of this work). Both effects can be minimized but sometimes not avoided and strategies to extract useful information from noisy or obscured datasets are valuable.

During the work on this thesis different approaches for removing noise from experimental signals have been tested, with varying success dependent on the use case. First we will present the basics for principal component analysis (PCA) applied to EELS- and EDXS spectrum images. In this context PCA is an established method for noise reduction [61]. However, dependent on the use case, there are also some pitfalls that need to be considered.

Later in this section we will apply a similar, patch-based method to single HAADF images and show that PCA can also be used very effectively to reduce noise in 2D images. Finally we show how blind deconvolution techniques can be applied to such images, with the aim to estimate the ground truth image as well as the probe size and shape from single, as acquired STEM images.

2.6.1. Principal Component Analysis

Generally PCA is used where huge datasets need to be classified, visualised or whose dimensionality needs to be reduced. Dimensionality reduction can be used for data compression, but also to remove less valuable information (e.g. noise).

In modern, analytical STEMs regularly multi-dimensional datasets are acquired, which can easily exceed sizes of 100x100x2048 pixels. Such a data set is obtained when spectral data (EELS or EDXS) is acquired at many sample positions (100x100), where each spectrum consists of 2048 sampling points. Such a data set represents a 3-dimensional data cube with a full spectrum at every pixel of the image and is referred to as spectrum image (SI) in the following. Due to continous improvements in data acquisition, SIs became larger over years. It would not be possible to extract relevant information from such data sets without computer assisted analysis tools. Modern CPUs together with large and cheap computer memory make it possible to analyse such large data sets by means of factor analysis. Its simplest and most ubiquitous form is principal component analysis (PCA). It is wide spread and can be found in several microscopy software suits, such as Hyperspy [62]. Hyperspy is developed by Francisco de la Peña and co-workers and is freely available online. It is specialised on the analysis of multi-dimensional datasets and has mostly been used within this work for the analysis of SI datasets.

Such a dataset can be described by a matrix **D** with dimensions $m \times n$. Where m denotes the number of spectra (pixels in the SI) and n the spectral channels. PCA is based on the idea

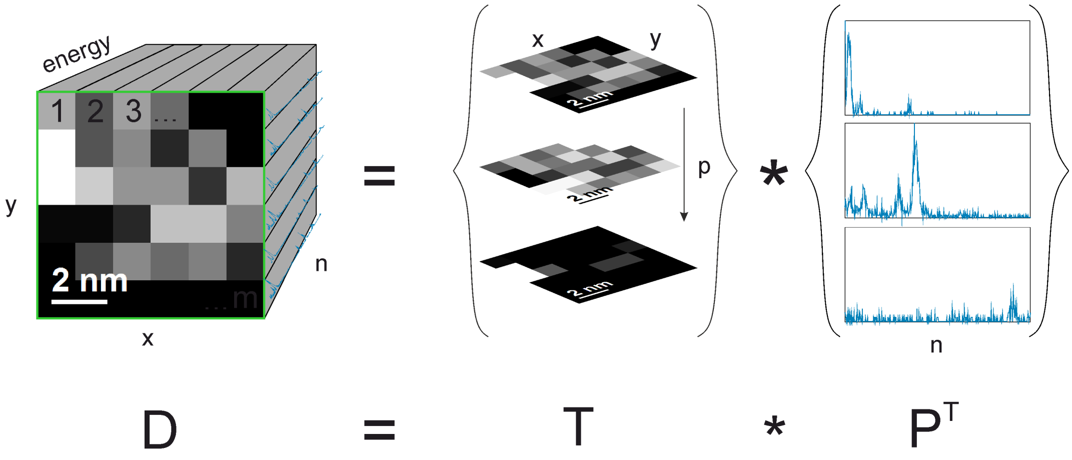

Figure 2.9.: Schematic representation of the dimensional reduction by PCA according to Eq. (2.11), note that the spectral image cube with dimensions x*y*n is unfolded spatially to a m*n matrix before performing the calculations.

that the dimensions of a multi-dimensional dataset can be reduced by finding orthogonal components best representing the original data. These components are sorted by variance so that most of the data is already represented by the first few components (the principle components) with the largest variance. The latter provides a measure of how much the data is spread in the feature space. Without loss of generality we assume in the following that the data has zero mean. That means we subtract the mean value from each data point, which reduces the rank of the data matrix by one. Otherwise the mean will be the first component in our analysis, because it resembles the best one-component model for the data.
Performing PCA means mathematically that the data matrix $\mathbf{D}$ is factorised by a $m \times p$-matrix $\mathbf{T}$ and a $n \times p$-matrix $\mathbf{P}$ so that:

$$\mathbf{D} = \mathbf{T}\mathbf{P}^T \tag{2.11}$$

where $\mathbf{T}$ has orthogonal columns and is called the score matrix, while $\mathbf{P}$ has orthonormal columns and is called the loading matrix [63]. Thereby, we implicitly assume that the underlying data generation process follows a linear, additive model [64]. The principle components are corresponding to the largest eigenvalues (diagonal elements) of the covariance matrix $\mathbf{D}\mathbf{D}^T$. The number of principle components p is chosen from a scree plot, where the variance of the components is plotted over the component number. If p is chosen properly the remaining components $n-p$ can be rejected without much loss of useful information. Due to the variance maximisation of PCA, noise is suppressed effectively, if components with small variance are omitted. The remaining components consist of linear combinations of the original channels. What also has to be noted here is that the single components of both the loadings and the scores are abstract and do not have a lot of physical meaning. They can even be negative [65].
Performing PCA numerically means to calculate the covariance matrix with its eigenvalues and eigenvectors. Since PCA is closely related to singular value decomposition (SVD), this

offers an elegant and effective way to perform these calculations. The data matrix $\boldsymbol{D}$ can then be factorised in a way as shown in equ. 2.12.

$$\mathbf{D} = \mathbf{U}\boldsymbol{\Sigma}^T\mathbf{V} \tag{2.12}$$

This equation is related to PCA in Eq. (2.11) over:

$$\mathbf{T} = \mathbf{U}\boldsymbol{\Sigma} \quad \text{and} \quad \mathbf{P} = \mathbf{V} \tag{2.13}$$

The singular values on the diagonal of $\boldsymbol{\Sigma}$ provide an ordering for the rows of **T** and **P** according to the variance of the loadings. The variance of the ith loading is given by the square of the ith singular value. The singular values can then be plotted in the scree plot. SVD provides the optimal low-rank approximation of the matrix **D**, which corresponds to the minimisation of the square of the Euclidean (L2) norm [64].
Although most of principal component analysis done in this work was performed using the Hyperspy software suite, we also implemented PCA in a MATLAB program. This program was based on the SVD function included in MATLAB. That was done not only for the reason of better understanding, but also to be able to use the code on arbitrary datasets, others than spectrum images (e.g. image data), which has also been done within this thesis (see section 2.6.4). Before we start to apply PCA on real data sets we need to care about the characteristics of our data and the noise we would like to remove.

2.6.2. What Is Noise?

During low dose STEM analysis noise is the most prevalent obstacle and its origin and the implying complications during analysis are briefly outlined in the following. To distinguish a feature exhibiting a signal S_F from the underlying background S_B, the contrast ($C = S_F - S_B/S_B$) needs to be 3-5 times higher than the noise level of the background signal (Rose criterion, see also section 3.1) [2]. So whether an image or spectral feature can be detected is strongly dependent on the contrast. Noise, as a statistical phenomenon, is characterised by its probability distribution with their defining parameters. In the context of analytical electron microscopy we mainly have to deal with Poissonian noise and additive (Gaussian) noise.

- *Poissonian noise:* The noise level is determined by counting statistics, which is caused by the discrete nature of light and electric charge and is described by a Poissonian distribution. This is also referred to as shot-noise. The standard deviation of this type of noise depends on the signal intensity via $\sqrt{N}$, where N denotes the number of counts. For large numbers, the Poisson distribution approaches a Gaussian distribution with the same mean and standard deviation.
- *Gaussian noise:* Thermal noise (Johnson–Nyquist noise) of the detecting unit (CCD or EDXS detector) is amplified by the attached electronic circuits, which themselves introduce additional thermal noise. Ideal thermal noise is white noise, which means

> that the amplitude is constant for all frequencies. However, in practice high frequencies are damped efficiently, which leads to a Gaussian amplitude distribution of the noise. Gaussian noise is additive and independent of the signal intensity. Thus the same level of noise can be found in every pixel of an image independent of the pixel value.

Accordingly, every signal that can be acquired in the microscope suffers from these two types of noise. However, shot noise is practically dominating in many cases of microscopy work.

2.6.3. Accounting for the Poisson Statistics in Experimental Data

For the counting of events which are independent from each other (e.g. electrons on a detector) Poissonian statistics can be applied and hence the variance of any individual measurement is equal to the magnitude of the measurement itself ($\mathrm{var}(d_{ij}) = d_{ij}$, with d_{ij} being an element of the data matrix $\mathbf{D}$). For sufficient large values of d_{ij} the Poisson distribution can be approximated by a Gaussian distribution. To employ PCA we need to assume that the data follows a Gaussian distribution. If we are not considering the non-uniform nature of Poisson statistics in our data set, PCA tends to fit noise associated with high intensity signals, rather than to extract small, yet meaningful, features. This is because the higher intensity values stronger influence the least squares error that is minimised. To account for this, we can apply an Anscombe transform to the data set. It transforms a random variable with a Poisson distribution x into one with an approximate Gaussian distribution y, with standard deviation 1. This property is also known as variance stabilizing. Each data point is transformed according to:

$$x \mapsto 2\sqrt{x + \frac{3}{8}} \tag{2.14}$$

It has to be noted that the Anscombe transform is a good approximation as long as the mean value of x is larger than 3. Especially for EDS spectra, this assumption is often not fulfilled, because only a few photons per channel can be detected in a single spectrum. Furthermore, in EELS spectra and CCD images with poor SNR also negative values can occur, after subtraction of the dark reference. Such unphysical values are set to 0 before analysis.

After applying the noise removing algorithms usually a transformation back to the original intensity range has to be applied. Since the algebraic inverse of Eq. (2.14) would introduce an undesired bias to the mean after back transformation, we have to use an unbiased inverse. One possible approximate solution, that has also been used in our code, is given by Eq. (2.15).

$$y \mapsto \frac{y^2}{4} + \frac{1}{4}\sqrt{\frac{3}{2}}y^{-1} - \frac{11}{8}y^{-2} + \frac{5}{8}\sqrt{\frac{3}{2}}y^{-3} - \frac{1}{8} \tag{2.15}$$

Note that there are several alternative inverse transformations available, such as Makitalo and Foi [66]. Another way to account for Poissonian noise in a data set is to include it directly in the minimization algorithm via weighting factors [63, 64].

2.6.4. Noise Filtering and Deconvolution of Images

Due to digital photography with increasingly smaller sensors and optics, noise reduction is one of the most important research topics in modern image processing. A vast amount of fast and sophisticated algorithms have been developed, each with different strengths and drawbacks. However, the requirements of such an algorithm for use with STEM images differ from those developed for (colour) photography. As electron microscopists we are not only interested in "pretty images", but extracting valuable quantitative information from images. Besides increasing the signal-to-noise ratio, our main requirements to an ideal noise filtering algorithm are:

- it is fast enough to deal with images with image resolutions of up to 2048x2048 in a reasonable amount of time and memory, so that it can be used on a ordinary desktop computer
- it can handle 16-bit (or even more) datasets with reasonable computational demand (standard grey-scale images are mostly only 8 bit images (256 colors); color images mostly use 8 bit per color)
- it can handle periodic as well as non-periodic image structures (e.g. defects or quasi-crystals)
- it can be used for images with high dynamic range and large bright areas (e.g. a gold cluster on a thin carbon substrate)
- it does not require prior knowledge about the image
- the user does not need to set many parameters
- it preserves quantitative information (e.g. for quantitative HAADF or strain analysis)

The last point is the most critical one to realise and, to our knowledge, no existing code fulfils all points listed. The ability to preserve quantitative intensity information in an HAADF image will be of special interest later in this chapter.

Due to the success of PCA on spectrum image data, we thought about possibilities to adapt the algorithm for its use on high-resolution STEM images. Some preliminary work has been done in literature that showed that PCA based approaches can be used for noise filtering in single photographic images [67–69] as well as in positron-emission tomography data sets [70].

For image time series a code (PGURE-SVT) has been presented, that uses spatio-temporal correlations in small image patches (downloadable at[1]) [71]. One of these algorithms called Poisson Non-Local PCA (Poisson NLPCA) by Salmon et al. attracted our attention because it has been especially designed to deal with high levels of Poison noise [69], which we assume is the predominate type of noise in our image data. This algorithm is highly sophisticated and, unfortunately, also very computationally demanding. We did some tests with the freely available code[2] using some HAADF images with different contrast characteristics. For the tests we had to reduce the data depth of the images from 16 to 8-bit (simple grey-scale images)

---

[1] http://tjof2.github.io/pgure-svt/

[2] http://josephsalmon.eu

to get the filtering done in a reasonable amount of time on an ordinary desktop machine. The results, however, were visually astonishing in those cases were no large contrast differences occurred. Figure 2.10b shows an example using an HAADF image of a hexagonal boron nitride bilayer, after application of the Poisson NLPCA code on the raw data shown in Figure 2.10a). This image is not only obscured by noise but also by scan distortions and irregularities caused by sample drift.

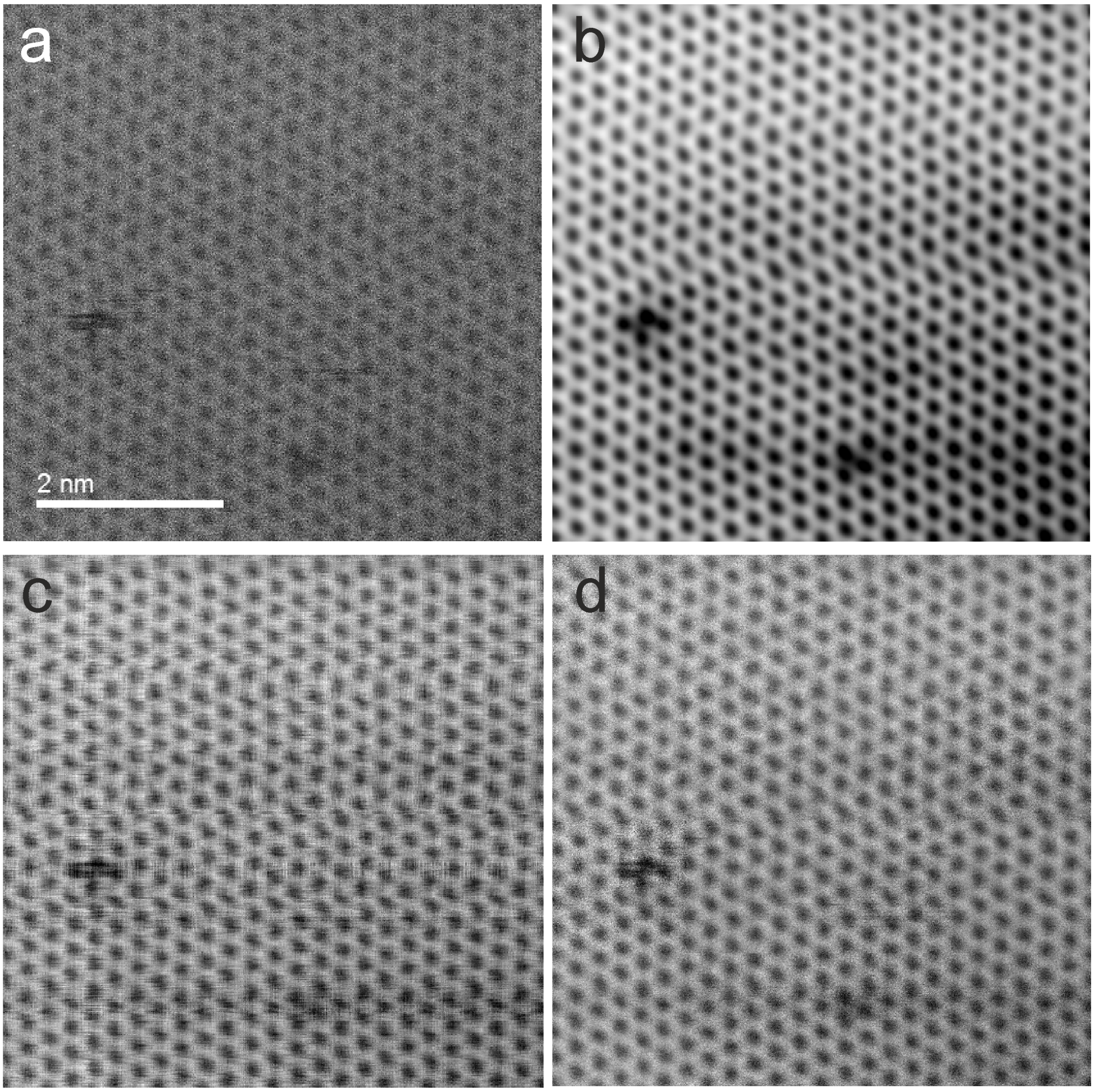

Figure 2.10.: The raw HAADF image data in (a) shows a bilayer of hexagonal boron nitride acquired at 60 kV. (b) Noise filtered image in using the Poisson NLPCA algorithm, developed by Salmon et al. [69]. (c) First simple PCA based filtering approach using the image directly as data matrix D. (d) Filtering using our patch based approach (patch sizes ranging from 32 to 512 pixels, 7 components for each step)

In the filtered image, especially the defect structures become very clear and even lattice distortions caused by a slight sample drift during image acquisition are largely preserved. Faint blocking artefacts from the patch based data treatment are, however, visible.

Since it turned out that it could be difficult to simply adapt the existing code to our needs, we decided to write our own very simple code in Matlab for some tests. Matlab is not the fastest option of course, but it allows to make use of the single value decomposition algorithm implemented therein to perform PCA, which reduces the coding effort.

The first question that arose is how to sort an image with dimensions $m \times n$ in a data matrix $\boldsymbol{D}$ that can be passed to (Eq. (2.12)). The simplest approach is to use the image directly as data matrix with the same dimensions after Anscombe transform (Eq. (2.14)). We consider the pixel values in each row m of the image as vectors with n dimensions. In other words, the intensity of each pixel is treated as feature and each feature vector contains the pixels of a row. So we use correlations between the rows for PCA. Since we presume that the pixels in each row do not change independently of one another, this approach works the best with periodic structures at higher magnification, and even better if the crystal structure is aligned with regard to the rows. Despite its simplicity the method actually worked surprisingly well in terms of noise reduction. However, the approach suffers from considerable linear artefacts in the images, due to the treatment of the data. This becomes evident especially close to regions with larger contrast changes and crystal imperfections in the images. Figure 2.10c shows such a filtering result on an HAADF image of hexagonal boron nitride.

Nevertheless, the early success of our tests motivated us to think about possible improvements of our code. One thing that can be done is to fight the artefacts in the PCA treated image in a post-processing step. If the PCA filtered images are further processed (e.g. with blind deconvolution) this is more than just a cosmetic action, since unwanted high frequency components in the data can hinder such a treatment. We applied two different, very basic filtering techniques, to get rid of these artefacts. Both make use of the high frequency character of the artefacts and thus basically work as low-pass filters. One approach was to use a spatial convolution filter with a square filter mask (the filter kernel, e.g. with a size of 3x3 pixels). According to the weighting factors in the mask each pixel is replaced by the weighted mean of the neighbouring pixels. The larger the filter kernel the more neighbour pixels are included. The second approach is to use a Butterworth filter, which basically is a filter mask with rotational symmetry, applied in the frequency domain of the image. Therefore, the image is transformed to the frequency domain via FFT. Frequencies above a certain threshold frequency are damped with a linear increase of damping with the frequency. After applying the mask the image is back-transformed. Mostly the spatial domain filter gives better results without introducing new artefacts, but one has to decide from case to case. We have to admit that obviously we lose most of the benefits of using PCA for image filtering with this post-processing step, which was quite unsatisfying.

2.6.4.1. Patch Based PCA

The origin of line artefacts lies in the way how correlations between single pixel values are used in our code. Therefore, we chose to try a patch based approach, where the original image is split into square shaped patches of equal size n, according to [69, 72]. Each patch is then reshaped to a vector with n^2 dimensions. All these vectors are then collected to built up the

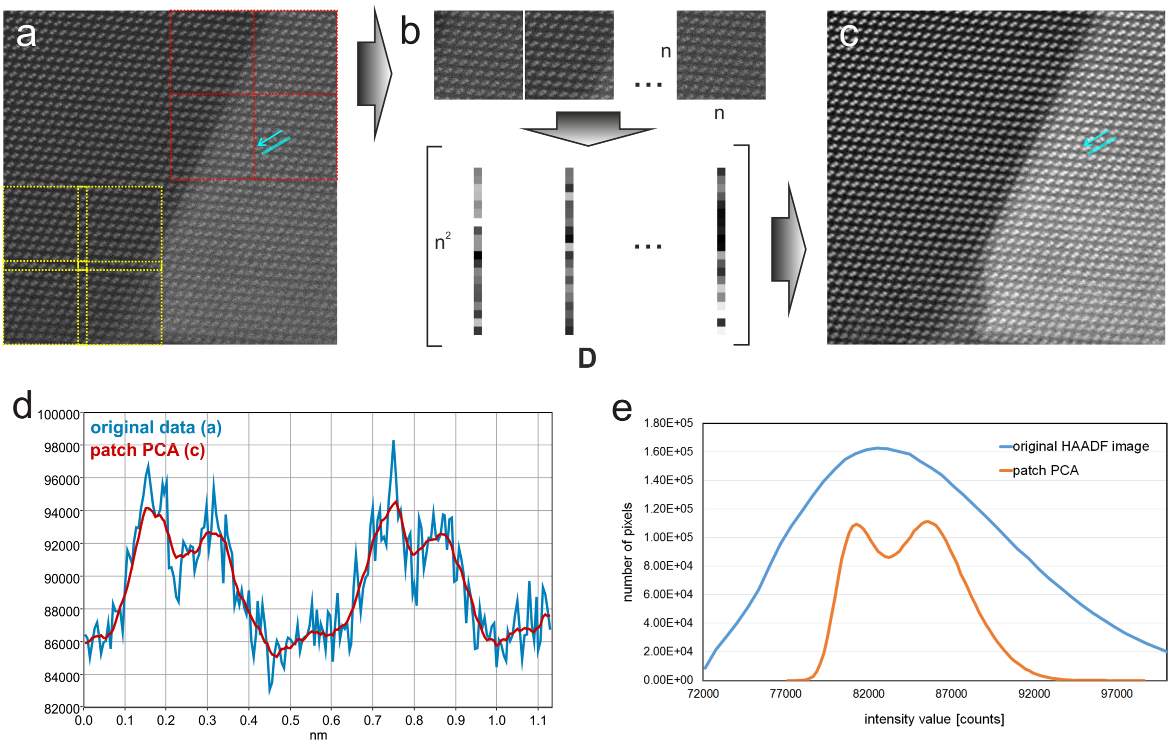

Figure 2.11.: Illustration of the patch based denoising process with overlapping (yellow) and non-overlapping patches with size $n * n$. In the image we can see a $NiSi_2$ precipitate in a Si matrix with (110) orientation [73]. Patches are extracted from the original HAADF image (with size 2048 × 2048) shown in (a). These patches are reshaped to vectors with length n^2 and collected to build up the data matrix $\boldsymbol{D}$ (b). After performing PCA using non-overlapping patches with varying patch size we obtain the image shown in (c). (d) Comparison of the intensity profiles along the paths drawn in (a) and (c) using a integration with of 20 pixels. (e) shows a histogram of both images, also demonstrating that the signal to noise ratio is considerably enhanced. Features with different intensity contributions that are covered by the noise can be clearly distinguished after PCA

data matrix $\boldsymbol{D}$, which corresponds to the formation of a Casorati matrix [71].

This procedure is illustrated in Figure 2.11 on an example image, showing a tetrahedral $NiSi_2$ precipitate in a Si matrix oriented in (110) orientation. To include image information with different grades of localisation, the patch size can be varied. In the example given in Figure 2.11c the original image 2048 × 2048 in (a) was fragmented into patches with sizes ranging from 8 × 8 up to 128 × 128. Starting with the lowest size, the patch length was doubled for every collection. Each set of patches was denoised separately and the final pixel values were obtained by averaging. In Figure 2.11d we show a comparison of the intensities along the path drawn in (a) and (c). We expect one half of each dumbbell in the precipitate to appear brighter than the other one, because every second column contains Ni atoms. Since the contrast is dominated by the high amount of Si atoms in the same column, the contrast between Ni containing and Ni free columns is quite faint. While in the original data set this difference can often hardly be seen, it becomes obvious after PCA.

We compared our simple image denoising approach also with other common image noise filtering methods, such as the adaptive Wiener filter and band-pass or butterworth filtering, which both use filter masks in the frequency domain [74]. An adaptive version of the Wiener filter, as it is implemented in MATLAB via the wiener2 function, was used here. It is designed for grey scale images that have been degraded by constant power additive noise (Gaussian white noise) [75]. It uses the local image mean and variance, estimated within a predefined neighborhood area, for pixel wise filtering. It also estimates the additive noise power beforehand.
The performance of our code depends on the used data set, but clearly outperforms all methods based on band-pass filtering in the frequency domain. Particularly, significant image artefacts and heavily distorted intensity relations are the reasons why these methods are not further considered here. Mostly, if the parameters are chosen properly, it even gives visually better results compared to the standard Wiener filter, as it is implemented in Matlab. The Wiener filter tends to blurring and saturation effects in many cases, when applied to HAADF images. In terms of quantitative performance of the algorithms, we are especially interested in how filtering influences the absolute and relative intensities. It is remarkable that the intensity relations seem to stay almost constant after PCA, in the $NiSi_2$ example, given in Figure 2.11. While the sum of detected electrons in the original image was $3.594\,86 \times 10^{11}$ it was $3.590\,84 \times 10^{11}$ afterwards. The small difference can be explained with the residual variance of the components that have been skipped. Although, the difference appears to be small in this case, it could hinder quantitative data evaluation [76]. Further tests would be needed, to explore the consequences on HAADF quantification.
However, these values are not really meaningful if it comes to atom-wise counting using the Z-dependent HAADF contrast of single atomic columns, that are often only represented by a few image pixels in single, high resolution STEM images. To evaluate the performance of the filter the underlying ground truth information without noise would be needed, which is not available in an experimental image. Therefore, we used HAADF image simulations of an artificial metallic cluster sample. The simulated image was afterwards corrupted by pure Poissonian noise on which the filter algorithms were applied. This has also the advantage that we can control the signal-to-noise ratio via scaling the pixel intensities before applying the noise.

2.6.4.2. Testing Data Set

We decided to use a the geometry of a supported cluster to generate a testing data set. As a demo cluster, an fcc geometry, merely consisting of 116 Au atoms, has been created. Single atoms in several columns were then replaced by Ag, and one atom from the innermost column has been deleted, so as to obtain contrast differences in the resulting HAADF simulation. Finally the cluster is comprised of 111 Au atoms and 4 Ag atoms, distributed over 45 atomic columns. The cluster was placed on a single layer of graphene, to avoid vacuum regions in the simulated scanning area. Due to their low Z, single carbon atoms have nearly no effect on the obtained HAADF contrast, compared to Ag and Au. Figure 2.12 depicts the resulting geometry.
With this model multislice simulations were performed by using QSTEM [77]. A quadratic

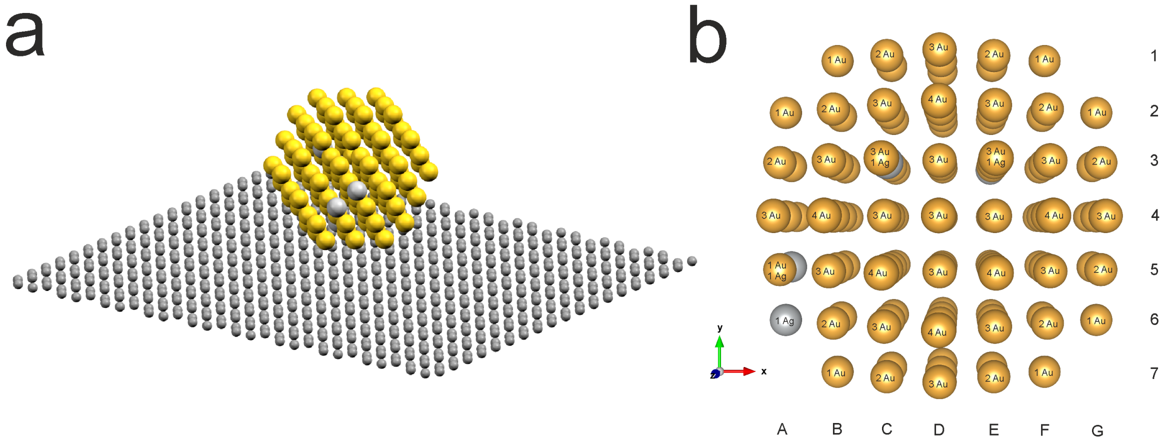

Figure 2.12.: (a) Full geometry of the Au-Ag demo cluster used to test the noise filters. (b) perspective view of the cluster, showing the positions of the inserted Ag atoms. Substrate atoms are not shown for clarity. The beam direction points out of the plane (positive z-direction). Captions show the number of Au and Ag atoms in each column.

area with a side length of 8 Å, containing the particle, has been defined. The resolution is set to128x128 pixels. This corresponds to a pixel size of 0.14 Å, which is in the range typically used for HAADF quantification experiments. An electron energy of 300 keV and a convergence angle of 20 mrad has been chosen. 30 TDS runs at 300 K have been performed. The HAADF detection angle was set to 60-200 mrad. The amount of spherical aberration was set to 100 nm and the probe size was 80 pm. Figure 2.13a shows the result of the image simulation. The intensities of the original image were scaled so that the maximum intensity value that occurs in the image was 40 counts. Figure 2.13b shows the same image, corrupted by Poisson noise.

2.6.4.3. Performance of PCA Based Image Filtering

After applying our patch-based PCA noise filtering algorithm on the noisy image we obtain the image shown in Figure 2.13c. In this example the patch size was varied between 4 and 64 pixels and in each step the 7 first components were selected to reconstruct the data. This values were chosen in an empirical way, from visual evaluation of the images. The result of a Wiener filter is shown in (d), so as to compare our method with a common noise filtering algorithm. Visually our approach gives a smoother result, with the present settings. To be able to compare filtering results we need a measure of image quality. With the known ground truth image I_o and the filtered image data I_f the signal-to-noise ratio (SNR) can be used for instance. The SNR is the ratio of signal power to noise power, as written in Eq. (2.16) in logarithmic scale. With a factor 10 the result is a decibel (dB) value. The Rose criterion states that a SNR of at least 4-5 (corresponds to approximately 6 dB) is necessary to identify image details with 100%

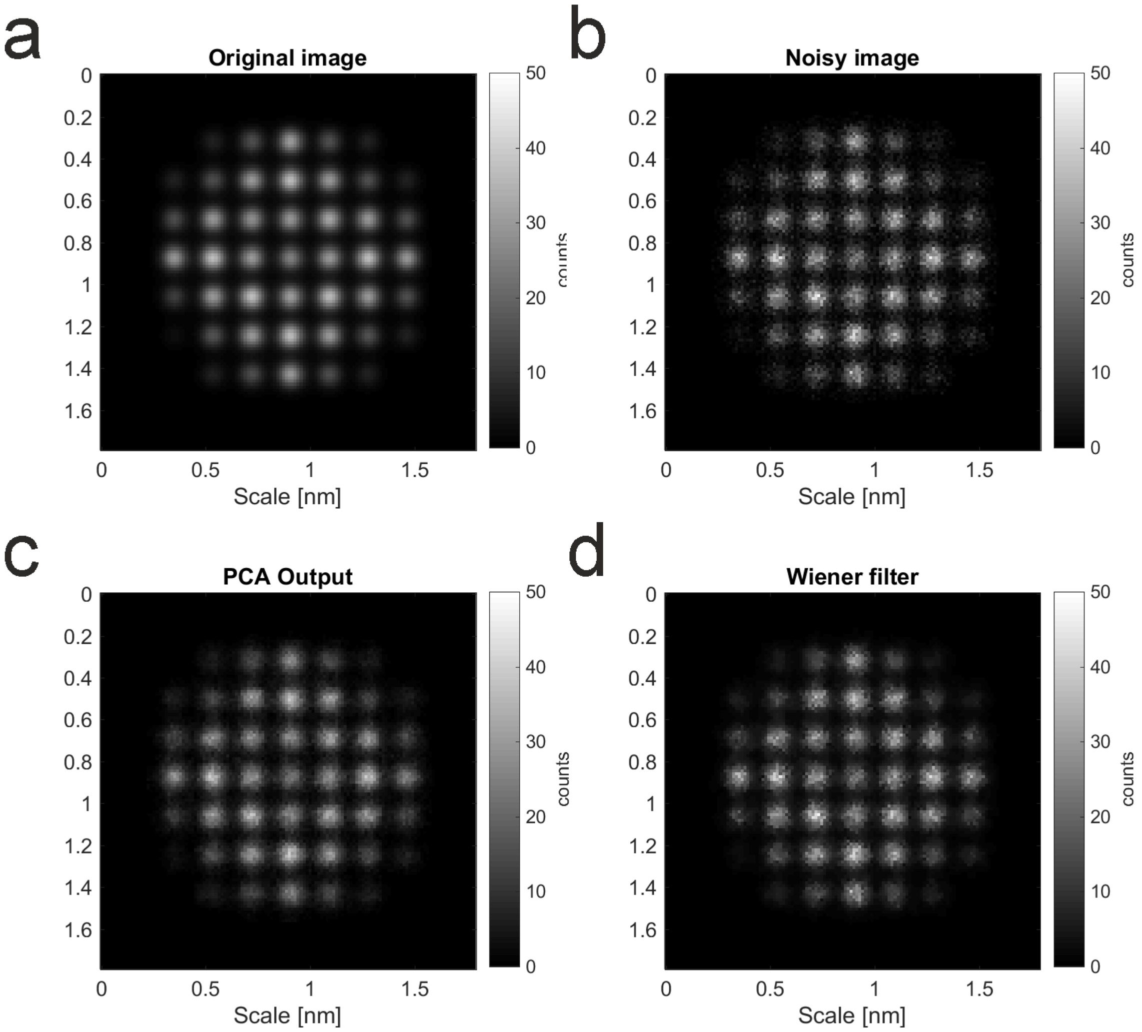

Figure 2.13.: Image simulation of the Au-Ag demo cluster (a) corrupted with Poisson noise (b) to demonstrate the noise filtering ability of our patch based PCA filtering approach (c) in comparison with a Wiener filter (c)

certainty (see also section 3.1).

$$\mathrm{SNR} = -10 \cdot \log_{10}\left(\frac{\sum_{i,j}\left[I_o(i,j) - I_f(i,j)\right]^2}{\sum_{i,j} I_o(i,j)^2}\right) = [\mathrm{dB}] \tag{2.16}$$

Note that the SNR directly depends on I_o and is therefore dependent on the image content, a property that is not always wanted.
Another useful quantity is the mean squared error (MSE), defined in Eq. (2.17).

$$\mathrm{MSE} = \frac{1}{mn}\sum_{i,j}\left(I_o(i,j) - I_f(i,j)\right)\big)^2 \tag{2.17}$$

Since the MSE strongly depends on the intensity scale, it is usually normalised by the maximum possible intensity in the image I_{max} and we obtain the definition of the more content specific peak signal-to-noise ratio (PSNR), given by Eq. (2.18).

$$\mathrm{PSNR} = -10 \cdot \log_{10}\left(\frac{\mathrm{MSE}}{I_{max}^2}\right) = [\mathrm{dB}] \tag{2.18}$$

In other words, the PSNR is defined as the ratio of mean square difference to the maximum mean square that can exist between any two images, expressed on a logarithmic scale. In the following, the image data is normalised to 1 ($I_{max} = 1$) before these quantities are calculated. The higher the PSNR the better the filtering result. If both images are exactly the same, PSNR becomes “infinite”[3]. Note that all this metrics come from signal theory and ignore features of human image perception, which means that an image that looks visually better may sometimes have a worse SNR or PSNR value.

To evaluate the noise filtering ability of our algorithm we applied different intensity scaling factors to the simulated HAADF image before obscuring the data with Poissonian noise. For each intensity scale our patch PCA filter (with patch sizes from 8-64 pixels, 7 components) were applied. The results were compared with that obtained with the Wiener filter (as implemented in Matlab with standard settings). The settings for the PCA filter were determined empirically to give the visually best results for the given dataset. For each result the SNR and the PSNR were calculated. Results are listed in following table (2.5) and depicted in Figure 2.14 over the maximum image intensity. In average the improvement in PSNR was around 3 dB for our PCA filter, while it was only 0.9 for the Wiener filter. The improvement in SNR was similar. So we can conclude that a PCA based algorithm is suitable to improve the SNR of an HAADF image, that has been obscured by Poison noise at different levels. Improving the SNR, however, does not necessarily improve the quality of a quantification based on filtered data.

Table 2.5.: SNR and PSNR values of the noisy image compared to the PCA and Wiener filtered images at different intensity scales of the ground truth data and thus different levels of Poisson noise

I_{max} [counts]	noisy image		PCA		Wiener	
	SNR [dB]	PSNR [dB]	SNR [dB]	PSNR [dB]	SNR [dB]	PSNR [dB]
41	10.7	25.3	14.4	29.1	12.5	27.2
20	7.9	22.3	12.2	26.6	9.0	23.3
10	5.9	20.3	8.6	23.0	6.8	21.2
7	4.9	19.6	7.0	21.7	5.6	20.3
5	4.0	18.2	6.8	20.9	4.5	18.6
4	3.7	17.8	6.4	20.5	4.2	18.3

---

[3] Strictly speaking PSNR is undefined if MSE=0.

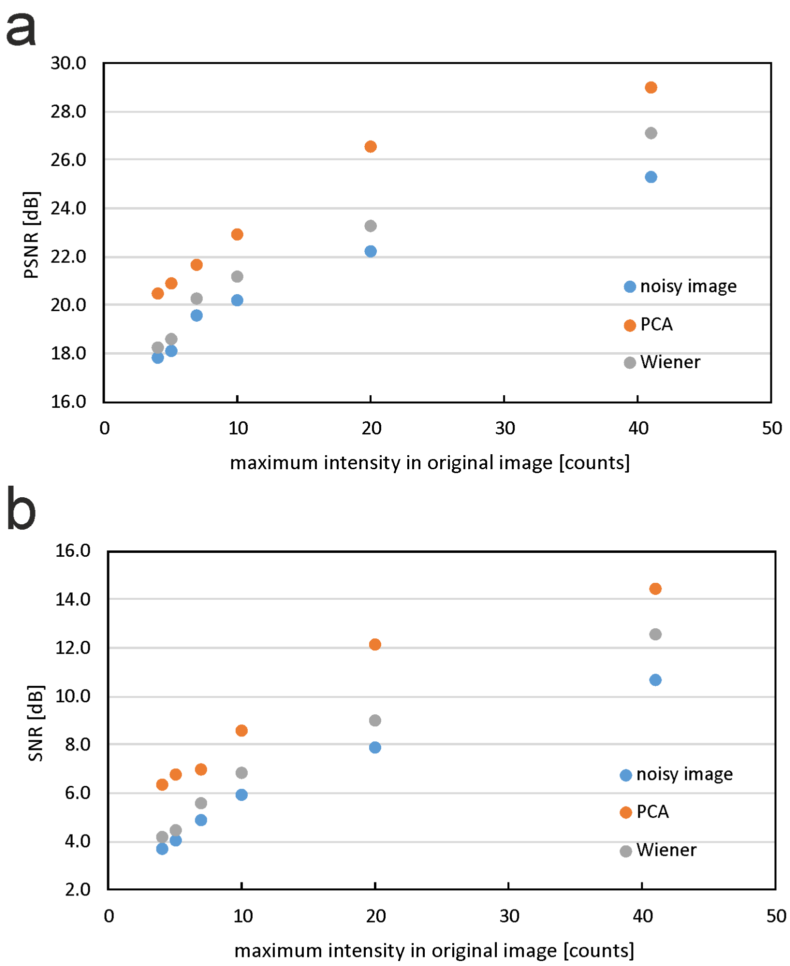

Figure 2.14.: PSNR (a) and SNR (b) values from table 2.5 plotted as a function of the maximum intensity occurring in the image

2.6.4.4. On Quantitative Intensity Information in Filtered Images

In order to test if the algorithm is able to preserve quantitative intensity information. To quickly assess this ability directly in GMS we can simply calculate the pixel wise difference of the filtered images to the original image. The result is then summed up over all pixels, to obtain an absolute error estimate. The obtained value was 208 for the PCA algorithm, which is less than half of the value we got for the Wiener filter (482). That would mean, that our algorithm preserves more quantitative information over the full image than the Wiener filter in this case. It is remarkable that both values are positive, which means that both algorithms in general tend to overestimate the intensity under present conditions. If we do the same operation on the noisy image we obtain a value of only 38. So both filters significantly obscure the original intensity values, even compared to the noisy data set. Any kind of noise treatment should, therefore, be avoided if one is interested in the absolute intensity values of single pixels.
Nevertheless, we are more interested in the intensity integrated over several pixels to perform

HAADF quantification based on Voronoi cells, as described in section 2.5 and applied in section 4.4. Therefore, we decided to test the filter algorithms in a realistic environment. To perform such an HAADF quantification we first need to find the exact peak position (local intensity maximum) in the image followed by Voronoi partitioning to determine the intensities corresponding to each atomic column in the image. The whole procedure has been introduced by Jones at al. and implemented into a software package called "Absolute Integrator" [4].
Although this program can be downloaded for free and was also written in Matlab, it is closed source and so we could not adapt it to our purposes. Luckily there exists a function "voronoi" in Matlab that performs Voronoi partitioning. So we decided to write a simple Matlab script to determine the intensity of each column automatically, having Jones' procedure in mind. The code is presented in the appendix of this thesis (see section **??**).
In a Voronoi partition each peak position corresponds to a Voronoi cell which consists of every point in the Euclidean plane whose distance to the peak is less than or equal to its distance to any other peak. We use this distance minimising property of the Voronoi partition to determine which image pixel belongs to which cell. Since the cells become too large in the edge regions of the cluster, we implemented a maximum radius around each peak from which the intensity is being calculated. This radius was set to 8 pixels in the following (see Figure 2.15). The result of a Voronoi partition is shown in Figure 2.15a, based on the image shown in Figure 2.13. Following this procedure we can obtain an intensity map, where each cell corresponds to an atomic column of the cluster. These intensities could further be used for HAADF quantification. However, for the evaluation of our noise filtering algorithm it is sufficient to have a measure for the consequences of filtering on the column wise intensity, because further quantification steps will be based on these values. All determined intensities are summarised in a histogram shown in Figure 2.16a, labelled with their corresponding columns. From this histogram all columns can be clearly identified. Figure 2.16b shows the column intensity over the number of Au atoms in that columns. Here, only columns comprised purely of Au atoms are considered and the mean value is plotted. Although, the relationship is almost linear, we clearly see some

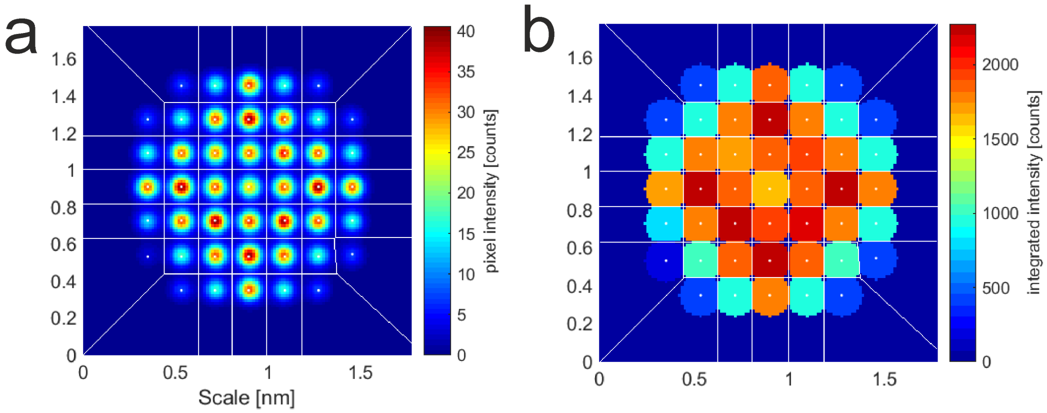

Figure 2.15.: (a) The simulated HAADF image shown in Figure 2.13 with overlayed intensity peaks and the corresponding Voronoi cells. (b) Result of the evaluation with the colour code corresponding to the integrated intensity over each cell

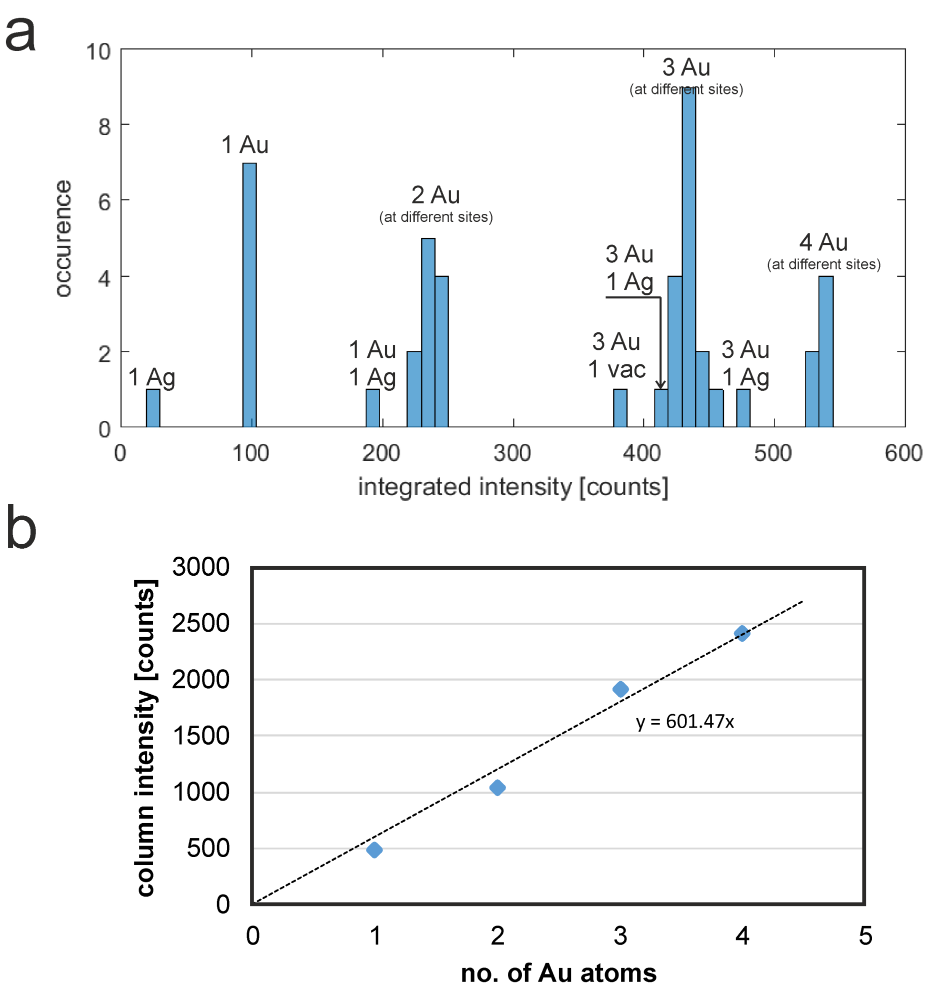

Figure 2.16.: (a) Histogram of the column wise intensity values of the ground truth image (Figure 2.15) with corresponding composition. (b) Mean column intensity values of columns only comprised of Au atoms over number of atoms in the column, exhibiting an approximately linear relationship.

variations that are cause by channelling effects. To allow direct comparison the quantification was repeated with identical settings with the noise obscured image, as well with the PCA and Wiener filtered images. Obtained results are depicted in Figure 2.17. Data sets shown in Figure 2.12 were used for these results. Exemplary, we pick three cases at different intensity scales, to evaluate the performance of the filters: The column that is represented by the weakest signal in the image is that one comprised of only one single Ag atom (Figure 2.12, column A6). The maximum pixel value in this column is only 3, which also means that the requirement for the Anscombe transform does not hold in this case. Accordingly, we will get a non-optimal result in this case. In sum, the column contains 203 counts. The value obtained from the PCA-filtered algorithm is 19 counts below that value, while the Wiener filter gives a intensity value that is 23 counts smaller. Since, the same region in the noisy image contains 179 counts (-24), PCA noise filtering has a slightly positive effect on the quantification result while the

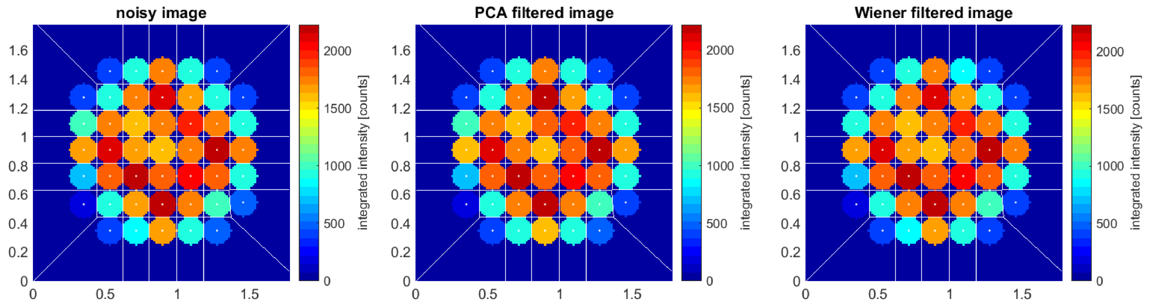

Figure 2.17.: Column wise intensities of the noisy image, the PCA filtered image and the Wiener filtered image. The voronoi cells and their corresponding center points are overlayed. x-y scale is in nm

Wiener filter would give the same result compared to the noisy image. The signal from a single Au atom was estimated from column B1, with 416 counts. Pixel values between 0 and 7 counts were found in the original image inside this cell. After noise filtering the region contained 427 counts in case of PCA and 434 in case of Wiener filtering. Both PCA and Wiener filter overestimate the intensity from this region. For comparison, using the noise corrupted image we obtain a signal of 424 counts. From a column purely comprised of 4 Au atoms (B4) we obtain a intensity value of 2151 from the original image, while we get 2095 (-56), 2132 (-19) and 2109 (-42) for the noisy, PCA and Wiener filtered image, respectively.

From these three examples one can already see that it is difficult to draw a generally valid conclusions. All differences are shown column wise in Figure 2.18. It can readily be seen that

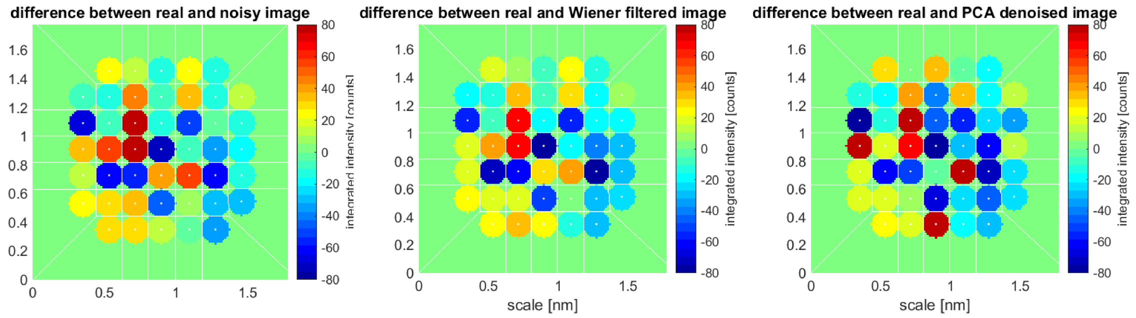

Figure 2.18.: The difference between the intensities determined from the noisy image to the ground truth intensities, compared to the filtered images

the differences not only depend on the ground truth intensity but also vary largely from column to column. This is, on one hand, due to local variations caused by the stochastic nature of noise and, on the other hand, by the patch-based treatment of the data in case of PCA. To obtain a directly comparable value we can normalise all intensity values in Figure 2.18 by the ground truth intensity and calculate the difference to the quantification based on the noisy data set. So we calculate $(|I_o - I_n| - |I_o - I_f|)/I_o$. With these values we can evaluate if noise filtering improves the quantification result, in comparison to the noisy image. The results are shown in Figure 2.19. A positive value in these images means that it is advantageous to quantify on base of the filtered image compared to the noisy one, for a certain column. If a negative value is shown the opposite is true. From these images we clearly see that PCA filtering has

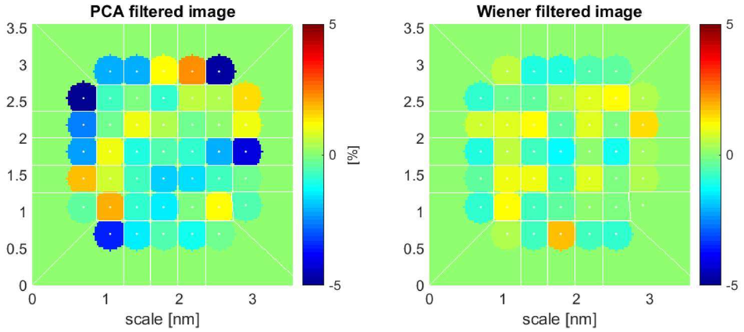

Figure 2.19.: Quantification based on PCA (I_{PCA}) and Wiener (I_W) filtered data sets, respectively, compared to intensity values obtained from the noise obscured image (I_n). The values where normalised by the ground truth intensities (Figure 2.15)

a unpredictable influence on the estimated intensity values. In some cases the quantification is improved, compared to the noisy image, but in most cases the filtered intensities differ significantly from the real (ground truth) image. The Wiener filter performs a bit better, but also gives no significant benefit, compared to the quantification based on noisy data. These results are also confirmed by the corresponding mean-square-error (MSE) values (Eq. (2.17)). We obtain a column wise MSE of 1.6×10^3 for the Wiener filter with regard to the ground truth. For PCA this value is 2.8×10^3 compared to 1.58×10^3 for the quantification based on the noisy data.

The position dependent performance of our algorithm under otherwise identical conditions suggests, that the way how the patches are chosen from the image relative to the image features (atomic columns) largely influences the result. This would be a point that would be worth to be improved in a future version of the code (see section 2.6.4.6).

2.6.4.5. Conclusion

Our tests suggest that the patch based PCA filter is very efficient to increase the SNR in STEM HAADF images. This could be interesting for the enhancement of weak features, not only in atomically resolved HAADF STEM images, but also for other imaging techniques.

However, we note that PCA filtering is not an improvement for HAADF quantification in its current form for the present demo data set. This is also true for the Wiener filter, albeit to a lesser extent. One advantage of our algorithm over the Wiener filter is, that filtered images appear smoother. This could improve the atomic column detectability and the accuracy of automatic peak finding algorithms, that are often used to find the exact positions of the atomic columns. Therefore, it could be advantageous to use a PCA filtered image to automatically determine the column position, while for the actual quantification, the original data set is used. Furthermore, for HAADF quantification approaches based on Gaussian peak fitting instead of Voronoi partitioning, although not considered here, could possibly take more advantage of PCA image filtering.

However, we are optimistic that the algorithm can be optimised with several improvement ideas that are discussed in the following section.

2.6.4.6. Outlook and Further Improvements for Patch Based PCA Noise Filtering

In the following we briefly discuss some possible improvements for our patch-based PCA noise filtering algorithm.
In some filtered images there are still some block shaped artefacts visible, especially in regions with high contrast variations. These "blocking" artefacts stem from the patch-wise treatment of the image. This issue can be prevented for instance by including overlap regions between different patches (as illustrated in Figure 2.11a), or by selecting the patches randomly. For a further improvement we could use larger training patches from which only the innermost pixels are then used as overlapping image patches to reconstruct the result image [72]. Furthermore, the patches can also be pre-sorted by their spatial proximity or by their similarity and collected to clusters, which are then treated separately [69]. Similarity, in this context, can be defined in different ways. For instance, structural or photometric criteria can be used [78]. Intelligent block-matching techniques, such as shown by [79], could also help to preserve quantitative intensity information during filtering.
The number of components considered to reconstruct the data set after decomposition would also require some improvement. In our examples we always use the same amount of components that was set manually before analysis. Especially in a multi-level approach as used in the example in 2.11 it would be advantageous to adjust the number of components automatically according to the variances occurring in the data. Another possible improvement is related to the variance stabilisation used here. The Anscombe transform is not applicable for data sets where significant Gaussian noise is contributing and/or where less than 4 counts per pixel need to be considered [63]. For mixed noise contributions we would need more general approaches, such as a generalized Anscombe transform [80, 81].
So there are still many things to do in order to improve the algorithm, but the first results seem promising for future work. However, if a really quantitative noise filtering can be obtained with this approach is still questionable, due to the non-zero variance of the removed components, as pointed out by Lichtert and Verbeeck [76].

2.6.4.7. Blind Deconvolution of HAADF Images

In every measurement process in physics the result is a convolution of the original physical quantity convolved with a function that describes the influence of the instrument on the measurement (instrument function). In high-resolution STEM HAADF imaging, the physical quantity is the number of electrons that are scattered by the atomic potential field to a certain angular range, dependent on the position x. The instrument function is the shape of the scanning electron probe, referred to as point spread function (PSF) in the following. Simplified, the detected signal f can be described using Eq. (2.19), with g the PSF and h the scattering pattern.

$$f = (g * h)(x) \tag{2.19}$$

The convolution operation is denoted with symbol "*" and corresponds to a multiplication in Fourier space:

$$f = \int_{-\infty}^{\infty} g(\xi) \cdot h(x-\xi) \cdot d\xi \tag{2.20}$$

with $\mathscr{F}$ denoting the Fourier transform we obtain:

$$\mathscr{F}(g * h) = k \cdot \mathscr{F}(g) \cdot \mathscr{F}(h) \tag{2.21}$$

and accordingly a deconvolution could be achieved with:

$$\mathscr{F}(h) = \frac{\mathscr{F}(f)}{\mathscr{F}(g)} \tag{2.22}$$

which gives h after inverse Fourier transformation of $\mathscr{F}(h)$.
Unfortunately, finding a solution for h is not that easy. Firstly, we do not know the exact form of the PSF g. Often the PSF is what we are searching for. Secondly, $\mathscr{F}(g)$ is probably zero at some points, which results in undefined values for Eq. (2.22). Lastly, our measurement signal is corrupted by noise, which has a huge influence on the result, if neglected. So we have to seek for the most probable shape of h. This problem is often referred to as "blind deconvolution". Image deconvolution techniques are used in variety of fields, such as optical microscopy, astronomy or medicine. For STEM images Watanabe et al. presented a iterative method for blind deconvolution based on entropy maximisation.
Here, we use a maximum-likelihood blind deconvolution routine as implemented in the Matlab image toolbox. It maximizes the likelihood that the resulting image, convolved with the corresponding PSF, is an instance of the original image. This routine can be called via following command:

```
[J,PSF] = deconvblind(I,PSF0,nit)
```

where the input variables are the original image `I` an initial guess for the point-spread-function `PSF0` and the number of iterations `nit`. The function returns the estimated probe shape `PSF` and the deconvolved image `J`.
Maximum likelihood methods attempt to fit data as closely as possible and therefore noise amplification is a common problem. After several iterations, artefacts become visible in the restored image. Therefore, the standard deviation of Poison noise in the data can be considered by a damping term within the algorithm, as well as additive Gaussian (readout) noise, if known.
We wrote a Matlab script to perform some testing using the blind deconvolution algorithm on our data sets. Since the exact noise characteristic of experimental HRSTEM images is usually not known we did not use the capability of the algorithm to account for noise. Instead we used pre-noise filtering in our script.
First we demonstrate the capability of image deblurring. For this we use the same image

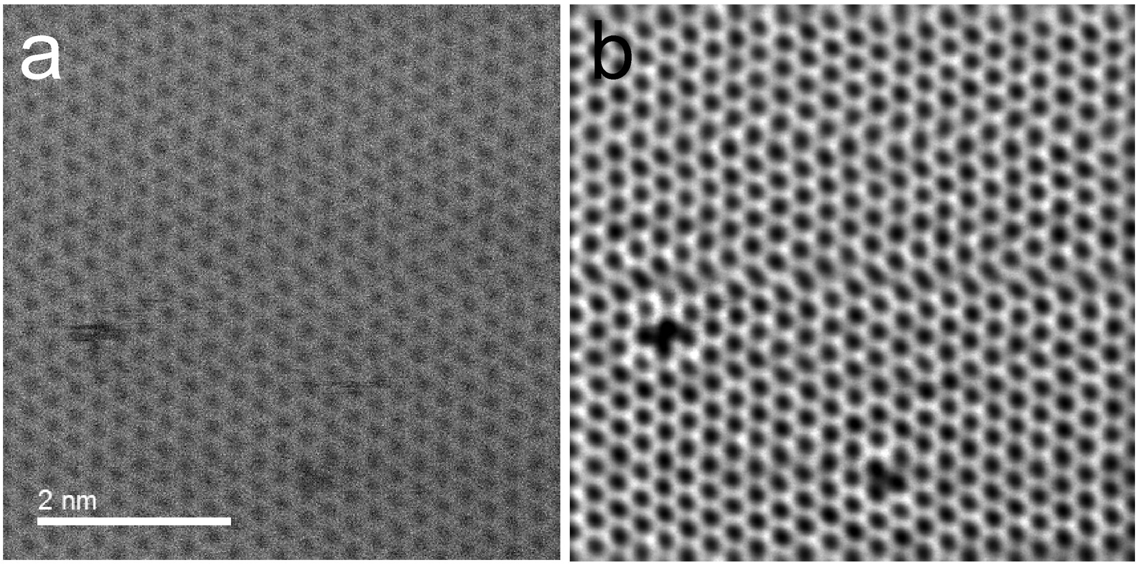

Figure 2.20.: (a) Raw STEM HAADF image of an h-BN bilayer (Titan@60kV). (b) Resulting deconvolved image after 30 iterations

(h-BN bilayer, Titan@60kV) as in the previous section (see Figure 2.10). For the sake of completeness and to allow direct comparison the raw image is shown here again in Figure 2.20a. We started with a Gaussian peak as an initial guess for the PSF to speed up the convergence of the algorithm. To reduce the influence of noise on the result, noise filtering can be applied before the convolution process is started. Here, the user can choose between three options, the patch-PCA based algorithm presented in the previous section, a Butterworth filter or the Wiener filter as implemented in Matlab. In Figure 2.20b the result of the algorithm after convergence (30 iterations) is shown. In this example the image was PCA filtered before deconvolution, with patch sizes between 8 to 256 pixels using 15 components at each step. To check the convergence behaviour of the deconvolution process, the number of iterations is increased sequentially. At each step the FWHM of the calculated probe is determined. The initial (Gaussian) PSF had a full-width-at-half-maximum (FWHM) of 400 pm and reached 129 pm until convergence, which is a realistic value for our Titan microscope at 60 kV and a convergence angle of 21.4 mrad. For the determination of the probe shape and size an image with less artefacts and higher magnification is advantageous. We have to bear in mind that the resulting PSF will have the same pixel size as the original image. Therefore, we should aim for an image at high magnification and resolution with high SNR, which is difficult in many cases, due to damage and sample drift. Both lead to blurring and image artefacts, which renders an estimation of the beam size difficult. In our example we used an HAADF image of a single crystalline silicon sample, oriented in (110) direction with regard to the electron beam.
Figure 2.21a shows the raw image used for the calculations. The image has a resolution of 1024x1024 pixels, and was acquired at 300 kV and a convergence angle of 19.6 mrad. Before deconvolution we applied a hierarchically, patch-PCA based noise filter with 5 components for each patch size, as presented in the previous section.

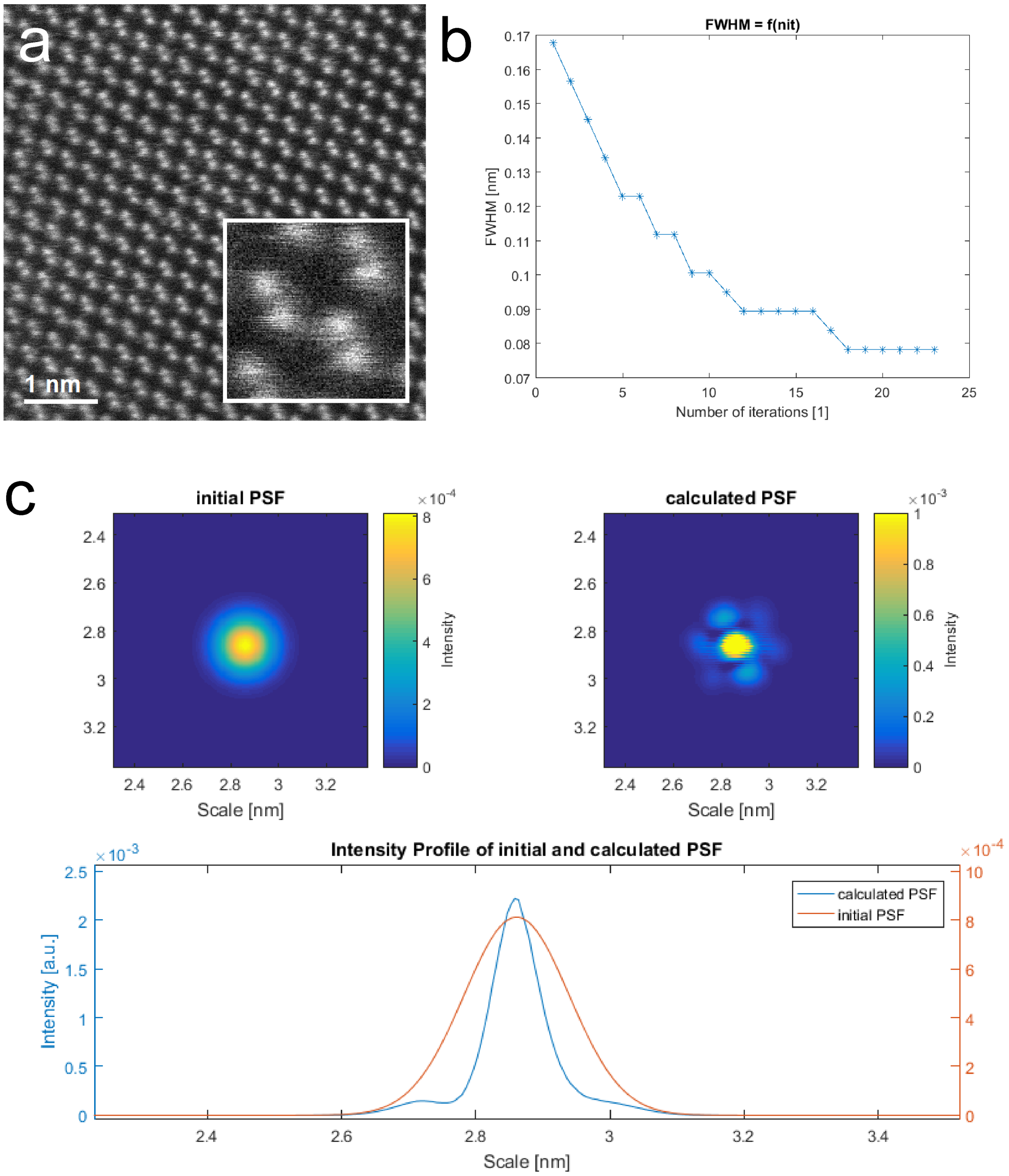

Figure 2.21.: (a) Raw STEM HAADF image of Si in (110) direction. Inset shows a part of the same image showing significant scanning artefacts. (b) Progression of the FWHM of the PSF over the number of iterations (c) Resulting deconvolved PSF after 23 iterations.

The raw image exhibits strong jittering effects due to electrical and mechanical distortions during image acquisition. These artefacts can also be seen in the resulting PSF (shown in 2.21c). These distortions together with residual noise in the image cause that the algorithm often does not converge to the true PSF. In such cases the user has to find the optimal amount of iterations by evaluating the PSF and the corresponding deconvolved image. Calculating the MSE (Eq. (2.17)) between the original image and the resulting PSF convolved with the resulting image at each iteration also helps to estimate a optimal amount of iterations, because the MSE at some optimum reaches a plateau before it further decreases. The periodic lattice also has an impact on the shape of the PSF. It causes small side peaks in the directions of the lattice vectors. For the present example we obtained a FWHM of the PSF of approximately 79 pm, starting with an Gaussian peak with a FWHM of 168 pm. This is also quite close to the resolution that can be expected for the present setting at this microscope. The typical probe size as given by the manufacturer is 70 pm on this machine.

Conclusively, we showed that blind deconvolution can be used in principle for both image restoration and determination of the probe size. However, we have to bear in mind its limitations. Residual noise and scanning artefacts can distort results. The choice of image magnification and resolution and the noise filter can have a big influence. The choice of the initial guess for the PSF can also have an effect. Furthermore, it could be considered to apply corrections for scanning artefacts to improve results as suggested by Jones et al. [82].

2.7. Hydrocarbon Contamination

This chapter is about a fundamental issue, that is known to every electron microscopist as one of the most annoying effects during TEM analysis: beam induced carbon deposition. Mobile carbon containing contaminants, typically composed of hydrocarbons with a wide range of stoichiometries and chain lengths, are adsorbed on the specimen and destroyed under electron beam irradiation. While gaseous dissociation products like H_2, O_2, CO or CO_2 can then leave the sample, a significant amount of carbon gets immobilized and remains on the sample surface. This process is known as electron beam induced deposition (EBID). Contamination results in a reduction of clarity of sample features during imaging and obscures characteristic elemental signals in EELS and EDS because of double scattering and absorption effects. Thereby, contamination poses a limit to the performance of the microscope. The lower the electron energy used for imaging the more significant the contamination problem becomes [83].

Although, in recent years these effects could be reduced via improved microscope vacuum techniques (use of oil free pumps), this is still a big problem in many cases. This is true especially for such small systems as metallic clusters, which anyway only give faint analytical signals. Even small amounts of contamination lower the attainable SNR and cause an increase of the background signal, hindering the extraction of valuable signal. Therefore, finding a way to avoid such contaminants was the first big challenge at the beginning of the experimental work within this thesis.

The two main questions that arose were:

- Where do the hydrocarbons come from?
- How can they be disposed?

The microscope vacuum was excluded at the beginning, because the amount of carbon deposition seemed to be unrelated to the vacuum pressure and only oil-free pumps are attached to the most sensible parts of our FEI Titan, that was mainly used in this work. Furthermore, hydrocarbons should be removed efficiently by the cooling trap and the ion getter pump of the microscope over time. The only part that is inserted into the microscope is the sample holder which is cleaned for at least 15 minutes in a dedicated plasma cleaner (Fischione, 80% Argon and 20% oxygen) every time before mounting the sample grid. It is known that contamination is also adsorbed directly from air. Therefore, an evacuated transfer vessel was build, to reduce the amount of time the sample is exposed to the environment during transfer from the synthesis apparatus to the microscope. Analysis of the amorphous carbon TEM grids in their as delivered state revealed the presence of significant amounts of carbon contamination. After several experiments it turned out that almost all hydrocarbon contamination can be attributed to these grids.

After identification of the source of our contamination a cleaning procedure for the TEM grids had to be found. There are several studies addressing hydrocarbon contaminants in electron microscopy. Most efficiently they are removed by plasma cleaning [84, 85], which is therefore used with different plasma species wherever possible. Since the thin amorphous carbon support would be damaged very rapidly in most plasmas available, this procedure was excluded. Alternative approaches were tested by McGilvery et al. [85]. They compared plasma cleaning, rinsing with ethanol and isopropanol and heating in a vacuum furnace in their work. They found the latter to be most efficient for sensitive specimens. Soong et al. showed that UV light can also be used efficiently to remove carbon contaminants [86]. Algara-Siller et al. showed the cleaning of graphene samples via heating in activated charcoal (30 min@210 °C in air) [87]. They stated that mobile contaminants on the sample get adsorbed by the charcoal.

In this work we followed the idea that this cleaning mechanism should also be applicable to other materials than graphene. We combined this approach with heating in a vacuum furnace. The substrates were baked for several hours at 200 °C in charcoal before mounted in the synthesis apparatus. There the substrates were again heated under UHV conditions over night at 200 °C before nanoparticle deposition.

In order to allow sample heating in a wide range of temperatures under high vacuum conditions a vacuum furnace was designed and build.

2.7.1. Vacuum Furnace

We build a vacuum furnace, not only with having sample cleaning in mind, but also to allow annealing experiments for arbitrary TEM and SEM samples. Therefore a flexible solution had to be found. The vacuum furnace was build with great support by the Institute of Experimental Physics (TU Graz). Especially the work of Philip Thaler who planned the furnace and Alexander Volk who helped with the installation is acknowledged at this point. The most important parts are shown in Figure 2.22

Performance characteristics of the vacuum furnace:

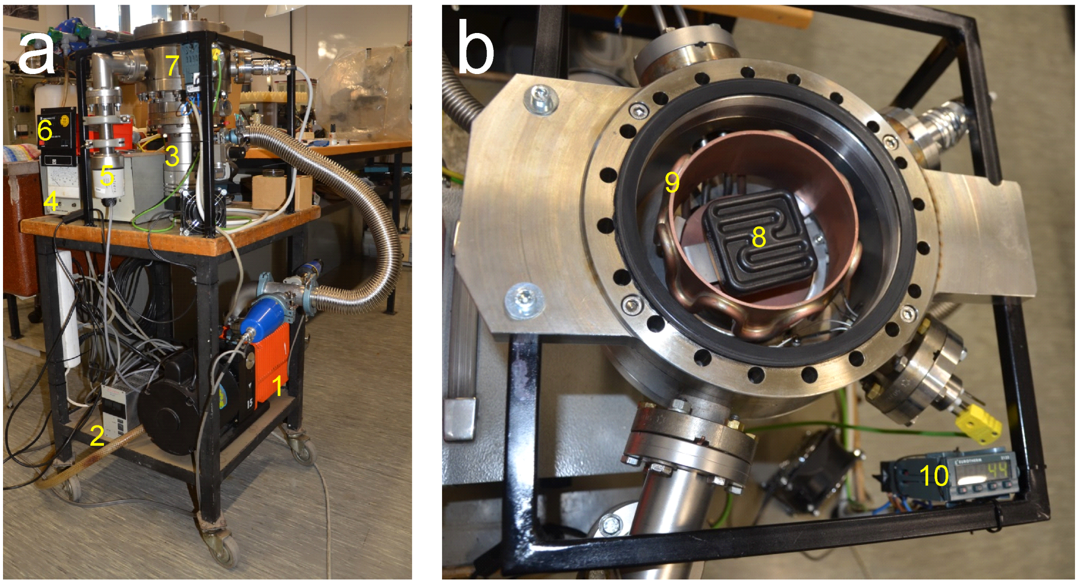

Figure 2.22.: Main parts of the vacuum furnace: a) 1: roughening pump (rotary vane pump) with attached vacuum gauges, 2: pressure gauge controller for the vacuum gauge of the main chamber, 3: turbo molecular pump for the main chamber, 4: pressure gauge controller for the pre vacuum, 5: vacuum gauge for the main chamber, 6: controller for turbo molecular pump, 7: main chamber. b) 8: heating area, 9: cooling shield, 10: temperature controller

- maximum temperature: 900 °C
- minimum pressure: $<1 \times 10^{-5}$ mbar

2.8. Cluster Synthesis Inside Superfluid Helium Droplets

In this work metallic clusters were grown inside superfluid He droplets, at the Institute of Experimental Physics (TU Graz) [29, 88]. A schematic representation of their synthesis apparatus is given in Figure 4.19. First droplets with diameters of approximately 80-1000 nm, consisting of about 10^7 to 10^{10} ^{4}He atoms are produced. To this end, pressurized (10-100 bar) high purity helium (99.9999 %) is expanded through a cooled (3-25 K) nozzle with a diameter of approximately 5 µm into vacuum. During the expansion, droplets are formed, which cool themselves to approximately 0.4 K by evaporative cooling. A droplet beam is shaped by a skimmer and enters a second vacuum chamber (pick-up chamber) housing the doping facilities. There, the metal of choice is thermally evaporated in a crucible and the droplet beam is guided through the vapor, where metal atoms colliding with helium droplets are deposited inside the droplets. Evaporated atoms are immediately cooled to droplet temperature and aggregate in the centre of the droplet. The maximum crucible temperature of 2000 K allows to evaporate a large variety of materials. After passing a second skimmer, the droplet beam enters a third vacuum chamber, where it is terminated on a TEM-grid. Upon collision with the substrate with a

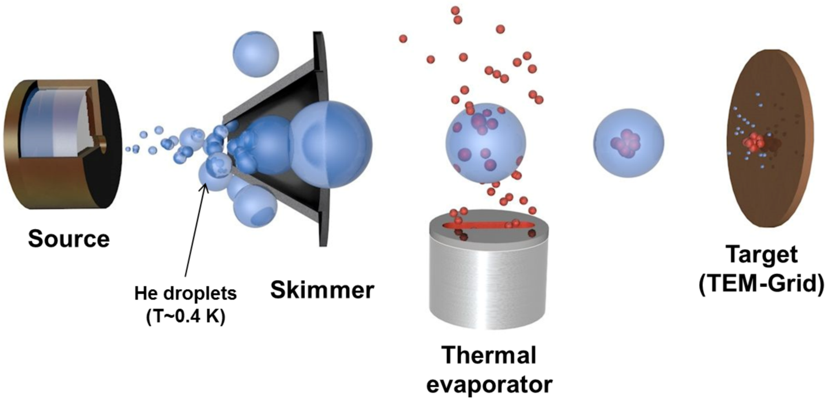

Figure 2.23.: A beam of superfluid He-droplets (blue) is generated by expansion through a cooled nozzle. After passing the skimmer they collide with Ni atoms (red) evaporated by the thermal evaporator. The particles congregate in the center of the droplet and finally land on the target (e.g. a TEM-grid)

droplet velocity of approximately 200 $\mathrm{m\,s^{-1}}$, the helium cushions the impact of the transported cluster and evaporates, leaving the bare cluster adsorbed on the surface. The base pressures in all chambers are sufficiently low, so that no other atoms are picked up by the droplets. Since for each dopant atom picked up, several thousand He droplets evaporate, dependent on the binding energy of the dopant species, the size of the clusters is limited by the droplet size. Deposition and storage of the samples in the last chamber take place under ultra-high vacuum (UHV) conditions ($p < 1 \times 10^{-7}$ Pa). This approach distinguishes itself from other cluster synthesis methods in terms of purity and flexibility concerning the materials. The method produces pure clusters without using templates or stabilisers. The universal doping capabilities of He allow to grow clusters of virtually any material and the synthesized particles can be deposited on arbitrary substrates. This gives us an ideal playground for studying fundamental cluster properties, develop characterisation methods and study electron beam induced damage effects. If more then one thermal evaporator is placed in the pick-up chamber, the sequence of the evaporators determines the sequence of the materials in the clusters. This can be used to produce core-shell particles with tailored elemental composition. The arrangement with 1 evaporator is shown in Figure 2.23. Note that due to the complex growth mechanisms inside a He droplet it is difficult to predict the final shape and composition of the obtained clusters. To learn how to control this process was one of the main goals of our work.

2.8.1. Substrates for Cluster Characterisation

The substrate considerably influences the morphology of the clusters. For most experiments substrates with an amorphous carbon film with <3 nm thickness, backed with a holey carbon support film and a 300 mesh gold grid (Ted Pella, Inc., Prod. No. 01824G) have been used. For some experiments also monolayered graphene on Quantifoil R2/4 holey carbon gold grids (purchased from Graphenea Inc.) and boron nitride bilayers. The latter were produced with the famous scotch tape method and transferred to Quantifoil R2/4 holey carbon gold grids.

To eliminate contamination all substrates were baked at 200 °C in air for 1 h before placed in the synthesis facility. The grids were brought into contact with active coal to support the cleaning process. After mounted in the deposition chamber the substrates were baked again at 200 °C in UHV conditions for several hours before cluster deposition. Although, an evacuated vessel was used for the transfer from the synthesis facility to the microscope vacuum, the samples were shortly (< 5 min) exposed to ambient conditions.

3. Theory and Simulations

3.1. Beam Damage Effects

Not least, electron microscopy relies on the highly effective interaction of electrons with matter. In principle this interaction complies of scattering processes of incident electrons with both nuclei and electrons of the sample atoms. Simplified, we can distinguish between elastic (mostly electron-nuclei) and inelastic (mostly electron-electron) scattering. The term elastic here refers to electrons whose energy loss can not be detected, limited not only by the energy spread of the incident electrons [2], but also by the collection angle of the EEL spectrometer. Even though Rutherford scattered electrons may also be scattered to high angles and thereby loose a significant amount of energy, they are still referred to as "elastic". Scattering processes are very often not reversible and hence lead to a variety of damage mechanisms, dependent not only on the sample composition, but also on its electronic structure, bonding configuration, crystal orientation and local chemical environment. The high efficiency of electron beam induced damage effects is practically used for example in cancer therapy, electron beam lithography or electron beam induced deposition techniques [89].

Modern aberration-corrected STEM machines provide high spatial and energy resolution at high signal-to-noise ratios. This implies the use of extremely high electron beam current densities. Under these conditions beam damage effects become unavoidable. This is true especially for nanostructures with a high amount of low-coordinated atoms, like nanoclusters or nanowires. For the characterization of such materials in STEM beam damage effects need to be considered. In these systems, consisting of only a few hundred to thousands atoms, even low electron doses may change composition, morphology and chemistry very rapidly. Nowadays, beam damage is the fundamental resolution limit in electron microscopy. The achievable resolution d_s under consideration of specimen damage can be understood using Eq. (3.1) following Harald Rose [90].

$$d_s = \sqrt{d_i^2 + \frac{\mathrm{SNR}^2}{C^2 D_c}} \tag{3.1}$$

where d_i denotes the instrumental resolution limit ($d_i = 0.61\lambda / \sin\alpha$, aberration terms left out for clarity), *SNR* the signal-to-noise ratio, C the contrast between two features in the image and D_c the maximum dose tolerated by the specimen before beam damage occurs.

In signal theory of imaging systems the signal-to-noise ratio is defined as the ratio of the average signal value in the image to the standard deviation of the background. Following the Rose criterion, named after Albert Rose, SNR should be $> 3-5$ to be able to discriminate an image feature from the noise [91]. If the tolerable dose D_c is very high, the resolution is limited by the instrumental resolution d_i. Practically, D_c is given by the specimen and can mainly be controlled by the high tension, but also by the temperature (cooling) or sample preparation (enhanced conductivity due to sample coating). The other two parameters SNR and C depend on the imaging technique, the high tension or the detector performance, but can also be enhanced by post-processing techniques (e.g. PCA, see section 2.6.1). These parameters need to be optimized to gain the best results, or sometimes to even get any interpretable result. To understand beam damage processes is therefore paramount for a reliable characterization of nanoscaled materials.

Egerton derived an expression for the dose-limited resolution after an electron dose D is applied to the specimen, taking into account the detective quantum efficiency DQE for the used recording system and the detection efficiency F (Eq. (3.2)) [92]. The latter is defined as the ratio of detected counts (electrons or X-rays) to the number of incident primary electrons.

$$d = \frac{\mathrm{SNR}}{|C|}\sqrt{\frac{e\left(C^2+3C+2\right)}{\mathrm{DQE}\cdot F\cdot D}} \tag{3.2}$$

According to [92], the contrast C of a beam sensitive sample feature decays roughly exponentially: $C = C_0 \cdot \exp\left(-D/D_c\right)$. In this study it is stated that this equation phenomenologically describes the fading of diffraction features during beam induced amorphisation of initially crystalline specimens. However, we have to bear in mind that all given relationships are only valid if the probability for a scattering event, that causes sample damage, is constant. Especially for nanoclusters this is generally not the case. For such small systems, displacement probabilities depend on the surface configuration, the orientation and the size of the clusters. All these quantities again change due to beam induced displacement and sputtering effects.

The probability of a certain scattering event to occur can be characterized by the scattering cross section σ and the mean free path λ. The two quantities are related to one another by Eq. (3.3).

$$\lambda = \frac{1}{N\sigma} \tag{3.3}$$

where N denotes the number of scattering atoms per unit volume. The total scattering cross section σ_{tot} can be written as a sum over all atoms of type k in the nanostructure and all types of scattering events l per species:

$$\sigma_{tot} = \sum_k \sum_l \sigma_{kl} N_k \tag{3.4}$$

where N_k denotes the number of atoms of type k.

With a given current density j also the mean time period τ_l between two scattering events of type l with cross section σ_l can be calculated:

$$\tau_l = \frac{1}{j\sigma_l} \tag{3.5}$$

One has to bear in mind that, despite the high current densities occurring in modern aberration-corrected microscopes, it is highly unlikely that there is more than one electron in the sample at one time. For a typical current of 100 pA we can calculate a time span of about 1.6 ns between two electron impacts.
In the following some of the most important damage mechanisms in electron microscopy are briefly explained, with focus on the most important ones for the STEM characterization of metallic nanoparticles. In general, several of these mechanisms act at the same time, and it is highly non-trivial to predict the damage behaviour of a certain material. However, we will see that beam induced sample changes of pure metallic nanoclusters can mostly be reduced to only one mechanism, namely the so-called knock-on damage.

3.1.1. Knock-on Damage

Elastic forward scattering of energetic incident electrons from the Coulomb field of atomic nuclei is the most important type of interaction of electrons with matter in electron microscopy. All imaging techniques in TEM rely on this type of scattering. The momentum transfer to the atom can be neglected in most cases for these electrons. Nevertheless, a few electrons are scattered to high angles and thus transfer energies up to several eV, which is in the energy range of atomic displacement, sputtering and defect generation in many solid materials. These types of damage events are subsumed under the term knock-on damage.
Generally, the maximum energy transfer E_{max} of a relativistic particle with energy E and mass m_0 to a nucleus with mass m is given by following equation:

$$E_{max} = \frac{2mE\left(E+2m_0c^2\right)}{\left(m_0+m\right)^2 c^2 + 2mE} \tag{3.6}$$

where c is the vacuum speed of light. For electron irradiation where $m_0 << m$ and $E << mc^2$ Eq. 3.6 can be simplified and the transferred energy E_t to an atom by an electron scattered to an angle θ can then be calculated via:

$$\begin{gathered} E_t = E_{max} \cdot \sin^2 \frac{\theta}{2} \\ \text{with} \quad E_0 = m_0c^2 \quad \& \quad E_{max} = \frac{2E\left(E+2E_0\right)}{mc^2} \end{gathered} \tag{3.7}$$

With Eq. (3.7) the transferred energy is directly related to the scattering angle. The angular dependent likelihood that a point-shaped, fermionic (spin-1/2) particle is scattered by a static, point-shaped and charged target particle can be described in a first approximation by the well known Rutherford model [93]. This description is valid for scattering angles between approximately 2°-20° for typical electron energies used in the TEM [94]. For lower angles screening effects need to be included and the Lenz-Wentzel model can be used as an approximation, whereas for an adequate description of higher scattering angles, especially for high Z elements, we need the Mott scattering cross section model, first proposed by Nevill Francis Mott in the year 1929 [95]. Exemplary, Figure 3.1 shows cross section curves of tabulated values of the differential cross section $\frac{\partial\sigma}{\partial\Omega}$ taken from the NIST database [58]. These values were used throughout this work. Usually, differential cross sections values are given as a function of scattering angle θ.

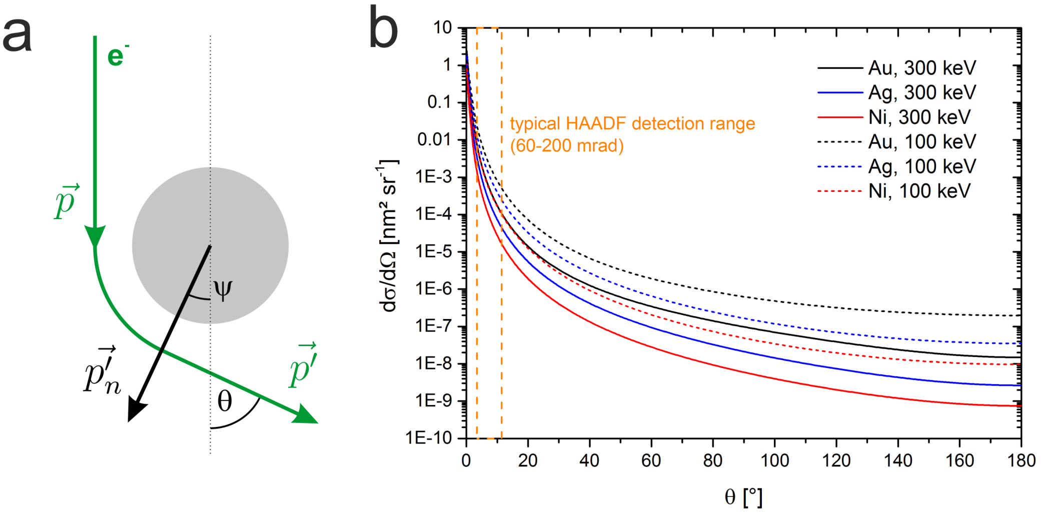

Figure 3.1.: (a) Elastic scattering event of an electron with momentum $\vec{p}$ from an atomic nucleus. The nucleus gains the momentum $\vec{p}'_n$ after scattering. (b) Illustration of the NIST differential elastic scattering cross sections for 100 keV and 300 keV electrons, exemplary for Au, Ag and Ni as a function of the scattering angle θ; The dashed line corresponds to a typical maximum HAADF detection angle range of 60-200 mrad (3.4-11.5°)

The elastic scattering cross section integrated over an angular interval $[\theta_{min}, \theta_{max}]$ can be calculated via [96, 97]:

$$\sigma_{[\theta_{min},\theta_{max}]} = 2\pi \int_{\theta_{min}}^{\theta_{max}} \frac{\partial\sigma}{\partial\Omega} \cdot \sin\theta \cdot d\theta \tag{3.8}$$

After rearrangement of Eq. (3.7), θ_{min} is given for a certain threshold energy E_d by:

$$\theta_{min} = \arcsin\left[2\left(\frac{E_{min}}{E_{max}}\right)^{1/2}\right] \tag{3.9}$$

The energy needed to displace an atom is determined by its local bonding energy and by the availability of empty lattice sites in its neighbourhood. Consequently, displacement energies are, on one hand, much lower for surface atoms compared to bulk atoms and, on the other hand, strongly dependent on the crystal orientation with regard to the direction of incident primary electrons. With knowledge of the differential scattering cross-section the cross-section for a displacement σ_D event can be calculated using Eq. (3.10) [98, 99].

$$\sigma_D = 2\pi \int_{\theta_{min}}^{\pi} P(E_t) \cdot \frac{\partial\sigma}{\partial\Omega} \cdot \sin\theta \cdot d\theta \tag{3.10}$$

Where $P(E_t)$ denotes the probability that an atom is displaced after a certain energy transfer E_t. The sputtering cross section σ_S can be defined in a similar way. Often $P(E_t)$ is assumed to be a step like function, being 0 below an energy threshold value E_d and 1 above. Practically, for metallic surfaces and clusters this is a very rough assumption, because several different displacement mechanisms occur dependent on orientation and local configuration, each with a different E_d value. Therefore, in crystalline species $P(E_t)$ is also a function of the incident angle, which is often ignored. For heavier elements $P < 1$ even for high scattering angles. Furthermore, for high beam energies and/or light elements an electron may also displace more than one atom, resulting in a displacement cascade. All these influences render displacement and sputtering phenomena dependent on the local anisotropy and therefore on the geometry. For flat or tubular shaped nanostructures with a high geometric symmetry, like graphene or carbon nanotubes, an emission energy threshold E_d can be calculated as a function on the direction of the scattering vector $\vec{p}_n'$ [100, 101].

With the knowledge of E_d one can calculate the displacement cross section with an analytical expression according to McKinley and Feshbach, as a function of the maximum transferred energy E_{max} [102, 103].

$$
\begin{aligned}
\sigma_D = \frac{4Z^2E_R^2}{m_0^2c^4}\left(\frac{E_{max}}{E_d}\right)\pi a_0^2\left(\frac{1-\beta^2}{\beta^4}\right)\Bigg\{1+2\pi\alpha\beta\sqrt{\frac{E_d}{E_{max}}}\\
-\frac{E_d}{E_{max}}\left[1+2\pi\alpha\beta+\left(\beta^2+\pi\alpha\beta\right)\ln\left(\frac{E_{max}}{E_d}\right)\right]\Bigg\}
\end{aligned}
\tag{3.11}
$$

This formula is valid for light elements with $Z < 21$ [102, 104]. Meyer et al. showed that the thermal movement of atoms leads to a smearing of the onset energy for a certain type of displacement, and found an expression to include this into Eq. (3.11). Accordingly, thermal contribution to atom movement effects its own displacement threshold. This means that the atom gains more energy if it is displaced while it moves parallel to the electron beam compared to the static case. (see [103] for more details).

In literature the general statement that knock-on damage increases with increasing beam energy can very often be read [1]. Unfortunately, this rule of thumb is only applicable for heavier elements (e.g. $Z > 10$ for $E_d = 10\,\mathrm{eV}$) or high values of E_d (e.g. $E_d > 17\,\mathrm{eV}$ for O) [99, 105]. Otherwise there is no simple relationship between knock-on cross section and primary electron energy and one has to decide from case to case. This can be quite complicated if, for example, the displacement cross section for a bulk atom increases with energy, whereas that of a surface atom may decrease. Often also the displacement cross section increases with prolonged beam exposure, due to an increase of the defect density in the material with time [99].

3.1.2. Beam Induced Heating in Metallic Nanoparticles

Electrons hitting the specimen lose energy due to (inelastic) interaction processes, mainly by plasmon and phonon excitations. The energy is dissipated to heat which is quickly balanced by heat loss due to radial conduction and radiation, forming a steady state ($P_t = P_c + P_r$). P_t is the heat deposited in the specimen volume per second and P_c is the heat flow away from the source along radial direction. The radiation term P_r, can be calculated according to the Stefan-Boltzmann law ($P_r = \sigma \varepsilon A T^4$, with ε being the absorptive power of the black body radiation, A the surface area and σ the Stefan-Boltzmann constant).

In literature there is some controversy about the electron beam induced heating effect in the (S)TEM. The majority of authors state that specimen heating can be neglected at least for metallic samples at conditions usually used for imaging in a TEM [106–110]. For the particle on a substrate configuration some authors, however, proposed a significant heating effect, especially at high current TEM conditions, poor thermal conducting samples and when the particle-substrate interface area is too small to dissipate the deposited heat fast enough. The latter can be the case especially for low surface energies between particle and substrate and larger particles with diameters of more than several tenth of nanometres, which in general exhibit higher contact angles to the underlying substrate (see 3.2a for the definition of the contact angle) [111–113]. The contact angle increases with increasing particle size and thus also the heating effect increases. Of course the picture of a contact angle is only a vehicle since it implies an isotropic medium and is not valid for a crystal. This rough approximation becomes more and more vague for smaller particles where edge energies are non-negligible and Wulff-shaped morphologies are preferred [114]. See section 3.4.1 for more details on the shape of supported nanoparticles.

The question whether beam heating can be neglected is crucial for our considerations. Therefore we took a closer look on this problem. We performed analytical heat flow calculations and finite element (FEM) simulations. To enable an analytical treatment in the following calculation the heat transfer problem is simplified to a 1-dimensional axial symmetric problem with cylindrical geometry (see Figure 3.2a). With this simplification the heat equation can be written in cylindrical coordinates with azimuthal symmetry:

$$\frac{d}{dr}\left(r\frac{dT}{dr}\right) = 0 \tag{3.12}$$

with the general solution $T(r) = C_1 \ln r + C_2$. The constants C_1 and C_2 can be obtained from boundary conditions, given by the heat flux P_t (energy deposited per second by incident electrons) at the inner radius of the cylinder $r = r_i$ (Neumann boundary), and a known temperature T_2 at the outside boundary $r = r_a$ (Dirichlet boundary). This geometric arrangement has its equivalent to a thin foil supported by a good heat conductor (e.g. a metal grid). It could also be a cylindrical shaped precipitate inside a heat conducting thin foil, for example. Despite the differences to the case of a supported particle surrounded by vacuum, this treatment in principle at least allows us to estimate the magnitude of the heating effect.

The heat deposited by the electron beam P_t can be calculated with Eq. (3.13).

$$P_t = \frac{I}{e} \cdot \frac{\Delta E}{\Delta x} d \tag{3.13}$$

The conducted heat can be calculated using Fourier's law for cylindrical symmetry:

$$P_c = -\kappa A \frac{dT}{dr} \quad \text{with} \quad A = 2\pi r d \tag{3.14}$$

We integrate:

$$\frac{P_c}{2\pi d} \cdot \int_{r_i}^{r_a} \frac{1}{r} \cdot dr = -\kappa \int_{T_1}^{T_2} dT \tag{3.15}$$

And obtain after rearranging:

$$P_c = -2\pi\kappa d \frac{T_2 - T_1}{\ln \frac{r_a}{r_i}} \tag{3.16}$$

For room temperature conditions the radiation term P_r can be neglected so that $P_t = P_c$. With Eq. (3.13) the temperature gradient $\Delta T = T_2 - T_1$ inside a cylindrical geometry under electron irradiation in STEM can be estimated:

$$\Delta T = \frac{I}{2\pi\kappa e} \left(-\frac{\Delta E}{\Delta x} \right) \cdot \ln \frac{r_a}{r_i} \tag{3.17}$$

where r_a is the outer radius of the cylinder, I the beam current and r_i corresponds to the inner radius (e.g. the beam radius). κ is the thermal conductivity of the sample and e the electron unit charge.

The energy loss per path length $\frac{\Delta E}{\Delta x}$ of an electron in a sample can be calculated by using the Bethe-equation for the stopping power of electrons in matter (Eq. (3.18)) [108].

$$\begin{aligned} -\frac{\Delta E}{\Delta x} = \frac{2\pi Z\rho \left(e^2/4\pi\varepsilon_0\right)^2}{mv^2} \Bigg\{ & \ln \left[\frac{E\left(E + mc^2\right)^2 \beta^2}{2I_e^2 mc^2} \right] \\ & + \left(1-\beta^2\right) - \left(1 - \sqrt{1-\beta^2} + \beta^2\right) \cdot \ln 2 + \frac{1}{8}\left(1 - \sqrt{1-\beta^2}\right)^2 \Bigg\} \end{aligned} \tag{3.18}$$

where:
ρ = atomic density
Z = atomic number
E = incident electron energy
$\beta = v/c$
ε_0 = vacuum permittivity ($\varepsilon_0 = 8.85 \times 10^{-12}\,\mathrm{C\,V^{-1}\,m^{-1}}$)
I_e = mean excitation energy

The mean excitation energy I_e can be obtained from data bases or calculated with the approximation by Berger & Seltzer [115] (for a rough approximation also $I_e = 13.5 \cdot Z$ [eV] can be found in literature [93]).

$$I_e = 9.96 \cdot Z + \frac{58.5}{Z^{0.19}} \quad [\text{eV}] \tag{3.19}$$

Exemplary for a gold nanoparticle (d_p = 10 nm, ρ = 8.81 × 10^{28} $\mathrm{m^{-3}}$, Z = 79 and κ = 314 $\mathrm{W\,m^{-1}\,K^{-1}}$) supported by an amorphous carbon film (d_c = 3 nm, κ = 1.5 $\mathrm{W\,m^{-1}\,K^{-1}}$) in a focused electron beam (E = 300 keV, I = 100 pA) we get for the energy dissipated in the particle:

$$\frac{\Delta E}{\Delta x} = 2.34\,\mathrm{eV\,nm^{-1}} \quad \text{with} \quad I_e = 796.5\,\mathrm{eV} \tag{3.20}$$

and for the contribution of the carbon film:

$$\frac{\Delta E}{\Delta x} = 0.46\,\mathrm{eV\,nm^{-1}} \quad \text{with} \quad I_e = 100.2\,\mathrm{eV} \tag{3.21}$$

To simplify we assume in the following that the heat brought in by the electron beam is simply the sum of the two contributions by the particle and the substrate. Due to the high heat conductivity of metals compared to that of the amorphous carbon film we further assume that there is no temperature gradient inside the metallic particle. This we will prove by FEM calculation in the following section. We set the radius r_i of our heat source to be the half diameter of the particle $d_p/2$ and the outer radius to the maximum distance of the particle to the metallic grid bar of the TEM-grid, which is e.g. 27 µm on a 300 mesh grid. Then, with κ = 1.5 $\mathrm{W\,m^{-1}\,K^{-1}}$ of the carbon support and Eq. (3.17), we obtain $\Delta T \approx 0.2\,\mathrm{K}$. Due to the logarithmic dependency of the temperature difference on the aspect ratio $\frac{r_a}{r_i}$, this estimation is valid for a high range of $\frac{r_a}{r_i}$- ratios. Therefore, we can assume that ΔT does not change in magnitude for all considered geometrical configurations within this work.

3.1.3. FEM Simulation of Beam Induced Heating in Metallic Clusters

Finite element (FEM) simulations show that the heat gradient induced by a stationary, localized electron beam inside a gold nanoparticle can be neglected. These simulations were performed with the multiphysical simulation software Elmer (v8.2), developed by the Finnish IT centre for science (CSC) and available online free of charge [1].

A particle diameter d = 10 nm, a beam current of 100 pA and a primary electron energy of 300 keV were chosen. The spherical particle was capped at a height of 7 nm, to approximate the shape of a supported particle. A temperature of 300 K was set at the intersecting surface of

---

[1] https://www.csc.fi/web/elmer/elmer

the particle to the substrate. A cylindrical heat source ($d = 0.1$ nm) was defined along the axis of rotational symmetry, representing the electron beam (heat according to Eq. (3.13)). The heat flux at the remaining surface was set to zero (no heat exchange with the surrounding vacuum). The maximum temperature calculated using these parameters was 0.0005 K, at the point were the electron beam enters the particle. See Figure 3.2b for results.

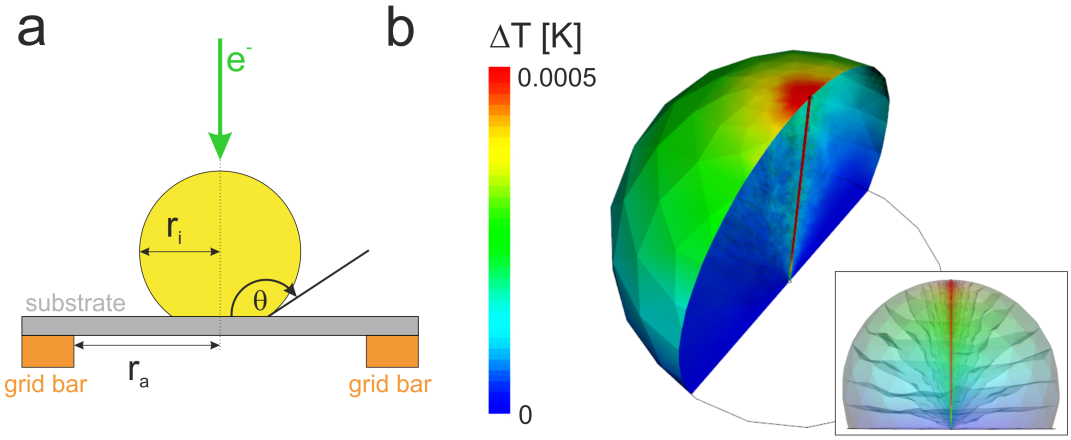

Figure 3.2.: a: Schematics showing the geometrical arrangement for the analytical calculation of the beam heating effect and definition of the contact angle θ. b: FEM simulation showing the temperature rise inside a supported gold nanoparticle.

Conclusively, we have to note that several simplifications have been made in both the analytical calculation as well as in the FEM simulations. These simplifications are not only concerning the geometrical setup and the boundary conditions, but also the treatment of the scanning electron beam as a stationary heat source and the limited validity of Fourier's law at length scales comparable to the wavelength of the heat carriers (electrons: 10 nm @300 K, phonons: 1 nm @300 K) [116]. Generally, in most metals electronic heat transport is dominating.
However, these effects are expected to have only minor impact on the order of magnitude of the calculated temperature rise. These results show that the heating effect due to electron beam irradiation can generally be neglected for carbon supported, metallic clusters at current densities typically used in aberration-corrected STEM. This is an important result for all beam damage related considerations within this thesis.

3.1.4. Radiolysis

Ionization processes can lead to bond breaking if the missing shell electron is not replaced within approximately 1 ps by an electron from the conduction band. If the excitation is not delocalised fast enough, the atom can gain enough momentum to leave its lattice site. After the chemical bond is broken, either thermal vibrations and local Coulomb repulsion cause the displacement of the atom. The time τ until an excitation is delocalized can be estimated via $\tau = \varepsilon_0 \varepsilon_r \rho_R$, where ε_0 is the vacuum permittivity, ε_r the relative permittivity and ρ_R the resistivity of the sample material [99].

Therefore, these damage processes occur in materials with a low electron density in the conduction band, such as insulators and the probability for radiolysis corresponds to the electrical resistivity of a material.
Similar to knock-on damage, preferentially weakly bond surface atoms are affected. In conducting materials, however, vacancies in the electron shell of an atom caused by inelastic scattering events are filled within very short time periods (<1 fs) due to the high electron density in the conduction band [117]. In metals, ionization and excitation events are therefore reversible and do not lead to radiolytic damage.

3.1.5. Electron Beam Induced Chemical Reactions

Electron beam damage products are usually very reactive and can lead to local chemical reactions if they remain on the sample surface. This can cause further sample damage, but may also be used to trigger chemical reactions in a local manner by electron irradiation. For example metallic nanostructures can get oxidized after radiolytic dissociation of water residues adsorbed on the sample. This has been observed in case of Ni, Ag and NiAu clusters and will be discussed in chapter 4.2.1, 4.2.2 and 4.3.2 in detail.

3.1.6. Electron Beam Induced Electric Field

Damage by induced electric field (DIEF) is an interesting but rather unknown damage mechanism that occurs in insulators or poor conducting materials. Within this picture beam damage is caused by charging effects due to excitations of atomic electrons to empty states above the Fermi level. The electron beam locally generates secondary electrons (SE) and Auger electrons, which can leave the local sample volume. Subsequently, remaining holes accumulate, which leads to a positive charge in the illuminated regions. Atoms are then displaced within this beam induced electric field. DIEF is dependent on the dose rate and exposure time but independent of the specimen thickness. For more details the reader is referred to Nan Jiangs work [99, 118, 119].

3.2. Molecular Dynamics

To get more insights into several cluster related phenomena, we use molecular dynamics (MD). MD is a well established and versatile computer simulation technique for atomistic simulations in material science, chemistry and biology. It was developed in the mid 50s and gives scientists insight into molecular motion on an atomic scale [120]. Although a vast amount of highly optimized MD codes is available nowadays (e.g. the freely available LAMMPS code[2]), we developed our own MD code within this thesis. The motivation for this was to maximize flexibility and to be able to implement Monte Carlo based beam damage simulations into our program. The code was developed using "Julia language" (v.5.0), a rather new programming language for scientific computation, available online for free[3]. It was chosen because of its much higher execution speed compared to MATLAB, while its syntax is quite similar, which the author was already familiar with. The simulation results were later evaluated and plotted in MATLAB. Our code is specialized on the simulation of (carbon) supported mono- or bimetallic nanoparticles, which are the main focus of this thesis.
In the following the applied techniques are briefly explained.

3.2.1. Numerical Integration of Newton's Equations

The basis for all MD simulations is the calculation of atom trajectories influenced by interatomic force fields [121]. These trajectories are calculated via numerical integration of Newton's equations of motion for each atom in the system. To achieve this, the velocity of a particle after a time step Δt is Taylor expanded:

$$\begin{aligned} \vec{v}(t+\Delta t) &= \vec{v}(t) + \dot{\vec{v}}(t)\cdot\Delta t + \ddot{\vec{v}}(t)\cdot\frac{\Delta t^2}{2} + \mathcal{O}(\Delta t^3) \\ \vec{v}(t-\Delta t) &= \vec{v}(t) - \dot{\vec{v}}(t)\cdot\Delta t + \ddot{\vec{v}}(t)\cdot\frac{\Delta t^2}{2} - \mathcal{O}(\Delta t^3) \end{aligned} \tag{3.22}$$

we combine these two equations: $\vec{v}(t+\Delta t) - \vec{v}(t-\Delta t) = 2\dot{\vec{v}}(t)\cdot\Delta t$ and get with the substitutions $\Delta t \rightarrow \frac{\Delta t}{2}$ & $t \rightarrow t + \frac{\Delta t}{2}$

$$\dot{\vec{v}}(t+\Delta t) = \vec{v}(t) + \dot{\vec{v}}\left(t + \frac{\Delta t}{2}\right)\cdot\Delta t \tag{3.23}$$

with the approximation:

$$\dot{\vec{v}}\left(t + \frac{\Delta t}{2}\right) \approx \frac{\dot{\vec{v}}(t) + \dot{\vec{v}}(t+\Delta t)}{2} \tag{3.24}$$

---

[2] http://lammps.sandia.gov

[3] http://julialang.org

we obtain the Velocity-Verlet algorithm to integrate Newton's equation of motion:

$$\boxed{\begin{aligned}\vec{x}(t+\Delta t) &= \vec{x}(t)+\dot{\vec{x}}(t)\cdot\Delta t+\ddot{\vec{x}}(t)\cdot\frac{\Delta t^2}{2}\\ \vec{v}(t+\Delta t) &= \dot{\vec{x}}(t)+\frac{1}{2}\cdot\left(\dot{\vec{v}}(t)+\dot{\vec{v}}(t+\Delta t)\right)\Delta t\end{aligned}} \tag{3.25}$$

As the time is propagated by the time step Δt, the coordinates $\vec{x}(t)$, velocities $\dot{\vec{x}}(t)$ and accelerations $\ddot{\vec{x}}(t)$ of the previous step are used to calculate the new positions $\vec{x}(t+\Delta t)$. The accelerations $\ddot{\vec{x}}(t+\Delta t)$ are then updated according to the inter-atomic potential using the actualized coordinates. Finally, the new velocities $\dot{\vec{x}}(t+\Delta t)$ can be calculated. These three steps are repeated until the desired time span of the simulation is reached. Although this is a rather simple algorithm it is insusceptible to numerical errors and usually one of the best algorithms available [121]. Therefore, it is very frequently used in molecular dynamic simulations.

The number of steps needed for the whole simulation time depends on the chosen time step. If the time step is too large two atoms may get to close to one another and strong repulsive forces lead to instabilities. For numerical stability and accurate energy conservation the time steps should be a magnitude smaller than the fastest time scale in the system. We immediately see the ultimate limitation of molecular dynamics, namely calculation speed. Since the inter atomic forces need to be evaluated at every time step between all possible atom pairs, the computational effort scales with the square of the number of atoms in the system. Even for small systems of several hundred atoms we are limited to a few nano seconds simulation time. Large time-scale processes like diffusion cannot be simulated with this technique. However, there are some tricks to speed up calculations a bit. Two of them have also been implemented in our code, potential cut off and cell lists. Without going into detail here, the first trick simply cuts the potential at some distance r_{cut}, so that only atoms within this distance need to be considered. Whereas in the cell list algorithm the simulation space is divided into cells with a size $> r_{cut}$ and the inter atomic forces are evaluated cell wise (see [121] for more details).

3.2.2. Variable Time-step

The choice of the time-step is critical in a molecular dynamics run. The time step determines the quality of the calculated trajectory. If it is chosen too high the dynamics of the system cannot be tracked correctly because atoms can move too far into the repulsive region of the potential. This causes unnatural energy values and can cause the divergence of the simulation. If the time step is chosen too small the computational effort rises without increasing the quality of the result. The highest frequency that can occur in the system determines the maximum time step. For light atoms and strong bonds this frequency is higher than for heavier atoms and weaker bonds. For example C-H bonds require time-steps below 1 fs. In our case of metallic bonds between rather heavy atoms we can choose relatively large time steps. Villarreal et al. [122] recommended some values for integrators of the velocity Verlet type and embedded atom potentials. For pure Au, Ag and Ni particles they found maximum time step values of

20 fs, 16 fs and 14 fs, up to temperatures of 1000 K.
We are interested in simulations of highly dynamic systems, which are out of equilibrium after each electron impact. Therefore it would be desirable to allow the simulation to adapt the time step if necessary. For this we decided to use an approach presented by Marks et al. [123]. They suggested to use the $\| F_{max} \| \cdot \Delta t$ metric in a Velocity Verlet scheme to adjust the time step. This means that at every time step the maximum norm of the force vector is calculated and the time step is chosen to keep the factor $\| F_{max} \| \cdot \Delta t$ constant. This guarantees that energy conservation is fulfilled and the maximum possible time step is chosen at every step, with a minimum of coding complexity. Marks et al. demonstrated the effectivity of this method describing ion radiation damage in graphite with molecular dynamics.

3.2.3. Thermostat Algorithm

All molecular dynamics simulations within this thesis are performed in the microcanonical ensemble NVE to conserve total number of atoms (N), total volume (V) and energy of the system. To control the temperature of the simulated system, a thermostat algorithm needs to be applied. In our case we chose the Andersen thermostat, where the system is coupled to a heat bath represented by stochastic collisions. This corresponds to a Markov Monte Carlo process [121, 124]. Practically, the velocities of a randomly selected particle are overwritten with a velocity vector generated from a Maxwell-Boltzmann distribution corresponding to the desired temperature. The probability distribution $P(t,\nu)$ of the time intervals between two successive collisions is Poissonian:

$$P(t,\nu) = \nu \cdot e^{-\nu t} \tag{3.26}$$

The collision frequency ν controls the strength of the coupling to the heat bath and is chosen to be approximately 0.5-2 THz in our simulations. It can be shown that the Andersen algorithm generates a canonical distribution [121]. Independently of ν we obtain the desired Maxwell-Boltzmann distribution. However, this parameter needs to be chosen properly. If it is too large the dynamics of the system is destroyed, because the velocity vectors are permanently overwritten. In our case where a nanoparticle only exchanges heat with the underlying substrate we only considered atoms close to the substrate for the thermostat. Thereby perturbations of the system are reduced. In our knock-on damage simulations, shortly after a scattering event the thermostat is even deactivated temporarily, to preserve the dynamics of the system (see section 3.5).
Figure 3.3 shows the simplified flow chart of a MD code based on the Velocity-Verlet algorithm with an Andersen thermostat, which was also used in our program.

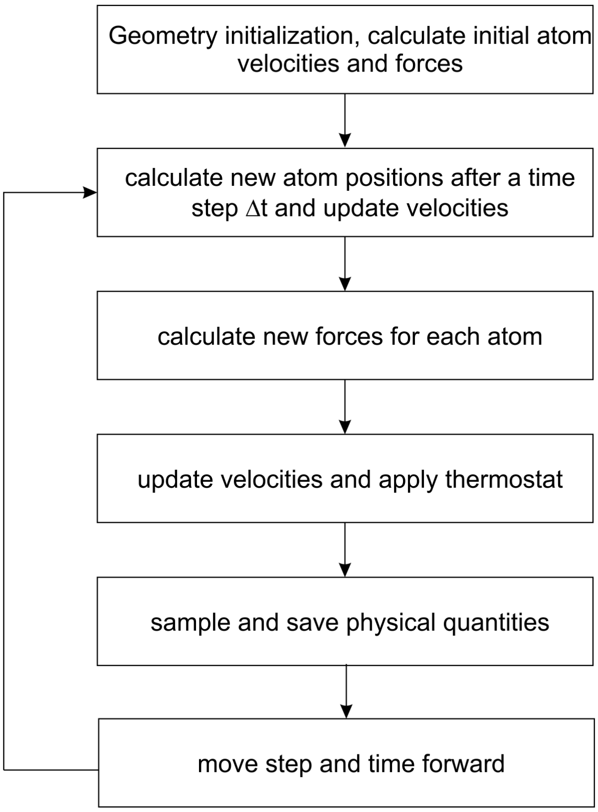

Figure 3.3.: Flow chart of a typical Velocity-Verlet algorithm with an Andersen thermostat

3.2.4. Metal-metal Interaction

In classical MD the force each atom exerts on each other is approximated via empirical potentials which can be of pair or many-body type. Thereby a trade-off between the computational effort and an as realistic model as possible has to be made. In our simulations the semi-empirical Sutton-Chen (SC) potential has been chosen, since it is a widely used many-body potential for the simulation of fcc metals [125, 126]. It is an embedded atom model (EAM) and has the form:

$$U = \varepsilon \left[\frac{1}{2} \sum_{ij} \left(\frac{a}{r_{ij}} \right)^n - C \sum_i \sqrt{\rho_i} \right] \quad \text{with} \quad \rho_i = \sum_j \left(\frac{a}{r_{ij}} \right)^m \tag{3.27}$$

Where a is the bulk lattice constant (in units of length), ε the depth of the potential (in units of energy) and C a dimensionless constant describing the form of the potential well. The exponents m and n are integer values describing the ratio between the attractive and the repulsive branch of the potential. Finally, ρ is the local density term which describes the dependency of the bonding energy on the number of involved electrons following a second-moment tight binding approximation [127]. With a given potential the force on a particle in this potential can be calculated with:

$$\vec{F_i} = -\nabla U(r_{ij}) \tag{3.28}$$

Accordingly, the force vector for atom number i is calculated with:

$$\vec{F_i} = \sum_j \vec{F_{ij}} \quad \text{with} \quad \vec{F_{ij}} = \varepsilon \left[n \left(\frac{a}{r_{ij}} \right)^n - \frac{Cm}{2} \left(\rho_i^{-\frac{1}{2}} + \rho_j^{-\frac{1}{2}} \right) \left(\frac{a}{r_{ij}} \right)^m \right] \cdot \frac{\vec{r_{ij}}}{r_{ij}^2} \tag{3.29}$$

A very important feature of the SC-potential is that, although it is truly a many-body potential, the forces can be calculated pair wise. The computational costs are therefore relatively modest. At each time step we need to loop over all possible pairs of i and j. Newton's third law (actio=reactio) can be used to reduce the number of iterations, because the force atom i acts on atom j is the same in magnitude and only in opposite direction as the force j acts on i ($F_{ij} = -F_{ji}$).
If the interactions between different species i and j need to be calculated, Eq. (3.27) becomes:

$$U = \sum_i \left[\sum_{j>i} \varepsilon_{ij} \left(\frac{a_{ij}}{r_{ij}} \right)^{n_{ij}} - \varepsilon_{ii} C_i \sqrt{\rho_i} \right] \quad \text{with} \quad \rho_i = \sum_j \left(\frac{a_{ij}}{r_{ij}} \right)^{m_{ij}} \tag{3.30}$$

The parameters for the interaction between different species are calculated from the pure element parameters via mixing rules. We mostly use following mixing rules [128]:

$$\begin{aligned} \varepsilon_{ij} &= \sqrt{\varepsilon_{ii}\varepsilon_{jj}} \\ n_{ij} &= \frac{n_i + n_j}{2} \\ m_{ij} &= \frac{m_i + m_j}{2} \\ a_{ij} &= \frac{a_{ii} + a_{jj}}{2} \end{aligned} \tag{3.31}$$

There is no mixing rule for C since it only depends on the type of atom at which the force is calculated. To use the geometric mean for the energy and the arithmetic mean for the distance parameter is also known as the Lorentz–Berthelot mixing rule. It is most widely used and is the default in many molecular simulation packages. Alternatively, it has been proposed that it may be advantageous in some cases to use the geometric mean also for the distance parameter in case of the Sutton-Chen potential [129].

3.2.5. Metal-substrate Interaction

To model the interaction of the cluster atoms with the amorphous carbon (a-C) substrate is a challenging task since the exact configuration of the substrate is not known. Local variations of morphology, adsorbed species and surface charge can largely influence the interaction with adsorbed metal atoms. Similarities in the electronic structure between a-C and graphite were found with EELS near edge fine structure analysis [130]. This lets us to conclude that sp^2 hybridisation is prevailing and we assume that the adsorption energies of metal atoms on a-C are comparable to graphite rather than diamond. For reasons of simplicity the substrate is mostly modelled as a rigid, flat and homogeneous surface in this work. The force the substrate exerts on each single metal atom in the cluster can therefore be described using a one-dimensional potential equation, only dependent on the distance z of a metal atom to the substrate.

For the interaction of Au atoms with a rigid and flat carbon substrate a modified Lennard-Jones potential, given in Eq. (3.32), was used [131].

$$U(z) = V_0 \left(\frac{297}{\left(\frac{z}{r_0} - 1.2\right)^{12}} - \frac{34.5}{\left(\frac{z}{r_0} - 1.2\right)^{6}} \right) \tag{3.32}$$

With $V_0 = 0.34\,\mathrm{eV}$ and $r_0 = 2.885\,\text{Å}$.

Unfortunately, there is no such parametrised potential available in literature for other metals in which we were interested. Therefore, the interaction between Ag and Ni atoms with the carbon substrate was modelled using a Morse potential of the form given in Eq. (3.33).

$$U(z) = D_M \cdot \left(e^{-n \cdot a_M (z - R_M)} - n \cdot e^{-a_M (z - R_M)} \right) \tag{3.33}$$

The parameters D_M and a_M were set to fit adsorption energies and potential widths found in previous work [132–135]. At the same time we ensured that the obtained cluster morphologies comply with experimental results [5, 29, 88].

As an enhancement of the flat substrate above, for the simulation of the equilibrium shape of pure Ni clusters the amorphous substrate was generated by placing atoms randomly in a confined volume until the desired density was reached. The interaction between Ni and carbon atoms was then modelled with a classic Lennard-Jones-(12,6)-potential:

$$U(r) = 4\varepsilon \left[\left(\frac{\sigma}{r}\right)^{12} - \left(\frac{\sigma}{r}\right)^{6} \right] \tag{3.34}$$

with ε being the depth of the potential in units of energy and σ the position of the zero in units of length. For C-Ni, C-Ag and C-Au these parameters can be found in literature [136–138]. The density of the carbon substrate was chosen to be $2000\,\mathrm{kg\,m^{-3}}$ [131]. A thickness of 0.8 nm was chosen, which corresponds approximately to a potential cut off 2.5σ. Although, the forces each substrate atom exerts on each cluster atom are now calculated separately, the positions of the substrate atoms were kept constant during each simulation run. Figure 3.4b shows a Ni cluster consisting of 600 atoms on such a substrate.

3.3. Metropolis Monte Carlo

The other important simulation technique for atomistic simulations beside molecular dynamics is the Monte Carlo method. In the frame of this work the conventional Metropolis Monte Carlo approach has been used to equilibrate a randomly generated cluster. This algorithm has first been proposed by Metropolis et al. in the year 1953 [139]. We use this method to prevent instabilities due to non stable initial configurations, which very often leads to a disintegration of the cluster in a dynamic simulation. Equilibrating a cluster is equivalent with finding its energy minimum. For this purpose Metropolis Monte Carlo is very efficient and easy to implement, which was the main reason to use it in our code. The algorithm in its simplest form in principle consists of following steps:

1. Choose an atom randomly
2. Displace this atom by a randomly chosen displacement vector with a length in an interval $[0, d_{\max}]$, with $d_{\max}$ being the maximum displacement
3. Calculate the energy difference ΔU between the old an the new configuration of the system (as sum over all particle potential energies according to the inter-atomic potential)
4. Apply the Metropolis accepting criterion:
    - If $\Delta U < 0$ (the new configuration is lower in energy): accept the new configuration
    - If $\Delta U > 0$: A random value r is chosen in an interval $[0, 1]$ and the configuration is accepted if $e^{-\frac{\Delta U}{T}} < r$, with T being the temperature of the system.
5. If the move is accepted continue with the new configuration, otherwise discard it and continue with the old one.

Another big advantage of this algorithm is that, although the Metropolis acceptance criterion biases us to a lower energy state it also allows steps to higher energy states. That avoids being trapped in a local minimum. After many iterations we ultimately obtain a canonical distribution at T [121]. The parameter $d_{\max}$ can be used to control the acceptance rate and thus the efficiency of our simulation. If $d_{\max}$ is chosen too large, moves into the repulsive regime of the inter-atomic potential result in a low acceptance rate. If $d_{\max}$ is too small the simulation will be very slow. Recommended values for the acceptance rate are between 30 and 50 percent. In our code $d_{\max}$ is chosen adaptively to reach a previously defined acceptance rate.

We have to note that the energy minimum of a cluster found by this method could also correspond to a local energy minimum corresponding to a metastable state. However, this is sufficient for our purpose, to obtain a starting configuration for molecular dynamics. Finding the global energy minimum of a cluster is a non-trivial task that requires more sophisticated strategies, such as basin-hopping or evolutionary algorithms [10, 140].

3.4. Simulation of Cluster Shapes and Morphology

With our molecular dynamics code it was now possible to simulate the soft-landing process of the cluster and the influence of the substrate on its morphology. Some initial work has already been done by Philipp Thaler for Ag clusters on amorphous carbon substrates [132]. We implemented his ideas in our code and extended it to other mono- and even bimetallic systems.

3.4.1. On the Shape of Supported Clusters

The equilibrium shape of supported metallic clusters is determined by their size, the surface energy of the clusters and the adhesion energy between the clusters and the substrate. Equilibrium is established by the transport of matter through surface diffusion. The anisotropy of the surface energy results in a faceted shape below a roughening temperature (usually considerably higher than room temperature). This leads to the Wulff-Kaichew theorem [114]. Within this picture the equilibrium shape of a small supported metal cluster at a constant temperature is given by a truncated Wulff shape as shown in Figure 3.4a, assuming that there is no strain between substrate and cluster. The height of truncation Δh is then given by:

$$\Delta h = \frac{h \cdot E_{\mathrm{adh}}}{\gamma} \tag{3.35}$$

where γ denotes the surface energy and h the distance of the substrate to the facet parallel to the interface. E_{adh} is the adhesion energy, defined as the energy required to separate the cluster from the substrate to an infinite distance. At elevated temperatures above the roughening temperature the faceted shape transforms into a spherical shape. Note that this picture includes some simplifications, which have an influence on the cluster morphology in practice.

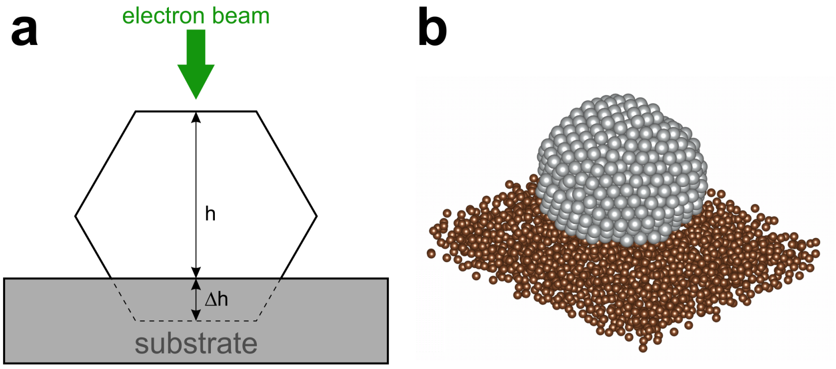

Figure 3.4.: Schematics illustrating the truncated Wulff shape of a supported cluster at equilibrium; the height of the truncation Δh is proportional to the interface energy. (b) MD simulation of a randomly generated and equilibrated Ni cluster (600 atoms) supported by amorphous carbon.

First, the shape of the clusters is not independent of their size. Unsupported small metal clusters with a bulk fcc structure tend to form (111) facets st 0 K , because this is the energetically most favourable surface (close-packed). In small clusters the surface energy is dominant over the bulk and the icosahedral morphology, only consisting of (111) facets, is preferred (figure 3.5a). In an icosahedron, the central atoms experience a high degree of compression, while the surface atoms are relaxed. Therefore, as clusters become larger they also tend to form (100) facets. This leads to the formation of Marks decahedra, mainly consisting of (111) and partly of (100) facets (Figure 3.5b). Both icosahedra and decahedra are non-crystalline[4], but highly symmetric arrangements with fivefold symmetry. Larger clusters finally form (truncated) cubic shapes (octahedrons) based on the bulk structure (Figure 3.5c). We have to note that the energy difference between different cluster configurations can be very low. Hence, a range of morphologies can be observed for similar cluster sizes [141]. However, if a substrate is included things get much more complicated. A previous paper from our group showed that amorphous carbon supported Ag clusters exhibit a high amount of fcc clusters [29]. That was even the most frequently observed configuration for the smallest clusters with diameters below 3 nm, whereas larger clusters up to 5 nm preferred icosahedral and decahedral shapes. This indicates that larger clusters tend to preserve their principle morphology during equilibration on the substrate, while for smaller clusters it is favourable to rearrange to fcc-crystals due to the attractive substrate potential. We will later show that electron beam irradiation can also enhance such restructuring processes, in experiment as well as in our beam damage simulations (see Figure 4.36 and section 3.5). It may be possible that the impact of the cluster itself, although it is cushioned by the remaining helium, may also influence the cluster morphology [132].

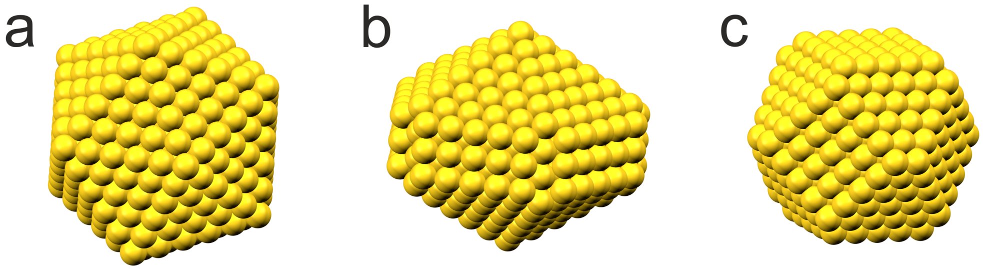

Figure 3.5.: Three principle closed-shell morphologies for clusters of a metal with fcc-bulk structure: (a) Icosahedron: close-packed, (111) only surface but high internal strain. preferable for small clusters (b) Marks decahedron: surface with (111) and partly (100) facets. (c) Truncated octahedron: crystalline, closed-packed volume, no internal strain, based on bulk structure

Second, the Wulff-Kaichew theorem assumes a perfect match between the cluster lattice and the substrate. In general this assumption is not valid. Lattice mismatch leads to strain and interface defects. Dependent on the magnitude of mismatch the cluster prefers to decrease the interface area. Therefore, large clusters tend to exhibit a different aspect ratio than small clusters. This we have to bear in mind if we try to approximate the amorphous carbon substrate by a flat and rigid potential as done in equations 3.33 and 3.32). We do not know the exact

---

[4] The term non-crystalline here refers to the lack of translational symmetry.

local configuration of the substrate. Parameters which give reasonable results for one range of cluster size may give less valuable results for another. This was also the reason for choosing a randomly generated carbon substrate for our Ni cluster size determination experiment (shown in Figure 3.4b). However, this is still a rough approximation but the best we can do to keep the computational effort relatively low.

The time for equilibration τ is strongly dependent on the cluster size. For elevated temperatures τ is proportional to R^4/D_s, where R is the particle radius and D_s the surface diffusion coefficient [114]. Kinetic effects can hinder the transformation into the equilibrium shape, especially of larger clusters. There is an energy barrier for the formation of a new layer on a facet; a 2D nucleus needs to be formed initially. This nucleation barrier increases with the size of the facet and needs to be overcome several times during rearrangement of the particle. At every step the cluster is in a metastable state. At elevated temperatures fluctuations lead to a higher probability to form a nucleus on a facet. Hence, the relationship given above is only valid for high temperatures. In a rough estimation the time for a transformation of a cubic particle to its equilibrium shape reduces then to the ns range for small metal clusters with R =1 nm [142].

Due to these kinetic effects the cluster shape is not necessarily the same as the equilibrium shape immediately after cluster landing. The clusters will arrange themselves such that their surface energy is minimized, mainly through surface diffusion processes. However, they may stay in a metastable local minimum in the energy landscape for quite a long time. Finding the global energy minimum for a given cluster via computational methods is therefore a quite challenging task [9]. So where we were interested in the equilibrated cluster shape in our simulations this was taken into account through an elevated substrate temperature during equilibration. Luckily, τ is dominated by the final equilibration steps. That means that the cluster shape is already very similar to its equilibrium long before the expiration of τ, especially if we already start with a cluster shape similar to the equilibrium shape. Thus it is reasonable to argue that the landing simulation of a small spherical cluster, which would have a hemispherical equilibrium shape on the support, gives valuable results, even though only a few ns equilibration time can be accessed with molecular dynamics.

3.5. Simulation of Beam Induced Dynamics

The basis MD code presented in the previous section is adapted for electron beam induced dynamics and damage effects, caused by elastic large-angle scattering. Therefore a Markow-Chain Monte Carlo approach, similar to the Andersen thermostat, is introduced into our code. The collision time of an electron with an atomic nucleus is extremely short (in the order of 10^{-21} s) compared to the time step used for the Molecular Dynamic simulation [143]. Thus, the atoms are considered to be stationary during scattering. For each elastic interaction a scattering angle is chosen randomly according to the NIST scattering cross section tables [58] for a specific electron beam energy and element.

The maximum energy E_{max} is being transferred at θ = 180°, which corresponds to the normal impact case. Since only higher angle scattering events may transfer a sufficient amount of energy to displace an atom, those over a certain threshold θ_{min} were pre-selected. Thereby, the computational effort can be reduced very efficiently, due to the power-law like behaviour of the scattering cross section (see Figure 3.1). It should be noted that the NIST cross section values are based on scattering by single, free atoms and therefore do not account for effects of bonding and crystallization in a solid material. However, it has been shown that deviations caused by such aggregation are only relevant for low electron energies and/or low scattering angles [144–147].

After equilibration and relaxation of the system, an atom is selected randomly and its velocity vector v is modified with an additional velocity term v_s. We assume that during the scattering event the whole amount of E_t is converted to kinetic energy again. Relativistic effects can be neglected for a nucleus with mass m, because $E_t << mc^2$. This allows use of classical mechanics to calculate the length of the velocity vector v_s:

$$|\vec{v_s}| = \sqrt{\frac{2E_t}{m}} \tag{3.36}$$

From the law of momentum conservation $\vec{p} = \vec{p'} + \vec{p'_n}$ we can deduce:

$$|\vec{p'}| \cdot \sin(\theta) = |\vec{p'_n}| \cdot \sin(\psi) \quad \text{with} \quad \vec{p'} = m_0\vec{v'}\gamma \text{ and } \vec{p'_n} = M\vec{v_s} \tag{3.37}$$

with γ being the Lorentz factor:

$$\gamma = \frac{1}{\sqrt{1 - \left(\frac{|\vec{v'}|}{c}\right)^2}} \tag{3.38}$$

Finally, the scattering angle ψ of the nucleus is obtained (Eq. (3.39)).

$$\psi = \arcsin\left(\frac{m_0 v' \gamma}{m v_s} \cdot \sin(\theta)\right) \tag{3.39}$$

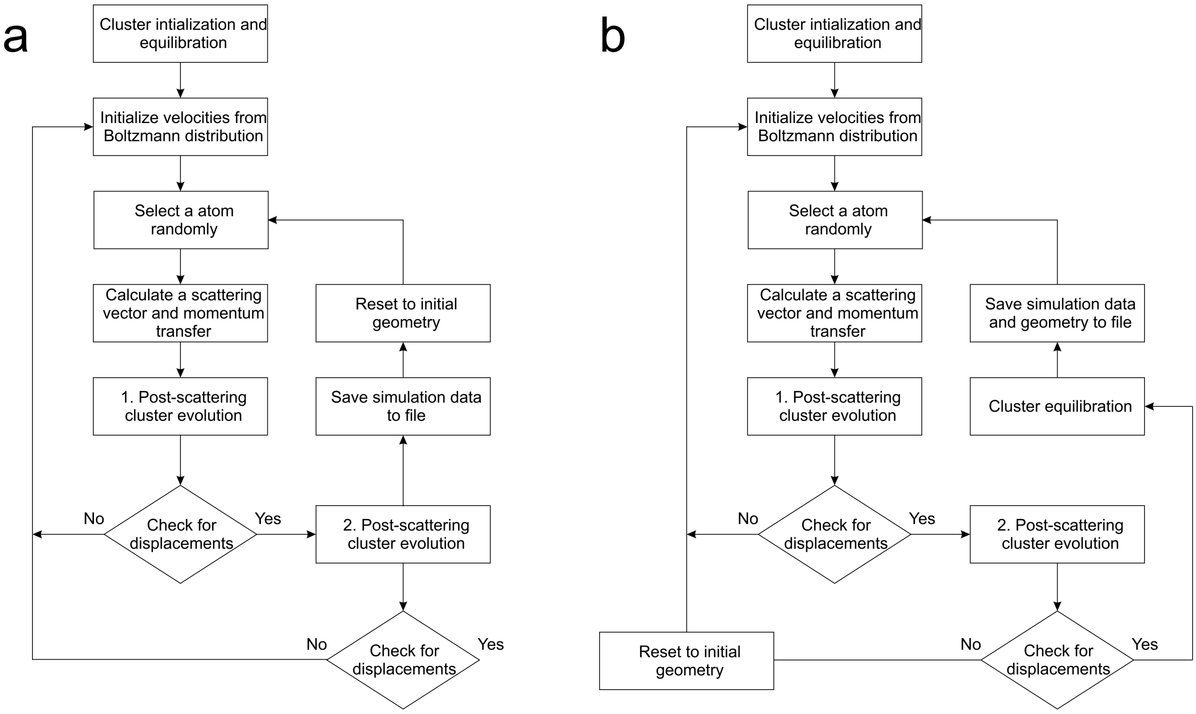

Figure 3.6.: The algorithms used for the beam damage simulations: Algorithm (a): Calculation of displacement and sputtering rates as a function of the scattering angle. Algorithm (b): Simulation of the cluster evolution during electron beam exposure

The azimuthal angle ϕ is generated randomly in the interval $[0, 2\pi]$. Together with ψ and $|\vec{v_s}|$ we now have a complete set of polar coordinates for the velocity vector $\vec{v_s}$ which can finally be converted to Cartesian space (Eq. (3.40)).

$$\boxed{\vec{v_s} = -\sqrt{\frac{2E_t}{M}} \cdot \begin{pmatrix} cos(\phi)sin(\psi) \\ sin(\phi)sin(\psi) \\ cos(\psi) \end{pmatrix}} \tag{3.40}$$

During a step of the molecular dynamics run, an atom of the cluster is chosen randomly and its velocity vector is modified according to Eq. (3.39) and Eq. (3.40).

3.5.1. Determination of the Displacement and Sputtering Probability

First we estimated the probability that an atom is being displaced by an elastic scattering event, dependent on the scattering angle θ and the energy transferred to the nucleus after scattering E_t. These two quantities are connected via Eq. (3.7). Clusters consisting of one of three different species have been simulated within these simulations; gold, silver and nickel. These materials were chosen because they can be modelled using the same inter-atomic potential and have

also been subjected by experimental work within this thesis. Here we aim to calculate the displacement and sputtering probabilities as a function of atomic mass, electron energy, cluster size and temperature.
Similar to the simulation of the landing process, initially the cluster geometry has been placed and equilibrated on a substrate, for each set of parameters. That means the exact geometrical conditions will slightly vary from run to run, except for estimation of the temperature dependency where the same geometry has been simulated at different temperatures. For all calculations a rigid and flat substrate potential has been used, with parameters corresponding to amorphous carbon (see 3.2.5).
After equilibration, scattering events are generated from a uniform angle distribution between 0 and 180°. Thereby we follow Algorithm 1 in figure 3.6a. After each scattering event the cluster is reset to the initial equilibrated configuration with new velocity vectors for each atom, generated from a Boltzmann distribution for the given temperature. This procedure is repeated until the desired maximum number of sampling electrons is reached (n_{max} = 25000-100000).
In Figure 3.7 plots of the displacement probability $P(E_t)$, as it has been introduced in Eq. (3.10) in section 3.1.1 are shown. The dependence of $P(E_t)$ on different experimental parameters such as cluster sizes, temperatures, materials and electron energies have been compared.

3.5.1.1. Displacements

In figure 3.7a clusters consisting of 55 atoms of either Au, Ag or Ni are compared as a function of the scattering angle.
The probability an atom is displaced by an electron with energy E that was scattered to an angle θ, increases with decreasing mass of the nucleus. It is remarkable that no well defined sharp onset can be found for the displacement threshold energy, especially for Au clusters. On one hand this can be explained with varying energy thresholds for different jump mechanisms. For surface atoms of a gold cluster, threshold energy values were found in literature to be between 0.1 and 0.4 eV [148, 149], dependent on their lattice sites. On the other hand also the thermal movement of the atoms contributes. Vibrations of an atom effect its own displacement, which means that the atom gains more energy if it is displaced while it moves parallel to the electron beam compared to the static case.
Values for the threshold energy where displacements start to occur can be estimated from the displacement probability plots and Eq. (3.7). For gold a value of approximately 0.5 eV was obtained which complies with previously found values given above. Therefore, θ_{min} was set to 25° for the simulation of cluster dynamics in the following section (3.5.2).
A comparison of the displacement probability for four different Ag cluster sizes is given in Figure 3.7b. It can be seen that the probability for a displacement increases with decreasing cluster size. Except for the largest clusters comprised of 490 atoms. Interestingly, clusters of this size show a higher displacement probability over the full range of scattering angles compared to the clusters with 309 atoms. The difference in displacement probability between 116 and 55 atoms also appears to be remarkably small. This behaviour was observed in every simulation run and for Ag as well as for Au-clusters (not shown here). We explain this with the existence of stability plateaus for certain cluster sizes (magic numbers). While 55 and 309 atoms form

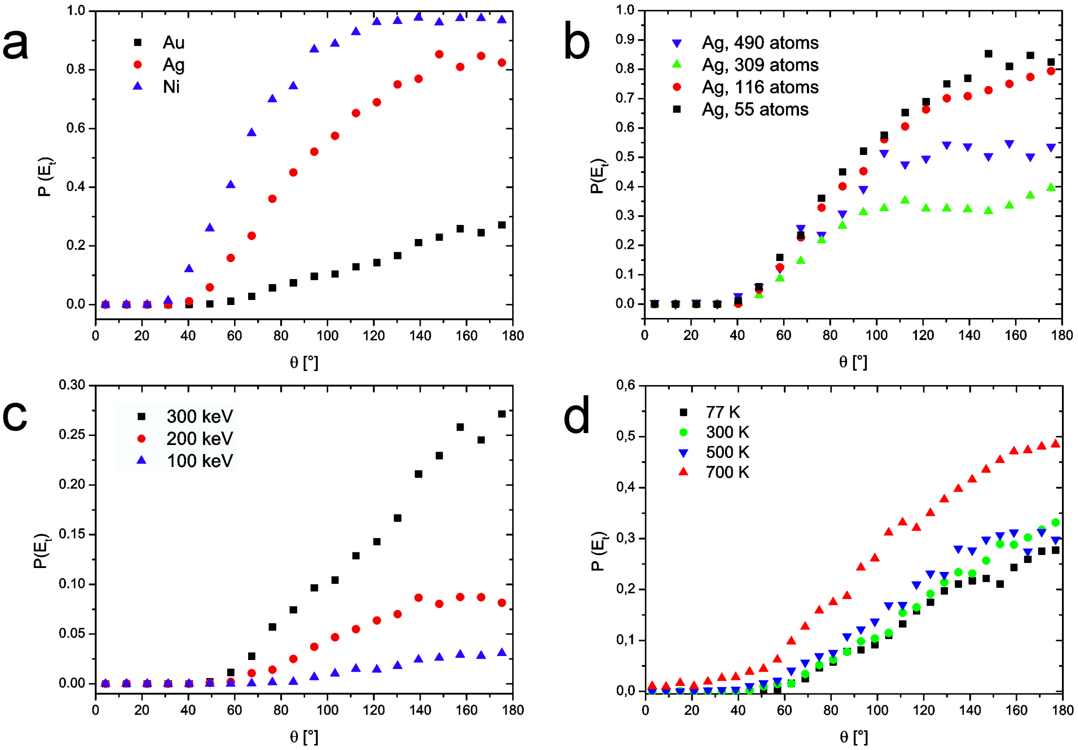

Figure 3.7.: (a) Displacement probability of cluster atoms, comprised of 55 atoms of 3 different species over the scattering angle of the scattered electron; E =300 kV. (b) Displacement probability for different Au cluster sizes over the scattering angle of the scattered electron; E =300 kV. (c) Displacement probability for different electron energies over the scattering angle of the scattered electron for a cluster comprised of 55 Au atoms. (d) Displacement probability for different cluster temperatures over the scattering angle of the scattered electron for a cluster comprised of 55 Au atoms.

such closed-shell clusters, this is not the case for 116 and 490 [150]. These non-closed shell clusters exhibit a higher number of weakly bound surface and edge atoms, which increases the overall displacement probability. Although, these stability criteria were found theoretically with unsupported clusters, this finding suggests that the support interactions does not have a big influence on the magic numbers in our case.

The displacement probability is also highly dependent on the primary electron energy as shown in Figure 3.7c. Here clusters consisting of 55 Au atoms were illuminated with 100, 200 and 300 keV electrons. It can clearly be seen that the displacement rate can significantly be reduced by lowering the electron energy, which comes as no surprise. At 100 keV the displacement probability drops to only about 3 % for the maximum scattering angle. By multiplying the angular dependent displacement probabilities $P(E_t)$ with the total elastic scattering cross section σ_{el} for a gold atom, obtained from the NIST database, and subsequent numerical integration over the full angular range (after Eq. (3.10)), the mean displacement cross section of an atom in a supported Au$_{55}$ cluster can be calculated, being 2.5×10^{-7} nm^2, 2.3×10^{-7} nm^2 and 1.4×10^{-7} nm^2, respectively [58]. For numerical integration trapezoidal rule was used.

Applying Eq. (3.5) with a typical current density j in STEM of the order of $10^7\ \mathrm{e^- nm^{-2} s^{-1}}$ and the cross section for 300 keV electrons gives that in average every few 10-100 ms a dis-

placement occurs in such a cluster under 300 keV electron irradiation. This explains the high dynamics of small Au clusters under electron beam irradiation, which has also been observed in experiment, see section 4.4 and therein especially Figure 4.37.
This has important consequences on STEM analysis of such small clusters. Typically several pixels are needed to represent an atomic column in a STEM data set. Considering a pixel time of several µs for image acquisition or even several ms for spectrum image acquisition, the acquired intensity that is assignable to a column is likely to vary while it is sampled by the electron beam. Accordingly, if beam induced displacements are too frequent, significant blurring can be observed and single atomic columns may not be resolved any more. This can often be observed especially at the surface regions of clusters, where atoms are more likely to be displaced than in the centre.
The temperature dependency of displacement and sputtering are of special interest in the rapidly growing field of *in situ* TEM. The influence of the temperature is depicted in 3.7d. In contrast to the previous simulations the cluster geometry is kept the same in every simulation run. A cluster consisting of 55 Au atoms has been equilibrated once and then used in every run (50000 electrons each). This to eliminate the influence of slightly different geometries. The cluster was equilibrated at four temperatures, 77 K, 300 K, 500 K and 700 K, before the beam damage simulations were started. We see that the displacement probability increases while the displacement threshold energy decreases with increasing temperature.
Although general trends remain valid, it has to be noted that the values given here for displacement probabilities and cross sections greatly vary with the cluster geometry and can therefore only be compared directly for a certain geometry.

3.5.1.2. Sputtering

We can calculate the probability that an atom is permanently removed from the cluster after displacement in the same manner as displacement probabilities were determined in the previous section. To determine weather an atom is sputtered we calculate the coordination number for each atoms at the end of an equilibration run. If one or more atoms is found with a coordination number of zero it is considered as lost. Such an atom is deleted from the coordinate list and recorded as sputtered atom. To prevent lost atoms from flying too far away from the cluster during equilibration we define a box with several nanometres in size. An atom is also considered as sputtered if it leaves this box during the equilibration step.
Since sputtering events are much less likely than displacement events it is difficult to give values for the sputtering probability as a function of the scattering angle as given in Figure 3.7. The computational effort would be very large to obtain sufficient statistics, especially for large clusters and heavy elements. Instead we only give general trends in this section. For each simulation 50000 scattering events were simulated.
For Au clusters generally almost no sputtering can be observed, even at the highest electron energy (300 keV) and the smallest cluster size (55 atoms). For these settings out of over 17000 displacement events only approximately 60 lead to a loss of an atom. We also found no temperature dependency up to 700 K, which leads us to the conclusion that the influence of thermal movement of atoms on the sputtering cross section is negligible in this temperature range. This

finding seems to be reasonable, considering the large threshold energy for sputtering events of several eV.
For Ag clusters on the contrary, sputtering is much more likely. For a size of 55 atoms and a beam energy of 300 keV, out of over 23000 displacement events approximately 2900 lead to sputtering.
This trend of increasing sputtering probability with decreasing atomic mass continues with Ni clusters where from detected 28000 displacements about 11300 sputtering events are detected.

3.5.2. Evolution of Clusters During Electron Beam Exposure

Simulation of the cluster evolution during electron beam exposure was performed using Algorithm 2 in Figure 3.6. After each detection of a displacement the new configuration is equilibrated. This new configuration is then used as a starting point for the next scattering event. Thereby, one possible evolution of the structure over time is simulated. The minimum scattering angle is chosen by means of the scattering probability plots obtained in the previous section. If two sorts of atoms are involved, the type of scattering atom is chosen randomly according to the ratio of their total cross sections integrated over the interval $[\theta_{min}, \pi]$ (Eq. (3.8)).

3.5.2.1. Evolution of Supported Au and Ag Clusters

To simulate the dynamics of electron irradiated clusters we chose Au and Ag as cluster material, due to their highly different sputtering probabilities. The clusters were generated randomly and equilibrated with the Monte Carlo code presented in section 3.3. Then the clusters were placed on a randomly generated amorphous carbon substrate. The substrate interaction is calculated with a Lennard-Jones potential (Eq. (3.34)) with parameters from [138] for Au-C and [137] for Ag-C. The dimensions of the substrate are 4x4x0.6 Å with a target density of $2000\,\mathrm{kg\,m^{-1}}$, which corresponds to approximately 650 carbon atoms. We used algorithm no. 2 to calculate the transient evolution of the cluster (see Figure 3.6b). The primary electron energy was set to 300 keV. We chose a minimum scattering angle θ_{min} so that the minimum energy transferred to an atom is 1 eV (after Eq. (3.9)), which corresponds to θ_{min} values of 41.68 deg and 57.49 deg for Ag and Au, respectively. This choice seems reasonable since we are mainly interested in the change in cluster size and no sputtering can be expected below this energy for both Ag and Au. Figure 3.8 shows the evolution of a Au cluster, comprised of 250 atoms under electron irradiation. The simulation included 125868 scattering events, which led to 8771 displacements, including 4 sputtering events.

Although, sputtering events are very rare, the Au cluster exhibits significant morphological changes during the simulation, which complies with experimental results (see section 4.4). Surface defects are generated and a twinned structure is formed. The cluster transforms to a more elongated and flattened shape, despite being thermodynamically unfavoured. This is probably due to kinetic effects, hindering the equilibration of the cluster within the short

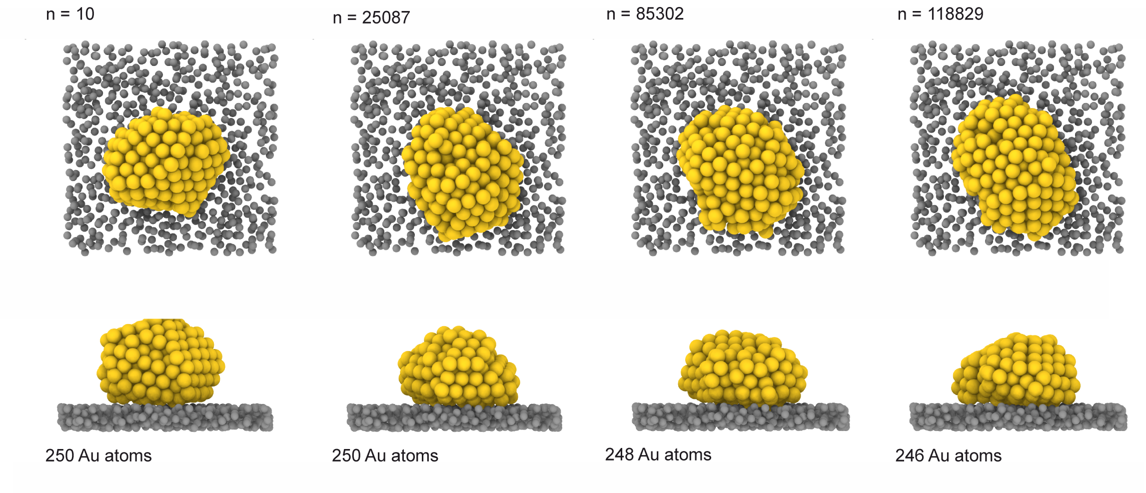

Figure 3.8.: Transient evolution of a Au cluster initially consisting of 250 atoms under 300 keV electron irradiation, n is the number of electron scattering events in the simulation

equilibration time after each scattering event. Figure 3.9 shows the evolution of a Ag cluster consisting of 350 atoms in comparison. The cluster shows significant sputtering effects and shrinks very rapidly. It loses about 100 atoms within the first 20000 simulated scattering events and completely dissociates after about 47000.

In principle we should be able to extrapolate from the number of scattering events that are used in the simulation to the total dose that must be applied to the system to generate the given number of scattering events. Using Eq. 3.8 we can define a scaling factor F (Eq. (3.41)) for this purpose.

$$F = \frac{\sigma_{\text{el}}}{\sigma_{\theta_{\min}}} = \frac{\int_0^{\pi} \frac{\partial\sigma}{\partial\Omega} \cdot \sin\theta \cdot d\theta}{\int_{\theta_{\min}}^{\pi} \frac{\partial\sigma}{\partial\Omega} \cdot \sin\theta \cdot d\theta} \tag{3.41}$$

The total number of elastically scattered electrons n_{el} can then be calculated from the number of scattered electrons $n_{\theta_{\min}}$ in an angular range $[\theta_{\min}, \pi]$ via:

$$n_{el} = F \cdot n_{\theta_{\min}} \tag{3.42}$$

The total number of incident electrons n_0 is the sum of the total number of elastically scattered electrons n_{el} and the number of unscattered electrons n:

$$n_0 = n + n_{\text{el}} \tag{3.43}$$

Scattering occurs if an electron strikes a fraction $N \cdot \sigma_t$ of the unit area, where N denotes the the areal density of the scattering atoms [93].
Accordingly we can write:

$$\frac{dn}{n} = -\sigma_{\text{el}} \cdot dN \tag{3.44}$$

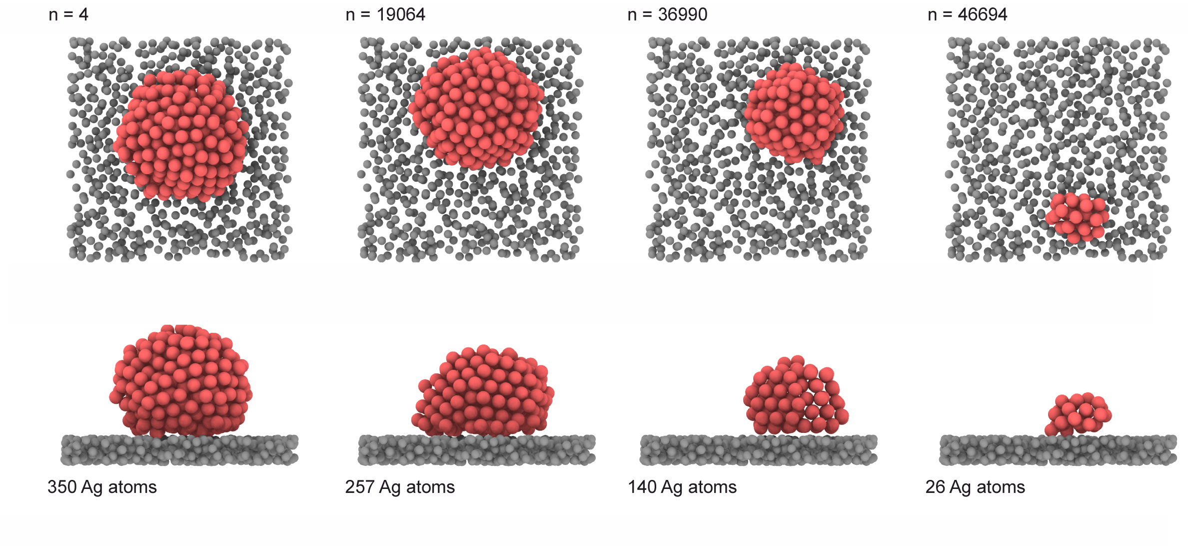

Figure 3.9.: Transient evolution of a Ag cluster initially consisting of 350 atoms under 300 keV electron irradiation, n corresponds to the number of electron scattering events in the simulation

which gives after integration:

$$\ln(n) = -\sigma_{\mathrm{el}} \cdot N + C \quad \text{with} \quad C = ln(n_0) \quad \text{since} \quad n(N=0) = n_0 \tag{3.45}$$

With Eq. (3.42), Eq. (3.43) and Eq. (3.45) we can finally calculate the total number of incident electrons that corresponds to the number of simulated scattering events for a certain angular range $[\theta_{\min}, \pi]$:

$$n_0 = \frac{n_{\theta_{\min}} \cdot F}{1 - e^{-\sigma_{\mathrm{el}} N}} \tag{3.46}$$

We have to note, however, that it is difficult to extract quantitative information in terms of dose effects from these simulations. If we try to use the scaling factor from Eq. (3.41) to calculate the total dose, we overestimate sputtering effects by a factor of approximately 2-3. The reason for this is not entirely clear yet, since there are several influences which could have an effect. For instance, similar to most empirical potentials the Sutton-Chen potential that is used to model the forces between metal atoms is originally not designed for such highly non-equilibrium processes like the ballistic motion of energetic atoms. Calculated forces might be wrong at close interatomic distances, which are unusual in standard equilibrium processes. To account for this an additional pair-potential term can be introduced [143]. This is also true for the potential that is used to model interactions between substrate and metal atoms. Potentials with an exponential term for repulsive forces are known to be too soft because they underestimate Coulomb repulsion ($1/r$), while Lennard-Jones potentials tend to overestimate repulsive forces due to the $1/r^{12}$ term [143].

The assumption that the substrate is considered as rigid in our simulations may also lead to errors. Dynamic interactions with the substrate are, hence, completely neglected.

Another effect that has not been included in the present simulation is the effect of multiple scattering and channelling. Therefore, the displacement probability is not equal for every atom in the cluster, as assumed in our simulations.
All these effects would be interesting to be explored in future work, towards a quantitative description of knock-on damage effects.

3.5.2.2. Evolution of Supported Au@Ag and Ag@Au Clusters

We also calculated the evolution of supported, elongated Au(Ag) and Ag(Au) core(shell) particles in a qualitative manner. The motivation was to find how the electron beam influences the morphology and the composition of such particles. This is an interesting material combination to study electron beam induced sputtering and alloying phenomena because of the very similar lattice distance of silver and gold (a_{Au} =408 pm and a_{Ag} =409 pm). This system was also studied experimentally within this work (see chapter 4.3.1) [24].
In the following an elongated core shell structure has been generated consisting of 205 atoms, 73 core atoms and 132 shell atoms. Dependent on the atoms position elements were assigned to obtain either Au(Ag) or Ag(Au) core(shell) particle. The structures were first equilibrated without support at 0.4 K, the approximate He-droplet temperature. Then they were landed and equilibrated on an amorphous carbon substrate, modelled to be rigid and flat. The substrate-particle interactions were calculated with an one-dimensional potential, given in section 3.2.5. Electron beam dynamics was then simulated with an electron energy of 300 keV, applying algorithm 2 (see section 3.5).
The results of the simulation run are given in Figure 3.10. In this figure n denotes the number of electrons in the simulation run. Both systems Au(Ag) and Ag(Au) show the tendency to rearrange to a more spherical shape, due to electron beam enhanced surface diffusion. This behaviour can be expected since the spherical shape is closer to thermodynamic equilibrium than the initial rod like shape. Interestingly we observe that electron beam induced sputtering of surface atoms almost exclusively occurs in the Au(Ag) core shell particle. The much lower displacement probability of Au compared to Ag seems to protect the core from beam damage. This effect should be considered during quantitative analysis of such systems.

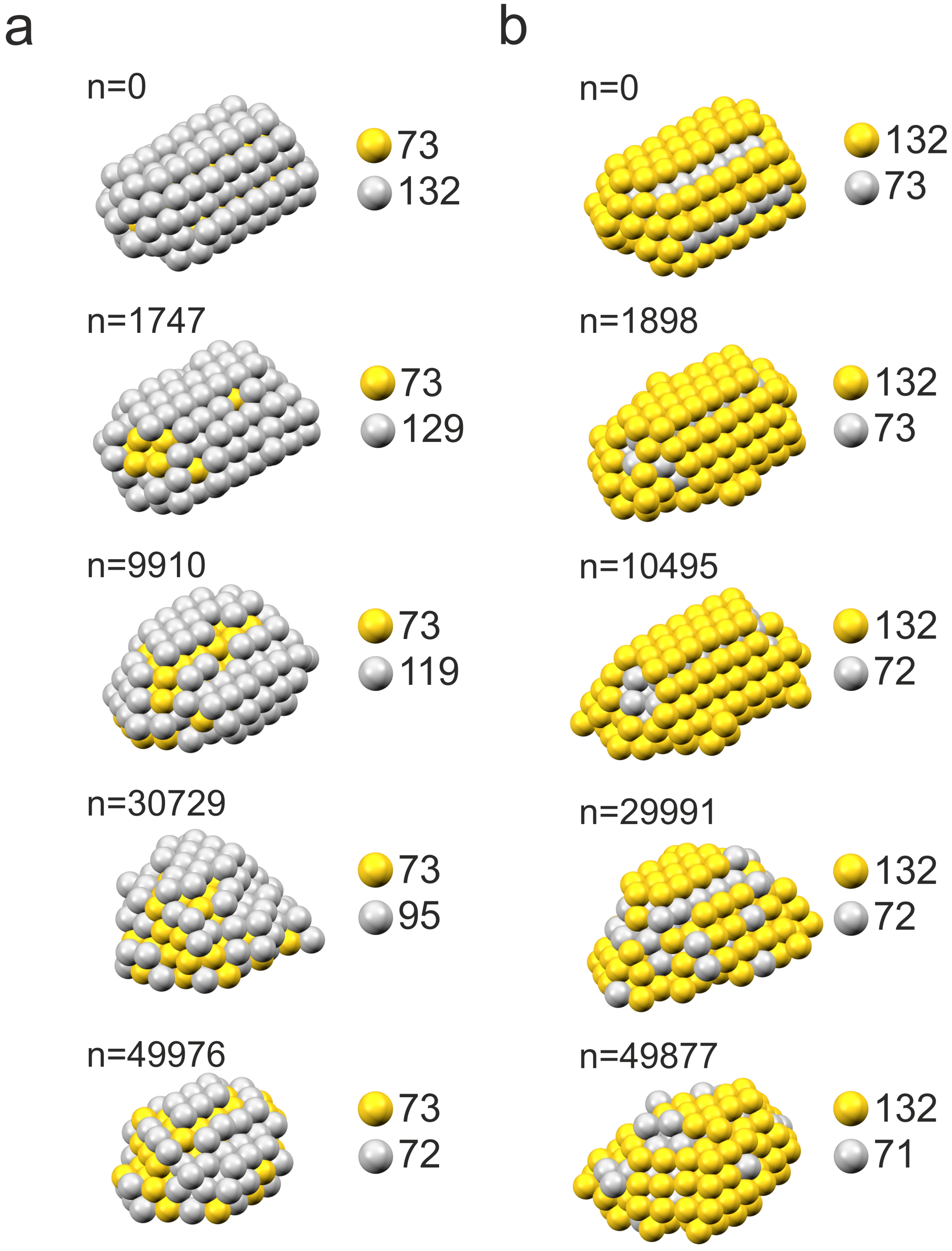

Figure 3.10.: Evolution of an Au(Ag) in (a) and an Ag(Au) in (b) core(shell) cluster consisting of 205 atoms (73 in the core and 132 in the shell) at different states during electron beam irradiation (300 keV)

Finally, we have to remark that a system consisting of tenths to hundreds of atoms can evolve in a large amount of different transformation paths due to the stochastic nature of the electron scattering events. To obtain exact information about all possible structure transformations, a vast amount of simulation runs with identical starting conditions would be required. This is especially demanding if different possible starting geometries need to be considered. Therefore, predictions of how a cluster can evolve are computational very expensive and practically impossible for larger systems. Nevertheless, in most cases this is not necessary. Often it is sufficient if displacement and sputtering rates can be estimated on a statistical basis and general transformation mechanisms can be identified with this calculations. Some results may also be extrapolated to larger systems, which are not directly accessible with this method, such as interfaces, surfaces or alloys.
Note that by using classical molecular dynamics we rely on the assumption of the Born-Oppenheimer approximation. That means that the wave function of an atom can be written as a product of the wave function of the electrons and that of the nucleus. Then the motion of the nuclei and the electrons can be calculated separately and the potential energy surface for the calculation of the atomic trajectories can be represented as a sum of ground state potentials. This means that the electron shell has been completely neglected in our considerations. So if we want to include bond breaking of covalent bonds by the electron beam due to excitation and ionization, we need much more sophisticated approaches such as ab-inito molecular dynamics.

Conclusively, we did first steps towards the simulation of beam induced processes in metallic clusters. However, there are still many open questions: For instance the equilibration time after each displacement could be too short. This should be considered for future work, with an optimised code. Furthermore, only qualitative information can be given with the present code. Sputtering, for instance, seems to be underestimated significantly compared to experimental results.

3.6. Multislice Image Simulation

Electrons interact strongly with matter (see section 3.1) and undergo multiple elastic scattering events even in thin samples. This is called dynamic scattering (for more details see section 2.5). If we want to understand image formation in TEM, we have to calculate the propagation of an electron from scattering event to scattering event until it reaches the detector. Furthermore, thermal diffuse scattering, which describes the scattering of an electron by thermal phonons, has to be included for a complete imaging simulation. In conventional TEM imaging, where high resolution images are generally not directly interpretable, such image simulations are important tools for image analysis. The most spread technique for this kind of calculations is the Multislice algorithm. In terms of quantum mechanics we have to solve the Schrödinger equation for a given potential field, representing lattice atoms. The sample, which has not to be crystalline, is then divided into small slices perpendicular to the electron beam. Within such a slice the potential field is approximated to be constant and the Schrödinger equation is solved slice by slice as the electron wave propagates through the sample. Eventually, the imaging system with its aberrations and angular conditions (convergence and detection angles) have to be included in the calculations. Figure 3.11 shows a schematic of the working principle of the multislice algorithm.

With this technique in principle all imaging and diffraction techniques in TEM and STEM can be treated. Although the sample has not necessarily to be crystalline for this method, less regular samples would require more slices and thus increase the computational demand. Usually the slices should correspond to the existing atomic layers in the specimen as depicted in Figure 3.11.

Among the available Multislice simulation packages, QSTEM (v2.4) by Christoph Koch and co-workers has been chosen in this work [77]. With the included converter tool it allows to import xyz-files, which are simple coordinate lists that can easily be exported directly from our MD-code. Furthermore, QSTEM gives quantitative results and is available online free of charge [5].

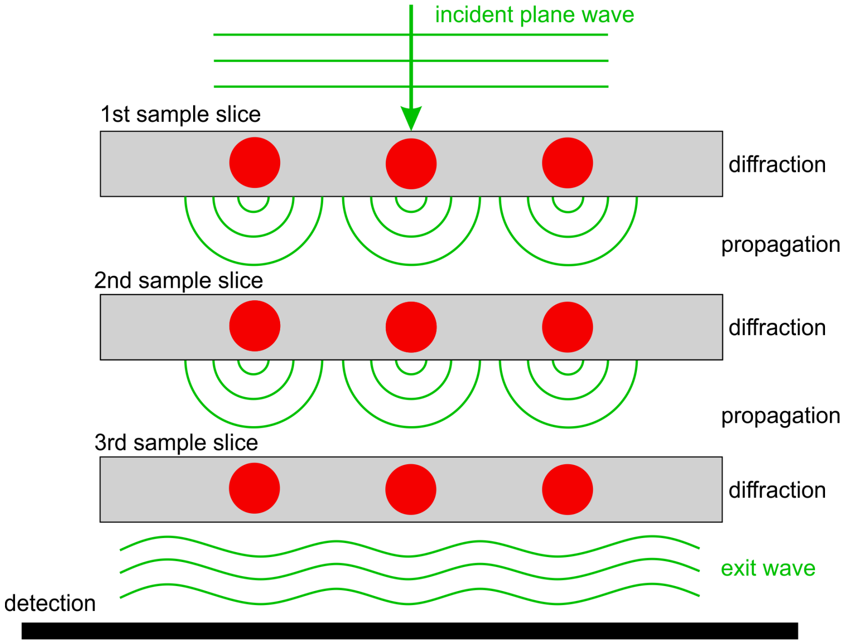

Figure 3.11.: Illustration of the multislice algorithm: An incident electron plane wave is propagated through a crystalline sample, represented by red atoms and cut into three sampling slices, each diffraction in a slice is followed by an propagation to the next slide until the exit wave reaches the detector

---

[5] qstem.org (accessed 31 January 2017)

4. Results and Discussion

In the following chapter the experimental findings will be presented and discussed. The focus, hereby, lies in the STEM analysis of mono- and bimetallic clusters comprised of Au, Ag, Ni, CrAu, AgAu and AuNi.
Accompanying, also 2D materials, such as hexagonal boron nitride and graphene have been prepared and tested for their suitability as TEM supports for metallic clusters. Some effort has also been put into the development of analysis tools and preparation techniques.

4.1. 2D-Materials as TEM Support

The work done with 2D-materials is based on the experiments and findings of the preceding master thesis with the title "Preparation and Electron Microscopy of Graphene", which was also performed at the Institute for Electron Microscopy (FELMI) by the author of the present doctoral thesis [151]. Within the scope of the present work the preparation techniques developed in the master thesis were applied to prepare hexagonal boron nitride (h-BN) thin films. These films were then used as a support of metallic clusters for TEM investigations.

4.1.1. Hexagonal Boron Nitride

The structure of hexagonal boron nitride (h-BN) is very similar to that of graphite. h-BN is the most stable modification of BN. It consist of layered arrangement of honeycomb structured sheets. Within these sheets the atoms are bond very strongly by covalent bonds while the interlayer bonds are relatively weak due to their van der Waals nature. In contrast to graphite which stacks preferentially in AB stacking mode, h-BN stacks in AA' mode. That means that each B atoms sits above a N atom instead of the centre of the underlying hexagon. This reflects the polarity of the B-N bonds. The B-N bond length is 1.44 Å and the interlayer distance 3.33 Å, which is very similar to graphite [152]. See Figure 4.1 for an illustration of the h-BN structure.

4.1.1.1. Properties

Despite the very similar structure of graphene and a single-layer h-BN their electrical properties are very different. Graphene is classified as a semi-metal with a zero band-gap, due to its delocalised π electrons. In h-BN these electrons are localised around the nitrogen atoms due to

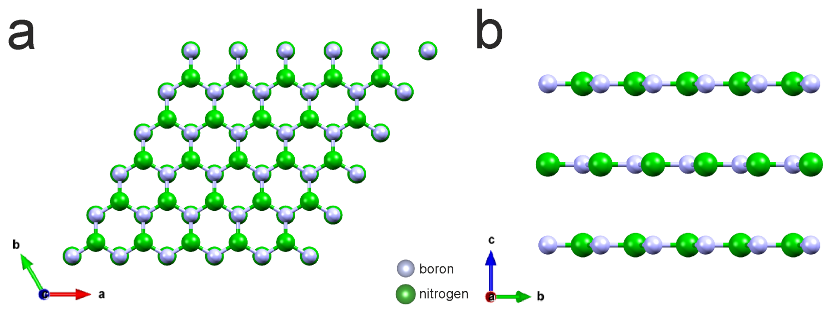

Figure 4.1.: Structure of hexagonal boron nitride: a) parallel and b) perpendicular to the crystallographic c-axis

the difference in electronegativity between B and N. Therefore, h-BN is an electrical insulator with a bulk band gap of 5.9 eV [153]. However, it has a high in plane thermal conductivity, comparable to graphene. Furthermore, h-BN is chemically stable to most etching solutions except hot phosphoric acid and it is heat resistant up to temperatures of 1000 °C in air and 1400 °C in vacuum.

4.1.1.2. Preparation

Due to the layered structure and the high discrepancy between the inter- and intra-layer bondings the individual layers can be separated mechanically. To this end we applied the well-known "scotch tape method" that has also been used for the preparation of graphene by Novoselov and Geim [154]. BN flakes were thinned via an ordinary scotch tape. Subsequently the flakes were transferred to a silicon wafer with a well defined SiO_2 layer thickness of 500 nm in order to allow the identification of the thinnest regions in a light microscope. Chosen flakes were then transferred to a TEM grid backed with a holey carbon film (Quantifoil R 2/1 from Quantifoil Micro Tools GmbH, Jena, Germany). Therefore, the grid was placed on the flake and a droplet of isopropanol (IPA) is dropped on the grid. During drying on a hot plate for 5 minutes at 200 °C the surface tension of the vaporising IPA pulls the grid to the substrate surface. Due to van der Waals forces the grid keeps sticking and finally the underlying SiO_2 can be etched in a 30 % KOH-water solution. This procedure follows an approach which has been used for the preparation of graphene before [151], based on early work by Mayer et al. [155].
Figure 4.2a shows an AFM analysis of the BN flake as prepared lying on the SiO_2 surface. A double layer could be identified. Figure 4.2c and d show the same flake in STEM HAADF and BF, respectively, after transfer to a TEM grid.

Figure 4.3 depicts high resolution STEM HAADF images of the BN double layer. The images were obtained on the FEI Titan at 60 kV with a convergent angle of 21.4 mrad. The bright regions at the border of (a) are immobile carbon contaminants, that can regularly be found on BN samples.

---

[1] AFM investigations done by Thomas Ganner

[2] Optical microscopy image acquired by Johanna Kraxner

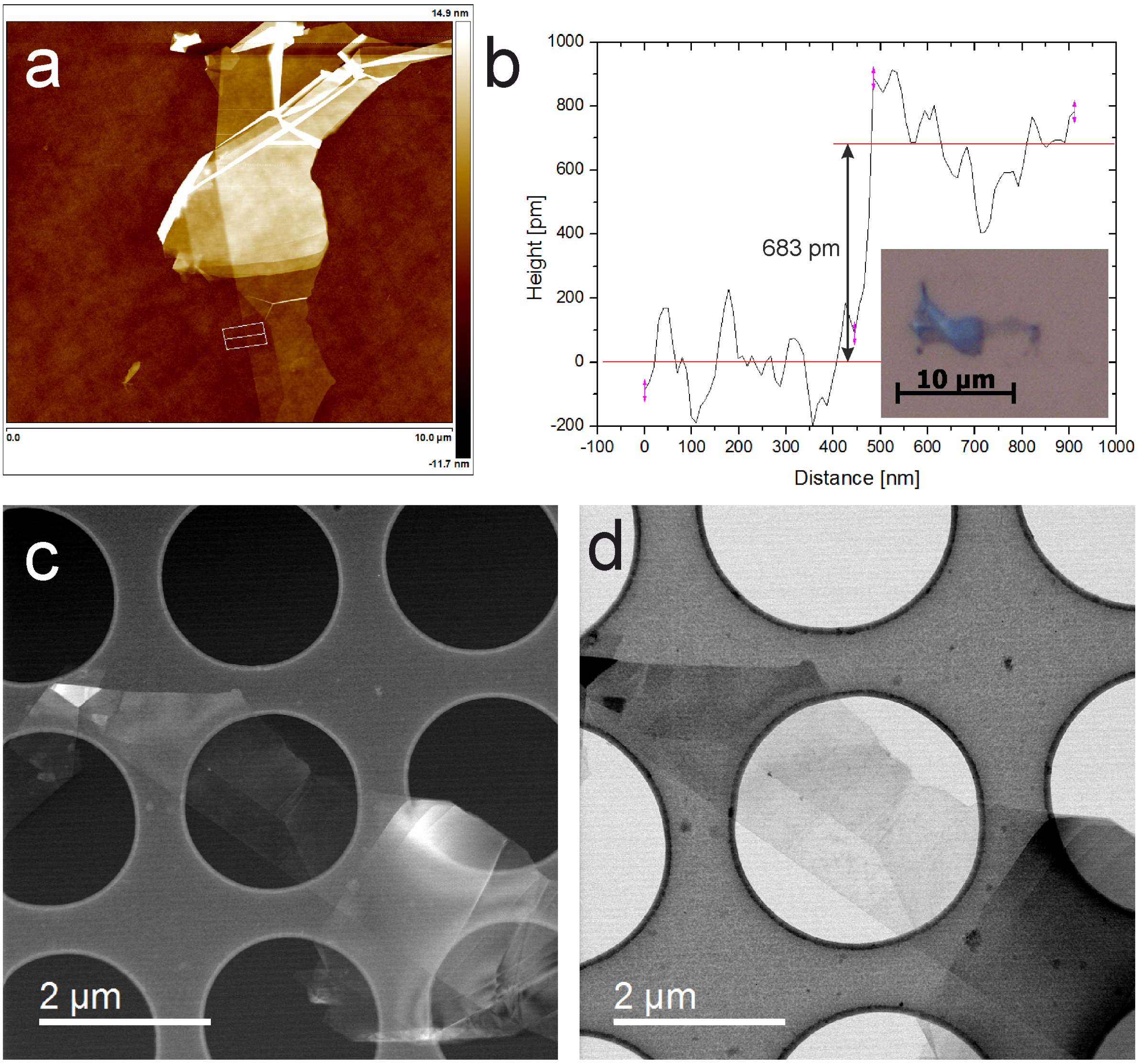

Figure 4.2.: (a) AFM image of a boron nitride flake as prepared on a SiO_2 surface[1]. (b) height profile corresponding to the area marked in (a) indicating the presence of a double layer. The inset shows a light microscopy image of the same flake[2]. (c) and (d) STEM HAADF and BF images of the same flake on the Quantifoil TEM grid

Since our interest lies in metallic cluster here, we wanted to test thin BN flakes as support for TEM analysis, in a next step.

4.1.2. Au Clusters on Hexagonal Boron Nitride Thin Films

In a first proof of concept, Au clusters were deposited on the BN sample that was analysed in the previous section. Figure 4.4a shows STEM HAADF overview images of the flake. The clusters can clearly be seen as bright dots in these images. Figure 4.4b shows a STEM BF images of 2 clusters, one attached to carbon contamination and one lying at the edge of a very thin

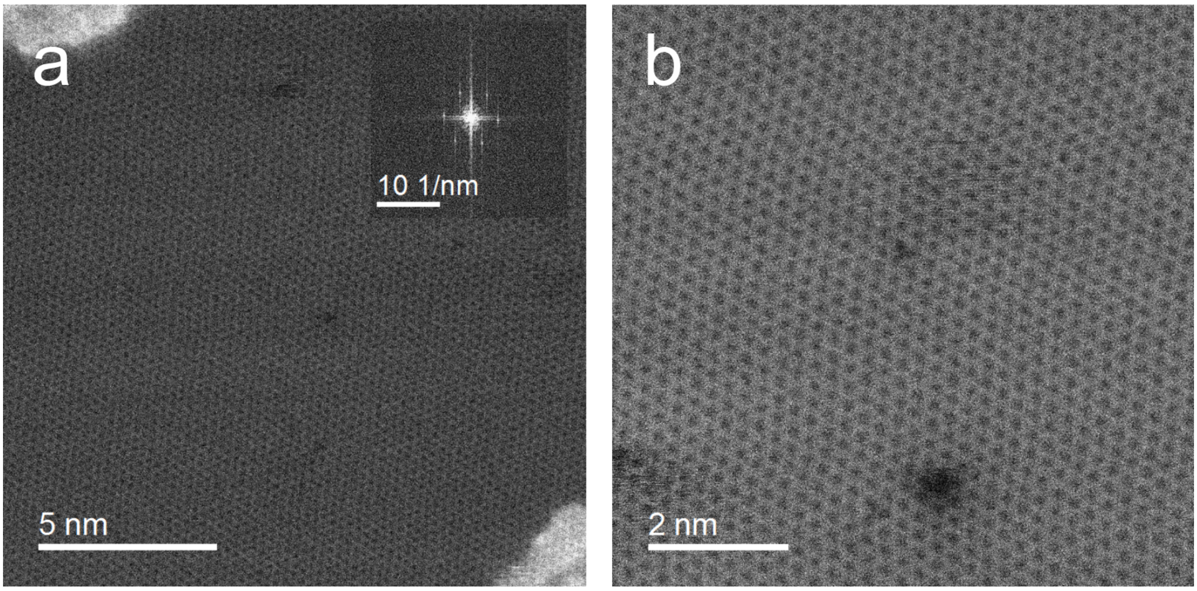

Figure 4.3.: Two high resolution STEM HAADF images at different magnifications: (a) bright areas are carbon contamination, inset shows a FFT of the image showing a typical hexagonal pattern. (b) higher magnification reveals several vacancies in the hexagonal lattice structure.

h-BN flake, which gives only a faint contrast in this image. Due to the big contrast difference between Au and h-BN it is impossible to image both using HAADF and, therefore, BF imaging was chosen in this case. Figure 4.4c show the results of a low-loss EELS study of a single Au cluster on h-BN with varying thickness. The differences of the plasmon peak structure between a monolayer and few layer h-BN, with the completely missing bulk contribution of the single layer h-BN can be seen. The inset table lists the characteristic plasmon losses that can be seen in the spectra [156, 157]. The plasmon features of the cluster can be identified clearly, what would be difficult even with the thinnest available amorphous carbon TEM supports (2-3 nm thickness). A spectrum of such a film is also shown for comparison. To this end, the intensity values have been normalised to the height of the zero loss peak. The inset shows an HAADF image of the analysed area, acquired simultaneously with the spectrum image. The regions, where the spectra have been extracted, are marked in corresponding colours. Each spectrum represents the sum of 16 single spectra (4x4 pixels). The cluster appears overexposed here due to the high contrast difference between Au and BN in HAADF, as mentioned before. The brightness was therefore adjusted to visualise the h-BN film. An example of how h-BN could also facilitate elemental TEM analysis of such small clusters can be given from the EELS experiments. In the following we take a closer look on the energy region between 50 and 100 eV were we would expect the presence of the $O_{2,3}$ (54 eV), $N_{6,7}$ (83 eV) and O_1 (108 eV) edges of Au. Therefore, an EELS SI has been acquired consisting of 150 x 162 spectra with a dwell time of 1 ms each. As shown in Figure 4.5a a single spectrum is dominated by noise, due to the relatively short pixel time used here. Nevertheless, if we apply PCA using 2 components (corresponding to BN and Au) we can still extract elemental information from each single spectrum and even the weak N edge can be identified (see section 2.6.1 for

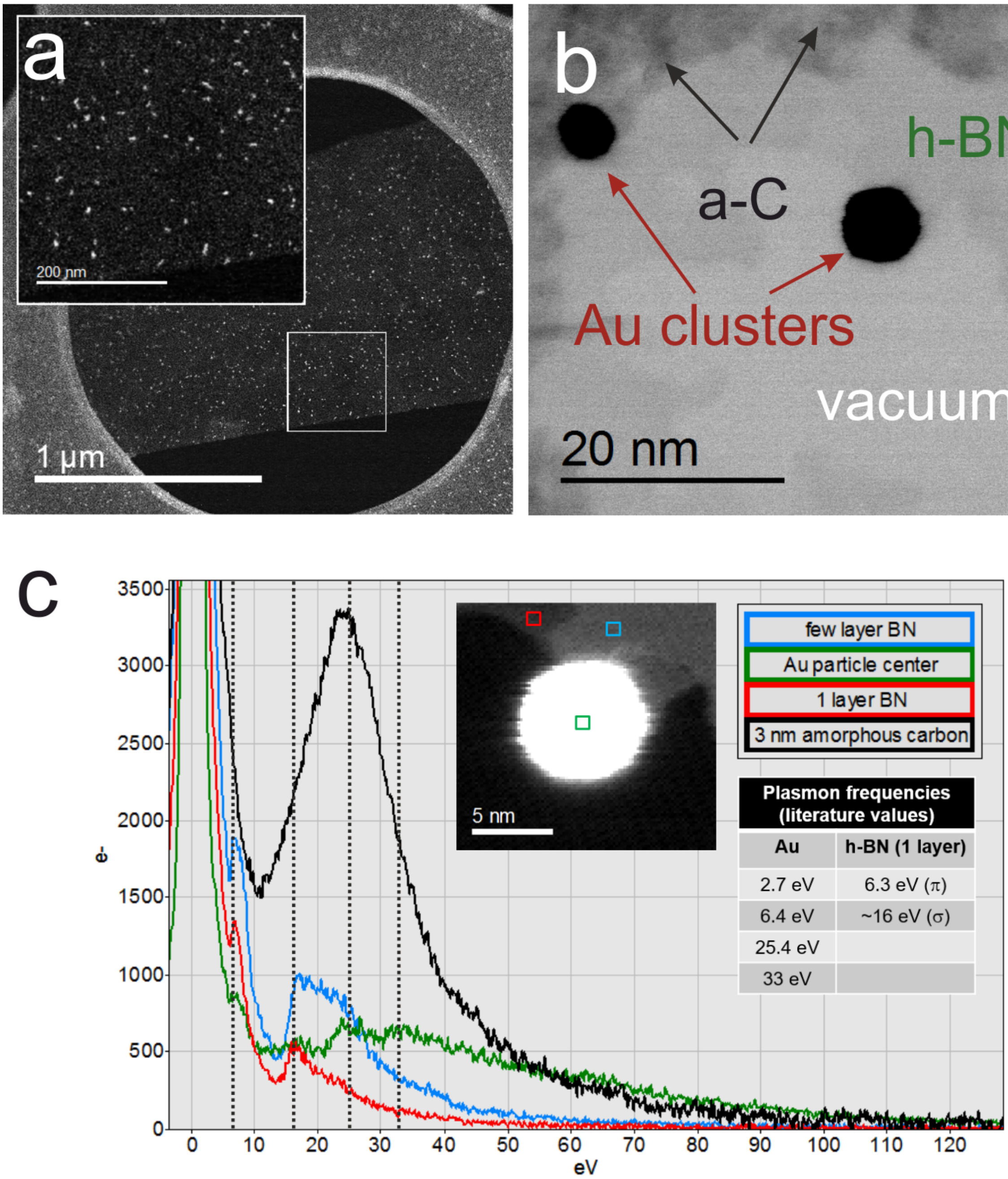

Plasmon frequencies (literature values)	
Au	h-BN (1 layer)
2.7 eV	6.3 eV (π)
6.4 eV	~16 eV (σ)
25.4 eV	
33 eV	

Figure 4.4.: Au Clusters deposited on h-BN: (a) STEM HAADF overview image, the inset shows the marked area enlarged (b) STEM BF image of 2 clusters in close-up view. (c) EELS low-loss analysis of an Au cluster lying on a h-BN film with varying thickness. The inset shows an HAADF image acquired simultaneously with the spectrum image. The areas where the spectra have been extracted are marked in corresponding colours. A spectrum from a 3 nm amorphous carbon film is shown for comparison. The spectra have been normalised on the height of the zero-loss peak. The table lists the important plasmon frequency values that can be identified in the spectra.

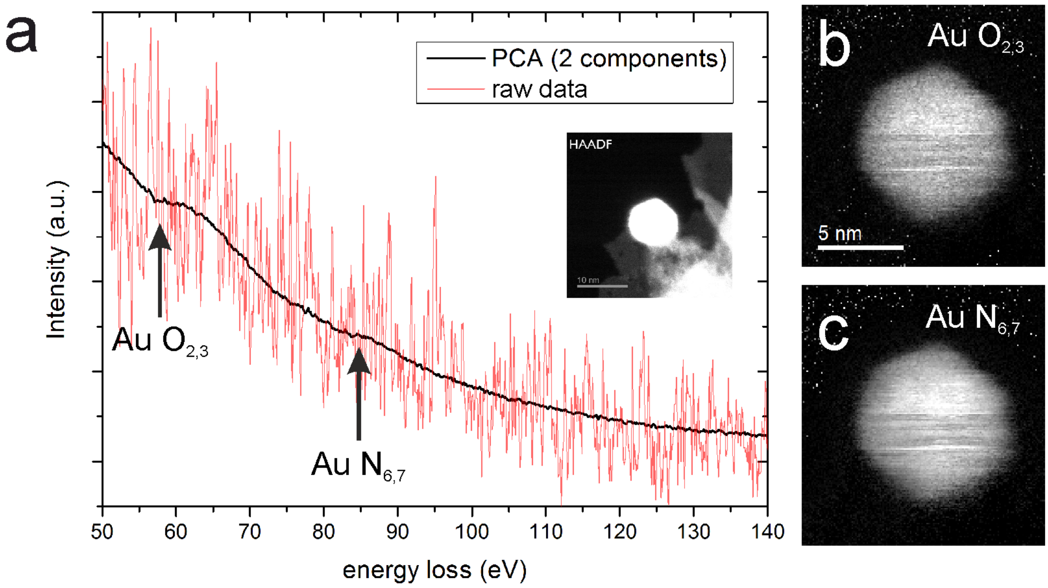

Figure 4.5.: (a) Single EELS spectrum extracted from the centre of an SI acquired from the Au nanoparticle shown in the HAADF image in the inset. Both the original signal (red) and the result of PCA with 2 components (black) is shown. (b) and (c) show an elemental map generated from the same PCA filtered data set using the Au $O_{2,3}$ and the Au $N_{6,7}$ edges respectively.

methodological details). Two Au elemental maps were generated from both edges, which are shown in Figure 4.5b and c, respectively. We were not able to identify the O_1 edge that should be located at 108 eV.

In possible future experiments this technique could be used to analyse clusters comprised of high-Z elements using EELS. Their edges often lie in the very high energy loss region above 2000 eV. High doses are then needed to acquire a usable signal, due to the power-law like decrease of the inelastic scattering cross section with energy loss (according to Bethe) [3]. Lower energy edges of such elements, on the other hand, often lie below 150 eV, where they are covered by the increased background (plasmon tails). Furthermore, such small systems are also very beam sensitive, and would not be accessible otherwise by elemental analysis, neither by EELS nor EDXS. However, it should be considered that EELS interpretation can be very complex in the lower energy region, dependent on the elements contributing. To conclude, h-BN thin film have been prepared by using scotch tape thinning and a transfer method that was developed previously for graphene. Their suitability as support for metallic cluster analysis in the TEM has been shown using Au clusters. We could show that h-BN has several advantages over conventional amorphous carbon substrates. The background caused by the substrate is significantly lower in both imaging and EELS. This could be used for plasmon experiments on small clusters as well as elemental EELS analysis of high Z materials and at low doses. h-BN is also advantageous, compared to graphene substrates, wherever carbon needs to be avoided. This could be case wherever carbon needs to be detected, beam induced chemical reactions with carbon can be expected [34], or elemental information is covered by the carbon signal

(e.g. Ag in EELS).
Nevertheless, there are two main disadvantages that should be mentioned here. First, h-BN thin films are very sensitive to knock-on damage, reducing the beam energy to 80 kV (better 60 kV) is therefore arbitrary. Secondly, because TEM grids backed with a h-BN film are not commercially available yet, they need to be prepared in advance. The preparation of h-BN flakes with the scotch tape method is very time consuming and ineffective. Recently, large area monolayer boron nitride became commercially available[3] to relatively modest costs. These boron nitride films are grown with a chemical vapour deposition (CVD) technique on copper foils. If transferred to a TEM-grid, this could be an interesting alternative as cluster support in future.

4.2. Electron Beam Induced Oxidation

Among a large variety of beam damage mechanisms, electron beam induced chemical reactions are the most interesting ones. During our work with supported metallic clusters we observed beam induced sample changes on Ni, Ag and Cu, that can be clearly related to an oxidation. In most cases the oxidation is accompanied by a Kirkendall hollowing effect which leads to interesting, hollow cluster morphologies. Parts of the work related to Ni clusters have already been published [158].

4.2.1. Electron Beam Induced Oxidation of Ni Clusters

A phenomenon that was observed during TEM investigations of Ni clusters is presented in this section. Under electron beam irradiation the clusters transformed to NiO rings. The oxidation behaviour was related to a two-step Cabrera-Mott mechanism. We identified residual water adsorbed adjacent to the clusters as the main source of oxygen. The transient dynamics of the oxidation was documented by time lapse series using STEM HAADF imaging and EELS.

4.2.1.1. Experimental Conditions

The experiments were performed using our FEI Titan[3], operated either at 60 keV or 300 keV in STEM mode. Acquisition and evaluation of all data was carried out using Gatan DigitalMicrograph (GMS, version 2.31.764). Particle sizes in the HAADF image series were determined within MATLAB (version R2012b). As part of this procedure, each image was blurred using a 3x3 spatial averaging filter to reduce contrast variations introduce by the crystallinity of the clusters. Then a threshold based particle detection algorithm based on Otsu's method was applied (as implemented in the MATLAB image processing toolbox) [159]. In all measurements the convergent angle was 21.4 mrad for 60 keV and 20 mrad for 300 keV, respectively. For all EELS measurements a collection angle of 26.5 mrad was used.

---

[3] source: www.graphene-supermarket.com

Nickel clusters were grown inside superfluid He droplets with a mean diameter of 90 nm, consisting of about 10^7 ^{4}He atoms, using the technique described in section 2.8. The He pressure was set to 20 bar and the nozzle was cooled to a temperature of approximately 8 K. In the pick-up chamber Ni, with a purity of 99.998 %, was thermally evaporated. Atoms colliding with helium droplets are cooled to droplet temperature and aggregate in the centre of the droplet. Finally, the beam was terminated on a TEM-grid with either amorphous carbon or graphene. A schematic representation of the synthesis apparatus with a single thermal evaporator is given in Figure 2.23.

Substrates covered by amorphous carbon (film thickness <3 nm) and backed by a holey carbon support film on a 300 mesh gold grid (Ted Pella, Inc., Prod. No. 01824G) have been used. Suspended monolayer graphene on Quantifoil R2/4 holey carbon gold grids (from Graphenea Inc.) were used as graphene support. To eliminate contamination annealing techniques were applied, as described in section 2.7. Graphene grids were baked at approximately 200 °C in contact to active coal for 1 h in air before placed into the synthesis facility [87]. After mounting in the deposition chamber, all substrates were baked for several hours at 200 °C under UHV conditions before cluster deposition. Although an evacuated vessel was used for the transfer from the synthesis facility to the microscope vacuum, the samples had to be exposed shortly (<5 min) to ambient conditions during insertion into the TEM.

Figure 4.6a shows an overview image of three Ni clusters with different initial state sizes, deposited on amorphous carbon. Figure 4.6b shows particle 1 after exposure to the electron beam for about 9 s. The cluster exhibits a single crystalline structure and ring-shaped morphology after transformation. Lattice fringes can clearly be seen and the spacings correspond to the (2,0,0) and (1,1,1) lattice planes of rock salt structured NiO, being 0.21 and 0.24 nm, respectively. The corresponding Fast Fourier Transform (FFT) (Figure 4.6c) reveals the alignment of the cluster with the [0,-1,1] zone axis.

Figure 4.7 displays an elemental EELS analysis of two clusters, one in its initial state and one after transformation, with their spectra. These results provide further evidence that the morphology change is directly related to an oxidation of the particle. EELS quantification using the spectrum in Figure 4.7 gives a composition of 56 at% oxygen and 44 at% nickel. The difference to the expected ratio of 50:50 for NiO can be explained, on one hand, with the uncertainty of approximately 10 rel.%, that can typically be assumed for the method [3]. On the other hand, there is most likely still some oxygen adsorbed within this area, which contributes to the EELS signal but is not bound inside the NiO cluster.

4.2.1.2. Oxidation Kinetics

A STEM HAADF time lapse series consisting of 140 consecutive images was acquired over all three clusters in Figure 4.6a simultaneously, to study the oxidation kinetics under identical experimental conditions. A beam current I_P of 80 pA was chosen, corresponding with a dose rate of approximately 4.7×10^5 electrons $\mathrm{nm}^{-2}\,\mathrm{s}^{-1}$, and the energy E of the electrons was set to 300 keV. Exemplary, in Figure 4.8a five images of particle 1 from Figure 4.6a are given at different stages, including a graphical model in (b) to illustrate the morphological transformation process. At the beginning the cluster slowly expands without void formation.

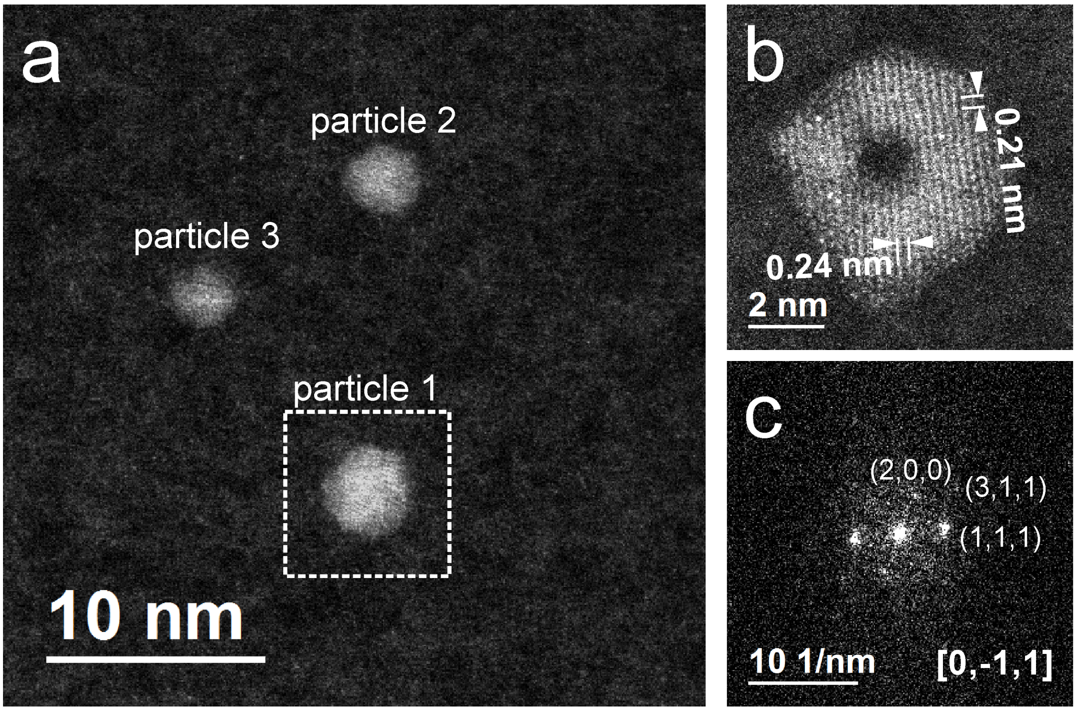

Figure 4.6.: (a) HAADF overview image of three clusters on amorphous carbon before oxidation. (b) Enlarged image of particle 1 after full transformation into a single crystalline NiO ring. (c) corresponding FFT from (b)

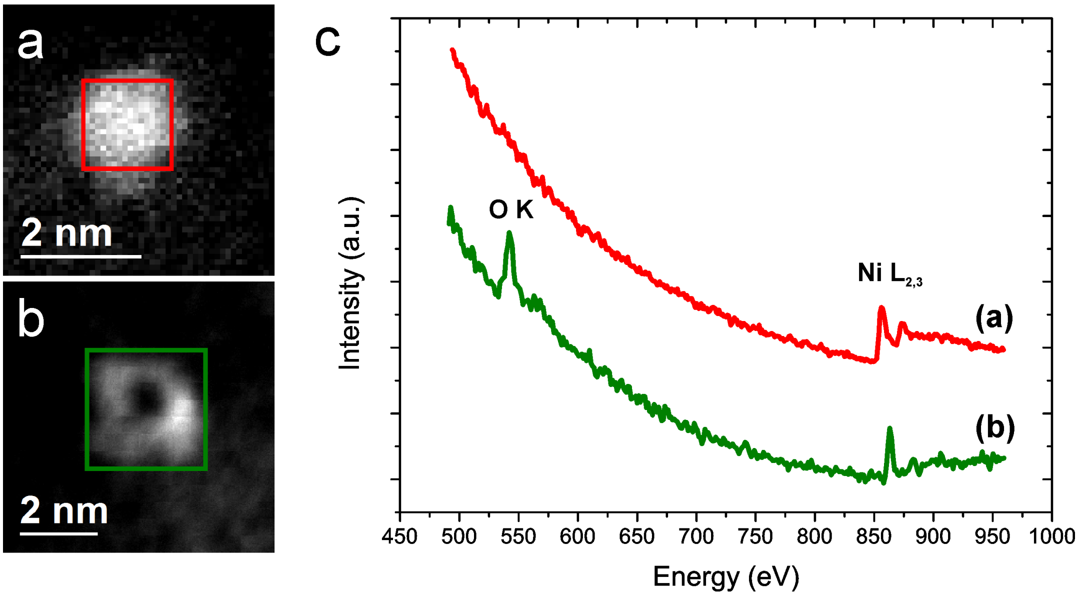

Figure 4.7.: Comparative EELS analysis of two clusters on amorphous carbon before and after transformation. The HAADF signal in (a) and (b) was recorded simultaneously with the spectrum images. The spectra in (c) shown in red (initial state) and green (fully oxidized) are taken from the areas marked by boxes with the corresponding colour in (a) and (b), respectively.

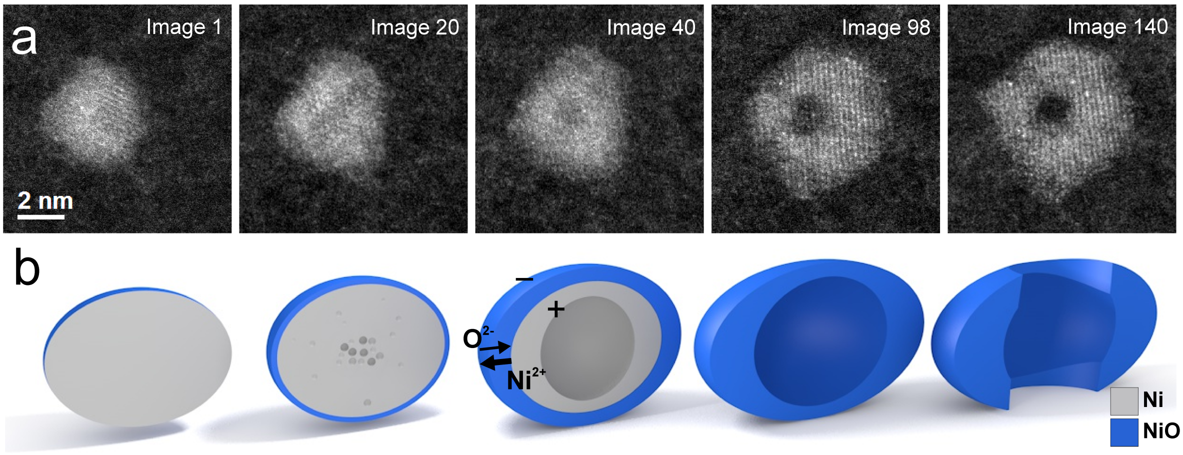

Figure 4.8.: (a) Selected images of the time lapse series from particle 1 in Figure 4.6a, showing the transformation to a hollow and finally ring-shaped NiO cluster (extracted from a HAADF image series consisting of 140 images (1024x1024 pixels), 3 µs pixel time and I_P = 80 pA). (f) Corresponding illustration of the transformation process according to the Cabrera-Mott model and the NKE. An electric field inside the oxide drives the diffusion of Ni cations to the NiO surface and O anions to the Ni/NiO interface (ion flux $j_{Ni^{2+}} > j_{O^{2-}}$), while voids aggregate in the cluster centre.

The discrepancy between the ionic radii of Ni cations and O anions leads to a lower diffusion rate of the latter. Vacancies, created due to Ni outward diffusion, start to agglomerate visibly after 20 images. After 40 images a single void in the middle of the cluster is formed. Under further beam exposure, this void grows until the cluster is fully converted into NiO. Finally, the centre collapses, forming a single crystalline, ring-shaped particle as shown in image 140 of Figure 4.8b. The central atoms have been completely removed, which happens in a very reproducible way. This can be explained with the small size of the clusters combined with the similar self-diffusion rate of Ni compared to the diffusion rate of Ni in NiO [36], which results in a clustering of vacancies immediately after formation. To document the hollowing process we determined the intensity values from the cluster centre for each single image of the time series. Results are plotted as a function of the sequential image number in Fig 4.9a.

By varying the interval between consecutive images we found, that the conversion develops only under the electron beam and stops immediately after the illumination is being stopped. Therefore, we presume that the integrated pixel time of the pixels contributing to the cluster area denotes the time needed for the transformation.

The growth kinetics of thin nickel oxide films can be described using a model proposed by Cabrera and Mott [160]. According to this model the presence of an oxide layer leads to a uniform electrostatic field inside the oxide, amplifying the diffusion of Ni cations to the surface and thereby increasing the oxidation speed (Figure 4.8b). The initial step within this process is the transfer of electrons from the metal through the oxide to the surface. In case of thermally induced oxidation the electron transfer rate is determined either by tunnelling or thermionic emission. We suppose that in an electron beam also secondary electrons, which are generated in excitation processes, can leave the illuminated sample volume and lead to an additional accumulation of positive charges, thus to an enhancement of radial ion diffusion.

When the oxide thickness approaches the length scale of the whole system, the electric field in the oxide scale strongly depends on its geometry. We found several approaches to obtain theoretical predictions for different geometries, such as spherical nanoparticles or cylindrically shaped nanowires [161–164]. However, an analytical solution can only be given for uniform oxide growth on a flat surface [165]. For this case the Cabrera-Mott model predicts a direct logarithmic behaviour ($L \propto k \cdot \log(t)$); with L being the scale thickness, k the growth rate and t the effective illumination time. The one-dimensional growth of the oxide scale can then be directly related to a corresponding growth in its cross-section area.

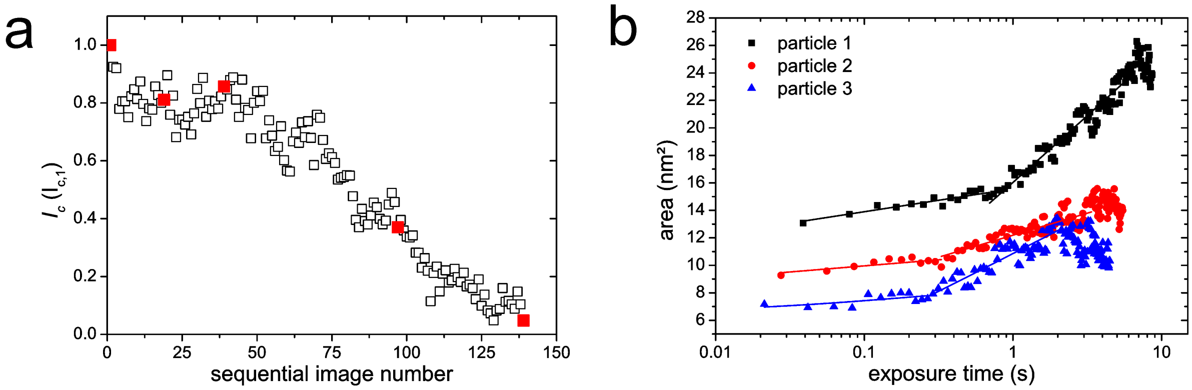

Figure 4.9.: (a) Intensity of the cluster centre I_c from the HAADF time lapse series shown in Figure 4.8a in units of the initial centre intensity $I_{c,1}$, plotted over the sequential image number during electron induced oxidation. The red filled symbols correspond to the five images shown in Figure 4.8a. (b) Evolution of the projected area of the three Ni-Clusters in Figure 4.6a with different sizes over the effective exposure time and the deposited dose in logarithmic scale (calculated from the whole HAADF image series); the logarithmic growth law was fitted to each growth regime separately as a visual aid.

The oxidation behaviour of the three clusters from Figure 4.6a is presented in Figure 4.9b, where the projected areas are plotted over the effective illumination time and the deposited electron dose in logarithmic scale, respectively. The direct evaluation of the oxygen content via HAADF quantification turned out to be impractical [4]. The difficulties can mainly be attributed to the small elastic scattering cross section of oxygen compared to nickel, the initially undefined orientation of the clusters with respect to the electron beam and beam damage effects. See section 4.2.1.10 for details.

By evaluation of the projected areas two different regimes of oxidation can be identified for each cluster, characterised by an increasing growth rate k in the second regime. This can be understood by the fact that for spherical particles conventional Cabrera-Mott theory can only be applied for thin oxide films. When the oxide thickness becomes comparable to the particle radius, the curvature of the surface must not be neglected anymore. This leads to a non-uniformity of the electric field in the oxide and consequently to an enhanced ion diffusion, resulting in an increased k-value in the second regime. Our findings agree with theoretical predictions [161, 163].

The Cabrera-Mott model furthermore assumes the injection of defects at the metal/oxide interface and at the oxide surface to be the rate determining steps. Due to the electric field, the energy needed for jumps of displaced metal atoms back to their initial position is greater than the energy for subsequent jumps inside the oxide. Presumably the electron beam mediated creation of these interface defects plays an important role for the electron induced oxidation process.

The volumetric expansion of a metal during oxidation is determined by the Pilling-Bedworth-Ratio (PBR), which can be calculated with Eq. (4.1).

$$\mathrm{PBR} = \frac{V_{\mathrm{Oxide}}}{V_{\mathrm{Metal}}} = \frac{\rho_{\mathrm{Ni}} \cdot M_{\mathrm{NiO}}}{\rho_{\mathrm{NiO}} \cdot M_{\mathrm{Ni}}} \tag{4.1}$$

With knowledge of the density ρ_{Ni} of Ni (8.91 $\mathrm{g\,cm^3}$) and NiO ρ_{Ni} (6.67 $\mathrm{g\,cm^3}$) and their molar masses (58.7 and 74.7) Eq. (4.1) gives a value of 1.65 for NiO/Ni [166]. In TEM the morphological transformation of the clusters can only be assessed by their projected area. Therefore, the change in volume implies a corresponding change in the projected area by a factor of 1.41, assuming isotropic oxidation. The projected area of particle 1 from Figure 4.6a grows from initially 13 $\mathrm{nm^2}$ to 24.7 $\mathrm{nm^2}$ when fully oxidized, giving an area expansion factor of 1.9, which is considerably higher than the expected value of 1.41. For particle 2 and 3 we obtain factors of 1.6 and 1.7 respectively. The particle height, hence, remains almost constant during oxidation for any cluster, when a prismatic morphology is assumed. This indicates that oxidative species are first adsorbed to the adjacent substrate and then diffuse to the side of the clusters where they react with Ni atoms, resulting in an enhanced lateral growth. In all cases the point of full oxidation was determined from the logarithmic growth plots in Figure 4.9b, defined by the point where the clusters reach their maximum lateral expansion. Beyond this point beam damage effects become visible; surface desorption, sputtering and collapsing of voids cause a shrinkage of the cluster. With prolonged electron beam exposure the centre void also vanishes and a spherical NiO cluster is formed. This is significant particularly for the two smaller clusters at the given dose rate.

4.2.1.3. Electron Beam Effects

The beam induced kinetics in metallic clusters mostly arises from elastic interactions (electrostatic deflections of electrons), as described in more detail in section 3.1. The maximum elastically transferable energy E_{max} by an incident electron with energy E can be calculated using Eq. (3.7). After inserting the atomic mass m of nickel, the speed of light in vacuum c and the electron rest energy E_0 one obtains $E_{\mathrm{max}} = 14.5\,\mathrm{eV}$ at $E = 300\,\mathrm{keV}$.

To permanently remove an atom from a surface site, the sputtering threshold energy E_s for Ni (7.5 eV) [104] needs to be transferred. Since $E_s < E_{\mathrm{max}}$, sputtering clearly damages Ni surfaces at 300 keV. Although the presence of an encapsulating oxide layer has a stabilizing effect, the creation of defects at the metal/oxide interface is likely to occur, which is crucial to the Cabrera-Mott mechanism.

In the case of NiO, surface erosion due to knock-on displacements arises for an electron energy above 103 keV [167]. Eqn. (3.7) then yields values for E_{max} of 4.2 eV for Ni and 15.6 eV for O respectively. Thus, the displacements of atoms (preferentially O) to interstitial lattice sites

in NiO and at the Ni/NiO interface promote the diffusion of atoms through the oxide. Defects introduced by the electron beam also act as charge traps and presumably lead to a space charge effect. This space charge, however, does not qualitatively affect the direct logarithmic behaviour, as shown by Chattopadhyay [165].
Besides elastic damage effects in NiO also radiolysis occurs and can be described in the picture of the Knotek-Feibelman mechanism, resulting in a surface localized reduction of the oxide above rather high doses [167, 168]. Both sputtering and surface reduction can partly explain the shrinkage of the clusters that is visible after full oxidation (Figure 4.9b).

4.2.1.4. On the Origin of Oxygen

An essential factor for the oxidation is the origin of oxygen. It can be found in small amounts but widely distributed on typical amorphous carbon TEM-substrates after being exposed to air. Hence, to study the original state of Ni clusters, monolayered graphene substrates were used due to their low chemical reactivity and highly hydrophobic properties [169]. In Figure 4.10 an EELS elemental map generated from the Ni $L_{2,3}$ and the O K signal can be seen. It is remarkable that no native oxide layer is visible on the Ni cluster in Figure 4.10a, despite exposure of the sample to ambient conditions. Nonetheless, the likely presence of a NiO monolayer may probably be below the minimum detection limit of the technique. Significant amounts of oxygen can, however, be found mainly adsorbed to the cluster surface. Even after several days under environmental conditions, the clusters remained unaltered, indicating effective passivation [170].

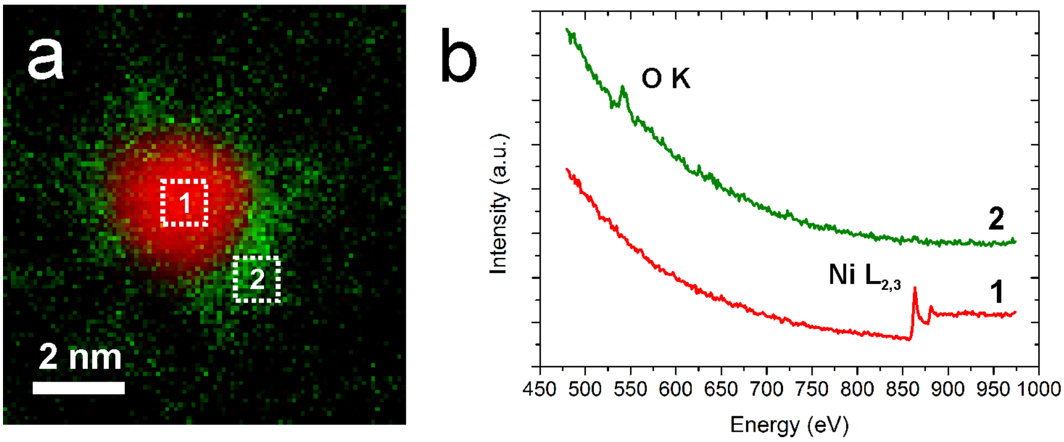

Figure 4.10.: (a) Ni cluster on a graphene substrate: EELS elemental map of a Ni cluster in its original state on graphene (red: Ni $L_{2,3}$ - signal, green: O K-signal, 91x96 spectra, E = 60 keV, 10 ms pixel time, I_P = 10 pA to decelerate oxidation). (b) EEL spectra extracted from the two areas marked with boxes in corresponding colours in (a).

Since the samples are prepared in a purely physical way in UHV without any solvents or detergents, no oxygen was involved in the cluster synthesis process. Organic compounds, possibly present on TEM substrates, can also be excluded as an oxygen source. This is

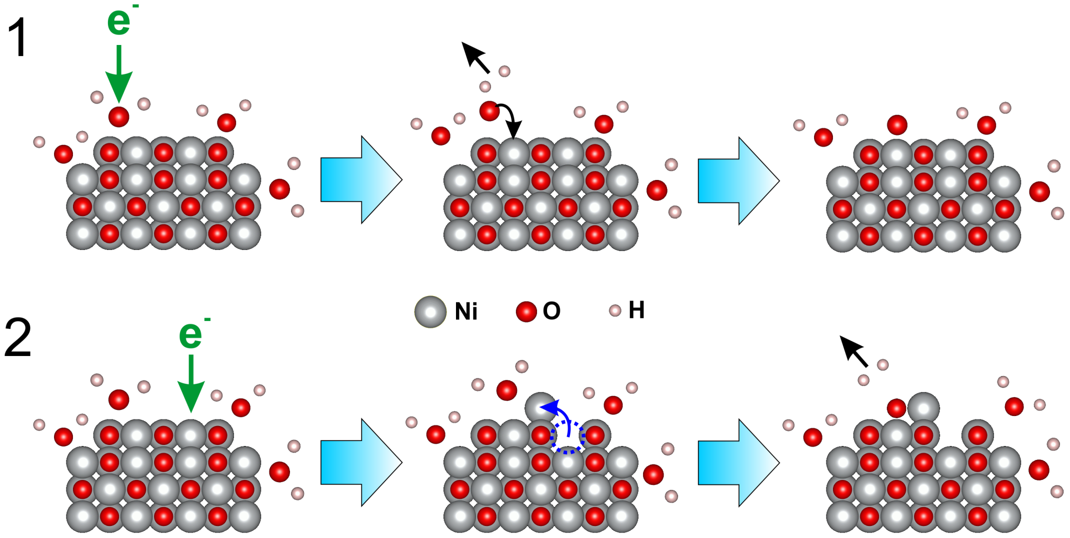

Figure 4.11.: Possible dissociation mechanisms of water adsorbed on NiO in an electron beam: 1. incident electrons dissociate H_2O and the oxidative dissociation product (e.g. O) chemisorbs to the surface. 2: An incident electron displaces surface atoms (Ni or O), generates a low-coordinated Ni atom which dissociates H_2O and leaves the Ni atom oxidized.

because single oxygen atoms bound in such molecules cannot be released inside an electron beam without the deposition of a significant amount of immobile carbon contamination on the sample surface, which is not the case here [22, 171]. This allows to conclude that the oxygen mainly originates from water residues adsorbed on the sample, introduced during transfer from the synthesis facility to the microscope. Dependent on the adsorption energy between water and the surface material, significant amounts of adsorbed water can even be present under high-vacuum conditions of typically 10^{-5} Pa in the column of a TEM [172]. Water molecules are dissociated either by radiolysis in the electron beam or in contact with low-coordinated Ni atoms [173, 174]. See Figure 4.11 for an illustration of the proposed processes.

1. *Direct dissociation:* Water molecules are dissociated directly in an electron beam via a series of excitation and ionization of H_2O and its decomposition products. During this radiolysis process, oxidative species like OH^- and O^{2-} are produced. Although, dissociation of water molecules can also be caused directly by elastic displacements of oxygen and hydrogen atoms, ionization processes are highly dominating [175]. The probability for a dissociation event is hence higher at lower primary electron energies and decreases roughly with the square root of the energy [176].
2. *Indirect dissociation:* Water is not dissociated on flat Ni(111) or NiO surfaces, while at low-coordinated Ni atoms at edges, steps and atomically corrugated surfaces (e.g. Ni(110)) it dissociates irreversibly forming H_2 and NiO [173]. Accordingly, H_2O molecules can get dissociated at surface defects, which are produced by interaction with incident electrons.

While hydrogen leaves the sample area after dissociation, oxidative species now become available for the oxidation of Ni atoms.

4.2.1.5. Estimation of the Cluster Size and the Oxidation Rate

As described in section 3.4.1, supported clusters show a truncated Wulff shape. Since the amount of flattening is unknown in case of our particles, the extraction of volumetric information from projected images, as obtained in STEM imaging, is challenging. Novel techniques like electron tomography, single particle reconstruction or Z-contrast quantification provide 3-dimensional information on the atomic scale but make additional demands on the stability, the symmetry or the orientation of the clusters [4, 5, 7]. In a beam sensitive system, like that of Ni clusters supported by amorphous carbon, none of this criteria is fulfilled. Therefore, we developed a technique to estimate the size of supported Ni clusters by single STEM HAADF images, which is described in the following. To allow this we obtain a theoretical model for our molecular dynamics code for these clusters and adjust it according to quantitative EELS measurements.

Determining the Shape of Supported Ni Clusters: In order to get as realistic configurations as possible in our model, the clusters were generated randomly by placing atoms in a volume confined by the cluster radius, calculated from the number of atoms and the bulk density of Ni. This was done without support and should imitate the cluster aggregation inside the helium droplets (see section B.1 for the corresponding code listing). The atoms were placed with a normal distribution in radial direction, accounting for the minimum nearest neighbour distance of 2.44 Å in Ni. The clusters were then relaxed by simulated annealing within a Metropolis Monte Carlo simulation run with 5000 steps per atom. See section 3.3 for a description of the algorithm. At the beginning of the molecular dynamics simulation the clusters were then thermally equilibrated without support at 0.4 K, which is the approximate temperature of a superfluid helium droplet. After equilibration the clusters were landed on rigid amorphous carbon substrates. The latter was modelled by randomly distributed carbon atoms in a box with a thickness of 0.7 nm and a density of $2000\,\mathrm{kg\,m^{-3}}$. The clusters were landed with a velocity of $200\,\mathrm{m\,s^{-1}}$. After landing, the clusters were first heated to 800 K, to accelerate equilibration and finally equilibrated at 300 K. This process allows the thermal lattice vibrations (phonon modes) to be established for a certain temperature. Typically this process requires approximately 10 ps [177]. The corresponding code is given in section B.1. To estimate the projected area of the clusters, without performing a time consuming image simulation for every cluster, each atom was projected to the substrate plane with a Gaussian intensity distribution (assuming a FWHM of 100 pm of the corresponding electron beam). For a few clusters we compared the projected areas that were obtained by this method with full STEM HAADF multislice simulations to ensure the validity of our method (see 3.6). Deviations were within a ±5 % interval, with respect to the values gained from Multislice simulation data. Interactions between Ni atoms were modelled using the conventional Sutton-Chen potential (Eq. (3.27)) with $m = 6$, $n = 9$, $\varepsilon = 0.0157\,\mathrm{eV}$, $C = 39.432$, $a = 0.352\,\mathrm{nm}$. For the Ni-C interactions a pair potential of the Lennard-Jones type was chosen (Eq. (3.34)). An Andersen thermostat with a frequency of 2 THz was used to control temperature. Only Ni atoms next to substrate atoms were considered by the thermostat to minimize perturbations of the system. For more details on the molecular dynamics simulations see section 3.2.

Cluster Size Determination: EEL spectrum image data was acquired for 68 clusters with diameters between 1.5 nm and 2.8 nm. The Ni $L_{2,3}$ edge and the low-loss range were recorded simultaneously in Dual-EELS mode, yielding the number of Ni atoms in each cluster via EELS quantification. To this end, background removal in the EEL spectra was performed by pre-edge power-law fitting and quantification was done by using a Hartree-Slater cross-section model within GMS. The projected area of each cluster was obtained from an HAADF image, acquired before spectra acquisition. The dose was kept as low as possible to minimize beam damage effects. Due to the limited signal-to-noise ratio, the threshold for particle detection was set manually for each single image. The projected area A of each particle was then plotted as a function of the number of atoms N. The plot is given in Fig. 4.12). This data set was compared to molecular dynamics simulations of supported clusters within the same size range from 200 to 1200 atoms and we found reasonable agreement. For each cluster size up to 3000 atoms, 5 simulation runs were performed and a power law function was fitted ($A \propto N^{\frac{2}{3}}$ for a spherical symmetry). The obtained fitting function was then used to extract volumetric information from the projected images of Ni clusters before oxidation. It should be noted that we rely on the assumption that the cluster shape is only determined by the thermodynamic equilibrium and kinetic effects can be neglected. This assumption seems reasonable due to size of the clusters and their initially spherical shape. However, especially for larger clusters the simulation results are a lower limit for the area values, because diffusion based equilibration processes cannot be addressed by molecular dynamics simulation due to their long time scale.
Following this procedure the projected area of the clusters as a function of their size was obtained (Figure 4.12). From Figure 4.6a the number of Ni atoms for the three clusters was estimated to be 3000, 1800 and 1100 atoms for particle 1, particle 2 and particle 3, and the oxidation rates were 430, 500 and 611 atoms s^{-1}, respectively. The higher rate for smaller particles complies with the Cabrera-Mott oxidation theory corrected for spherical symmetry [161, 163].

4.2.1.6. Electron Energy Dependency of the Oxidation Kinetics

Experiments were also performed with 60 keV electrons, in order to study the influence of the electron energy on oxidation kinetics. A STEM HAADF time lapse series consisting of 140 images was acquired over a cluster on amorphous carbon support and the projected area change was compared with the similar sized particle 2 from Figure 3 in the main paper. Results are given in Figure 4.13.

Elastic beam damage effects are decreased at 60 keV, resulting in reduced area variations. The morphological change proceeds much faster at lower electron energy. This indicates that radiolysis seems to be the dominating water dissociation mechanism (1. in Figure 4.11). In

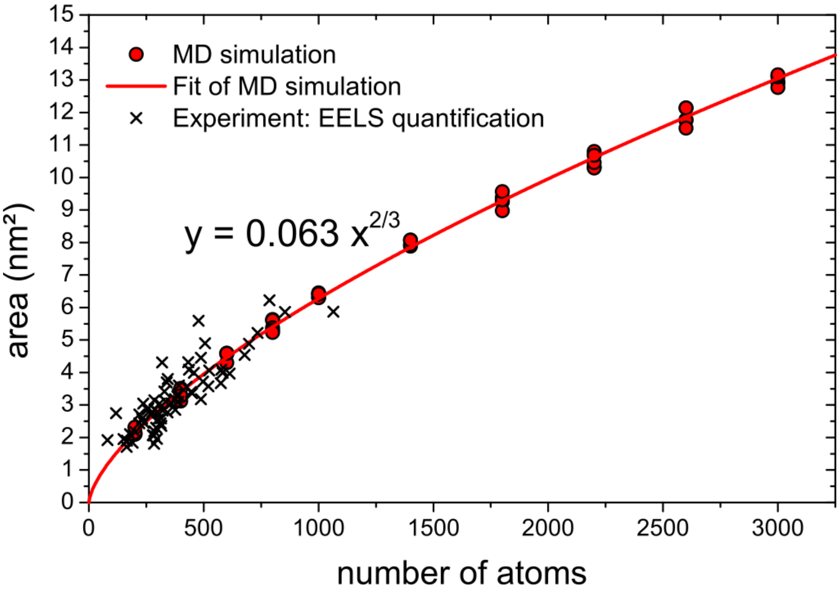

Figure 4.12.: Plot of the projected cluster area as a function of the cluster size in number of atoms. EELS quantification results are compared with MD simulations with a power law fitted to the MD data.

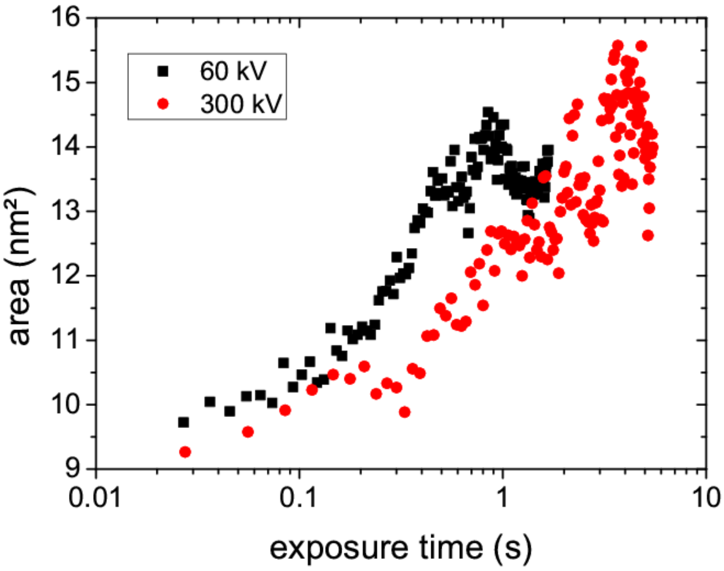

Figure 4.13.: Comparison of the areal growth of 2 clusters with similar size supported by amorphous carbon at different electron energies (60 kV and 300 kV, probe current I_P = 80 pA).

this case the oxidation rate has a value of 2250 atoms s^{-1}, compared to 500 atoms s^{-1} obtained from particle 2 at 300 kV.

4.2.1.7. Dissociation of Adsorbed Water in the Electron Beam

We found that the amount of oxygen on the TEM substrates decreases during electron beam exposure. In Figure 4.14 the O K edge signal from a time resolved EELS analysis is given. While constantly scanning over an empty substrate area (93 nm²), every 10 s an EEL spectrum was acquired.

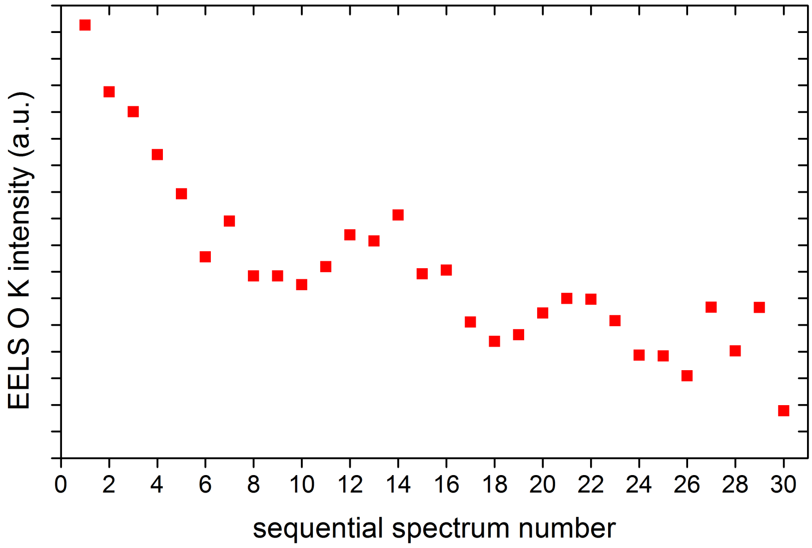

Figure 4.14.: EELS O K edge signal as a function of the spectrum number (IP = 80 pA, E = 300 keV), acquired from an empty substrate area.

This indicates that, without Ni present, adsorbed water is dissociated by incident electrons and leaves the sample area to the microscope vacuum, which results in a decrease of the O K signal over time.

4.2.1.8. Elemental EELS Analysis During Oxidation

To obtain more information about the source of oxygen for the transformation, a EELS time series integrated over the complete imaged area, including both the particle and the substrate, has been acquired. Comparison of the Ni $L_{2,3}$ and the O K edge intensities taken from such time resolved EELS data shows that the amount of nickel does not change significantly during the whole oxidation process, whereas the amount of oxygen slightly decreases. Figure 4.15b shows a plot of the edge intensities over the consecutive spectrum number and in Figure 4.15a four exemplifying STEM HAADF images, acquired simultaneously to the EELS time series, can be seen.

The slightly decreasing O K signal indicates that not the complete amount of oxygen adsorbed within this area is finally bound in the NiO cluster and can thus leave the sample to the vacuum. It should also be noted that the clusters are deposited on only one side of the substrate, whereas adsorbed water can be found on both sides. Hence, on the empty side oxygen released by

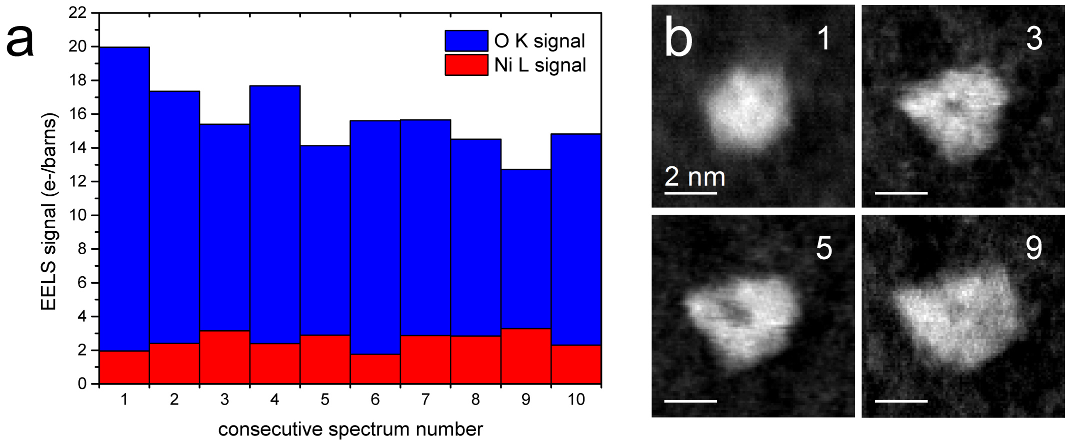

Figure 4.15.: EELS time lapse series; at every time step an EEL spectrum was acquired, integrated over the whole acquisition area of 106 nm^2 in (b) including particle and substrate, over an integration time of 10 s. (a) Plot of the Ni $L_{2,3}$ and O K EELS edge intensities, after background subtraction, as a function of the consecutive spectrum number. (b) HAADF images recorded simultaneously to the EELS time series

incident electrons can leave the sample area (similar to the situation in Figure 4.14). Oxidation of the amorphous carbon support can also be expected which would compensate this decrease to some extent. These results indicate that the majority of oxygen needed for the oxidation is initially adsorbed adjacent to the cluster.

4.2.1.9. Role of the Microscope Vacuum

The conclusions drawn from experimental data (Figure 4.15) are supported by simple considerations using statistical physics. We assume a hemispherical cluster with a diameter of 5 nm, which is exposed to the microscope vacuum. The incident molecular flux of an ideal gas on a surface is given by the Hertz-Knudsen formula (Eq. (4.2)).

$$\Phi = \frac{\alpha \cdot P}{\sqrt{2mk_BT}} \tag{4.2}$$

With p being the gas pressure in the microscope column ($p = 10 \times 10^{-5}$ Pa), m the mass of a gas particle, T the Temperature (300 K), α the sticking coefficient and k_B the Boltzmann constant. This results in a flux of $\Phi = 2.7 \times 10^{17}\,m^{-2}\,s^{-1}$ using the molecular mass of O_2. The surface area of a hemispherical cluster with a diameter of 5 nm, exposed to the microscope vacuum, is approximately 40 nm^2. This results in 11 gas molecules hitting the cluster per second. Such a cluster would consist of approximately 3000 nickel atoms. Even in the worst case, if every residual gas molecule in the microscope vacuum was O_2 and every collision led to an oxidation of two Ni atoms ($\alpha = 1$), the whole oxidation process would take 137 s, which is a lot longer than the time spans we observed in our experiments. Usually, the relative oxygen concentration of the residual gas in high-vacuum systems is rather low and the sticking coefficient α for O_2 on Ni and NiO is significantly less than unity [178]. Full oxidation would therefore take even more time. Hence, the influence of the residual molecular oxygen in the microscope vacuum can be neglected for our considerations.

4.2.1.10. On the Determination of the Oxygen Content Via HAADF Quantification

This interesting question arose during a discussion with a reviewer from Nanoletters. The idea of quantifying the oxygen content of a cluster via its HAADF intensity was tested on our data sets without success and was therefore abandoned. Here we list some reasons, why it had to fail in our case. The HAADF signal is strongly dependent on the atomic number Z ($I \propto Z^2$, in case of Rutherford scattering). See 3.1 for more details on elastic scattering theory. For incoherent imaging conditions the detected HAADF intensity is (roughly) the sum of all contributing atoms ($I \propto Z_1^2 + Z_2^2 + Z_3^2 + \ldots$) [2]. In principle this information can be used to quantify the number of atoms in a confined volume, which has been shown recently [4, 38]. Due to the Z^2 dependency of the HAADF intensity, however, the probability for elastic high angle electron scattering is much lower for an oxygen atom ($Z = 8$) compared to a nickel atom ($Z = 28$). This was confirmed by multislice simulations (Figure 4.16) using QSTEM. Thereby, it can be shown that for standard HAADF imaging conditions (semi-detector angle 60-200 mrad) the signal detected from a single oxygen atom is lower by a factor of approximately 10. In order to distinguish a pure Ni cluster from its fully oxidised state an overall intensity increase of only about 10 % needs to be detected. The situation becomes even worse if influences like changes in cluster orientation, Ni surface sputtering and oxidation of the underlying substrate must be considered in experiment. These difficulties render this method highly ineffective for the quantification of the oxygen content in a Ni cluster during the whole oxidation process. This holds true especially with the limited signal to noise ratio obtainable in such experiments.

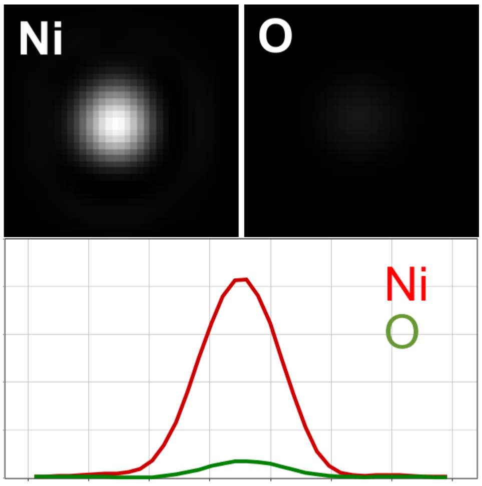

Figure 4.16.: Simulated HAADF intensity of a single nickel atom compared to that of an an oxygen atom. The corresponding intensity profiles illustrate the large discrepancy of the detectable signal.

4.2.2. Electron Beam Induced Oxidation of Ag

Electron beam induced oxidation was also observed in the case of silver. In the presented case we characterised Ag nanowires under liquid nitrogen temperature (cryo-TEM) in an FEI T12 operated at 120 keV. The whole synthesis process was done in cooled environment and the sample was kept in liquid nitrogen (with a boiling point of $-195.8\,°C$) until introduced into the microscope. At this temperature it is inevitable that water vapour from the ambient air condenses on the sample surface, forming a thin layer of ice. Radiolysis of this ice by incident electrons releases significant amounts of oxygen radicals, which react with silver atoms on the cluster, under formation of silver oxide (most likely Ag_2O, the most stable oxide of silver). Bright field TEM micrographs in Figure 4.17 show the conversion process.

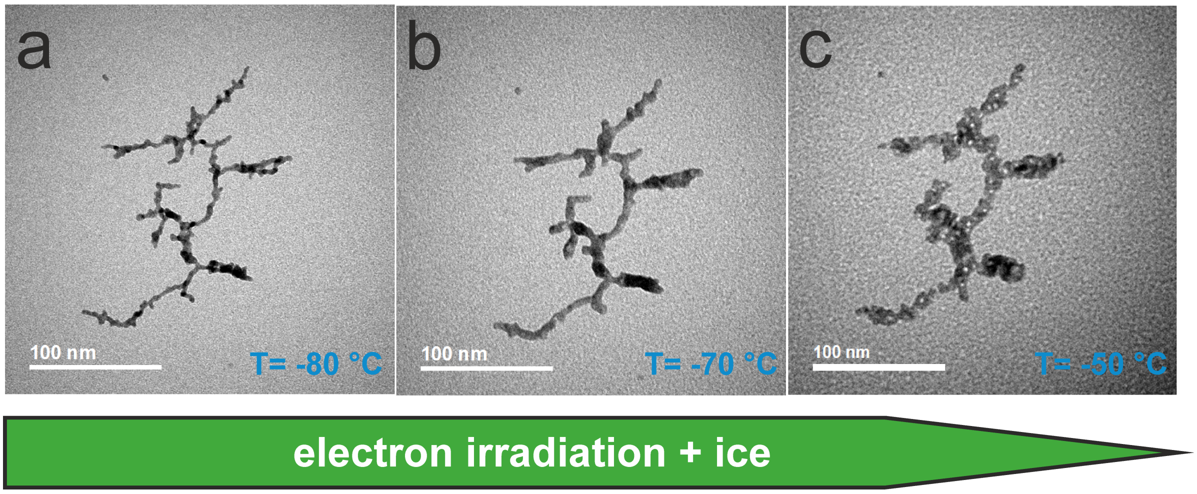

Figure 4.17.: Transformation of a Ag nanowire under parallel electron beam irradiation at Cryo conditions.

It is remarkable that in this experiment the hollowing effect was only observed above a certain temperature of approximately $-80\,°C$. That could be explained with the limited mobility of atoms and radiolysis products at lower temperatures. We believe that oxidising radicals, created by the electron beam, cannot reach the cluster surface in a sufficient amount at lower temperatures.

The mechanisms for the oxidation process are similar to those in the case of nickel, that was described in more detail in the previous section 4.2.1. Although, compared to Ni, the difference in ionic radius is smaller between Ag^+ (128 pm) and O^{2-} (140 pm) [59], the diffusion of Ag in Ag_2O still proceeds faster. This gives rise to the Kirkendall hollowing effect, that can be observed during oxidation. The Pilling-Bedworth ratio for Ag_2O can be calculated according to Eq. (4.1) and gives a value of 1.58. Therefore, a slightly lower volume increase is expected, compared to the oxidation of Ni to NiO.

After these findings we came up with the idea of using a focused electron beam to structure Ag nanowires in a controlled manner. The question was if it could be possible to use the ice that is adsorbed on the sample surface to trigger an oxidation very locally. A first proof of concept is given in Figure 4.18. In this experiment the microscope (FEI Titan) was operated in scanning mode at 200 keV. The clusters were synthesised and analysed under cryo conditions.

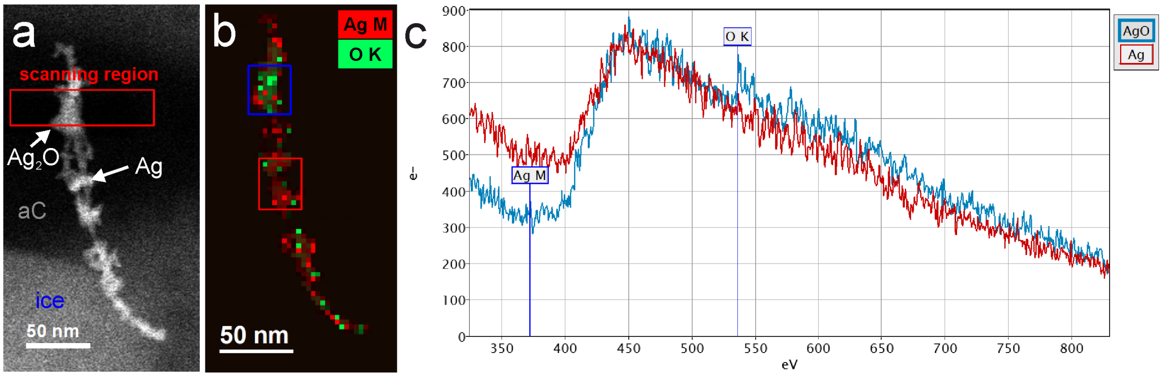

Figure 4.18.: Local triggering of a oxidation using a focused electron beam: (a) HAADF image of the particle and the region in which the electron beam was constantly scanned for approximately 30 s. (b) EELS elemental map which shows a significant higher oxygen content in the irradiated region (blue) compared with a untreated region (red). The corresponding spectra are depicted in (c)

The beam was scanned over a certain area, which was defined by an focus window. During oxidation the beam current was set to approximately 130 pA, according to the screen current measurement. For elemental analysis the current was lowered to < 40 pA in order to reduce the oxidation speed during EELS acquisition. In Figure 4.18a it can be seen, that the structural change in the irradiated region is accompanied by an increase of the oxygen content which clearly indicates an oxidation effect. To prevent initial oxidation during scanning no image of the initial state cluster has been acquired. The ice layer is removed by electron beam scanning very rapidly. In the lower part of the HAADF image in Figure 4.18a residual ice can be seen. Note that close to the scanning region also the amorphous carbon support is completely removed. Presumably, substrate atoms are oxidised too in the electron beam, forming CO and CO_2 molecules, which leave the sample surface to the microscope vacuum. Thereby, we end up with a free hanging nanowire that is attached on the remaining carbon film. It should also be remarked that after the spectrum image was acquired, the ice layer has been completely removed within this area. The majority of the oxygen signal that was found outside the scanning region can therefore be addressed to this residual ice layer and oxidation during SI acquisition.

Interestingly, in contrast to Ni and also to previous TEM experiments with Ag nanowires, no beam induced hollowing can be observed. Possibly, this can be explained with the smaller difference in the ionic radius between Ag and O in Ag_2O, due to the increased dose rate and the higher electron energy compared to previous experiments in the T12. We would also expect that beam induced displacement effects are more likely at the present conditions (aberration corrected STEM@200 keV with an X-FEG in the Titan compared to TEM@120 keV with an LaB_6 cathode in the T12). Faster diffusion and less pronounced hollowing could be the consequence. Under these conditions Kirkendall voids are quickly destroyed and can never accumulate to a single, growing void inside the particle. A similar behaviour can be observed with Ni, when the dose rate is chosen to high (see section 4.2.1).

4.3. Elemental Analysis of Bimetallic Clusters and Nanoalloys

While in the preceding section the results for experiments on monometallic clusters were presented, this chapter will be devoted to elemental and structural analysis on bimetallic clusters. In general, bimetallic nanoparticles are comprised of two different metals and show novel electronic, optical and catalytic properties compared to their pure compounds [10, 179]. For example, Au nanoparticles are highly interesting for heterogeneous catalysis, for instance for the hydration of CO_2 for the synthesis of methanol or for the oxidation of CO to CO_2 [180, 181]. In order to increase the catalytic activity of Au particles in oxidation reactions, their poor affinity to oxygen need to be increased. To this end Ag can be added to the Au nanoparticles, for example [181]. Understanding the mixing behaviour of Au and Ag on the nanoscale is therefore of paramount importance.

The structure of supported bimetallic nanoparticles is dependent on a vast amount of factors, such as the stoichiometry, the relative strengths of the intermetallic bonds, bonding distances, surface energies, atomic sizes or the metal-support interactions. They can be configured in a random alloy, an alloy with an intermetallic compound, or in different core–shell and Janus shapes.

Furthermore, one of the primary goals was to obtain information about the cluster growth inside the helium droplets, which is still not well understood. Analyses of the particle shape and structures allow conclusions to be drawn about the properties of a superfluid droplet [21, 24]. One of these properties is the occurrence of quantum vortices. This is one of the most interesting phenomena in context of superfluidity. Above a critical angular velocity one or more of these quantum vortices are formed inside the droplets. Dopant atoms and clusters then prefer to reside at vortex sites and aggregate to elongated structures, which can then be soft-landed on arbitrary substrates. TEM investigation of such structures provided the first evidence for the existence of quantum vortices in sufficiently large ^{4}He-droplets. Recently, this method has been introduced as a preparation technique for quasi one-dimensional nanostructures [21, 23].

To be able to control the size, shape and elemental distribution of the particles, generated with the superfluid helium droplet technique, not only the formation process inside the droplet needs to be understood. We also need to consider the interaction between the particles and the substrate and thermodynamic equilibration processes after the deposition. An interesting question in this context is whether a sequential pick-up scheme inside the apparatus leads to the formation of core-shell particles, where the elemental configuration corresponds to the pick-up sequence (see figure 4.19). To this end elongated Au-Ag nanostructures were investigated in the following.

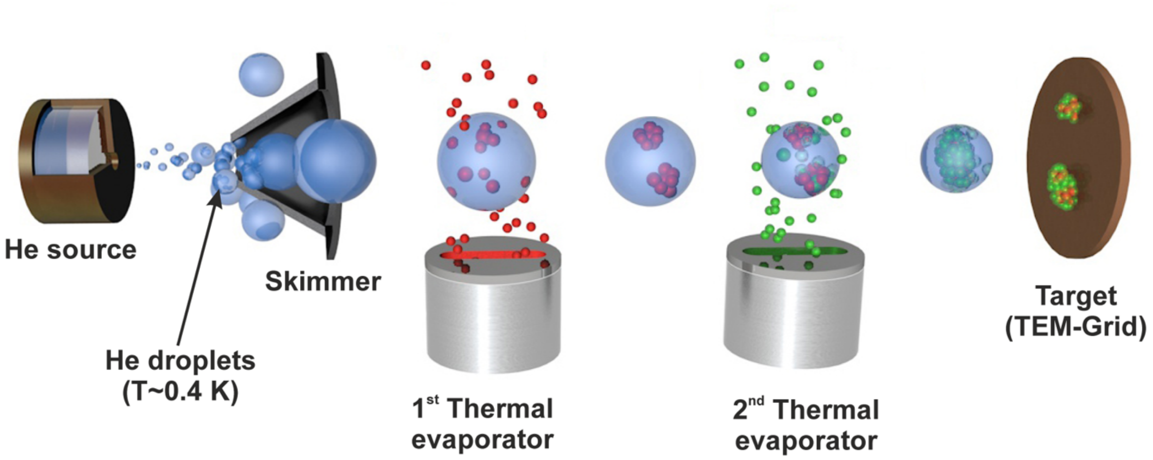

Figure 4.19.: A beam of superfluid He-droplets (blue) is generated by expansion through a cooled nozzle. After passing the skimmer they sequentially collide with atoms of the first species (red) and the second species (green) both evaporated by thermal evaporators. The particles congregate in the centre of the droplet and finally land on the target (e.g. a TEM-grid), the sequence of the thermal evaporators influences the morphology of the clusters that are finally obtained

4.3.1. The System Au-Ag

Ag and Au have been chosen as precursor materials not only because the interesting properties of Ag-Au clusters but also because this material combination is well suited as marker to study the cluster formation process inside a superfluid He-droplet. Both have the same face centred cubic lattice structure with very similar lattice constant, being 408 pm for Au and 409 pm for Ag [59]. Thus Au and Ag are fully miscible and it is difficult to keep both phases separated on nanometer length scales with conventional preparation techniques. There is some theoretical evidence, found with a EAM potential and Monte Carlo techniques, for the formation of onionlike structures with a Ag-rich shell for smaller particles at lower temperatures [182].
Another useful property of Au and Ag is that both elements are chemically relatively inert and do hardly oxidise in air, or react with the carbon support within time spans that are relevant for our experiment. The formation of Janus particles from initially alloyed AuAg nanoparticles has been reported within a time span of 2 years, due to slow oxidation of silver [183]. From the microscopist point of view the material combination is advantageous because of the high Z difference between Au ($Z = 79$) and Ag ($Z = 47$). Hence, it should be feasible to distinguish both phases via HAADF contrast. However, element sensitive STEM provides more detailed information about the elemental distribution and is needed to be able to exclude HAADF contrast changes due to thickness variations. Such thickness variations can obviously be expected at the border regions of particles with spherical cross sections but also at junctions were 2 clusters aggregated inside a droplet.

4.3.1.1. Experimental Details

To allow the formation of elongated clusters comprised of several thousand atoms the He droplets need to be large enough. This is because the formation of atoms to a cluster releases energy that results in the evaporation of He atoms. Furthermore, the droplets need to be large enough to contain a sufficient amount of vortices. To this end, He was expanded into vacuum with a pressure of 20 bar through the nozzle that was cooled below 6 K in this case. These parameters lead to an exponential droplet size distribution with an initial mean of 3×10^8He atoms, which corresponds to a mean droplet diameter of approximately 300 nm. The temperature of the evaporators is another crucial parameter for the obtained cluster size. They were chosen close to the melting points of Ag and Au with values of 1235 and 1337 K, respectively [59]. The target composition of the clusters was Ag:Au 50:50 at.%. That was controlled by the attenuation of the He-beam which was determined with a quadrupole mass spectrometer. The doping level was set to about 50 % of the He atoms in a droplet being evaporated upon pick-up.

The analysis was performed by using our FEI Titan microscope. The beam current was set to approximately 50 pA throughout this experiment. This seemed to be a good compromise between the requirement to reduce beam damage effects during long spectrum image acquisition times (up to 30 min for a complete spectrum image) and signal-to-noise ratio of obtained data sets (see section 3.1 for more details). The clusters were deposited on commercial TEM grids with a copper mesh (mesh size 300) baking a 3 nm thick amorphous carbon layer (Ted Pella, Inc., Prod. No. 01824) The mesh size corresponds to a pitch size of 85 µm (=25.4 mm/300) and a hole size of 54 µm.

Figure 4.23 and 4.21 show Ag@Au and Au@Ag core-shell particles, respectively with corresponding elemental maps. To obtain a silver map either EDX (Ag L) or EELS (Ag $M_{4,5}$) has been used. Both techniques give similar results although EELS gives a much better SNR. To separate the Ag $M_{4,5}$ edge located at 367 eV energy loss from the large tail of the C K edge at 282 eV multiple linear least squares (MLLS) fitting was used, as implemented in Digital Micrograph (DM). MLLS fitting finds the best representation of a given spectral data set by using reference spectra. Two carbon references were chosen from the data set, one for the amorphous carbon support and one to account for carbonaceous contamination. The reference for the MLLS fit for Ag was taken from the EELS atlas that is also included in DM.

For Au only EDX (M + L peaks) can be used. Au is not accessible with EELS in beam sensitive specimens, due to the high energy loss of the M edges (>2200 eV) and the weak low energy edges below 100 eV, that are obscured by the background. For more details on using thin h-BN supports for the elemental characterisation of Au clusters using EELS see the previous section 4.1.2.

The elemental composition for each cluster was determined by means of EDS quantification using the Cliff-Lorimer k-factor approach. Theoretical k-factors based on the Casnati cross-section parametrization have been used, as implemented in DM [184, 185]. The background has been removed using both the Kramer's background model and top-hat filtering (see section 2.4 for more details). Results have been cross checked for consistency. The quantification has been done by using the Au M (M_α@2.12 keV) and the Ag L (L_α@2.98 keV) peak families, because of their similar energies. Influences of energy dependent effects (e.g. absorption in sample or specimen holder, detector efficiency) on the quantification result can thereby be minimised [45]. The Au L (L_α@9.71 keV) peak family has been used to verify results. The k-factor values that were used relative to Si K were 1.7, 4.0 and 3.0 for the Ag L, Au M and Au L intensities respectively. Since theoretical k-factors may have systematic errors, results were also validated with k-factor values that were extracted from the Bruker Esprit software package (2.9 for Ag L and 4.9 for Au M).

4.3.1.2. Size, Morphology and Elemental Composition

The length of the clusters was about 30 nm average. The thickness, as seen in projection in the micrographs, was between 5 to 10 nm. Besides linear nano wires also kinked and branched particles have been observed. These shapes indicate the presence of multiple vortices inside the droplet. Overlapping of subsequently deposited linear nano wires can be excluded, due to the low coverage and the high contrast in HAADF that can be expected in overlapping regions, caused by large thickness variations. A cross section of the diversity of possible cluster morphologies is shown in Figure 4.20 for both Au@Ag (a) and Ag@Au (b) particles.

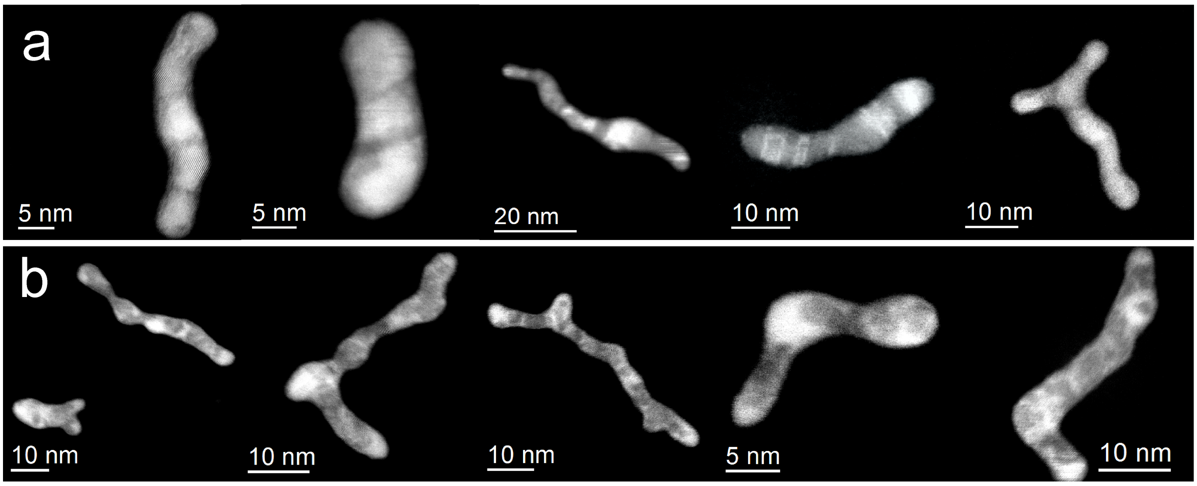

Figure 4.20.: HAADF images of different particles with Au@Ag (a) and Ag@Au configuration (b), respectively.

Au@Ag Particles: In first experiments the sequence of the thermal evaporators in the pick-up chamber was chosen so that first Au was picked up by the droplet followed by Ag. Accordingly, an Au@Ag core-shell structure was expected. Figure 4.20a shows images of some particles. Bright contrast areas in the HAADF images suggest the presence of multiple Au cores, completely covered by dark Ag rich regions. This is also confirmed by the elemental maps. In Figure 4.21 exemplary two clusters are shown, together with corresponding elemental maps. Several bulging parts with constrictions in between can be seen along the wires, which suggests a multicenter growth process inside the droplet. It seems that the Au wire growth along the vortex is not completed until the droplet starts to pick-up Ag atoms. Single spherical core-shell particles are formed before they align along the vortices and start to built up a wire. Remarkably, we found a relative silver content x_{Ag} of 0.2-0.3 (20-30 at,%), by using quantitative EDXS. This is significantly below the expected value of 0.5, even if considering the large uncertainty with using theoretical k-factors. This could be the consequence of selective sputtering of Ag atoms from the particle surface, thus reducing their Ag content during spectrum image acquisition. This behaviour has also been observed in molecular simulations, as described in chapter 3.5. One EDXS quantification result is shown exemplary in Figure 4.22, together with the elemental map, the spectrum summed over the whole particle, and the corresponding fits for the the Au and Ag peaks and the background.

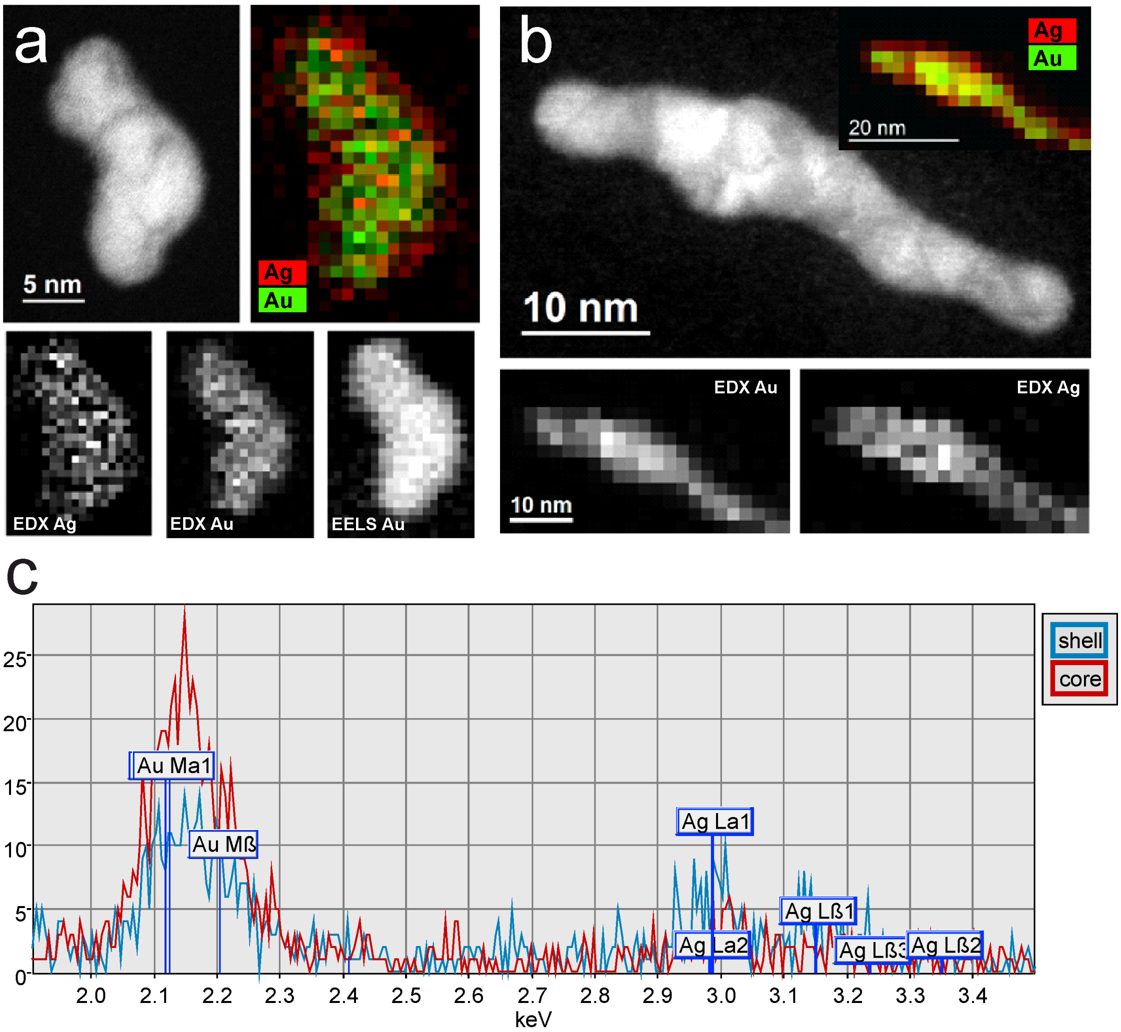

Figure 4.21.: (a) and (b): Two examples for Au@Ag core-shell particles with corresponding elemental maps using the Au L and M EDXS signal for Au and the Ag M EELS or Ag L EDXS signal for Ag respectively. (c) Extracted EDX spectra from the Au rich core compared to the Ag rich shell.

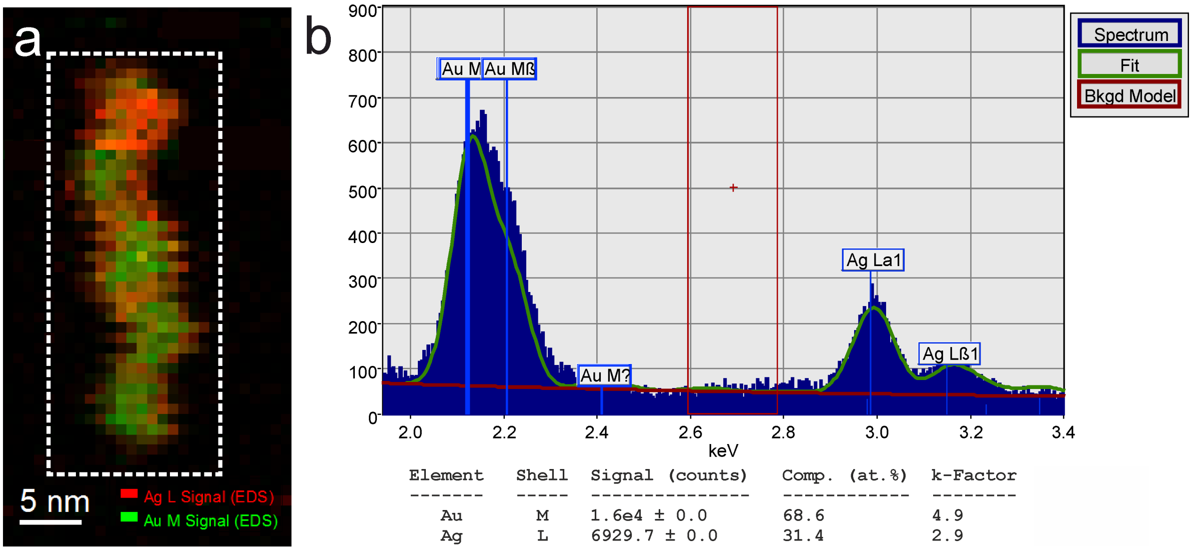

```
Element   Shell  Signal (counts)   Comp. (at.%)   k-Factor
-------   -----  ---------------   ------------   --------
  Au        M    1.6e4 ± 0.0       68.6           4.9
  Ag        L    6929.7 ± 0.0      31.4           2.9
```

Figure 4.22.: (a) EDXS elemental map using the Ag L and Au M lines. (b) EDXS spectrum summed over the region marked in (a) with corresponding quantification result using Kramers' background fit and the Casnati cross section model)

Ag@Au Particles: In the second experiment we reversed the pick-ups sequence, with Ag being evaporated first and Au second. Analogue to the first experiment we expected to obtain Ag@Au core-shell particles with this setup. Dark regions in the HAADF images depicted in Figure 4.23 reveal the likely presence of multiple Ag rich cores.

Interestingly, the core-shell structure is much less distinctive than it was in the case of Au@Ag in the elemental maps. The structures exhibit a complex sub-structure consisting of domains with varying elemental composition. These composition variations can also be found between different clusters. EDXS quantification gave values ranging from less than 0.1 up to 0.5 at.% for the Ag content x_{Ag} of the clusters. This suggests a non-homogeneous agglomeration of atoms inside the He droplet. Ag atoms may not have enough time to align completely to particles and wires inside the droplets before they reach the second evaporation chamber. Remarkably, no cluster with a higher Ag content than 0.5 at.% was found.

However, we have to note that only a few datasets could be analysed for each material combination Au@Ag and Au@Ag. Therefore, especially the EDXS quantification results are not representative for all clusters and cannot be compared directly with mass spectrometry data, that gave an average composition of almost $\mathrm{Ag}_{0.5}\mathrm{Au}_{0.5}$ for both Au@Ag and Au@Ag.

Summarizing, for both experiments bulged nano wire structures were observed with multiple centres comprised of the first element picked-up by the He droplet. The results suggest that the wire formation of the first element has not been completed before the droplet reaches the second thermal evaporator. As a result, core-shell particles are formed before they form a wire along the vortices. The liquid He-environment ensures that the binding energy that is released during cluster formation is quickly dissipated and thus prevents the alloying of the two materials. Therefore this synthesis technique could also be interesting for future in-situ studies of alloying processes.

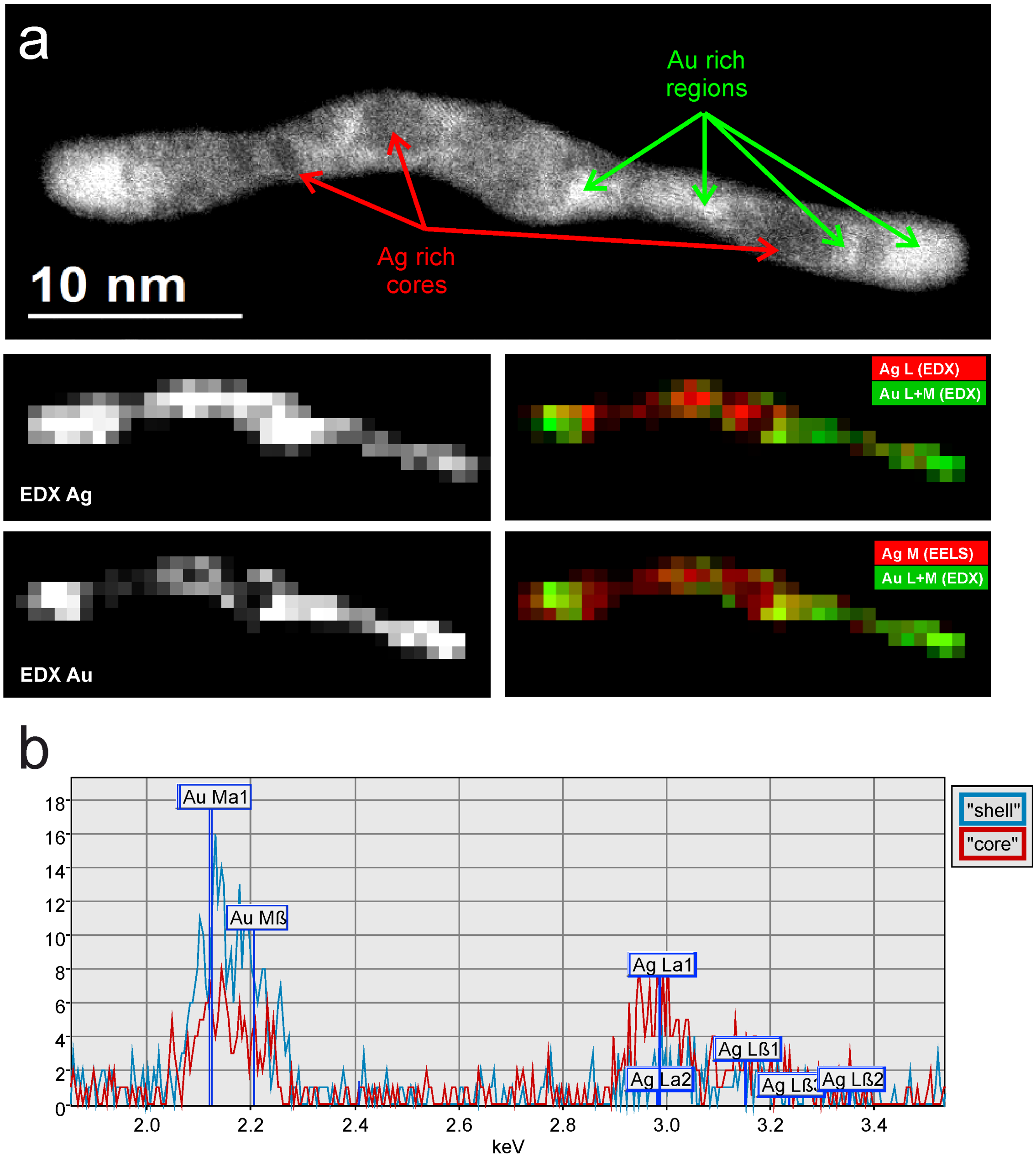

Figure 4.23.: (a) Au@Ag core-shell particle with corresponding elemental maps using the Au L and M EDXS signal for Au and the Ag M EELS or Ag L EDXS signal for Ag respectively. (b) Extracted EDX spectra from the Au rich core compared to the Ag rich shell.

Some of the results presented here have been published in a collaborative paper [132]. Sample preparation was done by Philipp Thaler and Alexander Volk. Electron microscopy analysis was performed by Daniel Knez. The data was interpreted by Philipp Thaler, Alexander Volk and Daniel Knez. The manuscript has been written by Philipp Thaler with contributions from all authors.

4.3.2. The System Ni-Au

The system Ni-Au has a relatively simple phase diagram but highly interesting thermodynamic properties [186]. It exhibits a miscibility gap at low temperatures for all Ni/Au ratios. Figure 4.24 displays a phase diagram of the bulk Ni-Au system from [187].

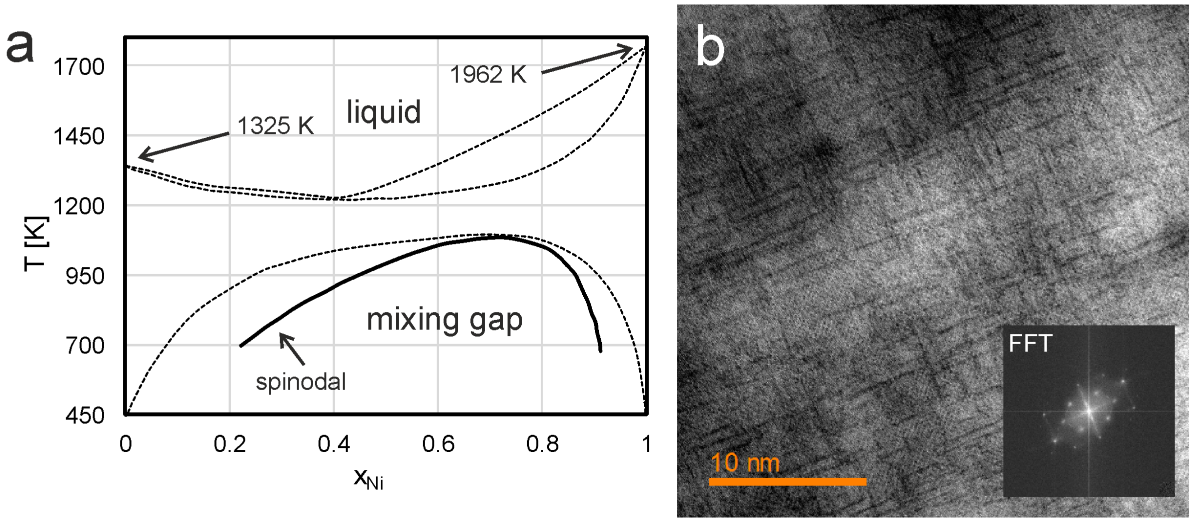

Figure 4.24.: (a) Experimental phase diagram of bulk NiAu (reproduced from [187]). The spinodal was reproduced from Hofer [188]. (b) STEM HAADF image of a NiAu sample with a mean Ni content of 30at.%, aligned in [1,0,0]-orientation. Typical periodical concentration variations due to spinodal decomposition can be seen. Ni rich regions appear darker. The inset shows an FFT of image. (sample homogenised at 850 °C and aged at 150 °C for 10 h, TEM sample preparation via electropolishing according to [188])

In principal the solubility of two metals can be assessed by applying the empirical Hume-Rothery rules [189]. Accordingly, a solute is expected to have a high solubility in a host metal if the following criteria are fulfilled:

1. The solute has a similar crystal structure.
2. Its atomic radii differs by less than a factor 1.15.
3. The difference in electronegativity between solute and host is small.
4. The solute has a lower valency than the host.

Both Ni an Au crystallise in the same, face-centred cubic, crystal structure. The size difference between the atomic radii of Ni and Au is slightly above 15 % (r_{Au} = 1.46 Å, r_{Ni} = 1.24 Å [59]). This results in a lattice mismatch between the Ni and the Au lattice ($a_{0,\text{Ni}}$ = 3.524 Å, $a_{0,\text{Au}}$ =

4.079 Å [59]). This mismatch again results in a positive contribution to the formation enthalpy, and thus contributes to the miscibility gap in the phase diagram at lower temperatures. For the electronegativity we find 1.91 for Ni and 2.54 for Au in literature. This difference contributes negatively to the mixing enthalpy. These two contributions with different signs result in phase separation in the long range at low temperatures and short range ordering at higher temperatures. Moreover, there is a also a significant positive entropy contribution to the Gibbs energy due to changes in the phonon modes during alloy formation, which also contributes to the miscibility gap [190].

Due to these different contributions the thermodynamic behaviour of this system is very interesting and has been studied in several papers [186, 188, 190–193]. The competition between ordering and phase separation leads to spinodal decomposition in the bulk. Periodic concentration variations are formed when the homogenised Au rich crystal is aged within the miscibility gap, as shown in Figure 4.24b.

In contrast very little is known about the behaviour of this system on the nanoscale. NiAu nanoparticles are also interesting from the application point of view. Being comprised of a ferromagnetic and a highly conductive material, they are studied for their magneto-optical properties, as well as for their application in heterogeneous catalysis [13, 194]. Although alloying is thermodynamically unfavoured at low temperatures, it was found that a stable surface alloy is build upon deposition of Au atoms on single crystalline Ni(110) and Ni(111) surfaces by scanning tunneling microscopy (STM) investigations [195]. In this work it was stated that there is a preference of an Au atom to be surrounded by 8 Ni atoms, which leads to surface alloying. There is also some theoretical evidence that this also occurs at the surface of NiAu nanoclusters [13]. This work also demonstrated that the catalytic activity of Ni particles can be preserved by NiAu surface alloying, during *n*-butane reformation.

To obtain more information about the thermodynamics of NiAu on the nanoscale we performed high resolution STEM imaging and *in situ* heating experiments.

4.3.2.1. Experimental Details

Similar to the AuAg experiments, bimetallic nanoparticles were synthesised by means of the superfluid He-droplet technique at the Institute of Experimental Physics at the Graz University of Technology. The two evaporators were configured in such a way that Ni@Au core-shell particles were obtained (Figure 4.19). The cluster morphologies and sizes largely depend on the He droplet size. To obtain a variety of clusters we used two different growth regimes. While the pressure was kept at 20 bar, the droplet size can be controlled by the temperature of the nozzle with which the droplet beam is formed (See Figure 4.19). Firstly, we aimed for a He droplet size of approximately 7×10^6 atoms. Spherical shaped clusters with a size of less than 10 nm are produced in such droplets. Secondly, a relatively large droplet size was chosen (approximately 1×10^8 He atoms) so as to allow the formation of larger particles. Since quantum vortices start to occur in this regime inside the droplets, the clusters start to agglomerate in elongated shapes (see previous section). If the droplets are chosen too large multiple Ni centres can aggregate, which has been avoided here. Thus we expect single Ni cores for smaller clusters. Both size regimes were deposited on the same substrate. The average composition of the clusters, that was measured with a quadrupole mass spectrometer, was 30wt.% Ni and 70 wt.% Au.

For *in situ* heating experiments we deposited the clusters on a heatable TEM substrate (DENSsolutions Nano-Chip XT carbon). These substrates consist of a 5 nm amorphous carbon film supported by a holey SiN_x film on a MEMS (microelectromechanical systems) chip, with a embedded heating spiral. The chips were baked out in vacuum at 300 °C to reduce contamination. For the actual experiments we used a DENSsolutions Wildfire D6 holder in our probe-corrected FEI Titan microscope, which was operated in STEM mode at 300 keV. The holder allows to control the substrate temperature very precisely. It is possible to reach every temperatures between room temperature and 1300 °C within a few milliseconds (with a heat and quench rate of $200\,\mathrm{K\,ms^{-1}}$).

4.3.2.2. Morphology

Figure 4.25 shows some STEM HAADF images of particles in their initial state. As expected, we found spherical and elongated morphologies, which presumably grew in smaller He droplets, as well as large NiAu structures with no distinct core-shell structure, from large He-droplets. In the smaller clusters it can clearly be seen that the bright contrast of the Au lattice is continued in the darker core of the particles. Therefore, we conclude that the core is completely surrounded by Au atoms.

Particles that were deposited with the largest droplet size were found to have elongated shapes with several kinks and branches. This has already been observed in other experiments with pure element particles as well as with bimetallic structures (e.g. AuAg, see section 4.3.1). The complex morphology of the structures indicates the presence of multiple quantum vortices inside large superfluid He droplets [132]. Overlapping of linear structures from several droplets on the substrate can be excluded due to the low surface coverage, as well as by the flat shape of the structures.

EELS analysis reveals that the Ni core does not contain oxygen in detectable amounts. Figure 4.26 demonstrates the absence of O in an EELS spectrum which has been extracted from the centre of a NiAu cluster. The corresponding HAADF image is given in the inset, with a yellow rectangle that marks the area from which the signal has been extracted.

Conclusively, the He droplet proved to be capable to produce stable core-shell Ni@Au clusters, with controllable morphologies. In smaller clusters the Au shell completely covers the Ni core and effectively hinders its oxidation. Larger clusters show more complex elemental distributions. To obtain information about the thermodynamic stability of the clusters we conducted heating experiments, which are described in the following section.

4.3.2.3. Heating Experiment

In the following we changed the substrate temperature step wise between room temperature and 400 °C. The temperature is measured 3 times each second. The heating profile is given in Figure 4.27b.

We imaged the same sample region repeatedly at each step over the full temperature range.

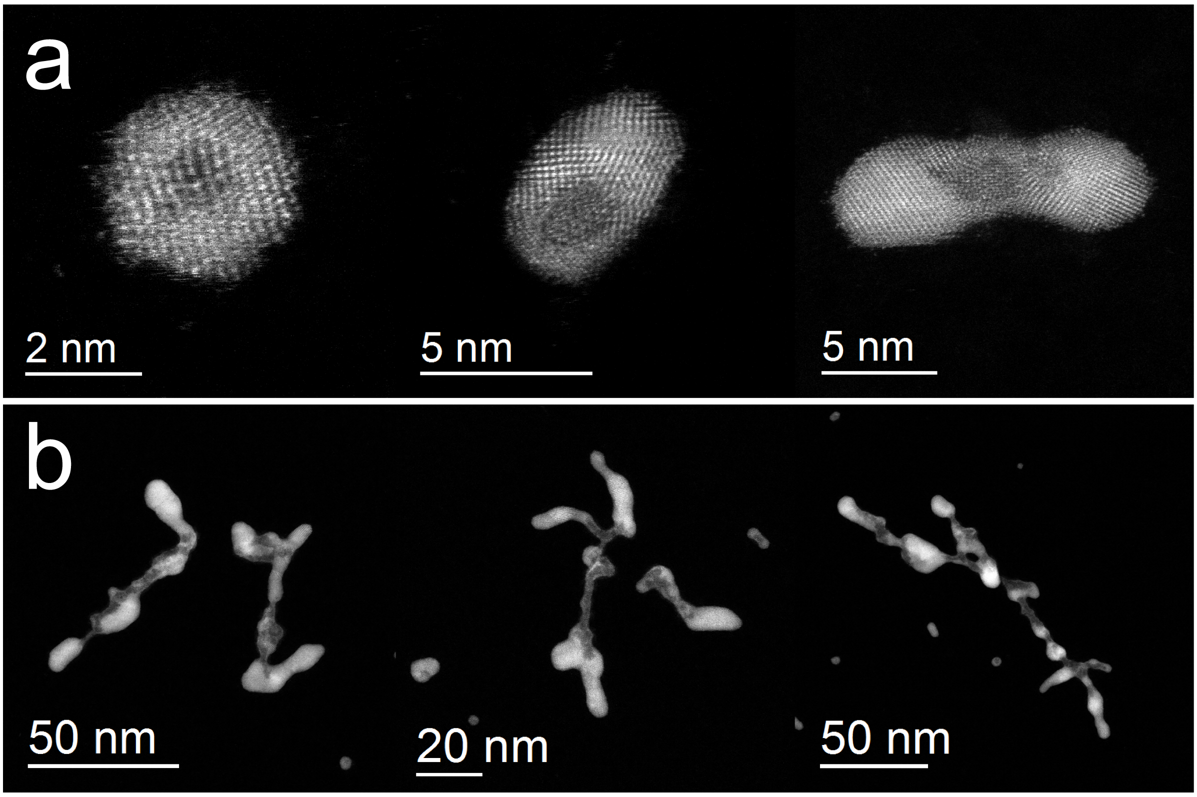

Figure 4.25.: STEM HAADF images of different NiAu clusters in their initial state, exhibiting a variety of morphologies: (a) Cluster grown in smaller He droplets; (b) examples for structures grown in large droplets.

For this we chose a region containing three particles with different sizes and morphologies. In order to decrease the influence of the electron beam we kept the current at ≈50 pA and avoided long exposures at high magnification. We acquired an image at each temperature step. HAADF images of the three clusters at different temperatures are shown in Figure4.27. From these images it can be seen that the Ni core shrinks with time and temperature and the particles transform from a core-shell morphology to an alloy. Interestingly the transformation appears to proceed faster the larger the particles. The large elongated particle looses its darker Ni core at around 200 °C, while it still can be identified inside the two smaller particles, even at 300 °C. Finally, at 400 °C, all three clusters were found to be alloyed. For the largest particle also a significant morphology change can be observed, from an elongated to a more spherical shape. This can be understood by the increased surface diffusion of atoms at the Au shell at elevated temperatures. That promotes the formation of new facets, which is necessary to overcome kinetic barriers [114] during surface energy minimisation (see 3.4.1 for further details).

Alloying effects can also be observed for large NiAu - structures as depicted in Figure 4.28 after heating. The HAADF contrast appears almost homogeneous, while Ni rich, darker and Au rich, brighter regions were clearly discriminable in Figure 4.25 before heating. However, high resolution HAADF imaging also reveals darker atomic columns with a presumably higher Ni content compared to neighbouring columns. Special attention should be given to the region marked with a red arrow. There, one bright column seems to be completely surrounded by

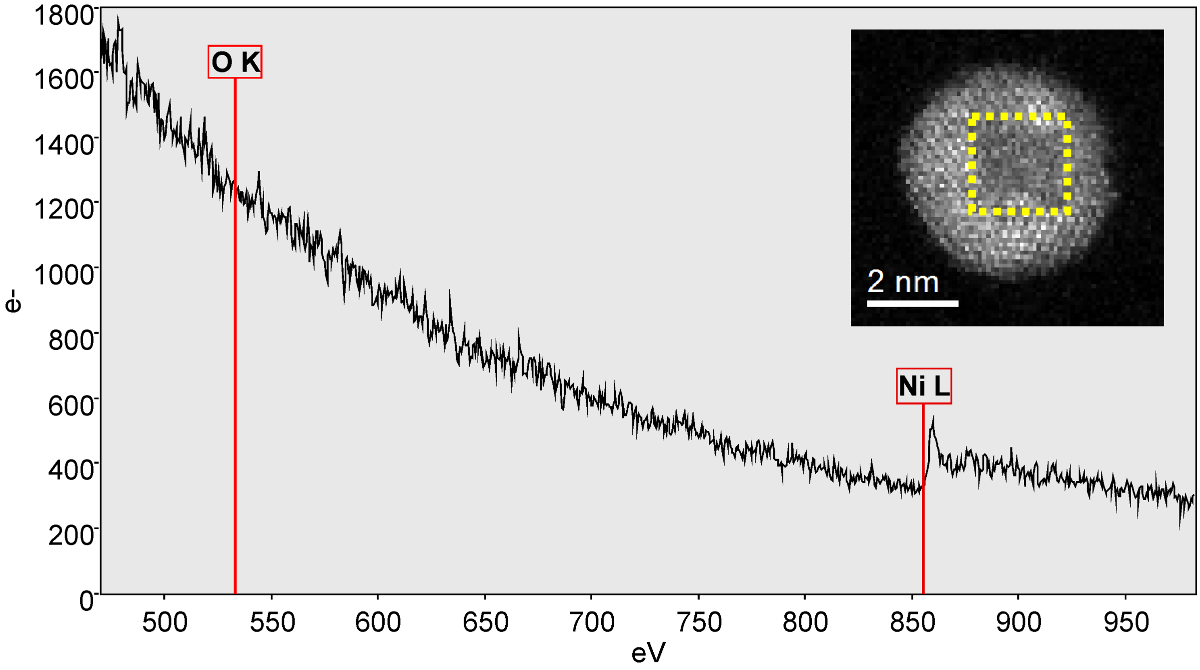

Figure 4.26.: EELS spectrum showing the presence of an unoxidised Ni core in the centre of the cluster. The inset shows an HAADF image of the cluster. The EEL spectrum was extracted from the region marked with a yellow rectangle in the inset (sum over 56 spectra, each with 0.1 s acquisition time, probe current 50 pA).

darker columns, which could indicate the existence of some kind of short-range ordering, similar to that in the bulk system. The red framed inset shows an FFT of the high resolution HAADF image in the main image. The rotational line profile of the FFT (yellow line) reveals a maximum at 4.3 Å^-1, which can be assigned to the (1,1,1) lattice spacing of Au ($d_{(1,1,1)}$ 2.35 Å). After short electron exposure during imaging the formation of NiO can be observed on the particle surface. Regions containing a growing NiO scale are marked with yellow arrows in the image. Note that the particle does not oxidise homogeneously. This could be explained with different sticking probabilities of oxygen, dependent on the facet structure as well as the presence of edges and defects. Local concentration variations of oxygen containing adsorbates may also have an influence. Remarkably, beam induced oxidation could not be observed before heating. We explain this with a stabilising effect of beam induced carbon contaminants. Such carbon deposits were clearly visible before heating in this case, in contrast to the experiments with pure Ni clusters in section 4.2.1. After heating no contamination effects were observed any more. Elevated temperatures can remove or immobilise adsorbed hydrocarbons, as described in section 2.7.

4.3.2.4. Beam Induced Surface Oxidation

Similar to the experiments discussed in section 4.2.1, beam induced oxidation was also observed here. However, in case of Ni@Au core-shell clusters this effect only occurs during and

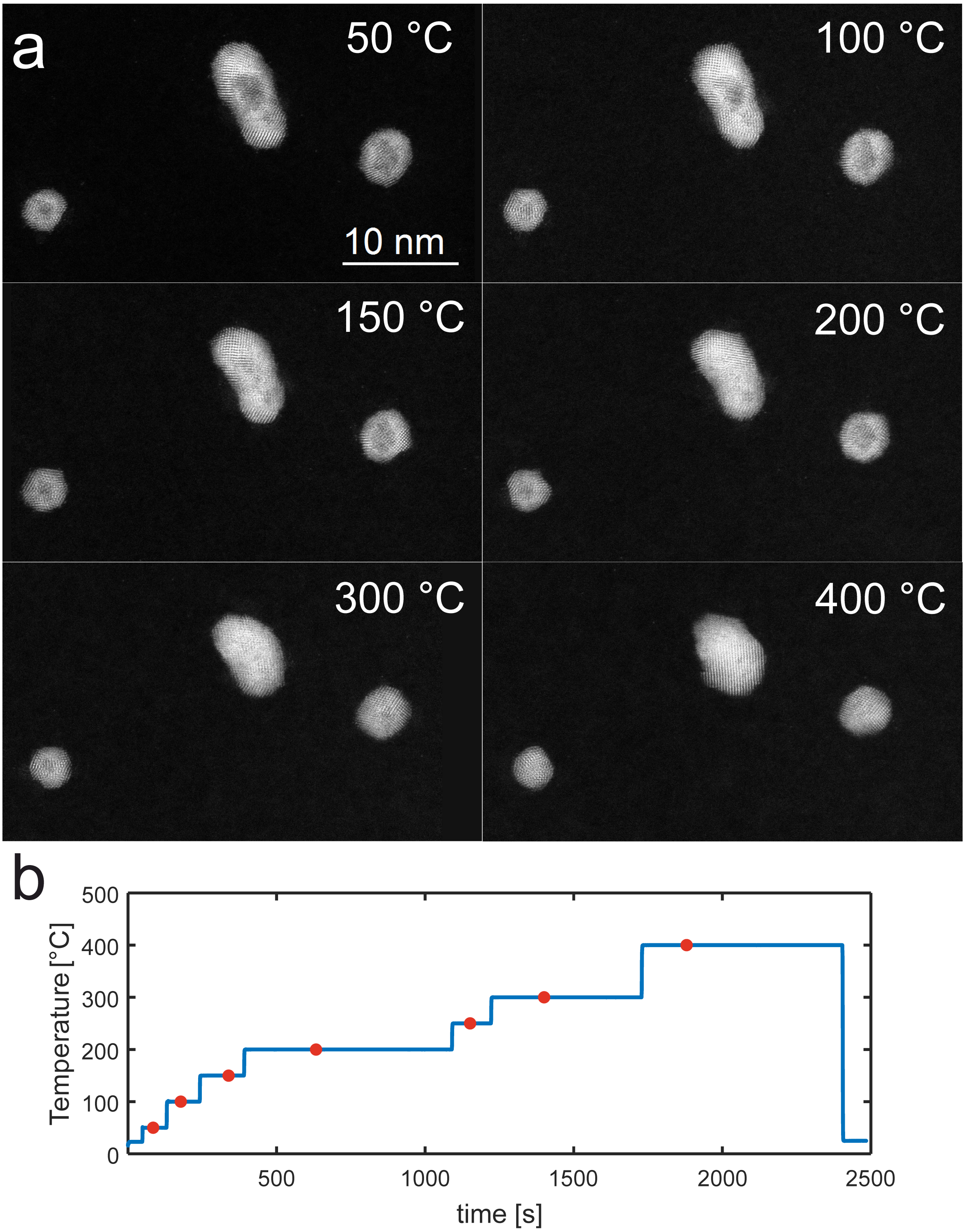

Figure 4.27.: (a) HAADF image series showing the transformation of three NiAu clusters from a Ni@Au core shell morphology to an alloy. (b) Experimental heating curve: temperature as a function of time. Red circles mark the time where the the corresponding images in (a) have been acquired.

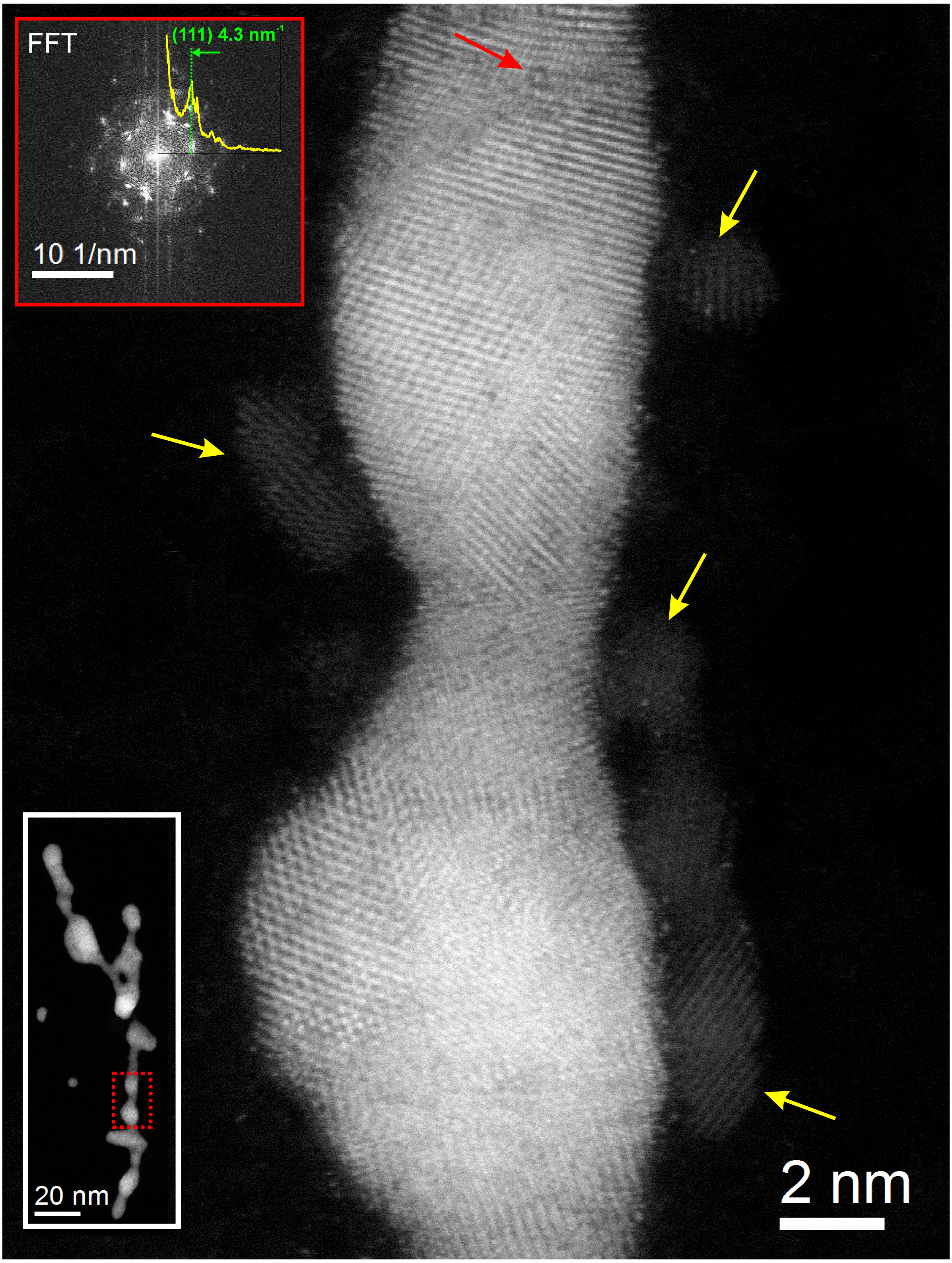

Figure 4.28.: NiAu nanowire after the heating experiment: The inset on the lower left shows an overview STEM HAADF image of the wire. The region marked with a red rectangle is shown in the main image at higher magnification. The red boxed inset shows an FFT of this image. The yellow curve in the inset shows a corresponding rotational line profile.

after the heating experiment. This leads us to the conclusion that a initially closed Au shell effectively protects the Ni core from beam induced oxidation. When a alloy is formed during heating, some Ni atoms can reach the cluster surface, where they react with oxidative species, which have been set free by the electron beam in the first place via radiolysis of adsorbed species (e.g. water). Therefore, the process only progresses under electron beam irradiation and stops if the illumination is stopped. The oxidation mechanisms are similar to those described in 4.2.1 and can be understood within the frame of Cabrera-Mott oxidation theory. Accordingly, the presence of an initial oxide layer leads to an increased outward diffusion of Ni ions to the cluster surface where they are oxidized. Instead of an aggregation of voids in the cluster centre, as it was the case for pure Ni clusters, the void is replaced by an Au core, whose Au content increases as the NiO is formed at the surface. The oxide growth was documented by a STEM HAADF time-lapse series. Figure 4.29 gives 6 images from this series, showing the cluster at different states. The images were coloured for better visibility of the oxide. The cluster exhibits a fcc structure with varying orientation over the image series. At the end we observe an orientation close to [011]. Slight misorientations and the high dynamics of the cluster impede structural characterisation from these images. However, in the region marked with a rectangle in image 106 it was possible to extract some information. This region is shown in more detail in Figure 4.30.

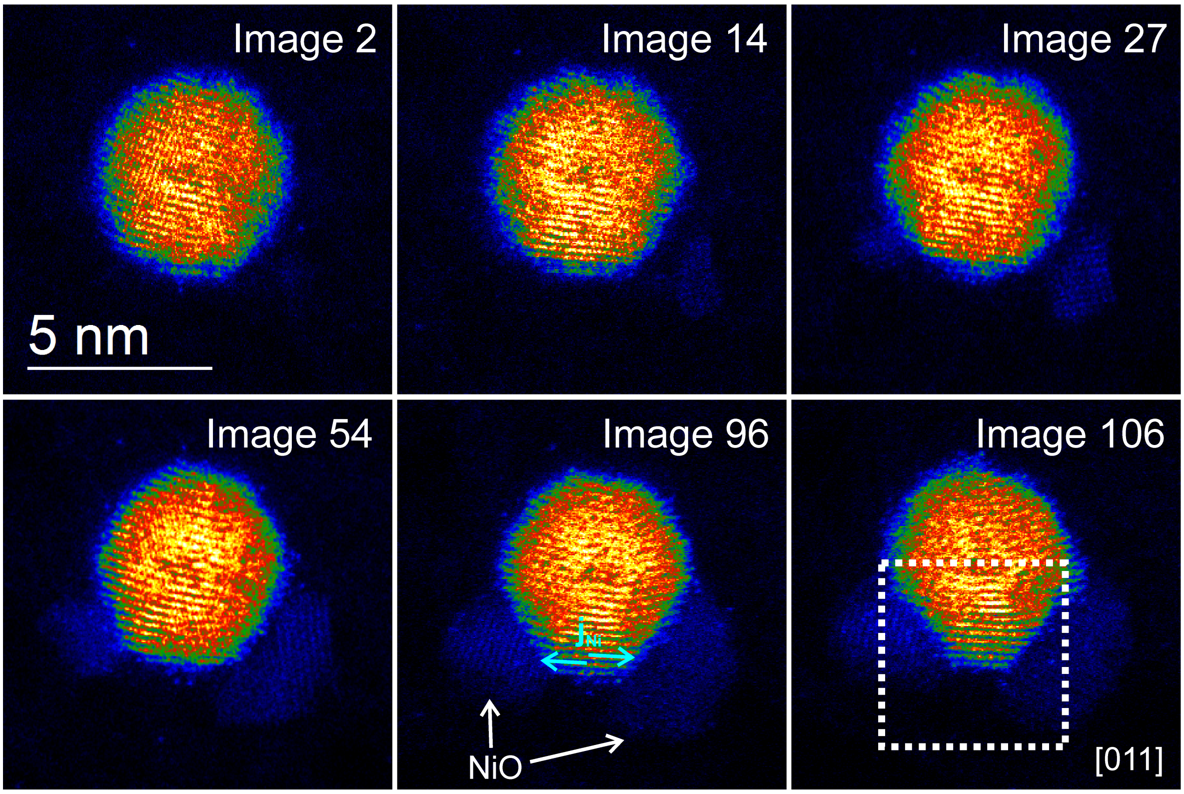

Figure 4.29.: Growth of the oxide shell of an alloyed NiAu cluster under electron beam irradiation, the images have been coloured for better visibility of the oxide growth (Titan@300keV, I_p = ≈50 pA, dwelltime: 5 µs, 315x315 pixel).

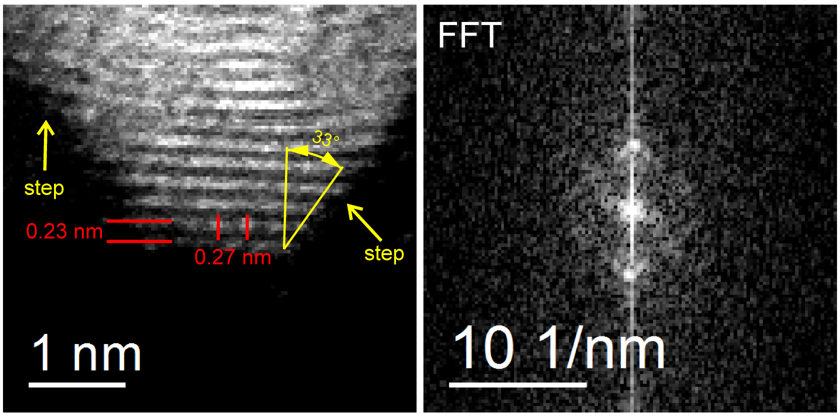

Figure 4.30.: Detailed view on the region marked in Image 106 of Figure 4.29 with its FFT. Lattice distances approximately fit to the the fcc Au lattice close to [011] direction with regard to the electron beam. We observe an angle of ≈30 deg between the normal of the lattice planes and the oxidised surfaces. Steps on these surfaces are indicated by arrows.

In Figure 4.29 we also see that the oxide growth is not homogeneous over the whole cluster surface. Two oxide regions are formed instead. Presumably, the lattice of the remaining, Au rich core determines the diffusion paths of the Ni atoms. Here, Ni atoms apparently diffuse through the crystal parallel to the [100] planes of the fcc lattice. The diffusion paths are indicated in Figure 4.29 in image 96.

Why the oxidation is limited to only two facets of the cluster is still an open question, which would need further examinations. Possibly, facet edges or steps promote the oxide growth. In Figure4.29 we see that the oxide initially forms at the most distant point from the cluster centre, which would suggest an edge mediated growth. Furthermore, in Figure 4.30 we can also see the presence of steps on the facets, which are marked with yellow arrows in that image. After an initial oxide is formed on the facet it subsequently acts as nucleus for further oxide growth, according to the Cabrera-Mott model. However, we have to note that the exact configuration of the facets is difficult to determine from the projective images. To gather more information about beam induced oxide growth on Ni@Au core-shell particles further studies with more sophisticated methods, such as tomography or HAADF quantification would be needed.

4.3.3. The System Cr-Au

The system CrAu is interesting due to its magnetic properties. Cr atoms were found to carry a large magnetic momentum in a Au environment [196]. Furthermore we wanted to know if the obtained Cr@Au structures retain their separated morphology, as found during the experiments with Au@Ag and Ag@Au. It was also interesting for us if an Au shell can prevent oxidation of the core material. Due to its affinity to oxygen Cr seemed to be ideal core material for such an experiment. Controlling the oxidation behaviour of Cr could be interesting for further studies of the magnetic properties of the clusters as well as for heterogeneous photo-catalysis applications [197].

4.3.3.1. Experimental Details

As in the previous experiments the clusters were synthesised with the superfluid He-droplet technique in the two evaporator configuration, which is shown in Figure 4.19. Based on the experiences we obtained from the AuAg experiments we chose to evaporate Cr first followed by Au to produce clusters with a Cr@Au core-shell configuration. Electron microscopy analysis of the clusters was done at the FEI Titan that was operated in STEM mode. We expected increased elastic beam damage effects and we therefore chose the lowest possible electron energy of 60 keV and a probe current of approximately 50 pA. Note that reducing the knock-on damage by decreasing the electron energy is bought by a loss in resolution.

Reversed Elemental Structure It is apparent from the HAADF images that the desired Cr@Au core-shell structure is reversed in all cases (Figure 4.31). Au, giving a bright HAADF contrast, appears inside mostly elongated core-shell particles. The Au cores are coated by a much darker shell.

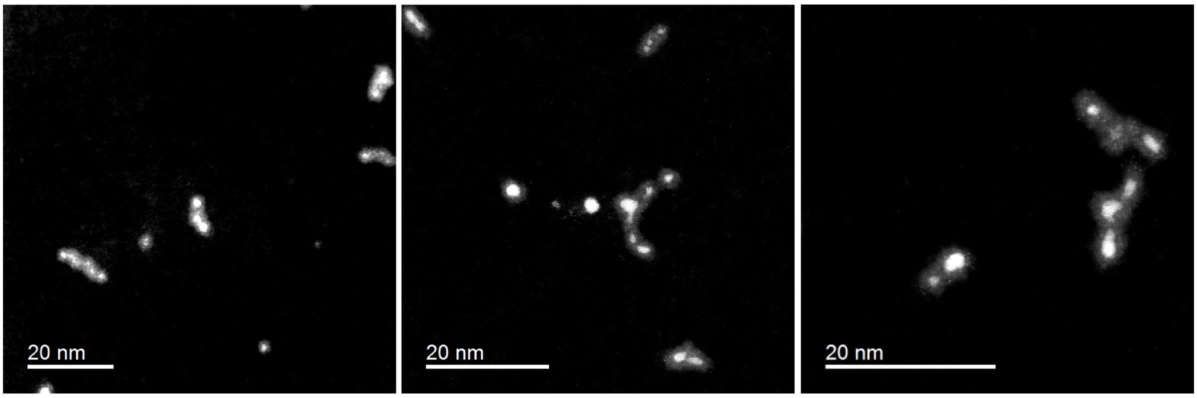

Figure 4.31.: Overview HAADF images of the CrAu - clusters on amorphous carbon substrate (Titan@60keV)

Further EELS elemental analysis, shown in Figure4.32, revealed that this shell consists of Cr that was apparently completely oxidized. This can be explained with the fast Au-Cr interdiffusion [198]. Cr atoms can diffuse very fast through the Au shell were they can react with O_2. Interestingly, despite the low-electron energy we still observe considerable beam damage effects, impeding the use of EDXS for elemental analysis (see 4.3.3.1).

Cr_2O_3 or CrO_2? One question that arose concerned the oxidation state of Cr in this case. In principle there are two ways to obtain this information using EELS. The first possibility is to use relative EELS quantification using Eq. (2.4). For CrO_2 (Cr^{4+}) a Cr concentration x_{Cr} of about $\frac{1}{3}$ can be expected while for Cr_2O_3 (Cr^{3+}) x_{Cr} should have a value of 0.4. Figure 4.33a depicts a histogram generated from a pixelwise EELS quantification of a spectrum image. We found a mean Cr concentration $\overline{x_{\mathrm{Cr}}}$ of 0.3 at%, which is closer to CrO_2 than to Cr_2O_3. These results indicate that the oxygen content is too low for pure Cr_2O_3. The presence of Cr^{4+},

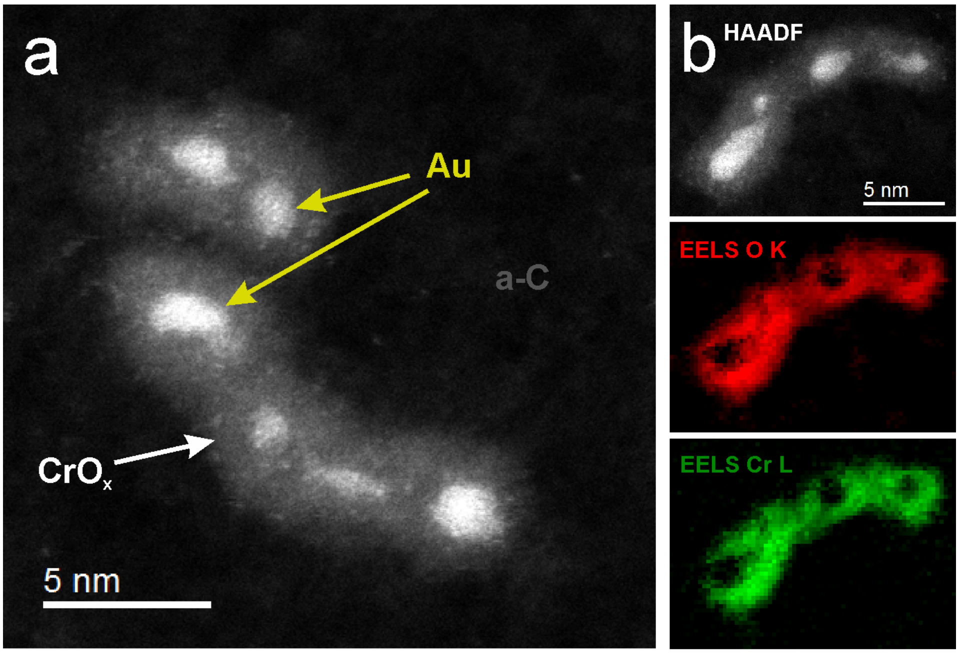

Figure 4.32.: (a) HAADF image of 2 Au@CrO_x core-shell particles. Multiple Au cores can be clearly distinguished from the shell by their bright contrast. (b) HAADF image of another cluster together with EELS elemental maps showing that the shell consist of CrO_x. (The O K and the Cr $L_{2,3}$ edges have been used. SI size: 70x52 spectra, dwell time: 0.05 s (multipass acquisition: 5 passes á 0.01 s), spectra were PCA filtered using 4 components)

however, seems to be unlikely, since the synthesis of CrO_2 usually requires high temperatures and pressures.

The second approach to obtain information about the oxidation state is directly via ELNES of either the O K or the Cr L edge. The intensities of the white lines of Cr L (L_2 and L_3) and the energy distance ΔE between the white lines could give information about the oxidation state, if compared with literature values [199]. Figure 4.33b shows the unmonochromated ELNES of these two peaks (FWHM of the zero loss: $\approx 1.2\,\text{eV}$).

From this spectrum we can estimate a ΔE of 8.5 eV and a L_3/L_2 peak ratio of 1.5 (135 counts/89 counts). Both values were determined from Gaussian Fits of the two lines after power-law background subtraction. In literature we find for CrO_2 a ΔE of 8.2 eV and L_3/L_2 peak intensity ratio of 1.49. For Cr_2O_3 these values would be $\Delta E = 8.4$ and $L_3/L_2 = 1.63$. These values would indicate that the shell consists of CrO_2 instead of Cr_2O_3. However, we have to be careful, since the errors are quite large. The energy uncertainty only caused by the channel width is already ±0.2 eV. Furthermore, a CrO_2 shell would be quite surprising because Cr normally oxidises by formation of Cr_2O_3. For the synthesis of CrO_2 high pressures (200 MPa) and temperatures (800 K) in the presence of water are necessary (hydrothermal synthesis) [200].

Both the EELS quantification and the ELNES results could be explainable if we consider the reduction of the oxide by radiolysis during the acquisition of the spectra. The oxide could then be a non-stoichiometric mixture of Cr and Cr_2O_3. However, for a well-founded statement on the oxide structure more experiments would be needed.

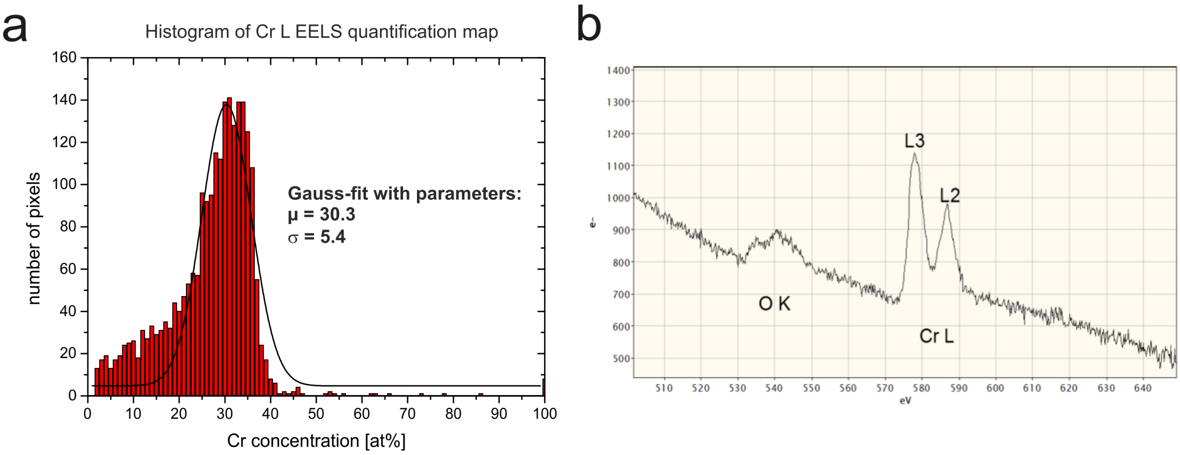

Figure 4.33.: (a) Result of the EELS quantification, shown as histogram of the Cr concentration. A Gaussian fit of the data gives a mean Cr concentration value of 30.1% with a standard deviation of 5.4. (b) ELNES of the O K and Cr $L_{2,3}$ edges.

Beam Induced Dynamics Regardless of the gentle scanning conditions we found that the clusters rapidly change under electron beam radiation, as demonstrated by four HAADF images in Figure 4.34, which were extracted from a time-lapse HAADF image series.

The beam induced dynamics of the clusters is surprising, especially with regard to the Au cores, which exhibit significant Ostwald ripening effects. Rapidly diffusing single atoms can be seen as bright spots in the CrO_x-shell as well as on the adjacent amorphous carbon substrate. This is in contrast, to previous experiments were even small Au clusters were found to be relatively stable, yet at 300 keV electron energy. This has also been observed in simulations (3.5). The reason for the high stability lies in the high mass and the relatively high binding energy of Au atoms in the clusters (see 3.1). Presumably, the reason for this is that Au atoms only weakly interact with Cr_2O_3. The low adhesion between both species has the effect that they try to minimize the interface to one another, which results in de-mixing and Ostwald-ripening, when energy is introduced by the electron beam. When we are looking closely to the image series shown in Figure 4.34, we see how single Au atoms move inside the Cr_2O_3 shell. From this we conclude that Au atoms are very mobile in the oxide, which is the reason for the efficient Ostwald ripening of the multiple Au cores inside the wire.

The high dynamics that was observed even at low electron energies shows that it can be difficult to prevent knock-on damage completely in some cases, only by lowering the electron energy.

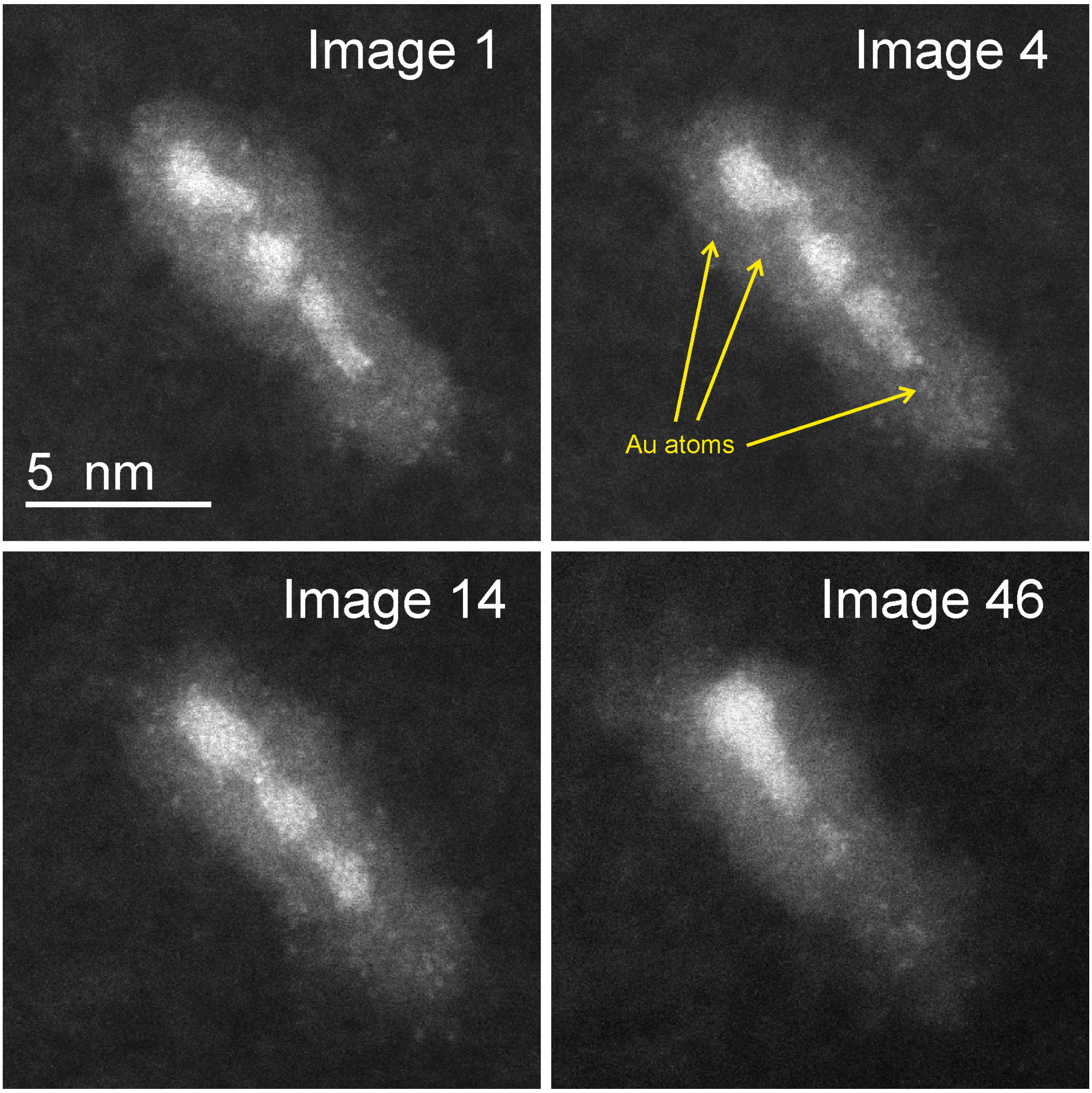

Figure 4.34.: HAADF image time series showing a elongated cluster with a Au core and a CrO_x shell. Significant knock-on damage effects can be seen resulting in Ostwald ripening of the Au cores. The diffusion of Au atoms is visible inside the cluster shell and on the amorphous carbon substrate (a-C). (Titan@60kV, 50 pA probe current, 642x642 pixel, 6 µs dwell time)

4.4. Quantitative Structural Characterization of Clusters

Fundamental properties of metallic clusters are determined by their size, structure and morphology [8]. Knowledge about such cluster characteristics is thus paramount to understand their properties and powerful methods for structural characterization have been developed in past decades. Especially the invention of scanning probe techniques such as scanning tunneling microscopy (STM) and atom force microscopy (AFM) in the 80s stimulated the early research on metallic clusters and surfaces [201]. These techniques have proven to be very useful to gain deeper insights into the structure and surface configuration of single supported clusters. Statistic information, such as size distributions, can also be obtained. Valuable information about structure, chemistry and bonding relations can be obtained with other methods like X-ray photoelectron spectroscopy (XPS) and synchrotron techniques, averaged over a large number of clusters [202].

It may be surprising that it took relatively long until electron microscopy played a significant role for cluster characterisation, despite its long and successful history since its invention in the 1930s by Ruska and Knoll [203]. However, with increasing resolution of electron microscopes over the years, they also gained more and more importance in this field. Early attempts on structural characterisation of single supported clusters in a TEM were based on phase contrast images which where compared with simulations [204, 205]. Often these techniques were limited on relatively large clusters, comprised of several thousand atoms, especially for lighter atoms and crystalline substrates. Also the early work of Treacy, Howie and Wilson in the end of the 1070s has to be mentioned here [206]. Based on pioneer work by Crewe, they developed the STEM HAADF technique for imaging of small metallic clusters. Although the resolution was not sufficient to allow detailed structural studies, this technique allowed to image supported clusters with a size of 2 nm, which are hardly visible with bright field imaging techniques due to overlaying substrate contrast. High voltage microscopes, operated with electron energies of about 1 MeV, on the other hand, were able to provide the required resolution, but beam damage hindered its application on such beam sensitive structures. This dramatically changed with the availability of aberration correctors in the past decade. Since then different techniques, such as tomography or single particle reconstruction have been developed to obtain 3D structural information of even small nanostructures [5, 7, 207]. Also nano beam diffraction techniques can be used for structural characterisation on individual, ligand stabilised clusters, which has been demonstrated recently [208].

However, structural characterisation of small clusters with less than 1000 atoms can be cumbersome and still bears a lot of experimental difficulties, which will be shown in the following on the example of a single gold cluster. Our approach is based on the Z-contrast quantification method, that has been presented in section 2.5 of this work[4].

4.4.1. Determination of the Shape of Supported Clusters

One possible way to determine cluster sizes was also presented in section 4.2.1.5, for small Ni clusters. Due to the beam sensitivity of these clusters their size was estimated by using the

projected area from a single HAADF image. A functional relation between the cluster areas and the their size was found with quantitative EELS and molecular dynamics simulations. However, to determine the 3 dimensional morphology of a single cluster was not possible with this method.
Due to the high mass of Au atoms, Au clusters are more stable under the electron beam which allows the acquisition of atomically resolved images that can be quantified with the HAADF quantification technique (see section 2.5 for details) even at 300 keV. However, it turns out that acquiring an image were every atomic column is clearly visible with sufficient counting statistics, is experimentally difficult for small clusters, consisting of less than 1000 atoms, because of the high probability of beam induced displacements of surface atoms, even for Au (also see section3.5). So we decided to acquire an image series, consisting of 255 images with low dwell time (3 µs in this case). From previous experiments and simulations we know that sputtering is unlikely for Au clusters, so we can choose the best image for quantification at any time in the image series without being worried about beam induced changes in cluster size. This assumption is justified by the integrated intensity of the particle. Fig 4.35 shows this quantity as a function of sequential image number. The values in this plot were determined by applying a 10x10 pixel spatial average filter followed by a threshold based particle detection within Matlab. This method is similar to the procedure that was used in chapter 4.2.1 for the determination of the clusters projected areas. While during the first 30 images the intensity drops by about 10%, probably due to beam induced cluster rearrangement, it stays almost constant during the remaining image series. Outliers are caused by sudden position jumps during acquisition.
The resolution of the acquired images was 512x512 pixels and we chose a beam current of approximately 70 pA. The Fischione HAADF detector was used the camera length was set to 91 mm. A detector sensitivity map has been acquired according to the procedure presented in section 2.5.2.1 using a beam current of 10 pA. Settings for contrast, brightness and dwell time were kept the same later in the experiment. A larger field of view than necessary has been chosen, to allow efficient automatic drift correction (see Figure 4.37a). Drift correction was done with the image alignment tool in GMS, after applying a bandpass filter, so as to reduce influence of noise and atom movement on the drift correction.
To illustrate the beam induced dynamics of the cluster on the amorphous carbon support, 6 images were chosen from the image series and depicted in Figure 4.36. These images represent cut-outs with a size of 373x373 pixels from the region marked in Figure 4.37a.

Figure 4.37a shows a HAADF image of a single-crystalline Au cluster in (100) orientation with regard to the electron beam. In Figure 4.37b the corresponding quantification result, that was obtained using Absolute Integrator [4], is given. Using this software the raw data was background corrected, the positions of the atom columns were determined and the intensities were weighted by the radial detector sensitivity, that was obtained from the detector sensitivity map. The influence of the flux pattern was neglected in this case. The cross section values that were calculated for each atom columns were normalized by a mean cross section value extracted from 5 regions, that were considered to contain only one single Au atom. Thereby, a map of the number of atoms per column was obtained as shown in Figure 4.37b. Another advantage of such a normalization is, that systematic errors, introduced linearly as multipliers,

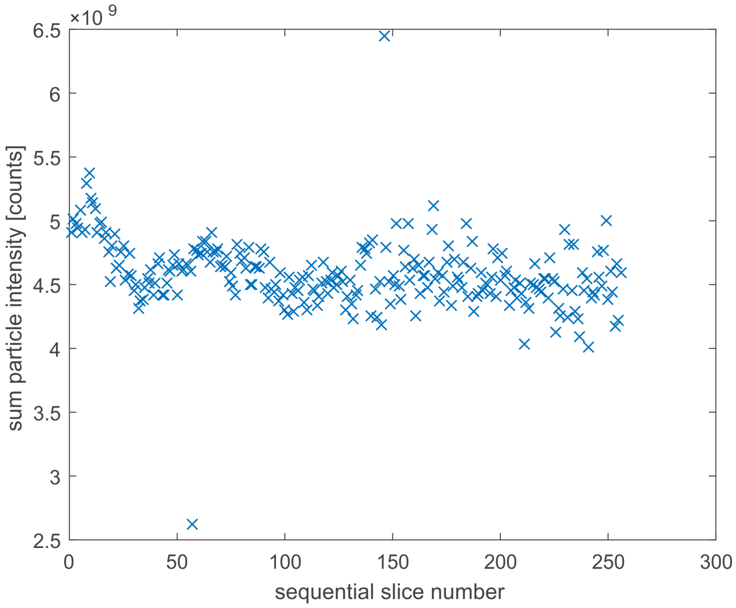

Figure 4.35.: Integrated intensity values as a function of the sequential image number of the cluster shown in 4.36

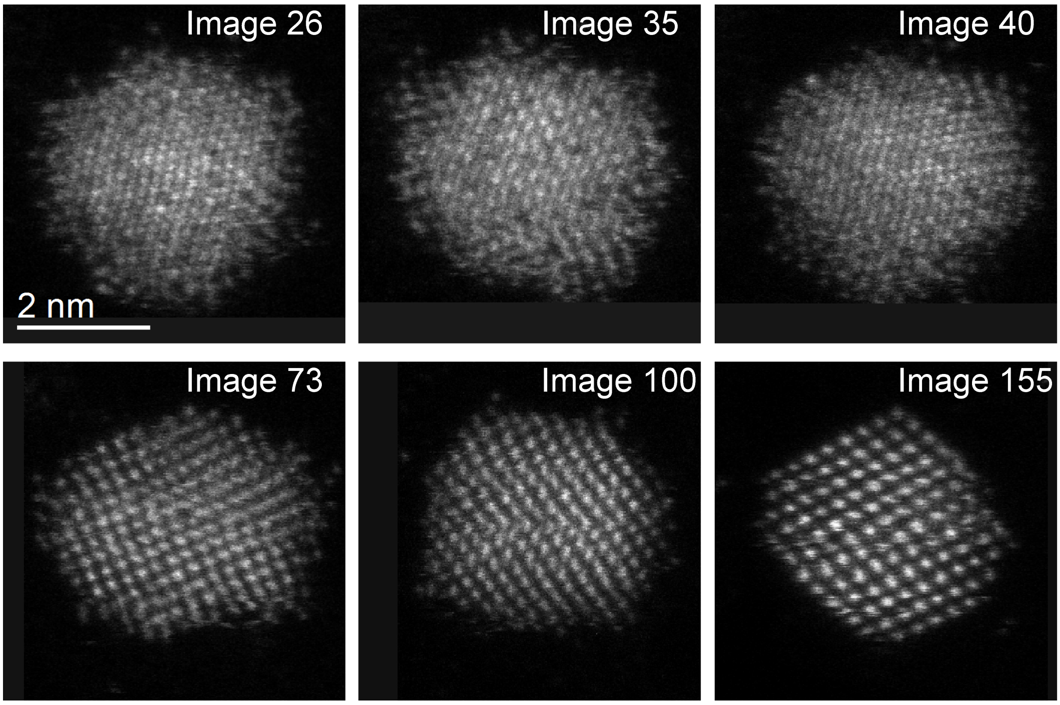

Figure 4.36.: 6 image cut-outs with 375x375 pixels size, from an HAADF image series (512x512) comprised of 255 images, illustrating the significant beam induced dynamics. Image 100 has been chosen for HAADF quantification in Figure 4.37

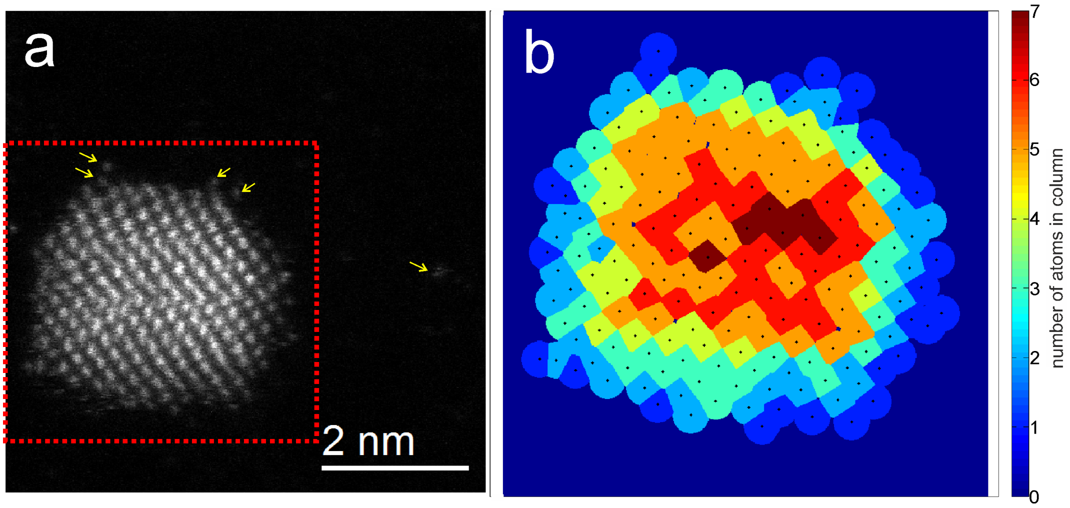

Figure 4.37.: (a) HAADF image of a Au cluster on amorphous carbon, extracted from a image series. Single atoms that were used for cross section scaling in (b) are highlighted with arrows. (b) HAADF quantification result of the region marked in (a), obtained with Absolute Integrator by Lewys Jones [4], The black dots correspond to the positions of the atom columns and are the centres of the the Voronoi cells.

cancel out. However, additive systematic errors (e.g. background subtraction) still influence the result. This is true also for random errors, caused by noise or atom movement. The latter is especially important when we experimentally determine the scattering cross section of a single atom from the image. Due to the relatively high mobility of these atoms, they tend to move away from the electron beam during image acquisition and the determined intensity values vary significantly by approximately ±10rel%. Accordingly, it is reasonable to assume a counting error of approximately ±1 atom per column in this case.

All in all, the cluster was found to be comprised of 592 atoms. This value was found simply by adding up all columns. From the quantification results we were also able to estimate the amount of flattening of the cluster due to support interactions. While its lateral dimensions are between 15 and 18 atoms (corresponds to about 8-9 unit cells), its maximum height was found to be 6 atoms (= unit cells). Compared to results obtained from tomography series of larger Ag@Au core-shell clusters, a similar amount of flattening was found [5].
Assuming roughly a hemispherical morphology we can calculate the expected amount of atoms N_c in a cluster with diameter d, using the volume of the cluster V_c, the bulk density of Au (ρ_{Au} =19 300 kg m^{-3}) and its mass number (u_{Au} =197). The approximate diameter of the cluster is d =3.4 nm, estimated via a diagonal intensity profile directly from the image. Inserting these quantities into Eq. (4.3) gives a value of 602 atoms for N_c. This complies well with our quantification result, considering our rough approximations regarding morphology and diameter.

$$N_c = V_c \frac{\rho_{Au}}{u_{Au}} \quad \text{with} \quad V_c = \frac{4(d/2)^3\pi}{6} \tag{4.3}$$

In the following we want to use this quantification result to generate a three-dimensional model of the supported Au cluster.

4.4.2. From HAADF Quantification to the Cluster Morphology

Jones et al. demonstrated that it is possible to obtain a three-dimensional model from the HAADF quantification data [4] with a Monte Carlo based energy minimisation procedure. However, they made several simplifications, such as using a Lennard-Jones pair potential for the energy calculation, only allowed integer multiples of the discrete z-separation, or ignored the influence of the substrate interaction.

We decided to follow a similar approach, using an adapted version of our Metropolis Monte Carlo code (see section 3.3 for details) to find a possible cluster configuration that fits the HAADF quantification results. In a first step, the data presented in Figure 4.37b was used to generate atom coordinates that can be passed to our code for energy minimisation. Atoms were placed according to the rules of an fcc-lattice in (100)-orientation. The x- and y-coordinates are determined by the positions of the atom columns, as determined in Figure 4.37, while in z-direction the atoms are placed column wise, with a distance of one lattice constant within each atom in a column. Between each column, a z-offset of a half of the lattice constant was maintained. Hence, each column was filled sequentially starting with $z = 0$ or $z = a/2$ with the amount of atoms determined in Figure 4.37b.

For the equilibration the amorphous carbon substrate was modelled as rigid and flat, using the potential by Werner et al. [131] (Eq. (3.32)). The interaction between the Au atoms was included by using the Sutton-Chen potential [125] (Eq. (3.27)).The main difference to the conventional Metropolis Monte Carlo algorithm, as presented in section 3.3 is, that we only allow full atom movement in z-direction. Changes of the x-y coordinates are only allowed to a certain maximum distance from the initial position. This maximum distance value was set to 0.4 Å in the present case. This was done to minimise lattice strain due to small errors in image calibration and drift. A simulated annealing approach was applied, starting with a temperature of 1000 K. During calculation the temperature is sequentially lowered to 10 K with a cooling rate of $4.9 \times 10^{-4}\,\mathrm{K\,step}^{-1}$. The number of steps of the whole equilibration was set to 10000 steps per atom. The obtained geometry is depicted in Figure 4.38b.

We have to note, however, that the morphology we found with HAADF quantification does not necessarily correspond to the equilibrium shape of the cluster at room temperature, due to the high amount of beam induced displacements, which become obvious when observing the cluster during acquisition of image series. Thus, the shape shown in Figure 4.38b is only a snap-shot.

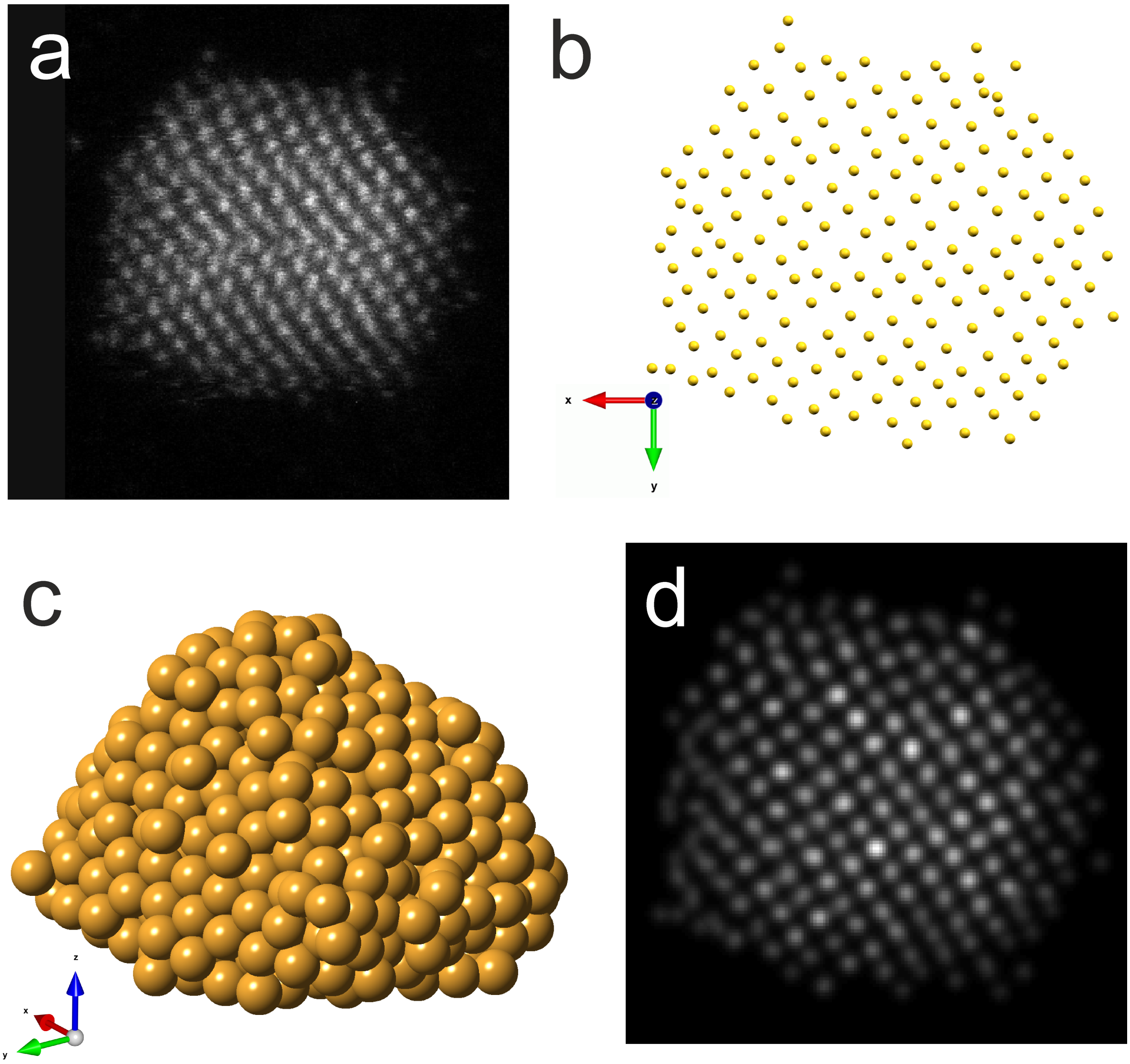

Figure 4.38.: (a) The original raw image that was used for quantification. (b) The model generated from the atom positions, determined from (a). (c) Energy minimised 3D model generated from the HAADF quantification results. (d) Multislice HAADF simulation based on the energy minimised model shown in (c), using the same angular conditions as used for image acquisition (300 kV, 91 mm camera length, Fischione detector inner detection angle 62.2 mrad, outer angle 216 mrad, 40 slices with 160x160 pixel)

5. Conclusion and Outlook

Within this thesis we studied supported metallic nanostructures and clusters in experiments and simulations. The structures were grown inside superfluid helium droplets and analytical STEM was used for their characterisation. The main difficulties that regularly occur during analysis of such small systems are addressed, namely beam damage, hydrocarbon contamination and low signal intensity. These three effects ultimately limit the spatial resolution and signal-to-noise ratio (SNR) of all signals that can be obtained within a STEM experiment. We applied experimental and computational methods to develop counter-strategies in order to increase the quality of STEM analysis of clusters that are often comprised of less than a few hundred atoms. These methods include preparation, data acquisition and data evaluation techniques.

In the methods section we describe a procedure that was developed for the determination of STEM detector angles. This information is paramount for both image simulation and Z-contrast quantification purposes. Furthermore, hydrocarbon contamination was found to mainly come from the substrates that were used. We showed that such contaminants can greatly be reduced by a preceding heating treatment of the substrates before cluster deposition in either vacuum or active coal.

Regarding data analysis, we adapted the noise filtering capabilities of principal component analysis, which is a well established method to increase the SNR in hyperspectral datasets, to single, two-dimensional images. To this end we implemented a patch based approach and tested its performance compared to a common Wiener filter. Although we were able to prove the high ability of the PCA algorithm to reduce noise, we also note that quantitative intensity information is not preserved by the algorithm in its present form. Generally, the use of noise filtering algorithms for quantification purposes must be evaluated in each individual case and should be avoided if its effects on the results are not clear. However, these first results are a good starting point for future improvements of the algorithm.

Another important point of this thesis was to understand and minimise beam damage effects during data acquisition. We observe high surface atom mobility under the electron beam. This is due to the complete absence of hydrocarbon contamination and the lack of stabilisers and surfactants during cluster synthesis, which would otherwise have a stabilising effect. The clusters are therefore an ideal model system to study such processes. We used classical heat flow calculations and finite element simulations to estimate the amount of heat that is dissipated by the electron beam in small, carbon supported nanoparticles, during a standard STEM experiment. Heating and ionisation effects were found to be negligible and knock-on damage was identified as the dominating mechanism for metallic clusters. Based on this findings a molecular dynamics code has been developed from scratch to study beam induced damage effects in metallic clusters, including a Metropolis Monte Carlo code for cluster generation and equilibration. With this code, we calculated the dynamics of small mono- and bimetallic clusters under electron beam irradiation. In principle, this enables us to predict displacement and sputtering cross sections dependent on size, morphology, material, beam energy, and temperature. We are able to simulate how a system will evolve under the electron beam. In future work we aim to replace the molecular dynamics core with the freely available LAMMPS code to take advantage of its high speed and flexibility. We could then be able to apply our technique to explore beam induced dynamics in larger systems and other geometries, such as surfaces, interfaces or alloys.

In experiments, we demonstrated the high flexibility of the He droplet technique for the synthesis of metallic nanostructures. Our investigations are focused on Au, Ag and Ni clusters, as well as on bimetallic AuAg, AuNi and CrAu particles with varying size and morphology. We used different substrates such as amorphous carbon, graphene or hexagonal boron nitride (h-BN) thin films. h-BN films were prepared by means of a cleaving method using adhesive tape due to the lack of suitable, commercially available TEM-substrates at this time (2013). We showed that especially h-BN may be a promising candidate as cluster support due to its inertness and the low attainable thickness down to a monolayer. Therefore, the signal contribution from the substrate can be kept as low as possible for both imaging and analytical techniques in the TEM. Due to the large band gap h-BN could also be interesting for plasmonics or plexcitonics experiments with clusters. Meanwhile, also monolayer h-BN grown on metal substrates is commercially available, which could lower the experimental effort. With appropriate preparation techniques we envision to use such substrates even on heatable MEMS devices or to build h-BN liquid cells for *in situ* investigations.

Structural and chemical analysis of clusters with different sizes and morphologies allow to draw conclusions about the physical properties of He droplets as well as to study these systems with high purity on the nanoscale. We found that the morphology of core-shell particles not only depends on the pick-up sequence of the thermal evaporators in the synthesis facility, but is also determined by thermodynamics and chemistry (e.g. oxidation behaviour) after deposition. We also showed that electron irradiation during TEM characterisation can largely affect the cluster properties. For instance, Ni and Ag clusters were found to oxidise in the electron beam under formation of hollow and toroidal shapes, mediated by the nanoscale Kirkendall effect. Presumably, water, that is adsorbed adjacent to the clusters, provides the oxygen. In case of Ni we studied the oxidation kinetics and related it to a two step Cabrera-Mott process. Via EELS quantification and molecular dynamics simulations we were able to relate the projected area of the cluster to their volume, which allows us to extract three-dimensional information from single HAADF images. With this information we estimated the oxidation speed as a function of cluster size. For Ag nanowires we showed that they can be modified very locally by taking advantage of this beam induced oxidation effect. Potentially, this observation could be interesting for nanostructuring applications in future.

Our experiments with elongated and wired clusters approve the presence of multiple quantum vortices inside larger superfluid droplets due to kinked and branched morphologies that are found. Furthermore, the presence of multiple cores was shown for certain growth conditions

in bimetallic particles, with both elongated or lenticular shape.
We used Z-contrast quantification to estimate the number of atoms in a Au clusters from an atomically resolved HAADF image. The cluster was found to be comprised of approximately 600 Au atoms. The column wise quantitative information was then used to generate a three-dimensional model of the cluster which was equilibrated via a Metropolis Monte Carlo code. The advantage of this approach is the low required dose, compared to electron tomography. We showed that this makes the method even applicable to smallest systems, which show high beam induced dynamics. It would be desirable to improve this method to allow to gain quantitative structural information even from clusters comprised of more than one species or non-crystalline clusters in future.

Summarising, we showed that aberration-corrected STEM is a highly valuable method for the characterisation of high-purity mono- and bimetallic clusters, despite its destructive nature. The present work represents a small step forward to the ultimate goal of quantitative, elemental analysis of arbitrary clusters with atomic resolution. We believe that recent developments in electron microscopy, which aim to harness techniques such as *in situ* TEM [209], machine learning and compressed sensing [210, 211], or low-voltage TEM [212] will provide completely new insights and drive forward the field of cluster research.

A. Appendix: Matlab Source Code

In this appendix chapter we list the most important Matlab codes that were used in this thesis.

A.1. Intensity Determination from STEM Images Based on Voronoi Tessellation

For the determination of intensity values in an atomically resolved HAADF STEM image following MATLAB code was used. Experimental and simulated images can be used. After a simple peak finding step to determine the coordinates of the atom columns in the image we followed an approach suggested by Jones et al. [4] to assign intensity values pixel wise to each columns based on Voronoi segmentation. For this we use the voronoi function included in MATLAB. Optionally, noise filtering can be applied before evaluation, either based on the patch-PCA approach also presented in this thesis or on average filtering. The following listing only represents the core part of the code. In more recent versions also a graphical user interface was added, which is not shown here.

Listing A.1: EvaluateExperimentalImages.m

```
binningfactor = 1;
maxcellradius = 20;
minneighbourradius = 5; % for peak intensity determination

startw = 16;
PCn = 10;
ansctrans = 1;

histogramvalues = 50;

%----------------------------------
% INPUT
%----------------------------------

%standardpath = 'E:\Diss_workfolder\Simulationen\Multislice\Democluster
   ↪ \results\defocus-1.5'
standardpath = [pwd '\det2\'];

[I,ps] = ReadMicImageFromFile(standardpath);  % Import image with
   ↪ calibration
```

```
ps = ps.*binningfactor;

N = min(size(I));
xyscale = (0:N-1).*ps;

cmax = max(I(:));
cmin = min(I(:));
Imax = max(I(:)); % save maximum value of the original data
% I = (I-min(I(:)))./(max(I(:))-min(I(:)))*1; % Scale to 1


fig1 = figure; movegui('north');
imagesc(xyscale,xyscale,I);
set(fig1,'DefaultAxesFontName', 'Arial', 'DefaultAxesFontSize', 14, '
    ↪ DefaultAxesFontWeight', 'Demi' );
axis equal
xlabel('Scale [nm]');
colormap gray;
cb = colorbar;
caxis([cmin cmax])
imdisplayrange;
imcontrast(fig1);
ylabel(cb,'counts')


% noise filtering:
% via PCA:
[Ifilt,~] = HirPatchPCA(I, startw, PCn, ansctrans);
Ifilt = imresize(Ifilt,1/binningfactor); % image binning if needed
write32bittiff(Ifilt,strcat('filteredimg.tif'));

% via Averaging:
% h = ones(w,w) / w^2;
% I = imfilter(I,h);

figfilt = figure; movegui('north');
imagesc(xyscale,xyscale,Ifilt);
set(figfilt,'DefaultAxesFontName', 'Arial', 'DefaultAxesFontSize', 14,
    ↪ 'DefaultAxesFontWeight', 'Demi' );
axis equal
xlabel('Scale [nm]');
colormap gray;
cb = colorbar;
caxis([cmin cmax])
imdisplayrange;
imcontrast(figfilt);
ylabel(cb,'counts')


%define a threshold value:
minpeak = mean(Ifilt(1:round((N/binningfactor)^2))) % mean pixel value
    ↪ as guess for intensity threshold
```

```
Ifilt(Ifilt<minpeak)=0;

%------------------------
% peak finding:
%------------------------
% variant 1:
mask = ones(2*minneighbourradius); mask(minneighbourradius,
   ↪ minneighbourradius) = 0;
peaks = Ifilt > ordfilt2(Ifilt,length(mask(mask==1)),mask);
[peakpxy,peakpxx] = find(peaks==1);

%variant 2:
% [m,n]=size(Ifilt);
% B=Ifilt;
% for ii=1:m+1-minneighbourradius
%    B(ii,:)=max(Ifilt(ii:ii+minneighbourradius-1,:),[],1);
% end
% for ii=1:n+1-minneighbourradius
%    B(:,ii)=max(Ifilt(:,ii:ii+minneighbourradius-1),[],2);
% end

% peaks = imregionalmax(Ifilt);
% [peakpxy,peakpxx] = find(peaks==1);


peakpxy = peakpxy.*binningfactor;
peakpxx = peakpxx.*binningfactor;
peakx = (peakpxx*ps-ps);
peaky = (peakpxy*ps-ps);

[vx,vy] = voronoi(peakx,peaky);  % vx and vy contain the the finite
   ↪ vertices of the Voronoi edges
%[V,C] = voronoin([peakx,peaky]); % determine vertices V of the Voronoi
   ↪  cells C around said maxima with coordinates x,y
% C is a cell where each line corresponds with the same line from Z.
   ↪ The line contains up to six indices referring to given lines of V
   ↪ . In other words, the coordinates of the corners of the Voronoi
   ↪ cell. Each pixel belongs to exactly one Voronoi cell according to
   ↪  definition.

figmaxima = figure;
set(figmaxima,'DefaultAxesFontName', 'Arial', 'DefaultAxesFontSize',
   ↪ 14, 'DefaultAxesFontWeight', 'Demi' );
ax = gca();
scatter(ax,peakx,peaky,'.')
xlim([0 max(xyscale)])
ylim([0 max(xyscale)])
axis square;
xlabel('Scale [nm]');
colormap jet;
cb = colorbar;
ylabel(cb,'pixel intensity [counts]')
```

```
%set(ax, 'YDir', 'reverse')
hold(ax, 'on');
imagesc(xyscale,xyscale,I)
voronoi(peakx,peaky,'w')
hold(ax, 'off')
title('Voronoi segmentation');
%set(ax,'position',[0 0 1 1],'units','normalized');

% find pixels corresponding to voronoi cells:
% source: http://de.mathworks.com/matlabcentral/newsreader/view_thread
   ↪ /303167
[X,Y] = meshgrid(xyscale,xyscale);
[SX,XX] = ndgrid(peakx, X);
[SY,YY] = ndgrid(peaky, Y);
D2 = (SX-XX).^2+(SY-YY).^2;
clear SX SY XX YY
[~, LOC] = min(D2, [], 1);
LOC = reshape(LOC, size(X));

figcells = figure;
clf
ax = gca();
imagesc(xyscale,xyscale,LOC);
cb = colorbar;
set(ax, 'YDir', 'reverse')
hold on
voronoi(peakx, peaky)
hold off

% sum up all pixel intensities in each voroni cell:
cellintensities = zeros(1,max(LOC(:)));
[rr,cc] = meshgrid(1:N);
cellintensityimage = zeros(size(I));
for i=1:max(LOC(:))
cellmask = false(size(LOC));
cellmask(LOC==i)=true;
circlemask = logical(sqrt((rr-peakpxx(i)).^2+(cc-peakpxy(i)).^2)<=
   ↪ maxcellradius);
cellmask = cellmask & circlemask;
cellintensities(i) = sum(I(cellmask));
cellintensityimage = cellintensityimage + cellmask.*cellintensities(i);
end

find(cellintensities==min(cellintensities(:)))

% plot histogram:
figcellintenshist = figure;
histogram(cellintensities,histogramvalues);
set(figcellintenshist,'DefaultAxesFontName', 'Arial', '
   ↪ DefaultAxesFontSize', 16, 'DefaultAxesFontWeight', 'Demi' );
xlabel('integrated intensity [counts]')
ylabel('occurence')
```

```
[histcounts,histcountsedges] = histcounts(cellintensities,
   ↪ histogramvalues);

figcellintens = figure;
%clf
set(figcellintens,'DefaultAxesFontName', 'Arial', 'DefaultAxesFontSize'
   ↪ , 14, 'DefaultAxesFontWeight', 'Demi' );
ax = gca();
scatter(ax,peakx,peaky,'.')
xlim([0 max(xyscale)])
ylim([0 max(xyscale)])
axis square;
cb = colorbar;
ylabel(cb,'integrated intensity [counts]')
xlabel('scale [nm]')
colormap jet(30);
%set(ax, 'YDir', 'reverse')
hold(ax, 'on');
imagesc(xyscale,xyscale,cellintensityimage);
voronoi(peakx, peaky,'w')
title('cells with corresponding intensities');
hold(ax, 'off');
```

A.2. Patch-based PCA Image Noise Filtering

HirPatchPCA.m

The function `HirPatchPCA.m` performs patch based filtering with varying patch sizes. The results are then combined and returned (`Iden`). The residual noise, that was extracted from the data set is also returned in `Ires`. `I` contains the image data. `startw` gives the minimum patch size in pixels, `PCn` the number of components that are used for the reconstruction of the data. With the flag `ansctrans` it can be chosen whether or not (with values 1 or 0) a variance stabilizing Anscombe transform is used.

Listing A.2: HirPatchPCA.m

```
function [Iden,Ires] = HirPatchPCA(I, startw, PCn, ansctrans)

  w = startw;
  minpatchno = 2; % this value defines the minimum patch size (=image
     ↪ size/minpatchno)
  ro = size(I,1);

  % perform a Anscombe transform:
  if ansctrans
    I = 2.*sqrt(double(I)+3/8);
    disp('Anscombe transform performed')
```

```
  end

  index = 1;
  tempIden = zeros(size(I));
  tempIres = zeros(size(I));
  Iden = zeros(size(I));
  Ires = zeros(size(I));

  while ro/w > minpatchno
    [tempIden,tempIres] = patchpca(I,1,PCn,w);
    Iden = Iden + tempIden;
    Ires = Ires + tempIres;
    w=w*2;
    index = index+1;
  end
  Iden = Iden./(index-1);
  Ires = Ires./(index-1);

  if ansctrans
    Iden = Iden.^2./4+sqrt(3/2)./(4.*Iden)-11./(8.*Iden.^2)+5.*sqrt
       ↪ (3/2)./(8.*Iden.^3)-1/8;
    Ires = Ires.^2./4+sqrt(3/2)./(4.*Ires)-11./(8.*Ires.^2)+5.*sqrt
       ↪ (3/2)./(8.*Ires.^3)-1/8;
    disp('Inverse Anscombe transform performed')
  end
end
```

patchpca.m

In this file one finds the core function of the patch based PCA image filtering algorithm. The data is segmented into equal sized, non-overlapping patches, that are arranged to a data matrix, which is passed to the single value decomposition function. A variant without using this function is also implemented, to ease the migration to other programming languages, if necessary. The function needs the image data `I`, the range of principal components to keep `[startPCn,endPCn]`, and the size of the patches in pixel `w`. It returns the filtered image `Output` and the residuals `Residual`, that are generated from the skipped components.

Listing A.3: patchpca.m

```
function [Output, Residual] = patchpca(I, startPCn,endPCn,w)

  [co,ro] = size(I);
  PCn = endPCn;

  Output = zeros(size(I));
  Residual = zeros(size(I));

  paco = (co / w);  % no of patch columns
  N = (co / w)^2; % number of patches necessary (number of trials)
```

```
M = w^2;  % number of pixels in a single patch (number of dimensions)
if co ~= ro || mod(co,w)~=0   % error handling
  disp('Error: patch dimensions');
end

data = zeros(M,N);

% create data set width M vectors each with dimension = number of
   ↪ pixels in a patch
D = mat2cell(I,w*ones(1,paco),w*ones(1,paco));
Res = cell(size(D));  % create cell arrays for residual
Out = cell(size(D));  % and output patches

% generate data matrix for SVD:
for i=1:N
  data(:,i) = D{i}(:);
end

dimmn = mean(data,2);
data = bsxfun(@minus, data, dimmn); % shift data to zero-mean

Z = 1/sqrt(N-1) * data';

[U,S,PC] = svd(Z,'econ'); % Singular value decomposition (without
   ↪ covariance matrix after Shlens.2014)

% columns of V are the principal component directions, the SVD
   ↪ automatically sorts these components in decreasing order of "
   ↪ principality"
%variances = diag(S) .* diag(S); % compute variances (Eigenvalues)
variances = diag(S'*S)' / (size(I,1)-1); %variance explained

% without using SVD (Shlens.2014) :
% covZ = Z' * Z;
% [V,variances] = eig(covZ);
% variances = diag(variances);
% [junk, rindices] = sort(-1*variances);
% variances = variances(rindices);
% V = V(:,rindices);

var_normalised = variances/sum(variances);
fig2 = figure;
plot(var_normalised,'*');  % scree plot of variances
set(gca,'YScale','log')
%xlim([0 50]);
xlabel('eigenvector number');
ylabel('explained variance ratio');

% automatically select number of components (experimental feature,
   ↪ TODO):
if PCn == 0
  PCn = length(var_normalised(var_normalised > 2e-2));
```

```
  end

  title(['scree plot (patchsize ' num2str(w) '), ' num2str(PCn) '
     ↪ components selected']);

  PCeff = PC(:,startPCn:PCn); % select range of PCs to keep

  PCres = PC(:,PCn:end);  % residual PCs

  PCdata = PCeff' * data; % project data onto PCs

  PCA_res = PCres * (PCres' * data);
  PCA_Out = PCeff * PCdata; % convert back to original basis

  PCA_Out = bsxfun(@plus, PCA_Out, dimmn); % shift data back
  PCA_res = bsxfun(@plus, PCA_res, dimmn); % shift data back

  % rearrange data matrix to image:
  for i=1:N
    Out{i} = reshape(PCA_Out(:,i),w,w);%+mean(D{i}(:));
    Res{i} = reshape(PCA_res(:,i),w,w);%+mean(D{i}(:));
  end

  Output = cell2mat(Out);
  Residual = cell2mat(Res);
end
```

B. Appendix: Julia Language Source Code

In the following we list the two most important Julia codes that were used in this thesis. The code is structured according to the files that were used. Both algorithms use the same file for functions (`Functions.jl`) and the definitions of constants (`Constants.jl`) which are both given at the end of this chapter.

B.1. Simulation of Beam Damage on Supported Metallic Clusters

The following code was used to explore the dynamics of supported metallic clusters under electron beam irradiation. The elastic cross sections for a specific element and electron energy needs to be formatted and saved as Matlab data file (.mat) before the calculation can be started. In this file two variables are saved, one containing the scattering angles (in degree) and one the differential cross section values (in units of the Bohr radius a_0^2). The geometry of the cluster and the substrate (if no flat substrate is used) is needed as xyz-file or is generated on the fly. In the following we only give the example of a pure cluster that is landed on an amorphous carbon substrate, which is generated randomly at the beginning. This example follows algorithm 2 (see section 3.5).
The actual simulation consists of three main steps:

- Equilibration without substrate at 0.4 K (Thermalize.jl)
- Landing and equilibration on the substrate (ThermalizeonSubstrate.jl)
- Beam damage experiment (Experiment_Dyn.jl)

The simulation is set up and started with the main file (MDMain_Dyn.jl)

Main_Dyn.jl

```
Pkg.add("MAT")
Pkg.add("Combinatorics")
@everywhere using MAT
@everywhere using Combinatorics
```

```
@everywhere include("Functions.jl");  # Functions
@everywhere include("Constants.jl");  # Function for simulation steps

# program files:
step1 = "Thermalize.jl"
step2 = "ThermalizeonSubstrate.jl"
exper = "Experiment_Dyn.jl"
main = "MDMain.jl"

HT = 300;
Temperature = 500;
element1 = "Ag";
potential1 = "QSC";
#density = 8908; # Ni in kg/m^3
density = 10490; # Ag in kg/m^3
nPart = 20;
postfix = string(element1,"_Start20170621_",nPart,"atoms_",potential1,"
   ↪ _NIST_Dynamics_",HT," kV_",Temperature,"K_test")


infilename = string("random",element1,nPart);
#infilename = "Ico_Au6525atoms_Start20150430_Au@0.4_thermalization"
prefix = "randsub_Lewissub"

outfilename = string(prefix,postfix);

if isdir(outfilename) .== false
mkdir(outfilename)
end

# substrate parameters:
# with individual atoms:
LS = 4E-9;  # lateral size
dS = 0.4E-9;  # thickness
densityS = 2000;  # density
#Ni:
# for simulating LJ substrate potential atom for atom (Huang.2003,
   ↪ Ryu2010):
# sigS = 2.852E-10;
# epsS = 0.023049 .* elch;

#Ag-C (Akbarzadeh.2014):
# epsS = 0.0301*elch;
# sigS = 3.006e-10;

#Au-C: (Lewis.2000)
sigS = 2.74e-10;
epsS = 0.022*elch;
```

```
cp(string(element1,HT,".mat"),string(outfilename,"\\",element1,HT,".mat
   ↪ "),remove_destination=true)  # copy scattering cross section
   ↪ table
cp(step1,string(outfilename,"\\",step1),remove_destination=true)
   ↪      # copy program file for 1st equilibration
cp(step2,string(outfilename,"\\",step2),remove_destination=true)
   ↪      # copy program file for 2nd equilibration
cp(exper,string(outfilename,"\\",exper),remove_destination=true)
   ↪      # copy program file for experiment
cp(main,string(outfilename,"\\",main),remove_destination=true)
   ↪      # copy this file
cp("Functions.jl",string(outfilename,"\\","Functions.jl"),
   ↪ remove_destination=true)
cp("Constants.jl",string(outfilename,"\\","Constants.jl"),
   ↪ remove_destination=true)

juliafolder = pwd();
cd(outfilename)

(a1, eps1, mSC1, nSC1, C1, m1) = SetMatParameters(element1,potential1);
   ↪     # Get material parameters for given material and potential

rcluster = ((3*nPart*m1)/(4*pi*density))^(1/3); # estimated cluster
   ↪ radius assuming a spherical geometry with given density and atom
   ↪ number

# === Set initial geometry ===s

#create random cluster and relax with MC:
(coords1, L) = create_rnd_cluster(nPart,density,m1);
nDim = size(coords1,1);

# --------- read geometry data from file --------------

# MC equilibration:
trialsperatom = 3000;
sampleFreq = 1000;
startTemp = 1000;
coords1 = MC_Cluster_relaxation(coords1,L,element1,potential1,
   ↪ trialsperatom,sampleFreq,startTemp,outfilename);

#set centre of mass of the particle to 0 0 0:
centreofmass = sum(coords1,2)./nPart;
coords1 = broadcast(-,coords1,centreofmass);
coords1[3,:] = coords1[3,:]+2E-9;

#-------------------------------------------
# creating substrate consisting of single atoms:
coordssub = create_aCsubstrate(LS,dS,densityS);
substratefilename = string("Csubstr_L",LS,"_d",dS,"_dens",densityS)
outfilename = string(prefix,infilename,substratefilename);
nPartS = size(coordssub,2);
```

```
centreofmassS = sum(coordssub,2)./nPartS;
coordssub[1:3,:] = broadcast(-,coordssub[1:3,:],centreofmassS[1:3]);
subz=0;
writeXYZ(coordssub.*1E10,"C",substratefilename);
println(string("initial number of particles: ",nPart));
println(string("substrate particles: ",nPartS));
#-------------------------------------------

sqrt2 = sqrt(2)/2;
rc = 2*a1;  # cut off distance
maxd = rc^2;    # cut of distance squared to save computation time
rNN = a1 * sqrt2*1.15;
rNN2 = rNN*rNN;

# ===========================
# P A R A M E T E R S
# ===========================

println(string("Element1: ",element1));
println(string("initial number of particles: ",nPart));

t1=t2=t3=0;

#
   ↪ ========================================================================
   ↪
# ================= M O L E C U L A R D Y N A M I C S =================
#
   ↪ ========================================================================
   ↪


# =========================================
# I N I T I A L I S A T I O N
# =========================================

# =========================================
# T H E R M A L I S A T I O N
# =========================================

tic();

nSteps = 5000;            # no of thermalization timesteps
dt = 10E-15;
Temp = 0.4;
nu = 2E12;
sampleFreq = 10;            # sampling frequency for thermalization
include(step1);
t1=toc();

# ==========================================================
# T H E R M A L I S A T I O N   O N   S U B S T R A T E
```

```
# ==========================================================
tic();

# parameter for thermalization on substrate:
nSteps = 5000;            # no of thermalization timesteps
dt = 20E-15;                # Integration time
Temp = Temperature;             # Temperature for thermalization
nu = 2E12;              # Thermostat parameter for thermalization
sampleFreq = 10;            # sampling frequency for thermalization

include(step2);

t2=toc();

writeXYZ2el(coords1.*1E10,coordssub.*1E10,element1,"C",string(element1,
   ↪ nPart,"C",nPartS,potential1,"_afterthermonsub"));

# =========================================
# E X P E R I M E N T
# =========================================

# for the experiment:

Eel = HT * 1E3 * elch;          # energy of incoming electrons in J
electronFrequ = 5000;         # Frequency of incident electrons (
   ↪ maximum time between 2 electron impacts)
nelectrons = 500000;
nSteps = 20000;               # maximum number of simulation time steps
   ↪  per electron (in integration steps)
dtE = 20E-15;                 # Integration time
Temp = Temperature;             # Simulation temperature in
nu = 2E12;                  # Thermostat parameter - frequency of
   ↪ collisions with the heat bath (0.1)
sampleFreq = 20;              # Sampling frequency

include(exper);

print_with_color(:green,"Simulation finished...");
println(t1)
println(t2)
println(t3)
cd(juliafolder)
```

Thermalize.jl

In this code a cluster is thermally equilibrated without support at 0.4 K, which is the approximate temperature of a superfluid helium droplet.

```
println("-----------------------------");
print_with_color(:green,"Thermalisation started with \n");
```

```
println(string("Temp=",Temp,"K, nu=",nu/1E12," THz", ", Time step: ",
   ↪ round(dt*1E15,1)," fs"));
println("-----------------------------");

dt2 = dt*dt;
time = 0; # Following simulation time
Epot = 0;
samplecount = 1;

Ekin1 = zeros(nPart);
Epot1 = zeros(nPart);
countNN1 = zeros(nPart);

coord_temp = zeros(nDim,nPart,round(Integer,nSteps/sampleFreq));
vels_temp = zeros(nDim,nPart,round(Integer,nSteps/sampleFreq));
countNN_temp = zeros(nPart,round(Integer,nSteps/sampleFreq)+1);
time_temp = zeros(1,round(Integer,nSteps/sampleFreq));
E_temp = zeros(2,round(Integer,nSteps/sampleFreq));

# cell list parameters:
maxnrofpairs = size(collect(combinations(1:nPart,2)),1);

# calculate initial thermal velocities:
velSTDT1 = sqrt(kB*Temp/m1);          # standard deviation of the
   ↪ velocity per dimension
vels1 = InitVels(nPart, nDim, velSTDT1, Temp);

forces1 = zeros(size(coords1));
(rhos,pairs) = calculate_rhopairs(coords1,a1, mSC1, maxd, maxnrofpairs)
forces1 = SC_ForcePL(coords1,rhos,L,pairs,a1,eps1,mSC1,nSC1,C1, maxd);

for stept=1:nSteps

  # === First integration step ===
  coords1 = coords1 + dt.*vels1 + 0.5.*dt2.*forces1./m1;
  # Update velocities
  vels1 = vels1 + 0.5.*dt.*forces1./m1;

  (rhos,pairs) = calculate_rhopairs(coords1,a1, mSC1, maxd,
     ↪ maxnrofpairs)
  forces1 = SC_ForcePL(coords1,rhos,L,pairs,a1,eps1,mSC1,nSC1,C1, maxd)
     ↪ ;

  # classical Andersen thermostat:
  for part = 1:nPart
    # Test for collisions with the Andersen heat bath
    if rand() < nu.*dt
      # If the particle collided with the bath, draw a new velocity
      # out of a normal distribution
      vels1[:,part] = randGauss(0,velSTDT1,nDim);
    end
  end
```

```
  # === Second integration step ===
  # Update velocities:
  vels1 = vels1 + 0.5.*dt.*forces1./m1;

  # === Move time forward ===
  time = time + dt;

  # === Sample ===

  if mod(stept,sampleFreq) == 0

    (Ekin1, Epot1, countNN1) = calcEnergies(coords1,L,maxd,a1,eps1,m1,
       ↪ mSC1,nSC1,C1,vels1,rNN2);

    Ekin_sum = sum(Ekin1)
    Epot_sum = sum(Epot1)

    if mod(samplecount,100) == 0
      println(string("step no: ",stept))
      println(string("Temperature of Andersen Thermostat: ",Temp," K"))
      println(string("elapsed time in simulation: ",time," s"))
      println(string("Ekin = ",Ekin_sum," J = ",Ekin_sum/elch," eV"))
      println(string("Temperature from Ekin = ",2.*Ekin_sum/(3*nPart-3)
         ↪ /kB," K"))
      println(string("Epot = ",Epot_sum," J = ",Epot_sum/elch," eV"))
      println("
         ↪ -------------------------------------------------------------
         ↪ ")
    end

    # save
    time_temp[1,samplecount] = time;
    coord_temp[1:3,:,samplecount] = coords1
    vels_temp[1:3,:,samplecount] = vels1
    E_temp[1,samplecount] = Ekin_sum;
    E_temp[2,samplecount] = Epot_sum;
    countNN_temp[:,samplecount] = countNN1

    samplecount = samplecount+1;
  end
end

# save variables to file
file = matopen(string(outfilename,"_",element1,"_@",Temp,"K_",nSteps,"
   ↪ steps_thermalization.mat"),"w")
write(file, "time", time_temp)
write(file,"coords",coord_temp)
write(file,"vels",vels_temp)
write(file,"E",E_temp)
write(file,"L",L)
write(file,"subz",0)
```

```
write(file,"sig1",a1)
write(file,"eps1",eps1)
write(file,"countNN",countNN_temp)
write(file,"element1",element1)
write(file,"nPartel1",nPart)
close(file)

println("-----------------------------");
print_with_color(:green,"Thermalisation finished, files written.\n");
println("-----------------------------");
```

ThermalizeonSubstrate.jl

The following code performs the molecular dynamics simulation of a landing event of a cluster on an amorphous carbon substrate and simulates its thermodynamic equilibration on this substrate. In the presented code the substrate is modelled as a rigid agglomeration of single carbon atoms as described in section 3.2. A similar code was used to land Ni clusters on amorphous carbon substrate, as described in section 4.2.1.

```
println("-----------------------------");
print_with_color(:green,"Thermalisation started with \n");
println(string("Temp=",Temp,"K, nu=",nu/1E12," THz", ", Time step: ",
   ↪ round(dt*1E15,1)," fs"));
println("-----------------------------");

dt2 = dt*dt;
time = 0; # Following simulation time
Epot = 0;
samplecount = 1;

v_0 = [0 0 -200]; # initial velocity of the whole cluster in m/s

Ekin1 = zeros(nPart);
Epot1 = zeros(nPart);
countNN1 = zeros(nPart);

coord_temp = zeros(nDim,nPart,round(Integer,nSteps/sampleFreq));
vels_temp = zeros(nDim,nPart,round(Integer,nSteps/sampleFreq));
countNN_temp = zeros(nPart,round(Integer,nSteps/sampleFreq)+1);
time_temp = zeros(1,round(Integer,nSteps/sampleFreq));
E_temp = zeros(2,round(Integer,nSteps/sampleFreq));

# cell list parameters:
maxnrofpairs = size(collect(combinations(1:nPart,2)),1);

# calculate initial thermal velocities:
velSTDT1 = sqrt(kB*Temp/m1); # Thermostat parameter - standard
   ↪ deviation of the velocity
vels1 = InitVels(nPart, nDim, velSTDT1, Temp);
```

```
vels1 = broadcast(+,vels1,v_0’);  # add initial velocity of the whole
   ↪ cluster

forces1 = zeros(size(coords1));

(rhos,pairs) = calculate_rhopairs(coords1,a1, mSC1, maxd, maxnrofpairs)
forces1 = SC_ForcePL(coords1,rhos,L,pairs,a1,eps1,mSC1,nSC1,C1, maxd);

for stept=1:nSteps
  tempcount = 0;
  # === First integration step ===

  coords1 = coords1 + dt.*vels1 + 0.5.*dt2.*forces1./m1;

  # Update velocities - All velocities are updated at once

  vels1 = vels1 + 0.5.*dt.*forces1./m1;

  # parallel calculation using 3 CPUs:

  parad1 = calculate_rhopairs(coords1,a1, mSC1, maxd, maxnrofpairs);

  # substrate interaction
  parad2 = @spawn sub_LJforces(coordssub[:,1:convert(Int64,round(nPartS
     ↪ /3))],coords1,sigS,epsS);
  parad3 = @spawn sub_LJforces(coordssub[:,convert(Int64,round(nPartS
     ↪ /3))+1:convert(Int64,round(2*nPartS/3))],coords1,sigS,epsS);
  parad4 = @spawn sub_LJforces(coordssub[:,convert(Int64,round(2*nPartS
     ↪ /3))+1:end],coords1,sigS,epsS);

  (subforces1,thermpartlist1) = fetch(parad2);
  (subforces2,thermpartlist2) = fetch(parad3);
  (subforces3,thermpartlist3) = fetch(parad4);
  (rhos,pairs) = fetch(parad1);

  subforces = subforces1 + subforces2+subforces3;
  thermpartlist = thermpartlist1 | thermpartlist2 | thermpartlist3;


  forces1 = SC_ForcePL(coords1,rhos,L,pairs,a1,eps1,mSC1,nSC1,C1, maxd)
     ↪  + subforces;

  #forces1 = forces1 + sub_LJforcesAuC(coords1,subz,r0,V0);
  #forces1 = forces1 + Morse_forces(coords1,subz,DM,aM,RM,rcS);

  #forces1 = forces1 + sub_LJ93forces(coords1,subz,sigs,epss,rhosub);
  #println(sub_LJ93forces(coords1,subz,sigs,epss,rhosub))

  # Implement the surface Andersen thermostat
  list = find(thermpartlist.==true)
  for part = list
```

```
  # Test for collisions with the Andersen heat bath
  if rand() < nu.*dt
    # If the particle collided with the bath, draw a new velocity out
       ↪  of a normal distribution

    vels1[:,part] = randGauss(0,velSTDT1,nDim);
    vels1[3,part] = abs(vels1[3,part]);
  end
  tempcount = tempcount + 1;
end

# === Second integration step ===
# Update velocities:
vels1 = vels1 + 0.5.*dt.*forces1./m1;

# === Move time forward ===
time = time + dt;

# === Sample ===

if mod(stept,sampleFreq) == 0

  (Ekin1, Epot1, countNN1) = calcEnergies(coords1,L,maxd,a1,eps1,m1,
     ↪ mSC1,nSC1,C1,vels1,rNN2);

  Ekin_sum = sum(Ekin1)
  Epot_sum = sum(Epot1)

  if mod(samplecount,100) == 0
    println(string("step no: ",stept))
    println(string("Temperature of Andersen Thermostat: ",Temp," K"))
    println(string("number of atoms considered for thermostat: ",
       ↪ tempcount))
    println(string("elapsed time in simulation: ",time," s"))
    println(string("Ekin = ",Ekin_sum," J = ",Ekin_sum/elch," eV"))
    println(string("Temperature from Ekin = ",2.*Ekin_sum/(3.*nPart
       ↪ -6)/kB," K"))
    println(string("Epot = ",Epot_sum," J = ",Epot_sum/elch," eV"))
    println("
       ↪ -------------------------------------------------------------
       ↪ ")
  end

  # save
  time_temp[1,samplecount] = time;
  coord_temp[1:3,:,samplecount] = coords1
  vels_temp[1:3,:,samplecount] = vels1
  E_temp[1,samplecount] = Ekin_sum;
  E_temp[2,samplecount] = Epot_sum;
  countNN_temp[:,samplecount] = countNN1

  samplecount = samplecount+1;
```

```
    end
end

# save variables to file
file = matopen(string(outfilename,"_",element1,"_@",Temp," K_",nSteps,"
   ↪ steps_substrate-thermalization.mat"),"w")
write(file, "time", time_temp)
write(file,"coords",coord_temp)
write(file,"vels",vels_temp)
write(file,"E",E_temp)
write(file,"L",L)
write(file,"subz",subz)
write(file,"sig1",a1)
write(file,"eps1",eps1)
write(file,"countNN",countNN_temp)
write(file,"element1",element1)
write(file,"nPartel1",nPart)
close(file)

println("------------------------------");
print_with_color(:green,"Thermalisation finished, files written.\n");
println("------------------------------");
```

Experiment_Dyn.jl

In this file the beam damage simulation in performed. All parameters, forces and coordinates are taken from a previous equilibration run as defined in the main file (`Main.jl`)

```
scatterfile = matopen(string(element1,HT,".mat"));
scattercross = read(scatterfile, "cross_section");  # list of cross
   ↪ sections in units of a0^2
scatterangle = read(scatterfile, "deg");  # list of angles in deg
close(scatterfile)
println(string(scatterfile," loaded."));

dt = dtE;
dt2 = dt*dt;
timeC = dt*maximum((forces1[1,:].^2+forces1[2,:].^2+forces1[3,:].^2)
   ↪ .^0.5); # variable time step after Marks.2005

time = 0; # Following simulation time

samplecount = 1;
sputterindex = 1;

displThr = a1.*(2^0.5/2)*0.98;  # displacement threshold for detection
   ↪ of a displaced atom
```

```
nPartStart = nPart;

maxnrofpairs = size(collect(combinations(1:nPart,2)),1);

#experimental parameters:
Et = 0.0;
Etmax = 2*Eel*(Eel+2*Eel0)/(c^2*m1);
Etmin = 1*elch;
nel = 1;
partdisp = 0.0;
initcoords = coords1;
precoords = zeros(size(coords1,2));
indextemp = 0;

# set theta range and power law-parameters (300 kV):
#thetamin = 0;
thetamin = 2*asin(sqrt(Etmin/Etmax))*180/pi;
thetamax = 180;

X = scatterangle[scatterangle.>=thetamin];
X = X[X.<=thetamax];
indmin = find(scatterangle.==minimum(X));
indmax = find(scatterangle.==maximum(X));
P = scattercross[indmin[1]:indmax[1]];

#crosssec = 2*pi*sum(P.*sin(scatterangle[indmin[1]:indmax[1]]./180.*pi)
   ↪ );
crosstot = 2*pi*trapz(scatterangle./180.*pi,scattercross.*sin(
   ↪ scatterangle./180.*pi))*a0^2; # trapz performs a numerical
   ↪ integration after the trapezoidal rule
crosssec = 2*pi*trapz(X./180.*pi,P.*sin(scatterangle[indmin[1]:indmax
   ↪ [1]]./180.*pi))*a0^2;

scalingfactor = crosstot/crosssec;

shottimestep = 50;
waitsteps = 500;      # steps between scattering event and 1st
   ↪ displacement check
secdispcheckstep = 100;   # steps between 1st positive displacement
   ↪ check and 2nd displacement check
maxelFreq = electronFrequ;
minelFreq = 700;

shottime = 0.2e-12; #shottimestep*dt;
waittime = 2e-12 #waitsteps*dt;
secdispchecktime = 0.4e-12 # secdispcheckstep*dt;
equilibrationtime = 50e-12 # electronFrequ*dt;

println("----------------------------");
print_with_color(:green,"Experiment started\n");
println(string("Temp=",Temp,"K, nu=",nu/1E12," THz", ", Time step: ",
   ↪ round(dt*1E15,1)," fs"));
```

```
println("-----------------------------");

shotelectrons_temp = zeros(7,nelectrons);
sputteringevents = zeros(6,nelectrons);
nel=1;
theta = 0;
atomnr = 0;
resetconfig = false;       # reset configuration every electron?

index = 0;

while nel < nelectrons && nPart >= 5

tic();
samplecount = 1;
displacement = false;
dispcheck1 = false;
thermostaton = true;
shotflag = false;
dispcheckflag = false;

timedispevent = 0;

nPart = size(coords1,2);

countNN1 = zeros(nPart);

# calculate initial thermal velocities:
velSTDT1 = sqrt(kB*Temp/m1);
vels1 = InitVels(nPart, nDim, velSTDT1, Temp);

# prepare variables for sampling:
coord_temp = zeros(nDim,nPartStart,10*convert(Int64,round((maxelFreq+
   ↪ shottimestep)/sampleFreq)));
vels_temp = zeros(nDim,nPartStart,10*convert(Int64,round((maxelFreq+
   ↪ shottimestep)/sampleFreq)));
countNN_temp = zeros(nPartStart,10*convert(Int64,round(nSteps/
   ↪ sampleFreq)+1));
time_temp = zeros(1,10*convert(Int64,round((maxelFreq+shottimestep)/
   ↪ sampleFreq)));
E_temp = zeros(2,10*convert(Int64,round((maxelFreq+shottimestep)/
   ↪ sampleFreq)));

# Calculate initial forces
forces1 = zeros(size(coords1));

(rhos,pairs) = calculate_rhopairs(coords1,a1, mSC1, maxd, maxnrofpairs)
forces1 = SC_ForcePL(coords1,rhos,L,pairs,a1,eps1,mSC1,nSC1,C1, maxd);

print_with_color(:green,"next electron nr: ");
println(nel);
print_with_color(:green,"number of electrons in reality:");
```

```
println(scalingfactor*nel);
print_with_color(:green,"Nr of atoms: ");
println(nPart);
thermalized = false;

for stept=1:nSteps

  tempcount = 0;
  # ---------------------------------
  # shot an electron:
  # ---------------------------------

  if (timedispevent >= shottime) && shotflag == false

    precoords = zeros(size(coords1,2));
    precoords = coords1; # save atom coordinates displacement check

    #theta from NIST-file:
    cdf = cumsum(P);
    theta = X[sum(cdf.< rand()*cdf[end]) + 1];     # Generating a non
       ↪ uniform discrete random variable from, scattering data
    println(string("Scattering angle chosen: ",theta))
    theta = theta*pi/180;             # scattering angle in rad

    #------------------------------------------------------------------
    atomnr = rand(1:nPart);
    (v_sc, Et, psi, phi) = calcscatteringvelvector(m1,Eel,theta);

    # calculate new velocity vector of atomnr:
    #v_sc = [v_sc[1],v_sc[3],v_sc[2]]      # beam in y direction instead
       ↪  of z
    vels1[:,atomnr] = vels1[:,atomnr] -  v_sc # supported particle
    #vels1[:,atomnr] = vels1[:,atomnr] +  v_sc  # free hanging particle

    shotelectrons_temp[6,nel] = countNN1[atomnr];
    shotelectrons_temp[7,nel] = 1;

    shotelectrons_temp[1,nel] = atomnr;
    shotelectrons_temp[2,nel] = Et;
    shotelectrons_temp[5,nel] = theta;

    thermostaton = false;   # deactivate thermostat to avoid
       ↪ pertubations during scattering event
    shotflag = true;

    print_with_color(:green,"electron shot...\nEnergy transferred by
       ↪ electron [eV]: ");
    println(Et/elch)
    print_with_color(:green,"to atom number: ");
    println(atomnr)
```

```
elseif (timedispevent >= shottime+waittime) && shotflag && dispcheck1
   ↪ == false && dispcheckflag == false
  dcoords = precoords - coords1;

  dcoordsabs = (dcoords[1,:].*dcoords[1,:]+dcoords[2,:].*dcoords
     ↪ [2,:]+dcoords[3,:].*dcoords[3,:]).^0.5;
  dsorted = sort(dcoordsabs);

  noofdisplacements = size(find((dcoordsabs .> displThr) .== true),1)
     ↪  # number of atoms displaced over threshold
  index = find(dcoordsabs .== dsorted[end])   # find largest value
  index2 = find(dcoordsabs .== dsorted[end-1])  # find second largest
     ↪  value

  print_with_color(:green,"check atom displacements...\n maximum
     ↪ displacement found: ");
  println(string(dsorted[end]*1E9," nm (displacement threshold: ",
     ↪ displThr*1E9," nm) second displacement: ",dsorted[end-1]*1E9,
     ↪ " nm"));

  print_with_color(:green,"from atom number: ");
  println(index[1]);

  # --------------------------------
  # 1. check for atom displacements:
  # --------------------------------
  if noofdisplacements >= 1   # atom movement of about 0.9 .* sigma
     ↪ is considered as permanent displacement due to electron
     ↪ impact
    println(string("calculated number of steps for current electron:
       ↪ ",stept));
    dispcheck1 = true;
    print_with_color(:yellow,string("displaced atom detected (",
       ↪ noofdisplacements," found)"));
  else
    coords1 = precoords;  # go back to initial coordinates
    dispcheckflag == true
    print_with_color(:red,"atom not displaced --> new electron!\n");
    break;
  end
elseif dispcheck1 && displacement == false && timedispevent > (
   ↪ shottime + waittime + secdispchecktime)
  # when a displacement is detected in the first check, a second
     ↪ check I steps after the first is done
  print_with_color(:yellow,", check again...\n");
  dcoords = precoords - coords1;
  dcoordsabs = (dcoords[1,:].*dcoords[1,:]+dcoords[2,:].*dcoords
     ↪ [2,:]+dcoords[3,:].*dcoords[3,:]).^0.5;
  dsorted = sort(dcoordsabs);
  noofdisplacements = size(find((dcoordsabs .> displThr) .== true),1)
     ↪  # number of atoms displaced over threshold
```

```
  indexnew = find(dcoordsabs .== dsorted[end])    # find largest
     ↪ value
  indexnew2 = find(dcoordsabs .== dsorted[end-1]) # find second
     ↪ largest value
  println(string("maximum displacement found: ",dsorted[end]*1E9," nm
     ↪  (displacement threshold: ",displThr*1E9," nm) second
     ↪ displacement found: ",dsorted[end-1]*1E9," nm"));
  print_with_color(:green,"from atom number: ");
  println(indexnew[1]);

  # ---------------------------------
  # 2. check for atom displacements:
  # ---------------------------------
  # check if displacement is over certain threshold and the displaced
     ↪  atom is still the same or if 2 atoms changed their
     ↪ postitions
  if size(find((dcoordsabs .> displThr) .== true),1) >= 1
    print_with_color(:red,string("atoms still displaced (",
       ↪ noofdisplacements," found)\n"));
    print_with_color(:red,"displacement confirmed.\n");
    println(string("calculated number of steps for current electron:
       ↪ ",stept));
    displacement = true;

    # break;
    println("calculate relaxation:");
  else
    coords1 = precoords;  # go back to initial coordinates

    displacement = false;
    #dispcheck1 = false;
    print_with_color(:red,"displacement not confirmed. --> new
       ↪ electron!\n");
    break;
  end

  dispcheck1 = false
  thermostaton = true
  dispcheckflag = true

  shotelectrons_temp[3,nel] = maximum(dcoordsabs);
  shotelectrons_temp[4,nel] = index[1];

elseif displacement && dispcheckflag && (timedispevent > (shottime +
   ↪ equilibrationtime))  # wait until relaxation and end
  #initcoords = [coords1 coords2];  # continue with actual
     ↪ configuration
  print_with_color(:blue,"relaxation finished --> save results...\n")
     ↪ ;
  break;
end
```

```
# === First integration step ===
# Update positions
coords1 = coords1 + dt.*vels1 + 0.5.*dt2.*forces1./m1;

# Update velocities
vels1 = vels1 + 0.5.*dt.*forces1./m1;

if mod(stept,20)==0
  if displacement == true

    # Check for lost atoms:
    #calculate center of particle (without accounting for mass):
    centreofmass = sum(coords1,2)./nPart;

    #-----------------------
    # ELEMENT 1:
    #-----------------------

    part=1;
    while part <= nPart
      # check if particle is outside of z-boundary
      if coords1[3,part] > L
        partdisp = part;
        lastcoords = coords1[:,partdisp];
        #delete particle outside of boundary:
        coords1 = coords1[:,[1:partdisp-1;partdisp+1:end]];
        vels1 = vels1[:,[1:partdisp-1;partdisp+1:end]];
        forces1 = forces1[:,[1:partdisp-1;partdisp+1:end]];
        countNN1 = countNN1[[1:partdisp-1;partdisp+1:end]];

        sputteringevents[1,sputterindex] = nel;   # electron number
        sputteringevents[2,sputterindex] = theta; # scattering angle
           ↪ chosen
        sputteringevents[3,sputterindex] = Et;    # transferred
           ↪ Energy to atom
        sputteringevents[4,sputterindex] = atomnr;  # atom chosen for
           ↪  energy transfer
        sputteringevents[5,sputterindex] = partdisp;  # atom lost
        sputteringevents[6,sputterindex] = 1;   # element1
        nPart = size(coords1,2);

        print_with_color(:red,string("one atom left the box (z-
           ↪ boundary, Last atom coordinates:",lastcoords,") atoms
           ↪ remaining: "));
        println(nPart)
        partdisp = 0;

        part = part - 1;
        sputterindex = sputterindex + 1;
      elseif (coords1[2,part]-centreofmass[2]) > L || (coords1[2,part
         ↪ ]-centreofmass[2]) <-L
        partdisp = part;
```

```
      lastcoords = coords1[:,partdisp];
      #delete particle outside of boundary:
      coords1 = coords1[:,[1:partdisp-1;partdisp+1:end]];
      vels1 = vels1[:,[1:partdisp-1;partdisp+1:end]];
      forces1 = forces1[:,[1:partdisp-1;partdisp+1:end]];
      countNN1 = countNN1[[1:partdisp-1;partdisp+1:end]];

      sputteringevents[1,sputterindex] = nel;    # electron number
      sputteringevents[2,sputterindex] = theta; # scattering angle
         ↪ chosen
      sputteringevents[3,sputterindex] = Et;    # transferred
         ↪ Energy to atom
      sputteringevents[4,sputterindex] = atomnr;  # atom chosen for
         ↪  energy transfer
      sputteringevents[5,sputterindex] = partdisp;  # atom lost
      sputteringevents[6,sputterindex] = 1;   # element1
      nPart = size(coords1,2);

      print_with_color(:red,string("one atom left the box (y-
         ↪ boundary, Last atom coordinates:",lastcoords,") atoms
         ↪ remaining: "));
      println(nPart)
      partdisp = 0;

      part = part-1;
      sputterindex = sputterindex + 1;
    elseif (coords1[1,part]-centreofmass[1]) > L || (coords1[1,part
       ↪ ]-centreofmass[1]) <-L
      partdisp = part;
      lastcoords = coords1[:,partdisp];
      #delete particle outside of boundary:
      coords1 = coords1[:,[1:partdisp-1;partdisp+1:end]];
      vels1 = vels1[:,[1:partdisp-1;partdisp+1:end]];
      forces1 = forces1[:,[1:partdisp-1;partdisp+1:end]];
      countNN1 = countNN1[[1:partdisp-1;partdisp+1:end]];

      sputteringevents[1,sputterindex] = nel;    # electron number
      sputteringevents[2,sputterindex] = theta; # scattering angle
         ↪ chosen
      sputteringevents[3,sputterindex] = Et;    # transferred
         ↪ Energy to atom
      sputteringevents[4,sputterindex] = atomnr;  # atom chosen for
         ↪  energy transfer
      sputteringevents[5,sputterindex] = partdisp;  # atom lost
      sputteringevents[6,sputterindex] = 1;   # element1
      nPart = size(coords1,2);

      print_with_color(:red,string("one atom left the box (x-
         ↪ boundary, Last atom coordinates:",lastcoords,") atoms
         ↪ remaining: "));
      println(nPart);
      partdisp = 0;
```

```
        part = part-1;
        sputterindex = sputterindex + 1;
      end
      part = part + 1;
    end
  end
end


#--------------------------------------------
#------------------ with substrate:
#--------------------------------------------

# parallel:

parad1 = calculate_rhopairs(coords1,a1, mSC1, maxd, maxnrofpairs);

# substrate interaction
parad2 = @spawn sub_LJforces(coordssub[:,1:convert(Int64,round(nPartS
   ↪ /3))],coords1,sigS,epsS);
parad3 = @spawn sub_LJforces(coordssub[:,convert(Int64,round(nPartS
   ↪ /3))+1:convert(Int64,round(2*nPartS/3))],coords1,sigS,epsS);
parad4 = @spawn sub_LJforces(coordssub[:,convert(Int64,round(2*nPartS
   ↪ /3))+1:end],coords1,sigS,epsS);

(subforces1,thermpartlist1) = fetch(parad2);
(subforces2,thermpartlist2) = fetch(parad3);
(subforces3,thermpartlist3) = fetch(parad4);
(rhos,pairs) = fetch(parad1);

subforces = subforces1 + subforces2+subforces3;
thermpartlist = thermpartlist1 | thermpartlist2 | thermpartlist3;

forces1 = SC_ForcePL(coords1,rhos,L,pairs,a1,eps1,mSC1,nSC1,C1, maxd)
   ↪  + subforces;

# Implement the surface Andersen thermostat
if thermostaton
list = find(thermpartlist.==true)
for part = list
  # Test for collisions with the Andersen heat bath
  if rand() < nu.*dt
    # If the particle collided with the bath, draw a new velocity out
       ↪ of a normal distribution
    vels1[:,part] = randGauss(0,velSTDT1,nDim);
    vels1[3,part] = abs(vels1[3,part]);
  end
  tempcount = tempcount + 1;
  end
end
# === Second integration step ===
```

```
# Update velocities - All velocities are updated at once
vels1 = vels1 + 0.5.*dt.*forces1./m1;

# === Move time forward ===
time = time + dt;
timedispevent = timedispevent + dt;

# adaptive dt after Marks.2015:
dt = timeC/maximum((forces1[1,:].^2+forces1[2,:].^2+forces1[3,:].^2)
   ↪ .^0.5);
dt2 = dt*dt;

# === Sample ===
if mod(stept,sampleFreq) == 0


(Ekin1, Epot1, countNN1) = calcEnergies(coords1,L,maxd,a1,eps1,m1,
   ↪ mSC1,nSC1,C1,vels1,rNN2);

Ekin_sum = sum(Ekin1)
Epot_sum = sum(Epot1)

if mod(samplecount,100) == 0
  println(string("step no: ",stept,"; number of particles: ",nPart))
  println(string("Temperature of Andersen Thermostat: ",Temp," K"))
  println(string("number of atoms considered for thermostat: ",
     ↪ tempcount))
  println(string("elapsed time in simulation: ",time," s"))
  println(string("elapsed time in current displacement event: ",
     ↪ timedispevent," s"))
  println(string("current time step: ",dt," s"))
  println(string("Ekin = ",Ekin_sum," J = ",Ekin_sum/elch," eV"))
  println(string("Temperature from Ekin = ",2.*Ekin_sum/(3.*nPart-6)/
     ↪ kB," K"))
  println(string("Epot = ",Epot_sum," J = ",Epot_sum/elch," eV"))
  println(string("Thermostat is on: ", thermostaton))
  println("
     ↪ -------------------------------------------------------------
     ↪ ")
  end

  # convert to SI units and save
  fillzero = zeros(3,size(coord_temp,2)-nPart);

  time_temp[1,samplecount] = time;
  coord_temp[1:3,:,samplecount] = hcat(coords1,fillzero);
  vels_temp[1:3,:,samplecount] = hcat(vels1,fillzero);
  E_temp[1,samplecount] = Ekin_sum;
  E_temp[2,samplecount] = Epot_sum;
```

```
  countNN_temp[:,samplecount] = vcat(countNN1,zeros(size(coord_temp
     ↪ ,2)-size(coords1,2)));
  samplecount = samplecount+1;
  end
end

if displacement
  # are there atoms with 0 coordination?
  countNNzero1 = find(countNN1.==0);
  if length(countNNzero1) > 0
  for ind = 1:length(countNNzero1)
  partdisp = countNNzero1[ind];
  coords1 = coords1[:,[1:partdisp-1;partdisp+1:end]];
  vels1 = vels1[:,[1:partdisp-1;partdisp+1:end]];
  forces1 = forces1[:,[1:partdisp-1;partdisp+1:end]];

  sputteringevents[1,sputterindex] = nel;   # electron number
  sputteringevents[2,sputterindex] = theta; # scattering angle chosen
  sputteringevents[3,sputterindex] = Et;    # transferred Energy to
     ↪ atom
  sputteringevents[4,sputterindex] = atomnr;  # atom chosen for
     ↪ energy transfer
  sputteringevents[5,sputterindex] = partdisp;  # atom lost
  sputteringevents[6,sputterindex] = 1;   # element1

  sputterindex = sputterindex + 1;
end
nPart = size(coords1,2);

print_with_color(:red,string("one atom found without neighbours (
   ↪ atoms remaining from element1: "));
println(string(nPart,")"))
partdisp = 0;
end
end
nPart = size(coords1,2);

# ===================
# Simulation results
# ===================
if displacement
writeXYZ2el(coords1.*1E10,coordssub.*1E10,element1,"C",string("
   ↪ afterexperiment_",element1,nPart,"C",nPartS,potential1,"
   ↪ _withsub","_eln",nel));
end

nel = nel + 1;

println("save electron log");
file = matopen(string(outfilename,"_",element1,"_",nSteps,"
   ↪ steps_electronlog",".mat"),"w")
write(file,"shotel",shotelectrons_temp);
```

```
    write(file,"sputtering_list",sputteringevents);
    write(file,"displacementthreshold",displThr);
    write(file,"high_tension",HT);
    write(file,"element1",element1);
    close(file)

    if resetconfig
      # reset configuration:
      coords1 = zeros(nDim,nPartStart)
      coords1 = initcoords;
      # every experiment starts with same coordinates
      println("reset configuration")
    end

    print_with_color(:green,"files saved, ");
    toc();
  end

print_with_color(:green,"maximum number of electrons reached\n");
```

B.2. Monte Carlo equilibration from STEM HAADF quantification data

The following code aims to find a possible cluster configuration based on HAADF quantification data. The starting geometry is passed to the code in xyz file format and it writes the equilibrated result both as xyz and, together with several parameters, as Matlab file. The code is written in Julia language and is described in more detail in section 3.3.

Main.jl

This file sets up everything that is needed and then starts the calculation. It needs to be started via typing `include(‘‘Main.jl‘‘)` in the Julia command window.

Listing B.1: Main.jl

```
# following packages are installed if needed:
Pkg.add("MAT")
Pkg.add("DataArrays")
Pkg.add("DataFrames")

# include the packages:
@everywhere using MAT
@everywhere using DataArrays, DataFrames

# include definitions and functions from other files:
```

```
@everywhere include("Functions.jl");  # a collection of functions
@everywhere include("Constants.jl");  # some constants

infilename = "resultfrom20170103.xyz"   # the name of the geometry
   ↪ input file
main = "Main.jl"  # the name of this file
element1 = "Au"   # the element that is considered here (could also be
   ↪ read from xyz file)
potential = "SC"  # the potential that is used for the simulation (SC=
   ↪ Sutton-Chen, QSC=Quantum Sutton-Chen, LJ=Lennard-Jones)

# the name that is used to generate the path for the output files:
postfix = string(element1,"_Start201700209_",potential,"
   ↪ _equal_onestep_onlyz_editedgeom_fac1.03")
outfilename = string("Out_",postfix);

# if the output folder does not exist, generate it:
if isdir(postfix) .== false
  mkdir(postfix)
end

cp(string(infilename),string(postfix,"\\",infilename),
   ↪ remove_destination=true)  # copy geometry file
cp(main,string(postfix,"\\",main),remove_destination=true)  # copy this
   ↪  file
cp("Functions.jl",string(postfix,"\\","Functions.jl"),
   ↪ remove_destination=true)  # copy functions file
cp("Constants.jl",string(postfix,"\\","Constants.jl"),
   ↪ remove_destination=true)  # copy constants file

juliafolder = pwd();  # save current folder
cd(postfix) # change to output folder

(a1, eps1, mSC1, nSC1, C1, m1) = SetMatParameters(element1,potential);
   ↪   # Get material parameters for given material and potential (
   ↪ defined in functions file)


# --------- read geometry data from xyz file --------------

df = readtable(infilename, separator=’ ’,decimal=’.’, skipstart=2,
   ↪ header=false);
coords = zeros(3,size(df,1));

for i=1:size(df,1)
  coords[1,i] = df[i,2];
  coords[2,i] = df[i,3];
  coords[3,i] = df[i,4];
end
coords = coords.*1.0e-10; # convert from Angstrom to metres
coords[1,:] = coords[1,:]-minimum(coords[1,:]);
coords[2,:] = coords[2,:]-minimum(coords[2,:]);
```

```
coords[3,:] = coords[3,:]-maximum(coords[3,:]);

# find dimensions of geometry (only important if periodic boundary
   ↪ conditions are used, which is not the case here)
Lx = maximum(coords[1,:])-minimum(coords[1,:]);
Ly = maximum(coords[2,:])-minimum(coords[2,:]);
Lz = maximum(coords[3,:])-minimum(coords[3,:]);

L = maximum([Lx Ly Ly])*1.5;

subz = minimum(coords[3,:])-0.35e-9;  # define a substrate plane

trialsperatom = 10000;  # how many movements do we want to make per
   ↪ atom
sampleFreq = 1000;  # how often should we do a sampling step
startTemp = 600;  # start temperature of simulated annealing

onlyz = true; # should we allow x-y movements?
coords = MC_Cluster_relaxation(coords,L,element1,potential,
   ↪ trialsperatom,sampleFreq,startTemp,outfilename,onlyz,subz);  #
   ↪ start the equilibration and return geometry

cd(juliafolder) # change back to starting folder
```

Equilibration code

The following function is called in the `Main.jl` file and performs the actual equilibration.

Listing B.2: MC_Cluster_relaxation(...)

```
function MC_Cluster_relaxation(coords1,L,element1,potential,
   ↪ trialsperatom,sampleFreq,startTemp,outfilename,onlyz,subz)

  (sig1, eps1, mSC, nSC, C, m) = SetMatParameters(element1,potential);
     ↪   # read potential paramters

  # everything is calculated in length units of sig1:
  coords1=coords1./sig1;
  subz = subz ./ sig1;

  # potential paramters used for the interaction with flat carbon
     ↪ substrate:
  # LJ Parameter for Au-C interaction aus Werner, Wanner et. al
  V0 = 0.34*elch ./ eps1; # in energy units of eps1
  r0 = 0.2885e-9 ./ sig1;

  nPart = size(coords1,2);  # number of atoms
  nDim = size(coords1,1); # number of dimensions

  t1=0; # variable for time measurements
```

```
mass = 1.0; #mass in reduced units
sqrt2 = sqrt(2)/2;
rNN = sqrt2*1.2;  # definition of nearest neighbour distance (fcc)
rNN2 = rNN^2;
rc = 4 * rNN;   # distances are in units of sigma which is a in fcc
   ↪ in SC-units (rc = 2.5*rNN, sqrt(2)/2 = APF for fcc)
maxd = 100; # define cut off radius of potential (100=no cut off)

Ntrials = trialsperatom*nPart;

Temp = startTemp / (eps1/kB); # Temperature in reduced units
beta = 1.0/Temp;
# parameters for simulated annealing
tempstep = 0.3 / (eps1/kB);
tempchangeinterval = nPart;
templowlimit = 10 / (eps1/kB);

drmax = 0.1*rNN;  # maximum trial displacements

Naccepted = 0;
Nskipped = 0;
samplecount = 1;
acceptratio = 0;
atom = 1;

countNN = calcNN(coords1,rNN2); # calculate the number of nearest
   ↪ neighbours for each atom

# set up variables to save results for each sampling:
coord_temp = zeros(size(coords1,1),size(coords1,2),round(Integer,
   ↪ Ntrials/sampleFreq));
energy_temp = zeros(round(Integer,Ntrials/sampleFreq));
countNN_temp = zeros(nPart,round(Integer,Ntrials/sampleFreq));
steps=1;

# write geometry file:
writeXYZ(coords1.*sig1.*1E10,element1,string(outfilename,"_preMC"));
println(Ntrials/nPart);

# calculate potential energies:
energy = calcEpotSC(coords1,L,maxd,mSC,nSC,C);

coords_test = zeros(size(coords1))
tic();

for steps=1:Ntrials

  # simulated annealing:
  if mod(steps,tempchangeinterval) == 0 && Temp > templowlimit+
     ↪ tempstep
    Temp = Temp - tempstep;
    beta = 1/Temp;
```

```
    elseif Temp-tempstep < templowlimit
      Temp = templowlimit;
      beta = 1/Temp;
    end

    atom = round(Integer,floor(rand()*nPart)+1);  # select an atom randomly

    rnew = drmax.*(rand(nDim)-0.5); # generate random displacement vector
    if onlyz==true
      rnew[1:2] = 0;  # keep x-y coordinates constant
      #rnew[1:2] = rnew[1:2].*0.2;  # allow only small changes in the x-y plane
    end
    trialpos = coords1[:,atom] + rnew;

    if trialpos[3] <=subz # if the displacement points outside of surface potential
      trialpos[3] = subz+r0;
    end

    coords1_trial = deepcopy(coords1);
    coords1_trial[:,atom] = trialpos;

    deltV = calcdeltV_SC(coords1,trialpos,mSC,nSC,C,maxd,atom);

    # LJ Au-aC Interaction:
    deltV = deltV + sub_LJdeltaEAuC(coords1[:,atom],trialpos,subz,r0,V0,atom);

    deltVb = beta * (deltV);

    if deltVb < 0.0
      coords1[:,atom] = trialpos;
      energy = energy + deltV;
      Naccepted = Naccepted + 1;
    elseif exp(-deltVb) > rand()
      coords1[:,atom] = trialpos;
      energy = energy + deltV;
      Naccepted = Naccepted + 1;
    end

    # Sampling:

    if mod(steps,sampleFreq) == 0
      acceptratio = Naccepted/sampleFreq;

      # keep acceptratio at 0.5 and change drmax accordingly:
      if acceptratio > 0.5
        drmax = drmax * 1.05;
```

```
        println(string("maximum displacement changed to ",drmax.*sig1))
           ↪ ;
      elseif acceptratio < 0.5
        drmax = drmax * 0.95;
        println(string("maximum displacement changed to ",drmax.*sig1))
           ↪ ;
      end
      Naccepted = Nskipped = 0;

      coord_temp[1:3,:,samplecount] = coords1.*sig1;
      energy_temp[samplecount] = energy.*eps1;
      println(energy_temp[samplecount]);
      samplecount = samplecount + 1;
      println(string("Step: ",steps," of ",Ntrials," Temperature: ",
         ↪ Temp*(eps1/kB)," ",acceptratio*100," %"))
      t1 = toc();
      tic();
      println(string((Ntrials-steps)*t1/3600/sampleFreq," hours
         ↪ remaining..."))
      if mod(steps,sampleFreq*100) == 0
        writeXYZ(coords1.*sig1.*1E10,element1,string(outfilename,"_",
           ↪ element1,"_",Ntrials,"_",steps));
      end
    end
  end

  writeXYZ(coords1.*sig1.*1E10,element1,string(outfilename,"
     ↪ _MCresult_trialsteps",Ntrials));

  println(energy_temp[1])
  println(energy_temp[end])

  # save variables to file
  file = matopen(string(outfilename,"_",element1,"_",Ntrials,".mat"),"w
     ↪ ")
  write(file,"coords1",coord_temp)
  write(file,"energy",energy_temp)
  write(file,"countNN",countNN_temp)
  write(file,"L",L)
  #write(file,"subz",subz.*sig1)
  write(file,"sig1",sig1)
  write(file,"eps1",eps1)
  close(file)

return coords1.*sig1  # convert to SI length scale
end
```

General function definitions

Functions that are used in both codes above are bundled in the `Functions.jl` file that is given in the following.

Listing B.3: Function.jl

```
function randGauss(mu,sigma,nDim)
  # Generate normally distributed random numbers
  randNums = randn(nDim,1);

  # Shift to match given mean and std
  randNums = mu + randNums * sigma;
  return randNums
end

function rndPowerLaw(min,max,a,b)

  numberfound = false;
  randnum = 0;
  while numberfound != true
    randnum = (-rand()*(b+1)/a).^(1/(b+1));
    if randnum > min && randnum < max
      numberfound = true;
    end
  end

  return randnum
end

function PBC3D(vec,L)
    # Vector should be in the range 0 -> L in all dimensions
    # Therefore, we need to apply the following changes if it's not in
       ↪ this range:
  for dim=1:3
    if (vec[dim] > L)
      vec[dim] = vec[dim]-L;
    elseif (vec[dim] < 0)
      vec[dim] = vec[dim]+L;
    end
  end
  return vec
end

function create_rnd_cluster(nPart,density,Amass)

  println("creating cluster...")
  rmin = 0.25E-9; # nm
  coords = zeros(3,nPart);

  rcluster = ((3*nPart*Amass)/(4*pi*density))^(1/3);
```

```
  rmin2 = rmin^2;
  rmax = 1.3*rcluster;
  L = 2*rmax;

  accept = 1;
  count=1;

  skipped = 0;

  while count!=nPart+1

    r = abs(randn()) .* 1.2 .* rcluster;
    if r>rmax
      continue;
    end
    #r= rand().* 3.*rcluster;
    theta = rand()*pi;
    phi = rand()*2*pi;

    coords[:,count] = [r*sin(theta)*cos(phi);r*sin(theta)*sin(phi);r*
      ↪ cos(theta)];

    for part=1:size(coords,2)

      if part == count
        continue;
      end

      dr = coords[:,part] - coords[:,count];
      dr2 = dot(dr,dr);

      if dr2 < rmin2
        accept = 0;
      end
    end

    if accept == 1
      println(count)
      count = count + 1;
    else
      accept = 1;
      skipped = skipped + 1;
    end

  end

  return coords, L
end

function Morse_forces(coords,z,D,a,R,rc)
```

```
  # Parameters:
  nPart = size(coords,2);
  Mforces=zeros(3,nPart);
  #Epot = zeros(1,nPart);

  # Loop over all particles:
  for part = 1:nPart
    # Calculate particle-substrate distance
    dr = coords[3,part]-z;
    if dr<rc
      expf = exp(a*(R-dr));

      Mforces[3,part] = 2*a*D*expf*(expf-1);
      #Epot[part] = Epot[part] + (D*((1-expf)^2-1));
    end
  end
  return Mforces#, Epot
end

function sub_LJforcesAuC(coords,z,r0,D)

  # Parameters:
  nPart = size(coords,2);
  LJforces=zeros(3,nPart);
  #Epot = zeros(1,nPart);

  # D = 1.5;  # in units of epsilon
  # a = 1.5;     # a=(ke/(2*D))^0.5
  # R = 1;    # position of potential minimum (covalent radius of
     ↪ carbon 77 pm)

  # Loop over all particles:
  for part = 1:nPart
    # Calculate particle-substrate distance
    dr = coords[3,part]-z;
    #nen2 = (dr/r0-1.2)^6;

    # (-1211.76+70.38 (-1.2+x/r0)^6)/(r0 (-1.2+x/r0)^13)
    LJforces[3,part] = -D*(207*(dr/r0-1.2)^6-3564)/(r0*(dr/r0-1.2)^13);
    #Epot[part] = Epot[part] + (D*((1-expf)^2-1));
  end
  return LJforces#, Epot
end

function sub_LJforces(coordssub,coords,sig,eps)

  coordssub = coordssub./sig;
  coords = coords./sig;

  # Parameters:
  nPart = size(coords,2);
  nPartS = size(coordssub,2);
```

```
  LJforces = zeros(3,nPart);
  Epot=0;
  maxd = 16;#16;
  thermpartlist = falses(nPart);
  rNN2 = 1.3^2;

  # Loop over all particles:
  for part = 1:nPart
    for partS = 1:nPartS

      dr = coordssub[:,partS] - coords[:,part];

      dr2 = dot(dr,dr) # = dr[1].*dr[1]+dr[2].*dr[2]+dr[3].*dr[3]

      if dr2<maxd

        invDr2 = 1/dr2; # sigma/r^2
        invDr6 = invDr2^3;
        forceFact = invDr2^4 * (invDr6 - 0.5);

        LJforces[:,part] = LJforces[:,part] - dr*forceFact;

        if dr2<rNN2;
          thermpartlist[part] = true;
        end
        Epot = Epot + invDr6 * (invDr6-1);
      end
    end
  end
  LJforces = 48.*LJforces.*(eps./sig);  # convert forces to SI - units

  # delete double elements from thermalisation list:
  thermpartlist = [unique(thermpartlist);zeros(nPart-length(
     ↪ thermpartlist))];

  return LJforces,thermpartlist, Epot
end

function cell_list(pos,ncel,rcel) #generating cell_list

  # pos... coordinates of each particle (nDim,nPart)
  # ncel... number of cells per dimension
  # rcel... size of a cell
  # n... label of particles
  # cellx,celly,cellz... id of the cell for certain atom
  # link(nPart)
  # cell(1:ncel,1:ncel,1:ncel)

  nDim = size(pos,1);
  nPart = size(pos,2);

  # initialize link- and cell-list
```

```
  link = round(Integer,zeros(nPart));

  celll = zeros(ncel,ncel,ncel);

  # avoid negative indices:
  pos = broadcast(+,pos,abs(minimum(pos)));

  #set up the cell list
  for n = 1:nPart #scan all atoms
    #locate the atom to certain cell
    cellx = round(Integer,pos[1,n]./rcel)+1;
    celly = round(Integer,pos[2,n]./rcel)+1;
    cellz = round(Integer,pos[3,n]./rcel)+1;
    #insert the atom into the link list of the corresponding cell

    link[n] = celll[cellx,celly,cellz]; # link list: in which cell can
       ↪ each atom be found
    celll[cellx,celly,cellz] = n;      # cell list: contains the head of
       ↪  the corresponding link list
  end

  return link,celll
end

function distPBC3D(vec,L)
# Calculate the half box size in each direction
hL = L./2.0;
# Distance vector should be in the range -hLx -> hLx and -hLy -> hLy
# Therefore, we need to apply the following changes if it's not in this
   ↪  range:
  for dim=1:3
    if (vec[dim] > hL)
      vec[dim] = vec[dim]-L;
    elseif (vec[dim] < -hL)
      vec[dim] = vec[dim]+L;
    end
  end
return vec
end

function InitVels(nPart, nDim, velSTDT, TempT)
  # Set initial velocities with random numbers
  vels1 = zeros(nDim,nPart);
  for part=1:nPart
    vels1[:,part] = randGauss(0,velSTDT,nDim);
  end

  # Set initial momentum to zero
  totV = sum(vels1,2)/nPart; # Center of mass velocity
  for dim=1:nDim
    vels1[dim,:] = vels1[dim,:] - totV[dim];    # Fix any center-of-
       ↪ mass drift
```

```
  end
return vels1
end

function calculate_rho(coords, m, a, maxd)

  nPart = size(coords,2);
  rho = zeros(nPart);

  for partA = 1:nPart-1
    for partB = (partA+1):nPart

      dr = coords[:,partA] - coords[:,partB];
      # Fix according to periodic boundary conditions
      # dr = distPBC3D(dr,L);

      dr2 = dot(dr,dr) # = dr[1].*dr[1]+dr[2].*dr[2]+dr[3].*dr[3]

      if dr2<maxd
        sumrho = (a/(dr2^0.5))^m;
        rho[partA] = rho[partA] + sumrho;
        rho[partB] = rho[partB] + sumrho;
      end
    end
  end

  rhos = rho.^(-0.5);

  return rhos
end

function calculate_rhopairs2el(coords1,a1,m1,coords2,a2,m2,a12,m12,maxd
   ↪ ,maxnrpair)

  x = [coords1 coords2];

  nPart1 = size(coords1,2);
  nPart2 = size(coords2,2);
  nPart = size([coords1 coords2],2);

  rho1 = zeros(nPart1);
  rho2 = zeros(nPart2);
  rho = zeros(nPart);

  pairs = round(Integer,zeros(maxnrpair,2));

  pairlen = 1;

  for partA = 1:nPart-1
    for partB = (partA+1):nPart

      dr = x[:,partA] - x[:,partB];
```

```
      # Fix according to periodic boundary conditions
      # dr = distPBC3D(dr,L);

      dr2 = dot(dr,dr) # = dr[1].*dr[1]+dr[2].*dr[2]+dr[3].*dr[3]

      if dr2<maxd
        if partA < nPart1
          if partB < nPart1
            sumrho = (a1/(dr2^0.5))^m1;
            rho[partA] = rho[partA] + sumrho;
            rho[partB] = rho[partB] + sumrho;
          else
            sumrho = (a12/(dr2^0.5))^m12;
            rho[partA] = rho[partA] + sumrho;
            rho[partB] = rho[partB] + sumrho;
          end
        else
          if partB < nPart1
            sumrho = (a12/(dr2^0.5))^m12;
            rho[partA] = rho[partA] + sumrho;
            rho[partB] = rho[partB] + sumrho;
          else
            sumrho = (a2/(dr2^0.5))^m2;
            rho[partA] = rho[partA] + sumrho;
            rho[partB] = rho[partB] + sumrho;
          end
        end
        pairs[pairlen,:] = [partA,partB];
        pairlen = pairlen + 1;
      end
    end
  end

  # rhos1 = rho1.^(-0.5);
  # rhos2 = rho2.^(-0.5);
  rhos = rho.^(-0.5);
  pairs = pairs[1:pairlen-1,:];

  return rhos,pairs
end

function SC_ForcePL2el(coords1,coords2,rhos,L,pairs,a1,a2,a12,eps1,eps2
   ↪ ,eps12,m1,m2,m12,n1,n2,n12,C1,C2,maxd)

  nPart1 = size(coords1,2);
  X = [coords1 coords2];
  nPart = size(X,2);
  forces = zeros(size(X));
  # Loop over all particle pairs
  pairslen = size(pairs,1);
  for pair = 1:pairslen
      # Calculate particle-particle distance
```

```
      dr = X[:,pairs[pair,1]] - X[:,pairs[pair,2]];
      # Fix according to periodic boundary conditions
      # dr = distPBC3D(dr,L);

      dr2 = dot(dr,dr) # = dr[1].*dr[1]+dr[2].*dr[2]+dr[3].*dr[3]

      if pairs[pair,1] < nPart1
        if pairs[pair,2] < nPart1
          drs = a1/(dr2^0.5);
          forceFact = (eps1*n1*drs^n1-0.5*eps1*C1*m1*drs^m1*(rhos[pairs
             ↪ [pair,1]]+rhos[pairs[pair,2]]))/dr2;
        else
          drs = a12/(dr2^0.5);
          forceFact = (eps12*n12*drs^n12-0.5*eps1*C1*m12*drs^m12*(rhos[
             ↪ pairs[pair,1]]+rhos[pairs[pair,2]]))/dr2;
        end
      else
        if pairs[pair,2] < nPart1
          drs = a12/(dr2^0.5);
          forceFact = (eps12*n12*drs^n12-0.5*eps2*C2*m12*drs^m12*(rhos[
             ↪ pairs[pair,1]]+rhos[pairs[pair,2]]))/dr2;
        else
          drs = a2/(dr2^0.5);
          forceFact = (eps2*n2*drs^n2-0.5*eps2*C2*m2*drs^m2*(rhos[pairs
             ↪ [pair,1]]+rhos[pairs[pair,2]]))/dr2;
        end
      end

      forces[:,pairs[pair,1]] = forces[:,pairs[pair,1]] + dr*forceFact;
      forces[:,pairs[pair,2]] = forces[:,pairs[pair,2]] - dr*forceFact;
  end

  return forces
end

function SC_ForcePL(coords,rhosqrtr,L,pairs,a,epsilon,m,n,C, maxd)

  forces = zeros(size(coords));
  nPart = size(coords,2);

  # Loop over all particle pairs
  pairslen = size(pairs,1);

  for pair = 1:pairslen
      # Calculate particle-particle distance
      dr = coords[:,pairs[pair,1]] - coords[:,pairs[pair,2]];
      # Fix according to periodic boundary conditions
      # dr = distPBC3D(dr,L);

      dr2 = dot(dr,dr) # = dr[1].*dr[1]+dr[2].*dr[2]+dr[3].*dr[3]

      drs = a/dr2^0.5;
```

```
      forceFact = (n*drs^n-0.5*C*m*drs^m*(rhosqrtr[pairs[pair,1]]+
         ↪ rhosqrtr[pairs[pair,2]]))/dr2;

      forces[:,pairs[pair,1]] = forces[:,pairs[pair,1]] + dr*forceFact;
      forces[:,pairs[pair,2]] = forces[:,pairs[pair,2]] - dr*forceFact;
  end

  forces = epsilon .* forces;
  return forces
end

function SC_Force(coords,L,a,epsilon,m,n,C, maxd)

  forces = zeros(size(coords));
  nPart = size(coords,2);

  rhosqrtr = zeros(nPart);
  rhosqrtr = calculate_rho(coords, m, a, maxd);
  forceattr = 0;
  # Loop over all particle pairs
  for partA = 1:nPart-1
    for partB = (partA+1):nPart
      # Calculate particle-particle distance
      dr = coords[:,partA] - coords[:,partB];
      # Fix according to periodic boundary conditions
      # dr = distPBC3D(dr,L);
      dr2 = dot(dr,dr) # = dr[1].*dr[1]+dr[2].*dr[2]+dr[3].*dr[3]
      if dr2<maxd
        drs = a/dr2^0.5;
        forceFact = (n*drs^n-0.5*C*m*drs^m*(rhosqrtr[partA]+rhosqrtr[
           ↪ partB]))/dr2;
        forces[:,partA] = forces[:,partA] + dr*forceFact;
        forces[:,partB] = forces[:,partB] - dr*forceFact;
      end
    end
  end
  forces = epsilon .* forces;
  return forces
end

function calcEnergies(coords,L,maxd,a,epsilon,mass,m,n,C,vels,NNthres)

  nPart = size(coords,2);
  countNN = zeros(nPart);
  Ekin = zeros(nPart);
  Epot = zeros(nPart);

  rhosqrtr = zeros(nPart);
  rhosqrtr = calculate_rho(coords, m, a, maxd);

  # Loop over all particle pairs
```

```
  for partA = 1:nPart-1
    for partB = (partA+1):nPart
      # Calculate particle-particle distance
      dr = coords[:,partA] - coords[:,partB];
      # Fix according to periodic boundary conditions
      # dr = distPBC3D(dr,L);
      dr2 = dot(dr,dr) # = dr[1].*dr[1]+dr[2].*dr[2]+dr[3].*dr[3]
      if dr2<maxd
        drs = a/(dr2^0.5);
        Epot[partA] = Epot[partA] + drs^n - C* rhosqrtr[partA];
        Epot[partB] = Epot[partB] + drs^n - C* rhosqrtr[partB];
        if dr2<NNthres
          countNN[partA] = countNN[partA] + 1;
          countNN[partB] = countNN[partB] + 1;
        end
      end

    end
  end

  for i = 1:nPart
    Ekin[i] = dot(vels[:,i],vels[:,i])*0.5*mass;
  end
  Epot = Epot * epsilon;
  return Ekin, Epot, countNN
end

function calcEpotSC(coords,L,maxd,m,n,C)

  a = 1;
  epsilon = 1;
  Epot = 0;
  nPart = size(coords,2);
  rho = zeros(nPart);
  rho = calculate_rho(coords, m, a, maxd);

  # Loop over all particle pairs
  for partA = 1:nPart
    for partB = 1:nPart
      if partA == partB
        continue
      end

      # Calculate particle-particle distance
      dr = coords[:,partA] - coords[:,partB];
      # Fix according to periodic boundary conditions
      # dr = distPBC3D(dr,L);

      dr2 = dot(dr,dr) # = dr[1].*dr[1]+dr[2].*dr[2]+dr[3].*dr[3]

      if dr2<maxd
        drs = 1/(dr2^0.5);
```

```
        Epot = Epot + 0.5*(a*drs)^n;
      end
    end
    Epot = Epot - C*rho[partA].^0.5;
  end

  return Epot
end

function calcdrspairs(coords,pairs)

  pairslen = size(pairs,1);
  drspairs = zeros(pairslen);

  for pair = 1:pairslen

      # Calculate particle-particle distance
      dr = coords[:,pairs[pair,1]] - coords[:,pairs[pair,2]];

      dr2 = dot(dr,dr);
      drs = 1/(dr2^0.5);
      drspairs[pair] = drs;
  end

  return drspairs
end

function create_neighbourlist(x, rc, srgdat, frc, maxnebr)

  x = x';

  nx = size(x,1);
  maxd = rc^2;

  region = srgdat[1,4:6];
  (celllist, ncell, cell_offset, noffset, id_cell) = make_celllist_cube
     ↪ (region, 1.2*rc, broadcast(-,x,srgdat[1,1:3]), nx, frc);

  # init.
  # maxnebr = 200 * nx;
  maxnebr = 2*maxnebr;
  nebrTab = zeros(maxnebr, 1);
  nebrLen = 0;

  # creating neighborlist
  for k = 1:ncell[3]
    for j = 1:ncell[2]
      for i = 1:ncell[1]
        # 1st cell
        m1 = round(Integer,(k-1)*ncell[2]*ncell[1] + (j-1)*ncell[1] + i
           ↪ );
        for l = 1:noffset
```

```
          # 2nd cell
          m2v = [i j k] + cell_offset[l, :];
          p1  = celllist[ m1 + nx];
          if all( ncell - m2v .>= 0) && all( m2v .> 0)
            m2  = round(Integer,(m2v[3]-1)*ncell[2]*ncell[1] + (m2v
               ↪  [2]-1)*ncell[1] + m2v[1]);
            p2  = celllist[m2 + nx];
            while p1 != -1
              while p2 != -1
                if m1 != m2 || p1 > p2

                  dr = vec(x[p1, :] - x[p2, :]);
                  dr2 = dot(dr,dr);
                  if dr2 <= maxd
                      nebrLen = nebrLen + 2;
                    if nebrLen > maxnebr
                      println(string("too many neighbours (",nebrLen,"
                         ↪ > ",maxnebr,")"));
                      println();
                      return;
                    end
                    nebrTab[nebrLen - 1] = p1;
                    nebrTab[nebrLen]     = p2;
                  end
                end
                p2 = celllist[p2];
              end
              p2 = celllist[m2 + nx];
              p1 = celllist[p1];
            end
          end
        end
      end
    end
  end

  nebrTab = round(Integer,nebrTab[1:nebrLen]);

  nebrTab = [nebrTab[1:2:end] nebrTab[2:2:end]];
  nebrLen = nebrLen / 2;

  return nebrTab, nebrLen, ncell, id_cell
end

##############################################################
function make_celllist_cube(region, rc, atom, natom, frc)
  # create celllist, further used for neighborlist #
  # WZ. Shan                                       #
  ##################################################
  # input:
  #   region: region data [ W, H, D]
  #   rc    : cutoff radius of atomic potential
```

```
  #   atom  : [ x y z] of atoms
  #   natom : num. of atoms
  #   frc   : cell size factor
  # output:
  #   celllist: link-list of atoms in cells
  #   ncell   : num. of cells
  #   cell_offset : offset of neighboring cells
  #   noffset     : num. of offset
  #   id_cell     : cell coordinates

  cell_offset = [0 0 0;1 0 0;1 1 0;0 1 0;-1 1 0;0 0 1;1 0 1;1 1 1;0 1
     ↪ 1;-1 1 1;-1 0 1;-1 -1 1;0 -1 1;1 -1 1 ];
  noffset     = 14;

  # build cell list
  ncell = floor( region / rc / frc);

  # cell index for each atom
  id_cell = floor( atom / rc / frc) + 1;

  id_cell[id_cell[:, 1] .> ncell[1], 1] = ncell[1];
  id_cell[id_cell[:, 1] .< 1, 1]        = 1;
  id_cell[id_cell[:, 2] .> ncell[2], 2] = ncell[2];
  id_cell[id_cell[:, 2] .< 1, 2]        = 1;
  id_cell[id_cell[:, 3] .> ncell[3], 3] = ncell[3];
  id_cell[id_cell[:, 3] .< 1, 3]        = 1;

  # celllist, initialize
  celllist = -1 * ones(round(Integer,natom + prod(ncell)), 1);

  # assign celllist
  for i = 1:natom
    # linear index
    c = (id_cell[i, 3]-1) * ncell[1] * ncell[2] + (id_cell[i, 2]-1) *
       ↪ ncell[1] + id_cell[i, 1] + natom;

    # insert at the head of the linked list
    celllist[i] = celllist[c];
    celllist[c] = i;
  end

  return celllist, ncell, cell_offset, noffset, id_cell
end

function SetMatParameters(element1,potential)

if potential == "SC"
  if element1 == "Ni"
    # eps1 = epsNi;
    # sig1 = sigNi;
    m = 58.6934*u;
```

```
    # Sutton-Chen (aus Todd.1993):
    mSC=6;
    nSC=9;
    C=39.432;
    eps = 182.29 * kB;
    sig = 0.352E-9;

  elseif element1 == "Au"
    m = 3.27E-25;

    # Sutton-Chen (aus Sutton & Chen 1990):
    mSC=8;
    nSC=10;
    C=34.408;
    eps = 0.012793 * elch;
    sig = 0.408E-9;
  elseif element1 == "Ag"
    m = 1.791E-25;

    # Sutton-Chen (aus Sutton & Chen 1990):
    mSC=6;
    nSC=12;
    C=144.41;
    eps = 0.0025415 * elch;
    sig = 0.409E-9;
  elseif element1 == "Cu"
    m = 63.546*u;;

    # Sutton-Chen (aus Sutton & Chen 1990):
    mSC=6;
    nSC=12;
    C=39.432;
    eps = 1.2382E-2 * elch;
    sig = 0.361E-9;
  elseif element1 == "Pt"
    m = 195.08*u;

    # quantum Sutton-Chen
    mSC = 8;
    nSC = 10;
    C = 71.336;
    eps = 230.14*kB;
    sig = 0.392E-9;
  end
elseif potential == "LJ"

  # Lennard-Jones potentials:
  if element1 == "Au"
    eps =  0.229*elch;  # in J nach Heinz et al. Accurate Simulation of
       ↪ Surfaces and interfaces
    sig = 0.2951E-9;  # sigma in m
    m = 3.27E-25; # gold mass in kg
```

```
  elseif element1 == "Ag"
    #epsAg = 0.345.*elch; # Guan et al. MD simulations of Ag film
       ↪ growth using the Lennard-Jones potential
    #sigAg = 0.2644E-9;   # Guan et al.
    eps = 0.1977*elch;    # nach Heinz et al.
    sig = 0.2955E-9;    # Heinz et al.
    m = 107.86*u;

  elseif element1 == "Ni"
    eps = 0.245*elch;   # Heinz et al.
    sig = 0.2552E-9;    # Heinz et al.
    m = 58.6934*u;
  end
  mSC = nSC = C = 0;

elseif potential == "QSC"
#T. Cagin, Y. Qi, H. Li, Y. Kimura, H. Ikeda, W.L. Johnson, W.A.
   ↪ Goddard III, The quantum Sutton-Chen many-body potential for
   ↪ properties of fcc metals, MRS Symposium Ser. 554 (1999) 43.
  if element1 == "Ni"
    m = 58.6934*u;

    # quantum Sutton-Chen
    mSC = 5;
    nSC = 10;
    C = 84.745;
    eps = 7.3767E-3 * elch;
    sig = 0.35157E-9;

  elseif element1 == "Au"
    m = 3.27E-25;

    #quantum Sutton-Chen:
    mSC = 8;
    nSC = 11;
    C = 53.581;
    eps = 7.8052E-3 * elch;
    sig = 0.40651E-9;
  elseif element1 == "Ag"
    m = 1.791E-25;

    mSC = 6;
    nSC = 11;
    C = 96.524;
    eps = 3.9450E-3 * elch;
    sig = 0.40691E-9;

  elseif element1 == "Cu"
    m = 63.546*u;

    # quantum Sutton-Chen
    mSC = 5;
```

```
    nSC = 10;
    C = 84.843;
    eps = 5.7921E-3 * elch;
    sig = 0.36030E-9;
  elseif element1 == "Pt"
    m = 195.08*u;

    # quantum Sutton-Chen
    mSC = 7;
    nSC = 11;
    C = 71.336;
    eps = 9.7894E-3 * elch;
    sig = 0.39163E-9;
  end
end

return sig, eps, mSC, nSC, C, m
end

function writeXYZ(X,element,filename)

  nPart = size(X,2);
  file = open(string(filename,".xyz"),"w")
  write(file,string(nPart,"\n\n"));
  for ii = 1:nPart;
    write(file,string(element," ",X[1,ii]," ",X[2,ii]," ",X[3,ii],"\n")
       ↪ );
  end
  close(file);
  println(string(filename,".xyz"," written!"));
end

function writeXYZ2el(X1,X2,element1,element2,filename)

  nPart1 = size(X1,2);
  nPart2 = size(X2,2);

  file = open(string(filename,".xyz"),"w")
  write(file,string(nPart1+nPart2,"\n\n"));
  for ii = 1:nPart1;
    write(file,string(element1," ",X1[1,ii]," ",X1[2,ii]," ",X1[3,ii],"
       ↪ \n"));
  end
  for ii = 1:nPart2;
    write(file,string(element2," ",X2[1,ii]," ",X2[2,ii]," ",X2[3,ii],"
       ↪ \n"));
  end
  close(file);

  println(string(filename,".xyz"," written!"));
end
```

```
function calcdeltV_SC(coords,trialPos,mSC,nSC,C,maxd,part)

    a = 1;
    deltaE = 0;
    deltaErep = 0;
    repENew = 0;
    repEOld = 0;

        # Get the number of particles
        nPart = size(coords,2);

    coords_New = zeros(size(coords));
    coords_New = deepcopy(coords);
    coords_New[:,part] = trialPos;

    rho_Old = 0;
    rho_New = 0;
    rho_Old = calculate_rhoMC(coords, mSC, a, maxd,part);
    rho_New = calculate_rhoMC(coords_New, mSC, a, maxd,part);


        for otherPart = 1:nPart

            # Make sure to skip particle 'part' so that we don't
               ↪ calculate self
            # interaction
            if otherPart == part
                continue
            end
            # Calculate particle-particle distance for both the old and
               ↪  new
            # configurations
            drNew = coords[:,otherPart] - coords_New[:,part];
            drOld = coords[:,otherPart] - coords[:,part];

            # Get the distance squared
            dr2_New = dot(drNew,drNew);
            dr2_Old = dot(drOld,drOld);

      repENew = repENew + 0.5*(a/sqrt(dr2_New))^nSC;
      repEOld = repEOld + 0.5*(a/sqrt(dr2_Old))^nSC;
        end
    ENew = repENew - C*(rho_New)^0.5
    EOld = repEOld - C*(rho_Old)^0.5

    deltaE = ENew - EOld;

    return deltaE
end

function calculate_rhoMC(coords, mSC, a, maxd, part)
```

```
  nPart = size(coords,2);
  rho = 0;
  for partB = 1:nPart
    if partB == part
      continue
    end
    dr = coords[:,partB] - coords[:,part];
    dr2 = dot(dr,dr) # = dr[1].*dr[1]+dr[2].*dr[2]+dr[3].*dr[3]
    if dr2<maxd
      sumrho = (a/(dr2^0.5))^mSC;
      rho = rho + sumrho;
    end
  end
  return rho
end

function sub_LJdeltaEAuC(oldPos,trialPos,z,r0,D,part)

  # nach Wanner et al. (2005)
  deltaE = 0;

  drOld = oldPos[3] - z;
  drNew = trialPos[3] - z;

  # Get the distance squared
  dr_New = dot(drNew,drNew)^0.5;
  dr_Old = dot(drOld,drOld)^0.5;

  ENew = D * (297/(dr_New/r0-1.2)^12 - 34.5/(dr_New/r0-1.2)^6);
  EOld = D * (297/(dr_Old/r0-1.2)^12 - 34.5/(dr_Old/r0-1.2)^6);

  deltaE = ENew - EOld;
  return deltaE
end

function calcNN(coords,NNthres)

  nPart = size(coords,2);
  countNN = zeros(nPart);
  # Loop over all particle pairs
  for partA = 1:nPart-1
    for partB = (partA+1):nPart
      # Calculate particle-particle distance
      dr = coords[:,partA] - coords[:,partB];
      # Fix according to periodic boundary conditions
      # dr = distPBC3D(dr,L);

      dr2 = dot(dr,dr) # = dr[1].*dr[1]+dr[2].*dr[2]+dr[3].*dr[3]

      if dr2<NNthres
        countNN[partA] = countNN[partA] + 1;
        countNN[partB] = countNN[partB] + 1;
```

```
      end

    end
  end

  return countNN
end


function create_aCsubstrate(L,d,density)
  rmin = 0.145E-9; # nm
  # L=4;
  # d=0.5;
  range = [L ; L ; d]; # m
  # density = 2200; # kg/m2
  Amass = 12.011*u; # kg

  rmin2 = rmin^2;
  nPart = round(Integer,range[1]*range[2]*range[3]*density./Amass);
  accept = 1;
  count=1;
  coords = zeros(3,nPart);

  skipped = 0;

  while count!=nPart+1
    coords[:,count] = rand(3,1).*range;

    for part=1:size(coords,2)
      if count == part
        continue;
      end
      dr = coords[:,count] - coords[:,part];
      dr2 = dot(dr,dr);
      if dr2 < rmin2
        accept = 0;
      end
    end
    if accept == 1
    count = count + 1
    else
      accept = 1;
      skipped = skipped + 1;
    end
  end
return coords
end

function calcscatteringvelvector(m,E,theta)

  Et = 2*Eel*(Eel+2*Eel0)/(c^2*m) * sin(theta/2)^2;     # transferred
     ↪ Energy (electron to atom) in J
```

```
  ve = c*(1-Eel0^2/(Eel0+Eel-Et)^2)^0.5;  # speed of electron after
     ↪ scattering
  # ve0 = c*(1-Eel0^2/(Eel0+Eel)^2)^0.5;  # speed of electron before
     ↪ scattering

  vatom = (2*Et/m)^0.5;          # speed of hit atom after scattering

  psi = asin(mel*ve/(1-(ve/c)^2)^0.5/(m*vatom)*sin(theta)); # from
     ↪ momentum conservation (p_el*sin(theta) = p_atom *sin(psi) &
     ↪ relativistic p_el and classic pa=m*vatom
  phi = rand()*2*pi;

  v_sc = [cos(phi)*sin(psi); sin(phi)*sin(psi); cos(psi)] .* vatom;

  return v_sc, Et, psi, phi
end

function calcEnergies2el(coords1,coords2,L,maxd,a1,eps1,a2,eps2,a12,
   ↪ eps12,m1,m2,mSC1,nSC1,C1,mSC2,nSC2,C2,mSC12,nSC12,vels1,vels2,
   ↪ NNthres,maxnrpair)

  nPart1 = size(coords1,2);
  nPart2 = size(coords2,2);

  X = [coords1 coords2];
  nPart = size(X,2);

  countNN = zeros(nPart);
  countNN1 = zeros(nPart1);
  countNN2 = zeros(nPart2);
  Ekin1 = zeros(nPart1);
  Ekin2 = zeros(nPart2);
  Epot1 = zeros(nPart1);
  Epot2 = zeros(nPart2);
  Epot = zeros(nPart);

  rhos = zeros(nPart);
  pairs = round(Integer,zeros(maxnrpair,2));
  (rhos,pairs) = calculate_rhopairs2el(coords1,a1,mSC1,coords2,a2,mSC2,
     ↪ a12,mSC12,maxd,maxnrpair);

  # Loop over all particle pairs
  pairslen = size(pairs,1);

  for pair = 1:pairslen
    # Calculate particle-particle distance
    dr = X[:,pairs[pair,1]] - X[:,pairs[pair,2]];

    # Fix according to periodic boundary conditions
    # dr = distPBC3D(dr,L);
```

```
      dr2 = dot(dr,dr) # = dr[1].*dr[1]+dr[2].*dr[2]+dr[3].*dr[3]

      if dr2<NNthres
        countNN[pairs[pair,1]] = countNN[pairs[pair,1]] + 1;
        countNN[pairs[pair,2]] = countNN[pairs[pair,2]] + 1;
      end

      if pairs[pair,1] < nPart1
        if pairs[pair,2] < nPart1
          drs = a1/(dr2^0.5);
          Epot[pairs[pair,1]] = Epot[pairs[pair,1]] + eps1*drs^nSC1 -
              ↪ eps1*C1*rhos[pairs[pair,1]];
          Epot[pairs[pair,2]] = Epot[pairs[pair,2]] + eps1*drs^nSC1 -
              ↪ eps1*C1*rhos[pairs[pair,2]];
        else
          drs = a12/(dr2^0.5);
          Epot[pairs[pair,1]] = Epot[pairs[pair,1]] + eps12*drs^nSC12 -
              ↪ eps1*C1*rhos[pairs[pair,1]];
          Epot[pairs[pair,2]] = Epot[pairs[pair,2]] + eps12*drs^nSC12 -
              ↪ eps2*C2*rhos[pairs[pair,2]];
        end
      else
        if pairs[pair,2] < nPart1
          drs = a12/(dr2^0.5);
          Epot[pairs[pair,1]] = Epot[pairs[pair,1]] + eps12*drs^nSC12 -
              ↪ eps2*C2*rhos[pairs[pair,1]];
          Epot[pairs[pair,2]] = Epot[pairs[pair,2]] + eps12*drs^nSC12 -
              ↪ eps1*C1*rhos[pairs[pair,2]];
        else
          drs = a2/(dr2^0.5);
          Epot[pairs[pair,1]] = Epot[pairs[pair,1]] + eps2*drs^nSC2 -
              ↪ eps2*C2*rhos[pairs[pair,1]];
          Epot[pairs[pair,2]] = Epot[pairs[pair,2]] + eps2*drs^nSC2 -
              ↪ eps2*C2*rhos[pairs[pair,2]];
        end
      end
    end


    Ekin1 = (vels1[1,:].*vels1[1,:]+vels1[2,:].*vels1[2,:]+vels1[3,:].*
        ↪ vels1[3,:])*0.5*m1;
    Ekin2 = (vels2[1,:].*vels2[1,:]+vels2[2,:].*vels2[2,:]+vels2[3,:].*
        ↪ vels2[3,:])*0.5*m2;

    Epot1 = Epot[1:nPart1];
    Epot2 = Epot[nPart1+1:end];

    countNN1 = countNN[1:nPart1];
    countNN2 = countNN[nPart1+1:end];

    return Ekin1, Epot1, countNN1, Ekin2, Epot2, countNN2
  end
```

```
function sub_LJforces_aC(coordssub,coords,sig,eps,sigU,epsU)

  coords = coords .* sigU ./ sig;

  # Parameters:
  nPart = size(coords,2);
  nPartS = size(coordssub,2);
  LJforces = zeros(3,nPart);
  maxd = 9;#16;
  thermpartlist = falses(nPart);
  rNN2 = 1.3^2;
  # Loop over all particles:
  for part = 1:nPart
    for partS = 1:nPartS
      dr = coordssub[:,partS] - coords[:,part];
      dr2 = dot(dr,dr) # = dr[1].*dr[1]+dr[2].*dr[2]+dr[3].*dr[3]
      if dr2<maxd

        invDr2 = 1/dr2; # sigma/r^2
        invDr6 = invDr2^3;
        forceFact = invDr2^4 * (invDr6 - 0.5);

        LJforces[:,part] = LJforces[:,part] - dr*forceFact;

        if dr2<rNN2;
          thermpartlist[part] = true;
        end
        #Epot = Epot + invDr6 * (invDr6-1);
        end
      end
    end
  end

  # delete double elements from thermalisation list:
  thermpartlist = [unique(thermpartlist);zeros(nPart-length(
     ↪ thermpartlist))];
  LJforces = 48.*LJforces.*(eps./sig).*(sigU/epsU); # convert to SI
     ↪ units and convert back to LJ-units of the main system
  return LJforces,thermpartlist#, Epot
end

function trapz(x, y) # trapz performs a numerical integration with the
   ↪ trapezoidal rule
if (length(y) != length(x))
error("Vectors must be of same length")
end
Intresult = sum( (x[2:end] .- x[1:end-1]).*(y[2:end].+y[1:end-1]) ) / 2
return Intresult
end
```

Constants.jl

In this file physical constants, that are used in all codes that are listed here, are defined.

```
# Set constants:
kB = 1.3806488E-23    # Botzmanns constant in J/K
elch = 1.602176565E-19; # elmentary charge in C
c = 299792458;      # speed of light m/s
mel = 9.10938291E-31; # electron mass in kg
u = 1.660538E-27;   # unified atomic mass unit in kg
Eel0 = mel*c^2;     # electron rest energy
NA = 6.02214086E23    # Avogadro number
a0 = 0.52917721067e-10  # Bohrscher radius

barn = 1e-28      # 1 barn are 1e-28 m
```

Bibliography

[1] D. B. Williams and C. B. Carter. *Transmission Electron Microscopy: A Textbook for Materials Science*. Boston, MA, 2009.

[2] R. Brydson. *Aberration-corrected Analytical Electron Microscopy*. 2nd ed. Hoboken: John Wiley & Sons, 2011.

[3] R. F. Egerton. *Electron energy-loss spectroscopy in the electron microscope*. Third edition. The language of science. Springer, 2011.

[4] L. Jones, K. E. MacArthur, V. T. Fauske, van Helvoort, Antonius T J, and P. D. Nellist. “Rapid estimation of catalyst nanoparticle morphology and atomic-coordination by high-resolution Z-contrast electron microscopy”. In: *Nano letters* 14.11 (2014), pp. 6336–6341.

[5] G. Haberfehlner, P. Thaler, D. Knez, A. Volk, F. Hofer, W. E. Ernst, and G. Kothleitner. “Formation of bimetallic clusters in superfluid helium nanodroplets analysed by atomic resolution electron tomography”. In: *Nature Communications* 6 (2015), p. 8779.

[6] Y. Yang, C.-C. Chen, M. C. Scott, C. Ophus, R. Xu, A. Pryor, L. Wu, F. Sun, W. Theis, J. Zhou, M. Eisenbach, P. R. C. Kent, R. F. Sabirianov, H. Zeng, P. Ercius, and J. Miao. “Deciphering chemical order/disorder and material properties at the single-atom level”. In: *Nature* 542.7639 (2017), pp. 75–79.

[7] M. Azubel, J. Koivisto, S. Malola, D. Bushnell, G. L. Hura, A. L. Koh, H. Tsunoyama, T. Tsukuda, M. Pettersson, H. Häkkinen, and R. D. Kornberg. “Nanoparticle imaging. Electron microscopy of gold nanoparticles at atomic resolution”. In: *Science (New York, N.Y.)* 345.6199 (2014), pp. 909–912.

[8] G. Schmid, ed. *Nanoparticles: From theory to application*. 4. repr. Weinheim: Wiley-VCH, 2006.

[9] F. Baletto and R. Ferrando. “Structural properties of nanoclusters: Energetic, thermodynamic, and kinetic effects”. In: *Reviews of Modern Physics* 77.1 (2005), pp. 371–423.

[10] R. Ferrando, J. Jellinek, and R. L. Johnston. “Nanoalloys: From Theory to Applications of Alloy Clusters and Nanoparticles”. In: *Chemical Reviews* 108.3 (2008), pp. 845–910.

[11] T. J. Foley, C. E. Johnson, and K. T. Higa. “Inhibition of Oxide Formation on Aluminum Nanoparticles by Transition Metal Coating”. In: *Chemistry of Materials* 17.16 (2005), pp. 4086–4091.

[12] A. I. Maaroof, D.-g. Cho, B.-J. Kim, H.-T. Kim, and S. Hong. “Hybrid Nanostructures Based on VO 2 Semishells and Au Nanohemispheres for Tunable Plasmonic Coupling”. In: *The Journal of Physical Chemistry C* (2013), p. 130913150937001.

[13] A. M. Molenbroek, J. K. Nørskov, and B. S. Clausen. “Structure and Reactivity of Ni−Au Nanoparticle Catalysts”. In: *The Journal of Physical Chemistry B* 105.23 (2001), pp. 5450–5458.

[14] J. Higgins, C. Callegari, J. Reho, F. Stienkemeier, W. E. Ernst, K. K. Lehmann, M. Gutowski, and G. Scoles. “Photoinduced Chemical Dynamics of High-Spin Alkali Trimers”. In: *Science* 273.5275 (1996), pp. 629–631.

[15] S. Grebenev, J. P. Toennies, and A. F. Vilesov. “Superfluidity Within a Small Helium-4 Cluster: The Microscopic Andronikashvili Experiment”. In: *Science* 279.5359 (1998), pp. 2083–2086.

[16] M. Behrens, R. Fröchtenicht, M. Hartmann, J.-G. Siebers, U. Buck, and F. C. Hagemeister. “Vibrational spectroscopy of methanol and acetonitrile clusters in cold helium droplets”. In: *The Journal of chemical physics* 111.6 (1999), pp. 2436–2443.

[17] J. Tang, Y. Xu, A. R. W. McKellar, and W. Jager. “Quantum solvation of carbonyl sulfide with helium atoms”. In: *Science* 297.5589 (2002), pp. 2030–2033.

[18] L. F. Gomez, K. R. Ferguson, J. P. Cryan, C. Bacellar, R. M. P. Tanyag, C. Jones, S. Schorb, D. Anielski, A. Belkacem, C. Bernando, R. Boll, J. Bozek, S. Carron, G. Chen, T. Delmas, L. Englert, S. W. Epp, B. Erk, L. Foucar, R. Hartmann, A. Hexemer, M. Huth, J. Kwok, S. R. Leone, J. H. S. Ma, F. R.N. C. Maia, E. Malmerberg, S. Marchesini, D. M. Neumark, B. Poon, J. Prell, D. Rolles, B. Rudek, A. Rudenko, M. Seifrid, K. R. Siefermann, F. P. Sturm, M. Swiggers, J. Ullrich, F. Weise, P. Zwart, C. Bostedt, O. Gessner, and A. F. Vilesov. “Helium superfluidity. Shapes and vorticities of superfluid helium nanodroplets”. In: *Science* 345.6199 (2014), pp. 906–909.

[19] V. Mozhayskiy, M. N. Slipchenko, V. K. Adamchuk, and A. F. Vilesov. “Use of helium nanodroplets for assembly, transport, and surface deposition of large molecular and atomic clusters”. In: *The Journal of chemical physics* 127.9 (2007), p. 094701.

[20] E. Loginov, L. F. Gomez, and A. F. Vilesov. “Surface deposition and imaging of large Ag clusters formed in He droplets”. In: *The journal of physical chemistry. A* 115.25 (2011), pp. 7199–7204.

[21] L. F. Gomez, E. Loginov, and A. F. Vilesov. “Traces of Vortices in Superfluid Helium Droplets”. In: *Physical Review Letters* 108.15 (2012).

[22] A. Volk, D. Knez, P. Thaler, A. W. Hauser, W. Grogger, F. Hofer, and W. E. Ernst. “Thermal instabilities and Rayleigh breakup of ultrathin silver nanowires grown in helium nanodroplets”. In: *Phys. Chem. Chem. Phys.* (2015).

[23] A. Volk, P. Thaler, D. Knez, A. W. Hauser, J. Steurer, W. Grogger, F. Hofer, and W. E. Ernst. “The impact of doping rates on the morphologies of silver and gold nanowires grown in helium nanodroplets”. In: *Phys. Chem. Chem. Phys.* (2015).

[24] P. Thaler, A. Volk, F. Lackner, J. Steurer, D. Knez, W. Grogger, F. Hofer, and W. E. Ernst. “Formation of bimetallic core-shell nanowires along vortices in superfluid He nanodroplets”. In: *Physical Review B* 90.15 (2014).

[25] D. Spence, E. Latimer, C. Feng, A. Boatwright, A. M. Ellis, and S. Yang. “Vortex-induced aggregation in superfluid helium droplets”. In: *Physical chemistry chemical physics : PCCP* 16.15 (2014), pp. 6903–6906.

[26] E. Loginov, L. F. Gomez, N. Chiang, A. Halder, N. Guggemos, V. V. Kresin, and A. F. Vilesov. “Photoabsorption of Ag_N(N$\sim$6–6000) Nanoclusters Formed in Helium Droplets: Transition from Compact to Multicenter Aggregation”. In: *Physical Review Letters* 106.23 (2011).

[27] A. Boatwright, C. Feng, D. Spence, E. Latimer, C. Binns, A. M. Ellis, and S. Yang. “Helium droplets: a new route to nanoparticles”. In: *Faraday Discussions* 162 (2013), p. 113.

[28] E. Latimer, D. Spence, C. Feng, A. Boatwright, A. M. Ellis, and S. Yang. “Preparation of Ultrathin Nanowires Using Superfluid Helium Droplets”. In: *Nano Letters* (2014), p. 140421100145008.

[29] A. Volk, P. Thaler, M. Koch, E. Fisslthaler, W. Grogger, and W. E. Ernst. “High resolution electron microscopy of Ag-clusters in crystalline and non-crystalline morphologies grown inside superfluid helium nanodroplets”. In: *The Journal of Chemical Physics* 138.21 (2013), p. 214312.

[30] R. Zan, U. Bangert, Q. Ramasse, and K. S. Novoselov. “Evolution of gold nanostructures on graphene”. In: *Small* 7.20 (2011), pp. 2868–2872.

[31] H. Wang, K. Li, Y. Yao, Q. Wang, Y. Cheng, U. Schwingenschlogl, X. X. Zhang, and W. Yang. “Unraveling the atomic structure of ultrafine iron clusters”. In: *Scientific reports* 2 (2012), p. 995.

[32] Q. M. Ramasse, C. R. Seabourne, D.-M. Kepaptsoglou, R. Zan, U. Bangert, and A. J. Scott. “Probing the Bonding and Electronic Structure of Single Atom Dopants in Graphene with Electron Energy Loss Spectroscopy”. In: *Nano Letters* (2013), p. 130104155126009.

[33] T. C. Lovejoy, Q. M. Ramasse, M. Falke, A. Kaeppel, R. Terborg, R. Zan, N. Dellby, and O. L. Krivanek. “Single atom identification by energy dispersive x-ray spectroscopy”. In: *Applied Physics Letters* 100.15 (2012), p. 154101.

[34] Q. M. Ramasse, R. Zan, U. Bangert, D. W. Boukhvalov, Y.-W. Son, and K. S. Novoselov. “Direct Experimental Evidence of Metal-Mediated Etching of Suspended Graphene”. In: *ACS Nano* 6.5 (2012), pp. 4063–4071.

[35] R. Zan, Q. M., R. Jalil, and U. Bangert. “Atomic Structure of Graphene and h-BN Layers and Their Interactions with Metals”. In: *Advances in Graphene Science*. Ed. by M. Aliofkhazraei. InTech, 2013.

[36] J. G. Railsback, A. C. Johnston-Peck, J. Wang, and J. B. Tracy. “Size-dependent nanoscale kirkendall effect during the oxidation of nickel nanoparticles”. In: *ACS Nano* 4.4 (2010), pp. 1913–1920.

[37] R. Nakamura, J.-G. Lee, H. Mori, and H. Nakajima. “Oxidation behaviour of Ni nanoparticles and formation process of hollow NiO”. In: *Philosophical Magazine* 88.2 (2008), pp. 257–264.

[38] J. M. LeBeau, S. D. Findlay, L. J. Allen, and S. Stemmer. “Standardless atom counting in scanning transmission electron microscopy”. In: *Nano letters* 10.11 (2010), pp. 4405–4408.

[39] C. C. Ahn. *Transmission electron energy loss spectrometry in materials science and the EELS atlas*. 2nd ed. Weinheim and Chichester: Wiley, 2004.

[40] R. F. Egerton. “Quantitative analysis of electron-energy-loss spectra”. In: *Ultramicroscopy* 28.1-4 (1989), pp. 215–225.

[41] F. Hofer. “Determination of inner-shell cross-sections for EELS-quantification”. In: *Microscopy Microanalysis Microstructures* 2.2-3 (1991), pp. 215–230.

[42] P. Rez. “Cross-sections for energy loss spectrometry”. In: *Ultramicroscopy* 9.3 (1982), pp. 283–287.

[43] H. R. Zulliger and D. W. Aitken. “Fano Factor Fact and Fallacy”. In: *IEEE Transactions on Nuclear Science* 17.3 (1970), pp. 187–195.

[44] G. Kothleitner, M. J. Neish, N. R. Lugg, S. D. Findlay, W. Grogger, F. Hofer, and L. J. Allen. “Quantitative Elemental Mapping at Atomic Resolution Using X-Ray Spectroscopy”. In: *Physical Review Letters* 112.8 (2014).

[45] J. Kraxner, M. Schafer, O. Roschel, G. Kothleitner, G. Haberfehlner, M. Paller, and W. Grogger. “Quantitative EDXS: Influence of geometry on a four detector system”. In: *Ultramicroscopy* 172 (2017), pp. 30–39.

[46] H. A. Kramers. “XCIII. On the theory of X-ray absorption and of the continuous X-ray spectrum”. In: *Philosophical Magazine Series 6* 46.275 (1923), pp. 836–871.

[47] N. J. Zaluzec. “Processing and quantification of X-ray Energy-Dispersive Spectra in the Analytical Electron Microscope”. In: *Ultramicroscopy* 28.1-4 (1989), pp. 226–235.

[48] C. T. Chantler. “Detailed Tabulation of Atomic Form Factors, Photoelectric Absorption and Scattering Cross Section, and Mass Attenuation Coefficients in the Vicinity of Absorption Edges in the Soft X-Ray (Z=30–36, Z=60–89, E=0.1 keV–10 keV), Addressing Convergence Issues of Earlier Work”. In: *Journal of Physical and Chemical Reference Data* 29.4 (2000), p. 597.

[49] J. H. Hubbell and S. M. Seltzer. *Tables of X-ray mass attenuation coefficients and mass energy-absorption coefficients 1 keV to 20 MeV for elements Z= 1 to 92 and 48 additional substances of dosimetric interest*. Tech. rep. National Inst. of Standards and Technology-PL, Gaithersburg, MD (United States). Ionizing Radiation Div., 1995.

[50] G. Cliff and G. W. Lorimer. “The quantitative analysis of thin specimens”. In: *Journal of Microscopy* 103.2 (1975), pp. 203–207.

[51] M. M. Treacy. “Z Dependence of Electron Scattering by Single Atoms into Annular Dark-Field Detectors”. In: *Microscopy and Microanalysis* 17.06 (2011), pp. 847–858.

[52] O. L. Krivanek, M. F. Chisholm, V. Nicolosi, T. J. Pennycook, G. J. Corbin, N. Dellby, M. F. Murfitt, C. S. Own, Z. S. Szilagyi, M. P. Oxley, S. T. Pantelides, and S. J. Pennycook. “Atom-by-atom structural and chemical analysis by annular dark-field electron microscopy”. In: *Nature* 464.7288 (2010), pp. 571–574.

[53] H. E, K. E. MacArthur, T. J. Pennycook, E. Okunishi, A. J. D’Alfonso, N. R. Lugg, L. J. Allen, and P. D. Nellist. “Probe integrated scattering cross sections in the analysis of atomic resolution HAADF STEM images”. In: *Ultramicroscopy* 133 (2013), pp. 109–119.

[54] G. T. Martinez, L. Jones, A. de Backer, A. Béché, J. Verbeeck, S. van Aert, and P. D. Nellist. “Quantitative STEM normalisation: The importance of the electron flux”. In: *Ultramicroscopy* 159P1 (2015), pp. 46–58.

[55] A. de Backer, G. T. Martinez, K. E. MacArthur, L. Jones, A. Béché, P. D. Nellist, and S. van Aert. “Dose limited reliability of quantitative annular dark field scanning transmission electron microscopy for nano-particle atom-counting”. In: *Ultramicroscopy* 151 (2015), pp. 56–61.

[56] L. Jones. “Quantitative ADF STEM: Acquisition, analysis and interpretation”. In: *IOP Conference Series: Materials Science and Engineering* 109 (2016), p. 012008.

[57] F. F. Krause, M. Schowalter, T. Grieb, K. Müller-Caspary, T. Mehrtens, and A. Rosenauer. “Effects of instrument imperfections on quantitative scanning transmission electron microscopy”. In: *Ultramicroscopy* 161 (2016), pp. 146–160.

[58] A. Jablonski, F. Salvat, and C. J. Powell. *NIST Electron Elastic-Scattering Cross-Section Database: Version 3.2*. Gaithersburg, MD: National Institute of Standards and Technology, 2010.

[59] W. M. Haynes. *CRC Handbook of Chemistry and Physics, 95th Edition*. 95th ed. Hoboken: CRC Press, 2014.

[60] G. Taubin. “Estimation of planar curves, surfaces, and nonplanar space curves defined by implicit equations with applications to edge and range image segmentation”. In: *IEEE Transactions on Pattern Analysis and Machine Intelligence* 13.11 (1991), pp. 1115–1138.

[61] M. Watanabe, D. W. Ackland, A. Burrows, C. J. Kiely, D. B. Williams, O. L. Krivanek, N. Dellby, M. F. Murfitt, and Z. Szilagyi. “Improvements in the X-Ray Analytical Capabilities of a Scanning Transmission Electron Microscope by Spherical-Aberration Correction”. In: *Microscopy and Microanalysis* 12.06 (2006), pp. 515–526.

[62] Francisco de la Peña, Pierre Burdet, Vidar Tonaas Fauske, Tomas Ostasevicius, Mike Sarahan, Magnus Nord, Josh Taillon, Duncan Johnstone, Alberto Eljarrat, Stefano Mazzucco, Jan Caron, Eric Prestat, Gaël Donval, Luiz Fernando Zagonel, Michael Walls, and iygr. *hyperspy: HyperSpy 0.8.4*. 2016.

[63] M. R. Keenan and P. G. Kotula. “Accounting for Poisson noise in the multivariate analysis of ToF-SIMS spectrum images”. In: *Surface and Interface Analysis* 36.3 (2004), pp. 203–212.

[64] H. Grahn and P. Geladi. *Techniques and applications of hyperspectral image analysis*. Chichester: John Wiley, 2007.

[65] P. Potapov. “Why Principal Component Analysis of STEM spectrum-images results in "abstract", uninterpretable loadings?” In: *Ultramicroscopy* 160 (2015), pp. 197–212.

[66] M. Makitalo and A. Foi. “Optimal inversion of the Anscombe transformation in low-count Poisson image denoising”. In: *IEEE transactions on image processing : a publication of the IEEE Signal Processing Society* 20.1 (2011), pp. 99–109.

[67] S. Mika, B. Schölkopf, A. Smola, K.-R. Müller, M. Scholz, and G. Rätsch. “Kernel PCA and De-Noising in Feature Spaces”. In: *ADVANCES IN NEURAL INFORMATION PROCESSING SYSTEMS 11*. MIT Press, 1999, pp. 536–542.

[68] L. Zhang, W. Dong, D. Zhang, and G. Shi. “Two-stage image denoising by principal component analysis with local pixel grouping”. In: *Pattern Recognition* 43.4 (2010), pp. 1531–1549.

[69] J. Salmon, Z. Harmany, C.-A. Deledalle, and R. Willett. “Poisson Noise Reduction with Non-local PCA”. In: *Journal of Mathematical Imaging and Vision* 48.2 (2014), pp. 279–294.

[70] J. Axelsson and J. Sorensen. “The 2D Hotelling filter - a quantitative noise-reducing principal-component filter for dynamic PET data, with applications in patient dose reduction”. In: *BMC medical physics* 13 (2013), p. 1.

[71] T. Furnival, R. K. Leary, and P. A. Midgley. “Denoising time-resolved microscopy image sequences with singular value thresholding”. In: *Ultramicroscopy* (2016).

[72] D. D. Muresan and T. W. Parks. “Adaptive principal components and image denoising”. In: *Image Processing, 2003. ICIP 2003. Proceedings. 2003 International Conference on*. Vol. 1. 2003, I–101–4 vol.1.

[73] G. Z. Radnóczi, D. Knez, F. Hofer, N. Frangis, N. Vouroutzis, J. Stoemenos, and B. Pécz. “Inclusions in Si whiskers grown by Ni metal induced lateral crystallization”. In: *Journal of Applied Physics* 121.14 (2017), p. 145301.

[74] O. L. Krivanek, N. Dellby, M. F. Murfitt, M. F. Chisholm, T. J. Pennycook, K. Suenaga, and V. Nicolosi. “Gentle STEM: ADF imaging and EELS at low primary energies”. In: *Ultramicroscopy* 110.8 (2010), pp. 935–945.

[75] J. S. Lim. *Two-dimensional signal and image processing*. Prentice Hall signal processing series. Englewood Cliffs N.J.: Prentice Hall, 1990.

[76] S. Lichtert and J. Verbeeck. “Statistical consequences of applying a PCA noise filter on EELS spectrum images”. In: *Ultramicroscopy* 125 (2013), pp. 35–42.

[77] C. Koch. “Determination of core structure periodicity and point defect density along dislocations”. Dissertation. Tempe: Arizona State University, 1.01.2002.

[78] P. Chatterjee. “Patch-Based Image Denoising and its Performance Limits”. Dissertation. Santa Cruz: University of California, 2011.

[79] N. Mevenkamp, P. Binev, W. Dahmen, P. M. Voyles, A. B. Yankovich, and B. Berkels. “Poisson noise removal from high-resolution STEM images based on periodic block matching”. In: *Advanced Structural and Chemical Imaging* 1.1 (2015), p. 617.

[80] L. Azzari and A. Foi. “Variance Stabilization for Noisy+Estimate Combination in Iterative Poisson Denoising”. In: *IEEE Signal Processing Letters* 23.8 (2016), pp. 1086–1090.

[81] M. Makitalo and A. Foi. “Optimal inversion of the generalized Anscombe transformation for Poisson-Gaussian noise”. In: *IEEE transactions on image processing : a publication of the IEEE Signal Processing Society* 22.1 (2013), pp. 91–103.

[82] L. Jones and P. D. Nellist. “Identifying and Correcting Scan Noise and Drift in the Scanning Transmission Electron Microscope”. In: *Microscopy and Microanalysis* 19.04 (2013), pp. 1050–1060.

[83] A. Kumao, H. Hashimoto, and K. Shiraishi. “Studies on specimen contamination by transmission electron microscopy”. In: *Journal of Electron Microscopy* 30.3 (1981), pp. 161–170.

[84] A. J. V. Griffiths and T. Walther. “Quantification of carbon contamination under electron beam irradiation in a scanning transmission electron microscope and its suppression by plasma cleaning”. In: *Journal of Physics: Conference Series* 241 (2010), p. 12017.

[85] C. M. McGilvery, A. E. Goode, M. S. Shaffer, and D. W. McComb. “Contamination of holey/lacey carbon films in STEM”. In: *Micron* 43.2-3 (2012), pp. 450–455.

[86] C. Soong, P. Woo, and D. Hoyle. “Contamination Cleaning of TEM/SEM Samples with the ZONE Cleaner”. In: *Microscopy Today* 20.06 (2012), pp. 44–48.

[87] G. Algara-Siller, O. Lehtinen, A. Turchanin, and U. Kaiser. “Dry-cleaning of graphene”. In: *Applied Physics Letters* 104.15 (2014), p. 153115.

[88] P. Thaler, A. Volk, D. Knez, F. Lackner, G. Haberfehlner, J. Steurer, M. Schnedlitz, and W. E. Ernst. “Synthesis of nanoparticles in helium droplets-A characterization comparing mass-spectra and electron microscopy data”. In: *The Journal of chemical physics* 143.13 (2015), p. 134201.

[89] H. Plank, C. Gspan, M. Dienstleder, G. Kothleitner, and F. Hofer. “The influence of beam defocus on volume growth rates for electron beam induced platinum deposition”. In: *Nanotechnology* 19.48 (2008), p. 485302.

[90] H. H. Rose. “Future trends in aberration-corrected electron microscopy”. In: *Philosophical Transactions of the Royal Society A: Mathematical, Physical and Engineering Sciences* 367.1903 (2009), pp. 3809–3823.

[91] A. Rose. “The sensitivity performance of the human eye on an absolute scale”. In: *Journal of the Optical Society of America* 38.2 (1948), pp. 196–208.

[92] R. F. Egerton. “Choice of operating voltage for a transmission electron microscope”. In: *Ultramicroscopy* 145 (2014), pp. 85–93.

[93] L. Reimer and H. Kohl. *Transmission electron microscopy: Physics of image formation*. 5. ed. Vol. 36. Springer series in optical sciences. New York, NY: Springer, 2008.

[94] R. F. Egerton. “Beam-induced motion of adatoms in the transmission electron microscope”. In: *Microscopy and Microanalysis* 19.2 (2013), pp. 479–486.

[95] N. F. Mott. “The Scattering of Fast Electrons by Atomic Nuclei”. In: *Proceedings of the Royal Society A: Mathematical, Physical and Engineering Sciences* 124.794 (1929), pp. 425–442.

[96] F. Banhart. “Irradiation effects in carbon nanostructures”. In: *Reports on Progress in Physics* 62.8 (1999), pp. 1181–1221.

[97] G. S. Khandelwal and E. Merzbacher. “Displacement Cross Sections for Fast Electrons Incident on Gold”. In: *Physical Review* 130.5 (1963), pp. 1822–1825.

[98] H. M. Simpson and R. L. Chaplin. “Damage and Recovery of Aluminum for Low-Energy Electron Irradiations”. In: *Physical Review* 185.3 (1969), pp. 958–961.

[99] N. Jiang. “Electron beam damage in oxides: a review”. In: *Reports on progress in physics. Physical Society (Great Britain)* 79.1 (2016), p. 016501.

[100] A. Santana, A. Zobelli, J. Kotakoski, A. Chuvilin, and E. Bichoutskaia. “Inclusion of radiation damage dynamics in high-resolution transmission electron microscopy image simulations: The example of graphene”. In: *Physical Review B* 87.9 (2013).

[101] A. Zobelli, A. Gloter, C. Ewels, G. Seifert, and C. Colliex. “Electron knock-on cross section of carbon and boron nitride nanotubes”. In: *Physical Review B* 75.24 (2007).

[102] W. A. McKinley JR. and H. Feshbach. “The Coulomb Scattering of Relativistic Electrons by Nuclei”. In: *Physical Review* 74.12 (1948), p. 1759.

[103] J. Meyer, F. Eder, S. Kurasch, V. Skakalova, J. Kotakoski, H. Park, S. Roth, A. Chuvilin, S. Eyhusen, G. Benner, A. Krasheninnikov, and U. Kaiser. “Accurate Measurement of Electron Beam Induced Displacement Cross Sections for Single-Layer Graphene”. In: *Physical Review Letters* 108.19 (2012).

[104] R. Egerton, R. McLeod, F. Wang, and M. Malac. “Basic questions related to electron-induced sputtering in the TEM”. In: *Ultramicroscopy* 110.8 (2010), pp. 991–997.

[105] M. D. Rossell, R. Erni, M. Asta, V. Radmilovic, and U. Dahmen. “Atomic-resolution imaging of lithium in Al3Li precipitates”. In: *Physical Review B* 80.2 (2009), p. 101.

[106] R. Egerton. “Control of radiation damage in the TEM”. In: *Ultramicroscopy* 127 (2013), pp. 100–108.

[107] R. F. Egerton, F. Wang, and P. A. Crozier. “Beam-Induced Damage to Thin Specimens in an Intense Electron Probe”. In: *Microscopy and Microanalysis* 12.01 (2006), p. 65.

[108] H. Zheng, Y. Liu, S. X. Mao, J. Wang, and J. Y. Huang. “Beam-assisted large elongation of in situ formed Li_2O nanowires”. In: *Scientific reports* 2 (2012), p. 542.

[109] I. Jenčič, M. W. Bench, I. M. Robertson, and M. A. Kirk. “Electron-beam-induced crystallization of isolated amorphous regions in Si, Ge, GaP, and GaAs”. In: *Journal of Applied Physics* 78.2 (1995), p. 974.

[110] J. A. Sundararajan, M. Kaur, and Y. Qiang. “Mechanism of Electron Beam Induced Oxide Layer Thickening on Iron–Iron Oxide Core–Shell Nanoparticles”. In: *The Journal of Physical Chemistry C* 119.15 (2015), pp. 8357–8363.

[111] M. A. Asoro, D. Kovar, and P. J. Ferreira. “In situ transmission electron microscopy observations of sublimation in silver nanoparticles”. In: *ACS Nano* 7.9 (2013), pp. 7844–7852.

[112] V. G. Gryaznov, A. M. Kaprelov, and A. Y. Belov. “Real temperature of nanoparticles in electron microscope beams”. In: *Philosophical Magazine Letters* 63.5 (1991), pp. 275–279.

[113] S. B. Fisher. “On the temperature rise in electron irradiated foils”. In: *Radiation Effects* 5.2 (1970), pp. 239–243.

[114] C. R. Henry. “Morphology of supported nanoparticles”. In: *Progress in Surface Science* 80.3-4 (2005), pp. 92–116.

[115] D. Joy. “Fundamental Constants for Quantitative X-ray Microanalysis”. In: *Microscopy and Microanalysis* 7 (2001), pp. 159–167.

[116] C. Kittel. *Einführung in die Festkörperphysik*. 14., überarb. und erw. Aufl. München: Oldenbourg, 2006.

[117] R. Egerton, S. Lazar, and M. Libera. “Delocalized radiation damage in polymers”. In: *Micron* 43.1 (2012), pp. 2–7.

[118] N. Jiang. “Beam damage by the induced electric field in transmission electron microscopy”. In: *Micron* (2016).

[119] N. Jiang. “Damage mechanisms in electron microscopy of insulating materials”. In: *Journal of Physics D: Applied Physics* 46.30 (2013), p. 305502.

[120] B. J. Alder and T. E. Wainwright. “Studies in Molecular Dynamics. I. General Method”. In: *The Journal of chemical physics* 31.2 (1959), pp. 459–466.

[121] D. Frenkel and B. Smit. *Understanding molecular simulation: From algorithms to applications*. 2nd ed. Vol. 1. Computational science series. San Diego: Academic Press, 2002.

[122] M. A. Villarreal, O. A. Oviedo, and E. P. M. Leiva. “A Straightforward Approach for the Determination of the Maximum Time Step for the Simulation of Nanometric Metallic Systems”. In: *Journal of chemical theory and computation* 8.5 (2012), pp. 1744–1749.

[123] N. A. Marks and M. Robinson. “Variable timestep algorithm for molecular dynamics simulation of non-equilibrium processes”. In: *Nuclear Instruments and Methods in Physics Research Section B: Beam Interactions with Materials and Atoms* 352 (2015), pp. 3–8.

[124] H. C. Andersen. “Molecular dynamics simulations at constant pressure and/or temperature”. In: *The Journal of Chemical Physics* 72.4 (1980), p. 2384.

[125] A. P. Sutton and J. Chen. “Long-range Finnis–Sinclair potentials”. In: *Philosophical Magazine Letters* 61.3 (1990), pp. 139–146.

[126] B. D. Todd and R. M. Lynden-Bell. “Surface and bulk properties of metals modelled with Sutton-Chen potentials”. In: *Surface Science* 281.1-2 (1993), pp. 191–206.

[127] A. R. Leach. *Molecular modelling: Principles and applications*. 2nd ed. Harlow, England and New York: Prentice Hall, 2001.

[128] Y. Qi, T. Çağın, Y. Kimura, and W. A. Goddard. “Molecular-dynamics simulations of glass formation and crystallization in binary liquid metals: Cu-Ag and Cu-Ni”. In: *Physical Review B* 59.5 (1999), pp. 3527–3533.

[129] H. Rafii-Tabar and A. P. Sulton. “Long-range Finnis-Sinclair potentials for f.c.c. metallic alloys”. In: *Philosophical Magazine Letters* 63.4 (1991), pp. 217–224.

[130] F. Hofer and P. Golob. “New examples for near-edge fine structures in electron energy loss spectroscopy”. In: *Ultramicroscopy* 21.4 (1987), pp. 379–383.

[131] R. Werner, M. Wanner, G. Schneider, and D. Gerthsen. “Island formation and dynamics of gold clusters on amorphous carbon films”. In: *Physical Review B* 72.4 (2005), p. 045426.

[132] P. Thaler, A. Volk, M. Ratschek, M. Koch, and W. E. Ernst. “Molecular dynamics simulation of the deposition process of cold Ag-clusters under different landing conditions”. In: *The Journal of Chemical Physics* 140.4 (2014), p. 44326.

[133] R. C. Baetzold. “Calculated properties of metal aggregates”. In: *Surface Science* 36.1 (1973), pp. 123–140.

[134] M. Amft, S. Lebègue, O. Eriksson, and N. V. Skorodumova. “Adsorption of Cu, Ag, and Au atoms on graphene including van der Waals interactions”. In: *Journal of physics. Condensed matter : an Institute of Physics journal* 23.39 (2011), p. 395001.

[135] M. A. O. Quiroga and G. F. Cabeza. “Role of Van der Waals Forces in Graphene Adsorption over Pd, Pt, and Ni”. In: *Brazilian Journal of Physics* 43.3 (2013), pp. 126–129.

[136] J. H. Ryu, H. Y. Kim, D. H. Kim, D. H. Seo, and H. M. Lee. “Immobilization of Au Nanoclusters Supported on Graphite: Molecular Dynamics Simulations”. In: *The Journal of Physical Chemistry C* 114.5 (2010), pp. 2022–2026.

[137] H. Akbarzadeh and H. Yaghoubi. “Molecular dynamics simulations of silver nanocluster supported on carbon nanotube”. In: *Journal of colloid and interface science* 418 (2014), pp. 178–184.

[138] L. J. Lewis, P. Jensen, N. Combe, and J.-L. Barrat. “Diffusion of gold nanoclusters on graphite”. In: *Physical Review B* 61.23 (2000), pp. 16084–16090.

[139] N. Metropolis, A. W. Rosenbluth, M. N. Rosenbluth, A. H. Teller, and E. Teller. “Equation of State Calculations by Fast Computing Machines”. In: *The Journal of Chemical Physics* 21.6 (1953), p. 1087.

[140] G. G. Rondina and J. L. F. Da Silva. “Revised basin-hopping Monte Carlo algorithm for structure optimization of clusters and nanoparticles”. In: *Journal of chemical information and modeling* 53.9 (2013), pp. 2282–2298.

[141] C. Bréchignac, P. Houdy, and M. Lahmani. *Nanomaterials and Nanochemistry*. 1. Aufl. s.l.: Springer-Verlag, 2008.

[142] N. Combe, P. Jensen, and A. Pimpinelli. “Changing Shapes in the Nanoworld”. In: *Physical Review Letters* 85.1 (2000), pp. 110–113.

[143] A. V. Krasheninnikov and K. Nordlund. “Ion and electron irradiation-induced effects in nanostructured materials”. In: *Journal of Applied Physics* 107.7 (2010), p. 71301.

[144] A. Jablonski. “Comparison of Electron Elastic-Scattering Cross Sections Calculated from Two Commonly Used Atomic Potentials”. In: *Journal of Physical and Chemical Reference Data* 33.2 (2004), p. 409.

[145] M. Dapor and A. Miotello. “Differential, Total, and Transport Cross Section for Elastic Scattering of Low Energy Positrons by Neutral Atoms (Z= 1–92,E= 500–4000 eV)”. In: *Atomic Data and Nuclear Data Tables* 69.1 (1998), pp. 1–100.

[146] J. Rundgren. “Elastic electron-atom scattering in amplitude-phase representation with application to electron diffraction and spectroscopy”. In: *Physical Review B* 76.19 (2007).

[147] M. Vos, R. P. McEachran, E. Weigold, and R. A. Bonham. “Elastic electron scattering cross sections at high momentum transfer”. In: *Nuclear Instruments and Methods in Physics Research Section B: Beam Interactions with Materials and Atoms* 300 (2013), pp. 62–67.

[148] F. Baletto, C. Mottet, and R. Ferrando. “Molecular dynamics simulations of surface diffusion and growth on silver and gold clusters”. In: *Surface Science* 446.1-2 (2000), pp. 31–45.

[149] A. Surrey, D. Pohl, L. Schultz, and B. Rellinghaus. “Quantitative measurement of the surface self-diffusion on Au nanoparticles by aberration-corrected transmission electron microscopy”. In: *Nano letters* 12.12 (2012), pp. 6071–6077.

[150] R. Ferrando, M. Mazroui, R. Spadacini, and G. E. Tommei. “Jump rate and jump probabilities in the two-dimensional strong-collision model”. In: *New Journal of Physics* 7 (2005), p. 19.

[151] D. Knez. “Preparation and Electron Microscopy of Graphene”. Master Thesis. Graz: Technische Universität, 2013.

[152] C. Jin, F. Lin, K. Suenaga, and S. Iijima. “Fabrication of a Freestanding Boron Nitride Single Layer and Its Defect Assignments”. In: *Physical Review Letters* 102.19 (2009).

[153] K. H. Lee, H.-J. Shin, J. Lee, I.-y. Lee, G.-H. Kim, J.-Y. Choi, and S.-W. Kim. “Large-Scale Synthesis of High-Quality Hexagonal Boron Nitride Nanosheets for Large-Area Graphene Electronics”. In: *Nano Letters* 12.2 (2012), pp. 714–718.

[154] K. S. Novoselov, A. K. Geim, S. V. Morozov, D. Jiang, Y. Zhang, S. V. Dubonos, I. V. Grigorieva, and A. A. Firsov. “Electric Field Effect in Atomically Thin Carbon Films”. In: *Science* 306.5696 (2004), pp. 666–669.

[155] J. C. Meyer, A. K. Geim, M. I. Katsnelson, K. S. Novoselov, T. J. Booth, and S. Roth. “The structure of suspended graphene sheets”. In: *Nature* 446.7131 (2007), pp. 60–63.

[156] C. T. Pan, R. R. Nair, U. Bangert, Q. Ramasse, R. Jalil, R. Zan, C. R. Seabourne, and A. J. Scott. “Nanoscale electron diffraction and plasmon spectroscopy of single- and few-layer boron nitride”. In: *Physical Review B* 85.4 (2012).

[157] J. Leiro, E. Minni, and E. Suoninen. “Study of plasmon structure in XPS spectra of silver and gold”. In: *Journal of Physics F: Metal Physics* 13.1 (1983), pp. 215–221.

[158] D. Knez, P. Thaler, A. Volk, G. Kothleitner, W. E. Ernst, and F. Hofer. “Transformation dynamics of Ni clusters into NiO rings under electron beam irradiation”. In: *Ultramicroscopy* (2016).

[159] N. Otsu. “A Threshold Selection Method from Gray-Level Histograms”. In: *IEEE Transactions on Systems, Man, and Cybernetics* 9.1 (1979), pp. 62–66.

[160] N. Cabrera and N. F. Mott. “Theory of the oxidation of metals”. In: *Reports on Progress in Physics* 12.1 (1949), pp. 163–184.

[161] V. P. Zhdanov and B. Kasemo. “Cabrera–Mott kinetics of oxidation of nm-sized metal particles”. In: *Chemical Physics Letters* 452.4-6 (2008), pp. 285–288.

[162] V. P. Zhdanov and B. Kasemo. “Cabrera-Mott kinetics of oxidation of metal nanowires”. In: *Applied Physics Letters* 100.24 (2012), p. 243105.

[163] A. Ermoline and E. L. Dreizin. “Equations for the Cabrera–Mott kinetics of oxidation for spherical nanoparticles”. In: *Chemical Physics Letters* 505.1-3 (2011), pp. 47–50.

[164] B. D. Anderson and J. B. Tracy. “Nanoparticle conversion chemistry: Kirkendall effect, galvanic exchange, and anion exchange”. In: *Nanoscale* 6.21 (2014), pp. 12195–12216.

[165] B. Chattopadhyay. “Thin film oxidation and the logarithmic rate law”. In: *Thin Solid Films* 16.1 (1973), pp. 117–124.

[166] Q. Jeangros, T. W. Hansen, J. B. Wagner, R. E. Dunin-Borkowski, C. Hébert, J. van herle, and A. Hessler-Wyser. “Oxidation mechanism of nickel particles studied in an environmental transmission electron microscope”. In: *Acta Materialia* 67 (2014), pp. 362–372.

[167] M. Buckett and L. Marks. “Electron irradiation damage in NiO”. In: *Surface Science* 232.3 (1990), pp. 353–366.

[168] M. Knotek and P. Feibelman. “Ion Desorption by Core-Hole Auger Decay”. In: *Physical Review Letters* 40.14 (1978), pp. 964–967.

[169] D. J. Preston, D. L. Mafra, N. Miljkovic, J. Kong, and E. N. Wang. “Scalable graphene coatings for enhanced condensation heat transfer”. In: *Nano letters* 15.5 (2015), pp. 2902–2909.

[170] M. Schulze, R. Reißner, K. Bolwin, and W. Kuch. “Interaction of water with clean and oxygen precovered nickel surfaces”. In: *Fresenius’ Journal of Analytical Chemistry* 353.5-8 (1995), pp. 661–665.

[171] E. A. Lewis, Slater, T J A, E. Prestat, A. Macedo, P. O’Brien, Camargo, P H C, and S. J. Haigh. “Real-time imaging and elemental mapping of AgAu nanoparticle transformations”. In: *Nanoscale* 6.22 (2014), pp. 13598–13605.

[172] A. Berman. “Water vapor in vacuum systems”. In: *Vacuum* 47.4 (1996), pp. 327–332.

[173] M. Henderson. “The interaction of water with solid surfaces: Fundamental aspects revisited”. In: *Surface Science Reports* 46.1-8 (2002), pp. 1–308.

[174] B. G. Ershov and A. V. Gordeev. “A model for radiolysis of water and aqueous solutions of H2, H2O2 and O2”. In: *Radiation Physics and Chemistry* 77.8 (2008), pp. 928–935.

[175] H.-G. Heide. “Observations on ice layers”. In: *Ultramicroscopy* 14.3 (1984), pp. 271–278.

[176] E. Knapek, G. Lefranc, H. G. Heide, and I. Dietrich. “Electron microscopical results on cryoprotection of organic materials obtained with cold stages”. In: *Ultramicroscopy* 10.1-2 (1982), pp. 105–110.

[177] M. L. Hamilton, A. S. Kumar, S. T. Rosinski, and M. L. Grossbeck. *Effects of Radiation on Materials: 19th International Symposium*. 100 Barr Harbor Drive, West Conshohocken, PA 19428-2959: ASTM International, 2000.

[178] A. Winkler, K. D. Rendulic, and K. Wendl. “Quantitative measurement of the sticking coefficient for oxygen on nickel”. In: *Applications of Surface Science* 14.2 (1983), pp. 209–220.

[179] F. Calvo. *Nanoalloys: From fundamentals to emergent applications*. Burlington: Elsevier Science, 2013.

[180] A. Wang, J. Liu, S. Lin, T. Lin, and C. Mou. “A novel efficient Au–Ag alloy catalyst system: preparation, activity, and characterization: Preparation, activity, and characterization”. In: *Journal of Catalysis* 233.1 (2005), pp. 186–197.

[181] A. Sandoval, A. Aguilar, C. Louis, A. Traverse, and R. Zanella. “Bimetallic Au–Ag/TiO2 catalyst prepared by deposition–precipitation: High activity and stability in CO oxidation”. In: *Journal of Catalysis* 281.1 (2011), pp. 40–49.

[182] L. Deng, W. Hu, H. Deng, S. Xiao, and J. Tang. “Au–Ag Bimetallic Nanoparticles: Surface Segregation and Atomic-Scale Structure”. In: *The Journal of Physical Chemistry C* 115.23 (2011), pp. 11355–11363.

[183] D. Belić, R. L. Chantry, Z. Y. Li, and S. A. Brown. “Ag-Au nanoclusters: Structure and phase segregation”. In: *Applied Physics Letters* 99.17 (2011), p. 171914.

[184] E. Casnati, A. Tartari, and C. Baraldi. “An empirical approach to K-shell ionisation cross section by electrons”. In: *Journal of Physics B: Atomic and Molecular Physics* 15.1 (1982), p. 155.

[185] P. Rez. “Electron ionization cross sections for atomic subshells”. In: *Microscopy and microanalysis : the official journal of Microscopy Society of America, Microbeam Analysis Society, Microscopical Society of Canada* 9.1 (2003), pp. 42–53.

[186] F. Hofer and K. Torkar. “Thermodynamik Properties of Solid Gold-Nickel Alloys”. In: *Zeitschrift für Physikalische Chemie* 130 (1982), pp. 229–239.

[187] M. Bienzle, T. Oishi, and F. Sommer. “Thermodynamics and local atomic arrangements of gold-nickel alloys”. In: *Journal of Alloys and Compounds* 220.1-2 (1995), pp. 182–188.

[188] F. Hofer. “Thermodynamische Untersuchungen am System Gold-Nickel”. Dissertation. Graz: Technische Universität Graz, 1981.

[189] R. Abbaschian, L. Abbaschian, and R. E. Reed-Hill. *Physical metallurgy principles*. 4th ed. Stamford, CT: Cengage Learning, 2009.

[190] J. Marian and A. Caro. “Moving dislocations in disordered alloys: Connecting continuum and discrete models with atomistic simulations”. In: *Physical Review B* 74.2 (2006).

[191] B. Predel and E. Zehnpfund. “Thermodynamische Untersuchung des systems gold—nickel”. In: *Thermochimica Acta* 8.3 (1974), pp. 283–290.

[192] A. Perovic, J. Garrett, and J. Kirkaldy. “A unique state of solid matter: Stochastic spinodal modulations in the Au–50Ni transition above 600K”. In: *Scripta Materialia* 60.11 (2009), pp. 1020–1022.

[193] H. Reichert, A. Schöps, I. Ramsteiner, V. Bugaev, O. Shchyglo, A. Udyansky, H. Dosch, M. Asta, R. Drautz, and V. Honkimäki. “Competition between Order and Phase Separation in Au-Ni”. In: *Physical Review Letters* 95.23 (2005).

[194] D. Bochicchio and R. Ferrando. “Size-dependent transition to high-symmetry chiral structures in AgCu, AgCo, AgNi, and AuNi nanoalloys”. In: *Nano letters* 10.10 (2010), pp. 4211–4216.

[195] N. L. Pleth, Besenbacher, I. Stensgaard, Laegsgaard, Engdahl, Stoltze, Jacobsen, and Norskov. “Initial growth of Au on Ni(110): Surface alloying of immiscible metals”. In: *Physical review letters* 71.5 (1993), pp. 754–757.

[196] K. Hirsch, V. Zamudio-Bayer, A. Langenberg, M. Niemeyer, B. Langbehn, T. Moller, A. Terasaki, B. V. Issendorff, and J. T. Lau. “Magnetic moments of chromium-doped gold clusters: the Anderson impurity model in finite systems”. In: *Physical review letters* 114.8 (2015), p. 087202.

[197] M. G. Kibria, S. Zhao, F. A. Chowdhury, Q. Wang, H. P. T. Nguyen, M. L. Trudeau, H. Guo, and Z. Mi. “Tuning the surface Fermi level on p-type gallium nitride nanowires for efficient overall water splitting”. In: *Nature communications* 5 (2014), p. 3825.

[198] L. S. Weinman, T. W. Orent, and T. S. Liu. “Auger study of Cr/Au thin films deposited on alumina and sapphire”. In: *Thin Solid Films* 72.1 (1980), pp. 143–150.

[199] A. M. Arévalo-López and M. A. Alario-Franco. “Reliable method for determining the oxidation state in chromium oxides”. In: *Inorganic chemistry* 48.24 (2009), pp. 11843–11846.

[200] V. A. Jaleel and T. S. Kannan. “Hydrothermal synthesis of chromium dioxide powders and their characterisation”. In: *Bulletin of Materials Science* 5.3-4 (1983), pp. 231–246.

[201] H. E. Schaefer. *Nanoscience*. Nanoscience and technology. Berlin and London: Springer, 2010.

[202] E. C. Tyo and S. Vajda. “Catalysis by clusters with precise numbers of atoms”. In: *Nature nanotechnology* 10.7 (2015), pp. 577–588.

[203] E. Ruska and M. Knoll. “Die magnetische Sammelspule für schnelle Elektronenstrahlen”. In: *Z. Tech. Phys.* 12 (1931), pp. 389–400.

[204] P.-A. Buffat, M. Flüeli, R. Spycher, P. Stadelmann, and J.-P. Borel. “Crystallographic structure of small gold particles studied by high-resolution electron microscopy”. In: *Faraday Discussions* 92 (1991), pp. 173–187.

[205] K. Koga and K. Sugawara. “Population statistics of gold nanoparticle morphologies: direct determination by HREM observations”. In: *Surface Science* 529.1-2 (2003), pp. 23–35.

[206] M. M. J. Treacy, A. Howie, and C. J. Wilson. “Z contrast of platinum and palladium catalysts”. In: *Philosophical Magazine A* 38.5 (1978), pp. 569–585.

[207] C.-C. Chen, C. Zhu, E. R. White, C.-Y. Chiu, M. C. Scott, B. C. Regan, L. D. Marks, Y. Huang, and J. Miao. “Three-dimensional imaging of dislocations in a nanoparticle at atomic resolution”. In: *Nature* 496.7443 (2013), pp. 74–77.

[208] A. Bruma, U. Santiago, D. Alducin, G. Plascencia Villa, R. L. Whetten, A. Ponce, M. Mariscal, and M. José-Yacamán. “Structure Determination of Superatom Metallic Clusters Using Rapid Scanning Electron Diffraction”. In: *The Journal of Physical Chemistry C* 120.3 (2016), pp. 1902–1908.

[209] M. L. Taheri, E. A. Stach, I. Arslan, P. A. Crozier, B. C. Kabius, T. LaGrange, A. M. Minor, S. Takeda, M. Tanase, J. B. Wagner, and R. Sharma. "Current status and future directions for in situ transmission electron microscopy". In: *Ultramicroscopy* 170 (2016), pp. 86–95.

[210] A. Stevens, H. Yang, L. Carin, I. Arslan, and N. D. Browning. "The potential for Bayesian compressive sensing to significantly reduce electron dose in high-resolution STEM images". In: *Microscopy (Oxford, England)* 63.1 (2014), pp. 41–51.

[211] G. Gamez. "Compressed sensing in spectroscopy for chemical analysis". In: *J. Anal. At. Spectrom.* 31.11 (2016), pp. 2165–2174.

[212] U. Kaiser, J. Biskupek, J. C. Meyer, J. Leschner, L. Lechner, H. Rose, M. Stöger-Pollach, A. Khlobystov, P. Hartel, H. Müller, M. Haider, S. Eyhusen, and G. Benner. "Transmission electron microscopy at 20kV for imaging and spectroscopy". In: *Ultramicroscopy* 111.8 (2011), pp. 1239–1246.

[213] D. Knez, P. Thaler, A. Volk, W. Grogger, W. Ernst, and F. Hofer. *HR-STEM investigations of metallic nanoparticles grown with superfluid He-droplets.* Tagung der Österreichischen Physikalischen Gesellschaft. Pöllau, Austria, 24 September 2014.

[214] D. Knez, A. Volk, P. Thaler, E. Fisslthaler, W. Grogger, W. Ernst, and F. Hofer. *HR-STEM investigations of metallic nanoparticles grown with superfluid He-droplets.* 4th ASEM Workshop. Wien, Austria, 8 May 2014.

[215] D. Knez, A. Volk, P. Thaler, E. Fisslthaler, W. Grogger, W. Ernst, and F. Hofer. *HR-STEM investigations of metallic nanoparticles grown with superfluid He-droplets.* 18th International Microscopy Congress. Prague, Czech Republic, 7 September 2014.

[216] D. Knez, A. Volk, P. Thaler, E. Fisslthaler, W. Grogger, W. Ernst, and F. Hofer. *HR-STEM investigations of metallic nanoparticles grown with superfluid He-droplets.* European Workshop on Spatially-Resolved Electron Spectroscopy & Three Country Workgroup meeting on EELS&EFTEM. Graz, Austria, 25 April 2014.

[217] D. Knez, A. Volk, P. Thaler, W. Grogger, W. Ernst, and F. Hofer. *Electron beam induced oxidation of nickel nanoclusters.* 12th Multinational Congress on Microscopy. Eger, Hungary, 24 May 2015.

[218] D. Knez, A. Volk, P. Thaler, W. Grogger, W. Ernst, and F. Hofer. *Electron beam induced oxidation of nickel nanoclusters.* 5th ASEM Workshop. Graz, Austria, 7 May 2015.

[219] D. Knez, A. Volk, P. Thaler, W. Ernst, and F. Hofer. *Atoms in Motion: Electron beam induced dynamics in experiment and simulation.* The 16th European Microscopy Congress 2016. Lyon, France, 31 August 2016.

[220] D. Knez, M. Schnedlitz, M. Lasserus, G. Kothleitner, A. W. Hauser, W. Ernst, and F. Hofer. *In situ studies of high-purity mono- and bimetallic nanostructures in experiment and simulation.* 7th ASEM Workshop. Vienna, Austria, 20 April 2017.

[221] D. Knez, M. Schnedlitz, M. Lasserus, G. Kothleitner, A. W. Hauser, W. Ernst, and F. Hofer. *In situ studies of high-purity mono- and bimetallic nanostructures in experiment and simulation*. Microscopy Conference 2017. Lausanne, Switzerland, 22 August 2017.

[222] D. Knez, M. Dienstleder, W. Grogger, F. Hofer, and E. Fisslthaler. *In situ heating studies of diffusion barrier layers for semiconductor devices*. Microscopy Conference 2017. Lausanne, Switzerland, 21 August 2017.

[223] M. Schnedlitz, M. Lasserus, D. Knez, A. W. Hauser, F. Hofer, and W. E. Ernst. “Thermally induced breakup of metallic nanowires: Experiment and theory”. In: *Phys. Chem. Chem. Phys.* (2017).

[224] D. Knez, M. Dienstleder, W. Grogger, F. Hofer, and E. Fisslthaler. *Thermal vs. beam induced dynamics in the TEM: in situ experiments and simulation*. 13th Multinational Conference on Microscopy 2017. Rovinj, Croatia, 25 September 2017.

Author's Publications

Peer Review Articles

G. Haberfehlner, P. Thaler, D. Knez, A. Volk, F. Hofer, W. E. Ernst, and G. Kothleitner. "Formation of bimetallic clusters in superfluid helium nanodroplets analysed by atomic resolution electron tomography". In: *Nature Communications* 6 (2015), p. 8779.

A. Volk, D. Knez, P. Thaler, A. W. Hauser, W. Grogger, F. Hofer, and W. E. Ernst. "Thermal instabilities and Rayleigh breakup of ultrathin silver nanowires grown in helium nanodroplets". In: *Phys. Chem. Chem. Phys.* (2015).

A. Volk, P. Thaler, D. Knez, A. W. Hauser, J. Steurer, W. Grogger, F. Hofer, and W. E. Ernst. "The impact of doping rates on the morphologies of silver and gold nanowires grown in helium nanodroplets". In: *Phys. Chem. Chem. Phys.* (2015).

P. Thaler, A. Volk, F. Lackner, J. Steurer, D. Knez, W. Grogger, F. Hofer, and W. E. Ernst. "Formation of bimetallic core-shell nanowires along vortices in superfluid He nanodroplets". In: *Physical Review B* 90.15 (2014).

G. Z. Radnóczi, D. Knez, F. Hofer, N. Frangis, N. Vouroutzis, J. Stoemenos, and B. Pécz. "Inclusions in Si whiskers grown by Ni metal induced lateral crystallization". In: *Journal of Applied Physics* 121.14 (2017), p. 145301.

P. Thaler, A. Volk, D. Knez, F. Lackner, G. Haberfehlner, J. Steurer, M. Schnedlitz, and W. E. Ernst. "Synthesis of nanoparticles in helium droplets-A characterization comparing mass-spectra and electron microscopy data". In: *The Journal of chemical physics* 143.13 (2015), p. 134201.

P. Thaler, A. Volk, M. Ratschek, M. Koch, and W. E. Ernst. "Molecular dynamics simulation of the deposition process of cold Ag-clusters under different landing conditions". In: *The Journal of Chemical Physics* 140.4 (2014), p. 44326.

D. Knez, P. Thaler, A. Volk, G. Kothleitner, W. E. Ernst, and F. Hofer. "Transformation dynamics of Ni clusters into NiO rings under electron beam irradiation". In: *Ultramicroscopy* (2016).

M. Schnedlitz, M. Lasserus, D. Knez, A. W. Hauser, F. Hofer, and W. E. Ernst. "Thermally induced breakup of metallic nanowires: Experiment and theory". In: *Phys. Chem. Chem. Phys.* (2017).

Oral Conference Contributions

D. Knez, P. Thaler, A. Volk, W. Grogger, W. Ernst, and F. Hofer. *HR-STEM investigations of metallic nanoparticles grown with superfluid He-droplets*. Tagung der Österreichischen Physikalischen Gesellschaft. Pöllau, Austria, 24 September 2014.

D. Knez, A. Volk, P. Thaler, E. Fisslthaler, W. Grogger, W. Ernst, and F. Hofer. *HR-STEM investigations of metallic nanoparticles grown with superfluid He-droplets*. 4th ASEM Workshop. Wien, Austria, 8 May 2014.

D. Knez, A. Volk, P. Thaler, E. Fisslthaler, W. Grogger, W. Ernst, and F. Hofer. *HR-STEM investigations of metallic nanoparticles grown with superfluid He-droplets*. 18th International Microscopy Congress. Prague, Czech Republic, 7 September 2014.

D. Knez, A. Volk, P. Thaler, E. Fisslthaler, W. Grogger, W. Ernst, and F. Hofer. *HR-STEM investigations of metallic nanoparticles grown with superfluid He-droplets*. European Workshop on Spatially-Resolved Electron Spectroscopy & Three Country Workgroup meeting on EELS&EFTEM. Graz, Austria, 25 April 2014.

D. Knez, A. Volk, P. Thaler, W. Grogger, W. Ernst, and F. Hofer. *Electron beam induced oxidation of nickel nanoclusters*. 12th Multinational Congress on Microscopy. Eger, Hungary, 24 May 2015.

D. Knez, A. Volk, P. Thaler, W. Grogger, W. Ernst, and F. Hofer. *Electron beam induced oxidation of nickel nanoclusters*. 5th ASEM Workshop. Graz, Austria, 7 May 2015.

D. Knez, A. Volk, P. Thaler, W. Ernst, and F. Hofer. *Atoms in Motion: Electron beam induced dynamics in experiment and simulation*. The 16th European Microscopy Congress 2016. Lyon, France, 31 August 2016.

Poster Conference Contributions

D. Knez, M. Schnedlitz, M. Lasserus, G. Kothleitner, A. W. Hauser, W. Ernst, and F. Hofer. *In situ studies of high-purity mono- and bimetallic nanostructures in experiment and simulation*. 7th ASEM Workshop. Vienna, Austria, 20 April 2017.

D. Knez, M. Schnedlitz, M. Lasserus, G. Kothleitner, A. W. Hauser, W. Ernst, and F. Hofer. *In situ studies of high-purity mono- and bimetallic nanostructures in experiment and simulation*. Microscopy Conference 2017. Lausanne, Switzerland, 22 August 2017.

D. Knez, M. Dienstleder, W. Grogger, F. Hofer, and E. Fisslthaler. *In situ heating studies of diffusion barrier layers for semiconductor devices*. Microscopy Conference 2017. Lausanne, Switzerland, 21 August 2017.

D. Knez, M. Dienstleder, W. Grogger, F. Hofer, and E. Fisslthaler. *Thermal vs. beam induced dynamics in the TEM: in situ experiments and simulation*. 13th Multinational Conference on Microscopy 2017. Rovinj, Croatia, 25 September 2017.